



INVESTIGATING ICE MICROPHYSICAL PROCESSES BY COMBINING  
MULTI-FREQUENCY AND POLARIMETRIC DOPPLER RADAR OBSERVATIONS  
WITH LAGRANGIAN MONTE-CARLO PARTICLE MODELLING

INAUGURAL-DISSERTATION

ZUR

ERLANGUNG DES DOKTORGRADES

DER MATHEMATISCH-NATURWISSENSCHAFTLICHEN FAKULTÄT

DER UNIVERSITÄT ZU KÖLN

VORGELEGT VON

LEONIE VON TERZI

AUS STUTTGART

KÖLN, 19. SEPTEMBER 2022

BERICHTERSTATTER:  
DR. STEFAN KNEIFEL  
PROF. DR. YAPING SHAO

TAG DER MÜNDLICHEN PRÜFUNG:  
25.11.2022

## ABSTRACT

---

Clouds and precipitation strongly impact society and the earth system by influencing the water cycle, determining fresh water availability or causing natural disasters such as floods or droughts. However, many aspects of precipitation formation are still poorly understood, causing large uncertainties in the prediction of precipitation. Especially the microphysical processes, which describe the nucleation of cloud particle and their growth into precipitation lack understanding. As globally 63% of precipitation originates from the ice phase, increasing the understanding of ice microphysical processes is crucial to improve precipitation forecast.

The dendritic growth layer (DGL), located at temperatures between  $-20$  and  $-10$  °C, plays an important role in the formation of precipitation. Previous studies have found an increase in particle size and number concentration through depositional growth, aggregation and secondary ice processes. This dissertation investigates ice microphysical processes in the DGL by combining polarimetric and multi-frequency Doppler cloud radar observations with Monte-Carlo Lagrangian particle modelling.

Study I presents a statistical analysis of a three-month polarimetric and multi-frequency Doppler radar dataset. This combination of radar measurements allows to observe the full evolution of ice particle growth, as the polarimetric measurements are indicators of depositional growth and possible secondary ice processes, while the multi-frequency approach gives an indication of the increase in particle size through aggregation and riming. The statistical analysis revealed an increase of aggregate size at  $-15$  °C. The mean size of aggregates is found to be correlated to an updraft with a maximum of approximately  $0.1 \text{ m s}^{-1}$  at  $-14$  °C. The radar observations further indicate the growth of plate-like ice crystals at  $-15$  °C. Unexpectedly, aggregation is found to increase in the DGL alongside an increase in ice particle number concentration. This simultaneous increase necessitates a source of new ice particles, as aggregation is expected to decrease the total number of ice particles. Secondary ice processes, such as collisional fragmentation provide one explanation for this increase in ice particle size. Another possible explanation might be that small ice particles sediment from colder temperatures into the DGL and enhance the number concentration locally. The third explanation is linked to the observed updraft, as this updraft might increase the super-saturation with respect to ice at  $-15$  °C, leading to the activation of ice nucleating particles and a subsequent increase in ice particle number and growth of plate-like particles. Unfortunately, radar observations do not observe the formation of particles directly, it is difficult to predict the origin of the particles responsible for the increase in particle concentration and observed polarimetric signatures further.

With the observational dataset as a constrain, Study II uses the Monte-Carlo Lagrangian particle model McSnow to investigate the origin of the increase in ice particle number concentration in the DGL further. The comparison of the observations and McSnow simulations indicate that the particles responsible for the polarimetric signatures and increase in number concentration need to be nucleated at temperatures close to  $-15$  °C. This might indicate that in the observed clouds, sedimenting ice particles into the DGL play a lesser role. The McSnow simulations further indicate that neither collisional

fragmentation nor new ice particles due to activation of ice nucleating particles can explain the observed multi-frequency and polarimetric observations. A combination of both processes might explain the observed signatures.

This dissertation shows the potential of a combination of radar observations and modelling for increasing the understanding of microphysical processes in clouds. However, further laboratory studies are needed in order to further constrain the processes in the DGL and validate the findings of this dissertation.



## CONTENTS

---

1	INTRODUCTION	1
1.1	Motivation	1
1.2	Objectives and outline	5
1.2.1	Study I: Statistical analysis of ice microphysical processes in the dendritic growth layer	5
1.2.2	Study II: Investigating ice microphysical processes in the DGL with McSnow	5
2	THEORY	7
2.1	Ice microphysical processes	7
2.1.1	Ice crystal formation	7
2.1.2	Ice crystal growth	12
2.2	Observing ice microphysical processes with radar remote sensing	16
2.2.1	Short introduction into scattering from single particles	17
2.2.2	Radar observations of a distribution of particles	19
2.2.3	Doppler spectra and moments	20
2.2.4	Multi-frequency approach	22
2.2.5	Radar polarimetry	24
2.2.6	Summary of radar remote sensing	28
2.3	Modelling of ice microphysical processes	28
2.4	Linking model and observations by forward simulations	29
2.4.1	Short overview of common scattering approximations	29
3	DATA AND METHODS	35
3.1	The TRIPEX-pol dataset: description and processing	35
3.1.1	Description of radars and instruments installed during the TRIPEX-pol campaign	35
3.1.2	Evaluation of Cloudnet temperature and Humidity profiles	36
3.1.3	Processing of the zenith radar dataset	37
3.1.4	Processing of polarimetric dataset	43
3.1.5	Matching of polarimetric and zenith dataset	44
3.2	The Monte-Carlo Lagrangian particle model McSnow	44
3.2.1	Depositional growth	45
3.2.2	Sedimentation	46
3.2.3	Aggregation	46
3.2.4	Riming	47
3.2.5	Secondary ice production	47
3.2.6	1D Model	48
3.3	McRadar: a forward simulation tool for McSnow output	52
3.3.1	McRadar setup	54
4	ANALYSING ICE MICROPHYSICAL PROCESSES IN THE DGL	57
4.1	The MDV slow-down: an updraft in the DGL?	85
5	INVESTIGATING ICE MICROPHYSICAL PROCESSES IN THE DGL WITH MC-SNOW	89
5.1	Habit growth depending on the nucleation temperature	90

5.2	Forward simulations of particle depositional growth in the DGL	93
5.2.1	Description of particle evolution	93
5.2.2	Forward simulations	94
5.3	Investigating secondary spectral modes and their impact on aggregation	101
5.3.1	Impact of PSD on aggregation	101
5.3.2	Influence of a second mode on aggregation and corresponding radar observables	104
5.4	Conclusions	107
6	CONCLUSIONS AND OUTLOOK	109
6.1	Study I: Statistical analysis of ice microphysical processes in the DGL	109
6.2	Study II: Investigating ice microphysical processes in the DGL with McSnow	112
6.3	Outlook	114
A	RELATIVE HUMIDITY OBSERVATIONS	117
B	MCSNOW SIMULATIONS OF AGGREGATION AND SECONDARY MODE	119
B.1	PSD setup of fragmentation mode	119
B.2	Particle properties and forward simulations	119

## LIST OF FIGURES

---

Figure 2.1	Temperature dependent ice nucleating particle concentration	9
Figure 2.2	Ice multiplication factor	9
Figure 2.3	Schematics of secondary ice processes	11
Figure 2.4	Growth regimes of ice crystals	14
Figure 2.5	Schematic of aggregation	16
Figure 2.6	Schematic of Doppler spectrum	21
Figure 2.7	Schematic of particle interaction with electromagnetic wave	23
Figure 2.8	Single particle scattering calculations	23
Figure 2.9	Triple-frequency signatures	25
Figure 2.10	Schematic of interaction of particles with polarised electromagnetic wave	26
Figure 2.11	Schematic of differential phase shift	27
Figure 2.12	Schematic of microphysical models	29
Figure 3.1	Processed and unprocessed W-band Doppler spectra	38
Figure 3.2	Processed and unprocessed Reflectivity of W-band radar	39
Figure 3.3	Reflectivity histograms	40
Figure 3.4	Spectral differential reflectivity	43
Figure 3.5	Histograms of wind direction and velocity	45
Figure 3.6	Inherent growth function	47
Figure 3.7	1D setup of McSnow simulations	49
Figure 3.8	Comparison of physical properties of McSnow and DDA particles	54
Figure 4.1	Schematic of updraft calculation	86
Figure 4.2	Example of detected updraft	87
Figure 4.3	Updraft classified into DWR-KaW classes	88
Figure 5.1	Particle physical properties depending on the nucleation temperature	91
Figure 5.2	Evolution of particle size through depositional growth	95
Figure 5.3	Single particle scattering calculations of McSnow simulation	97
Figure 5.4	Integrated radar moments calculated from McSnow simulations	100
Figure 5.5	McSnow simulation and radar forward simulation with varying PSD	102
Figure 5.6	Particle properties differences	105
Figure 6.1	Overview of observations and models	110
Figure A.1	Distribution of relative humidity	117
Figure B.1	PSD of fragments during graupel-graupel collisions	119
Figure B.2	Particle properties differences narrow and wide PSD	120
Figure B.3	McSnow simulation with second mode caused by primary nucleation	121
Figure B.4	Particle properties differences with second mode caused by nucleation	122

Figure B.5	McSnow simulation with second mode caused by fragmentation	123
Figure B.6	Particle properties differences with second mode caused by fragmentation	124

## LIST OF TABLES

---

Table 2.1	Radar bands	17
Table 3.1	Technical specifications of the radars	36
Table 3.2	Setup of bimodality study with McSnow	52
Table 3.3	Setup of forward simulation of McSnow output	55

## INTRODUCTION

---

### 1.1 MOTIVATION

Clouds cover approximately 70% of earth's surface (e.g., Stubenrauch et al., 2013) and are important for the earth system and society as they influence the earth's radiative budget and water cycle. Clouds are an essential contributor to the water cycle by transporting and distributing water globally (chapter 1, Lohmann, 2016). Especially precipitation is important, as it determines the freshwater availability on earth's surface. Therefore, predicting when, where and how much a cloud is precipitating has a large societal and environmental impact. On the one hand, precipitation enables food stability. On the other hand, extreme precipitation rates can lead to floods (e.g. Ward et al., 2020), endangering millions of people per year. The recent flooding event on 14<sup>th</sup> and 15<sup>th</sup> July 2021 has lead to damages in Germany, Belgium, Netherlands, Austria and Switzerland. In parts of western Germany extreme rainfall amounts of up to 150 mm were observed in 24 hours. The states of North Rhine-Westphalia and Rhineland-Palatinate reported 184 deaths, more than 800 people injured and an estimated cost of damage of more than 20.3 billion Euros (Bundesministerium des Inneren und für Heimat, 2022).

Despite the importance of precipitation for the earth system and society, many aspects of cloud processes and precipitation formation still remain poorly understood. This leads to large uncertainties and misrepresentations in numerical weather prediction models as well as in climate models (Boucher et al., 2013; Eliasson et al., 2011). Especially microphysical processes, which describe the micro-scale physical and chemical processes acting on individual cloud and precipitation particles (hereafter referred to as hydrometeors) cause the largest uncertainties (Boucher et al., 2013). These uncertainties arise from a gap of knowledge and the difficulty to represent these processes in models (Morrison et al., 2020). The main issue is the complexity of microphysical processes, which are characterised by a large variety of hydrometeor shapes and sizes as well as complex interactions between different hydrometeors and interactions between hydrometeors and the (thermo-)dynamic environment (Morrison et al., 2020). Further issues arise as the physical processes in clouds are taking place over a multitude of scales, which can not be resolved. Therefore, microphysical processes need to be parameterised in numerical weather prediction models and climate models (Morrison and Milbrandt, 2015).

Globally, more than 70% of precipitation is found to be generated via the ice phase (e.g., Field and Heymsfield, 2015; Heymsfield et al., 2020; Mülmenstädt et al., 2015). Most precipitating particles are therefore first experiencing ice growth processes, such as depositional growth, aggregation or riming. If the particles sediment into temperatures regions warmer than 0 ° C, the particles melt and reach the ground as rain. Several aspects of the formation and subsequent growth of ice remain poorly understood. In order to form an ice particle in the atmosphere, either temperature colder than −38 ° C, where ice particles are nucleated homogeneously, or ice nucleating particles (INP) are needed (chapter 8, Lohmann, 2016; Pruppacher and Klett, 1997). However, (airborne) in situ observations have measured ice particle concentrations that often exceed the

number of INP by several orders of magnitude (e.g. Cantrell and Heymsfield, 2005; Hobbs and Rangno, 1985, 1990, 1998; Mossop, 1985; Schwarzenboeck et al., 2009). In a recent study, Wieder et al., 2022 observed a factor of 80 more ice particles than INP at temperatures between 0 and  $-30^{\circ}\text{C}$ . Mignani et al., 2019 found that one in eight ice crystals nucleated at temperatures in the vicinity of  $-15^{\circ}\text{C}$  did not contain an INP. Several mechanisms, frequently referred to as secondary ice production (SIP), have already been proposed in the 1950s to 1970s to explain this discrepancy in INP and ice particle number concentration. However, since then, little progress has been made in understanding SIP. According to Korolev et al., 2020 the main reason for this is that numerical models have focused on only one possible SIP (rime splintering), while other mechanisms have gotten less attention. For example, fragmentation due to ice-ice collision, a process which might be active over a large temperature range, has thus far only been investigated in three laboratory studies (Griggs and Choularton, 1986; Takahashi et al., 1995; Vardiman, 1978).

After ice particles have been nucleated, they are growing into ice crystals via depositional growth. Depending on the ambient temperature and super-saturation with respect to ice, the crystals grow into different shapes, such as dendrites, needles or bullet-rosettes (e.g., Bailey and Hallett, 2009; Bailey and Hallett, 2004; Libbrecht, 2017; Lohmann, 2016; Takahashi, 2014). Four main growth regimes have been identified in (airborne) in situ observations and laboratory studies: the plate-like growth regime between 0 and  $-5^{\circ}\text{C}$ , the columnar growth regime at temperatures between  $-5$  and  $-10^{\circ}\text{C}$ , a second plate-like growth regime between  $-10$  and  $-20^{\circ}\text{C}$  and a regime at temperatures colder than  $-20^{\circ}\text{C}$ , where a variety of shapes is found to occur simultaneously (e.g., Bailey and Hallett, 2009). Why particles are developing these distinct shapes depending on the ambient temperature, and how this is coupled to the ambient super-saturation with respect to ice is largely unknown (Libbrecht, 2017).

Rarely, single ice crystals can grow large enough to reach the ground. Most snowfall observed on the ground consists of aggregates (chapter 8, Lohmann, 2016). Aggregation is a process where a larger, faster falling ice particle collects a smaller, slower falling ice particle. Aggregation is increasing the size of ice particles rapidly, while reducing the total number concentration of ice particles (e.g., Field and Heymsfield, 2003; Kajikawa et al., 2000; Lawson et al., 1998, 1993). Many aspects of the aggregation process are difficult to describe and remain poorly understood. For example, the aggregation efficiency ( $E_{agg}$ ), which is the product between the collision efficiency ( $E_c$ ) and the sticking efficiency ( $E_s$ ), is a crucial component in order to understand and parameterise the aggregation process (Connolly et al., 2012). However,  $E_{agg}$  has not been investigated by many studies in the laboratory or by (airborne) in situ observations. Hosler and Hallgren, 1960 made a comprehensive study of  $E_{agg}$  of ice spheres in the laboratory. They found a maximum of  $E_{agg}$  at  $-15^{\circ}\text{C}$ . By analysing aircraft in situ observations, Mitchell, 1988 showed the temperature dependency of  $E_s$ , with a distinct peak between  $-12.5$  and  $-17^{\circ}\text{C}$ . In a later study, Connolly et al., 2012 investigated  $E_{agg}$  of ice crystals in a cloud chamber. By combining the laboratory observations with a bin model, they observed a clear maximum of  $E_{agg}$  and  $E_s$  at  $-15^{\circ}\text{C}$ . Phillips et al., 2015 derived a parameterisation and theoretical description of  $E_s$  based on the laboratory studies by Hosler and Hallgren, 1960 and Keith and Saunders, 1989. He concluded that snow aggregation is forming a positive feedback mechanism, as crystals collected by an aggregate make the aggregate surface rougher and therefore more sticky, which in turn leads to more collected ice crystals. Since there

are only a few laboratory investigations, more work needs to be done in order to fully understand the dependency of  $E_{agg}$  on temperature, shape and size of particles.

Large efforts have been made to improve the understanding of clouds and precipitation processes and to evaluate their representation in models with laboratory studies, in situ and remote sensing observations. Laboratory studies have increased the knowledge on specific ice microphysical processes (IMP) (Bailey and Hallett, 2009; Connolly et al., 2012; Takahashi, 2014; Takahashi et al., 1995), providing detailed information such as process rates, which are crucial to develop microphysical schemes (Morrison et al., 2020). However, laboratory studies lack the representation of the variety of processes and conditions acting on ice particles in natural clouds. In situ observations are able to observe natural clouds and provide a powerful tool to evaluate the laboratory studies and remote sensing observations. However, they do not observe microphysical processes directly, but rather their effect on the particle size distribution (PSD) and particle physical properties. Also, they are suffering from sampling problems, as they are only providing a 1D snapshot (e.g. Illingworth et al., 2007). Further, airborne in situ observations might affect the cloud properties, as for example shattering of ice particles on probes has been frequently observed, which artificially increases the ice particle concentration (Isaac et al., 2006; Korolev and Isaac, 2005). Remote sensing observations are a powerful tool, as they allow to retrieve cloud and precipitation properties while also providing large temporal and potentially spatial coverage. However, the observations of microphysical processes and particle properties with remote sensing instruments are indirect and therefore challenging (Heymsfield et al., 2018). Especially the large amount of assumptions required regarding the particle shape, lead to large uncertainties in retrieved particle properties. The large variety of complex shapes of ice particles leads to a large variety of possible scattering properties of observed particles. This large variety can not be considered on the individual particle level. Rather, it is often assumed that a specific shape of particle is representative for all observed particles (such as a spheroid, or more complex aggregate models as the one provided in Leinonen and Moisseev, 2015), causing large uncertainties in the retrieved particle properties (e.g. Mróz et al., 2021).

In recent years, the coverage of cloud remote sensing has increased. New technology allowed for the instalment of radars on satellites (e.g. Stephens et al., 2018), providing global information on for example cloud phase or ice and liquid water content. Further, remote sensing supersites and cooperations between different institutions dedicated to the investigation of cloud and precipitation processes have been growing globally. For example, Cloudnet (Illingworth et al., 2007) is a cooperation currently combining 22 sites. Cloudnet is focused on the evaluation of cloud processes in forecast models. Cloudnet combines model output with remote sensing observations to provide detailed information about cloud properties such as liquid water content, ice water content, sizes of drizzle drops or hydrometeor classifications. Another example is the Atmospheric Radiation Measurement (ARM) facility, which provides in situ and remote sensing observations of aerosol, clouds and precipitation and is aimed to improve the understanding and model representation of clouds as well as their interactions with the earth system. While ARM is running three fixed-location research sites, it also provides unique possibilities to use their observational facilities for field campaigns, especially in areas with sparse observational coverage. For example, the AWARE campaign (Lubin et al., 2020) investigated aerosol and cloud microphysics in Antarctica. Moreover, close to Cologne, the Jülich ObservatorY for Cloud Evolution Core Facility (JOYCE-CF) aims to characterise the micro- and



macrophysical processes of clouds and precipitation (Löhnert et al., 2015). At JOYCE-CF combined observations of various instruments, including a microwave radiometer, a disdrometer, X- and Ka-band Doppler cloud radars, and ceilometers are continuously running. Furthermore, different campaigns were conducted at JOYCE-CF, including the Triple-frequency and polarimetric radar experiment for improving process observation of winter precipitation (TRIPEX) campaign (Dias Neto et al., 2019).

Radars are especially suited to investigate cloud and precipitation processes, as they operate in the microwave frequency range and can penetrate through clouds. Weather radars operate at frequencies between 1 and 10 GHz (Raghavan, 2003) and can detect the backscattered signal of precipitation. Cloud radars operate at larger frequencies (e.g. Ka-band at 35 GHz and W-band at 94 GHz) and are thus able to detect the smaller cloud particles. Already in the 1940s and 50s, radars have been used to detect precipitation (Raghavan, 2003). Since then, technological advances have increased the capabilities of radars. For example, polarimetric observations provide information about the shape, orientation and phase of hydrometeors and are thus a powerful tool to investigate IMP, especially depositional growth and SIP (Kumjian et al., 2022). The distinct shapes that the ice crystals grow into via deposition can be detected. This allows to study regions that are populated with ice crystals. Especially at temperatures in the vicinity of  $-15^{\circ}\text{C}$ , strong polarimetric signatures have been detected, suggesting the enhanced depositional growth of dendritic particles (Andrić et al., 2013; Griffin et al., 2018; Kennedy and Rutledge, 2011; Moisseev et al., 2015; Oue et al., 2018; Schrom and Kumjian, 2016; Schrom et al., 2015; Trapp et al., 2001, among others). An increasing number of studies have combined polarimetric observations with vertically pointing Doppler cloud radar observations (Moisseev et al., 2015; Oue et al., 2018). Vertically pointing Doppler radars have the ability to measure the particles terminal velocity, thus giving further constraints on the observed particle populations. For example, while the fall velocity of snow aggregates is found to saturate at  $1\text{ m s}^{-1}$ , ice crystals are generally smaller and thus have slower fall velocities (e.g., Karrer et al., 2020).

While polarimetric radars can provide useful information about depositional growth, other microphysical processes, such as riming or aggregation can not be detected unambiguously. By combining observations of two or more radars, with one radar operating at smaller frequencies than the other, information about the mean size of the observed particle population can be obtained (e.g. Kneifel et al., 2011; Liao et al., 2005; Liao et al., 2008; Matrosov, 1992). Studies with such a multi-frequency radar setup have frequently observed an increase in the aggregate size at  $-15^{\circ}\text{C}$  (e.g. Barrett et al., 2019; Dias Neto et al., 2019; Ori et al., 2020).

Even though polarimetric and multi-frequency radar observations provide a powerful tool to investigate IMP, these processes are not observed directly. Only the effect of the ice microphysics on certain aspects of the particle properties (such as shape or size) can be observed. For example, the increase in size of plate like particles at  $-15^{\circ}\text{C}$  increases the received polarimetric signal. However, which processes have led to the nucleation and the appearance of these particles can not be observed. A model with a detailed implementation of IMP can help to further investigate these processes. Especially Monte-Carlo Lagrangian particle models, which are tracing the growth history of particles, can be used for microphysical studies (e.g. Brdar and Seifert, 2018; Grabowski et al., 2019).



## 1.2 OBJECTIVES AND OUTLINE

This dissertation was carried out in the framework of the project PROM-IMPRINT. The main objective of this project is to improve the understanding of IMP and their representation in models by combining state-of-art radar observations with Lagrangian Monte-Carlo particle modelling linked by a radar forward operator. The analyses provided in this dissertation are aimed at increasing the understanding of IMP within the dendritic growth layer (DGL). The DGL, usually located at temperatures between  $-20$  and  $-10$  °C, plays a significant role in the production of precipitation, since it influences the growth and evolution of ice particles significantly (e.g. Trömel et al., 2019).

## 1.2.1 Study I: Statistical analysis of ice microphysical processes in the dendritic growth layer

The combination of multi-frequency and polarimetric Doppler cloud radar observations provides a unique opportunity to combine the advantages of both approaches. The multi-frequency setup provides detailed observations of the increase of ice particle size through aggregation (and riming), while the polarimetric setup allows to observe ice crystal growth and helps to identify regions where SIP might be increasing the number concentration of ice crystals. Thus, this setup enables a complementary observation strategy of IMP. Most previous studies investigating IMP have focused on single case study observations. In this dissertation, a statistical analysis of three months of observations of winter clouds is presented. This analysis allows to identify correlations between IMP, estimate the significance of different IMP as well as their natural variability and provide constraints for microphysical models such as the Monte-Carlo Lagrangian particle model (McSNOW) (Brdar and Seifert, 2018). The analysis is focused on the correlation between enhanced aggregation, plate-like particle growth and SIP frequently observed in the DGL.

## 1.2.2 Study II: Investigating ice microphysical processes in the DGL with McSNOW

In Study I, three possible explanations for the particle evolution in the DGL are hypothesised:

1. Particles are sedimenting from higher altitudes into the DGL. Due to enhanced depositional growth in the vicinity of  $-15$  °C they grow into plate-like particles, thus explaining the observed polarimetric signatures.
2. An updraft found at  $-15$  °C enhances the relative humidity over ice ( $RH_i$ ) locally and leads to the activation of INP. The newly formed ice particles are then growing into plate-like particles, hence explaining the observed polarimetric signatures.
3. The collisions of ice particles during aggregation leads to fragmentation of fragile parts of aggregates or other ice particles, causing the observed polarimetric and multi-frequency signatures.

McSNOW allows the implementation of the current knowledge of IMP and provides the possibility to track the growth history of particles. By coupling McSNOW with a radar forward operator and comparing specific McSNOW simulations with the statistical observations, these hypothesis are investigated in detail.

*PROM-IMPRINT:  
First phase project of  
PROM (Fusion of  
Radar Polarimetry  
and Numerical  
Atmospheric  
Modelling Towards  
an Improved  
Understanding of  
Cloud and  
Precipitation  
processes):  
Understanding Ice  
Microphysical  
Processes by  
combining  
multi-frequency and  
spectral Radar  
polarImetry aNd  
super-parTicle  
modelling*

This dissertation is structured as follows: [Chapter 2](#) provides an introduction into [IMP](#) and how they can be observed with radar remote sensing and modelled with microphysical models. Further, the link between model and observations through forward simulations is introduced. The dataset used in Study I is introduced in [Chapter 3](#). All necessary processing steps, minimising the effects of attenuation and radar miscalibration, as well as the removal of spurious data are described there. Further, [McSnow](#) and the representation of [IMP](#) in [McSnow](#) are introduced. This chapter also gives an overview over the simulation setup in Study II as well as the radar forward operator that links [McSnow](#) and the observations. Study I was published in von Terzi et al., [2022](#) and is included here in [Chapter 4](#) together with further analyses concerning an observed updraft at  $-15^{\circ}\text{C}$ . [Chapter 5](#) comprises Study II. Finally, [Chapter 6](#) summarises and concludes the results of Study I and II and provides an outlook to future work.

This chapter provides an overview of important ice microphysical processes (Section 2.1). Remote sensing techniques that can be used to observe these processes are introduced in Section 2.2. Microphysical modelling techniques that can be used to simulate these processes are introduced in Section 2.3. Finally, simulations of radar variables based on model output (i.e. forward simulations) are introduced in Section 2.4 in addition to scattering properties of ice particles as a tool to compare model simulations and remote sensing observations in the observation space.

## 2.1 ICE MICROPHYSICAL PROCESSES

Ice microphysical processes play a significant role in the production of precipitation, for the life cycle of clouds and the interaction of clouds with radiation. The focus of this thesis is on ice microphysical processes occurring in frontal mid-latitudes winter clouds. These clouds are typically stratiform clouds, extending over 5 to 10 km vertically and lasting several hours. These clouds are exhibiting a large variety of ice microphysical processes. The following sections give an overview of the most relevant ice microphysical processes in stratiform clouds. First, an ice particle is nucleated via primary nucleation (Section 2.1.1.1) or secondary ice production (SIP) (Section 2.1.1.2). Primary nucleation refers to the nucleation of ice particles via heterogeneous (i.e. nucleation on an INP) or homogeneous nucleation (i.e. nucleation through the spontaneous formation of an ice cluster, usually at temperatures colder than  $-40^{\circ}\text{C}$ ). In contrast, SIP requires the presence of preexisting ice particles. Through various processes, these ice particles can act as INP. Second, the particles grow via depositional growth into ice crystals (Section 2.1.2.1). When the particles are large enough, they can collide with other ice particles (Section 2.1.2.2) or with super-cooled liquid water (SLW) droplets (Section 2.1.2.3), forming aggregates or rimed particles. If the particles cross the  $0^{\circ}\text{C}$  isotherm, they start to melt. Once melted, warm microphysical processes such as collision-coalescence or evaporation might occur.

### 2.1.1 Ice crystal formation

In order for ice particles to form in the atmosphere, large enough super-saturations with respect to ice, cold enough temperature for homogeneous nucleation or INP are needed. The processes that form an ice particle in clouds can be grouped into primary and SIP. Primary ice production can happen locally in clouds, as the ice particle is formed via homogeneous or heterogeneous nucleation (Section 2.1.1.1), or ice particles can be externally introduced by seeder-feeder processes from a higher cloud or levitated from the ground. Once ice particles are present, SIP can take place (Section 2.1.1.2). Then, new ice particles are formed via various processes involving the preexisting ice particles (e.g. formation of new ice on ice splinters that formed during the freezing of super-cooled liquid droplets)

#### 2.1.1.1 Primary ice production

During primary ice production, ice particles can be formed via multiple different nucleation processes, which can be grouped into homogeneous and heterogeneous nucleation. Homogeneous nucleation denotes all nucleation processes of ice particles without an ice nucleating particle. Homogeneous nucleation can happen from the vapour to the ice phase or from the liquid to the ice phase. Nucleation in general denotes a phase transition (from vapour to liquid, vapour to ice or liquid to ice), where a thermodynamically stable cluster forms (i.e. a cluster of ice) and grows within the meta-stable parent phase (i.e. liquid water) (chapter 8.1, Lohmann, 2016). For all nucleation processes, an energy barrier between the parent phase and the "new" phase has to be overcome. Because of this energy barrier, homogeneous nucleation from vapour to ice is very unlikely, as the super-saturation with respect to water ( $S_w$ ) needed are much higher than observed in the atmosphere (e.g.  $S_w \approx 13\%$  at  $-20^\circ\text{C}$ , Figure 8.2, Lohmann, 2016). In contrast, homogeneous nucleation of ice from the liquid phase becomes more likely at colder temperatures, as the surface tension between liquid and ice decreases and therefore the energy barrier decreases. For homogeneous nucleation, a spontaneous cluster of ice (also called ice embryo) has to form within a SLW droplet, which leads to the instantaneous freezing of the entire droplet. As has been shown by Pruppacher and Klett, 1997, spontaneous freezing occurs at temperatures colder than  $-38^\circ\text{C}$ .

Heterogeneous nucleation denotes all nucleation processes, where ice particles are formed on the surface of an INP. By offering a surface which provides an ice-like structure, the INP encourages the phase transition of vapour or liquid to ice, as it reduces the energy barrier. Different particles can serve as INP such as bacteria, pollen, dust particles or aerosols. However, since an ice-like surface structure is needed to nucleate ice particles, only approximately one in  $10^5$  to  $10^6$  aerosol particles are suited as an INP (Chapter 8.1.2, Lohmann, 2016). Kanji et al., 2017 provided an overview of the INP measured globally in dependency of the temperature (see Figure 2.1). Even if the measured number concentration of INP at each temperature has a large spread, the number of INP reduces with increasing temperatures. At  $-15^\circ\text{C}$ , INP concentrations ranging typically from  $10^{-3}$  to 2 INP per Litre can be found (Figure 2.1). At  $-10^\circ\text{C}$ , the number of INP observed has reduced to  $10^{-6}$  to 0.02 INP per Litre.

#### 2.1.1.2 Secondary ice production

As was explained in Section 2.1.1.1, INP are necessary to nucleate new ice particles at temperatures warmer than  $-38^\circ\text{C}$ . The number of ice particles in these temperature regions should therefore be determined by the number of INP present. However, ice particle concentrations measured by (airborne) in-situ observations (Cantrell and Heymsfield, 2005; DeMott et al., 2010; Hobbs and Rangno, 1985, 1990, 1998; Mossop, 1985; Schwarzenboeck et al., 2009, among others), often exceed the number of available INP by several orders of magnitude. Wieder et al., 2022 retrieved an ice multiplication factor (i.e. the ratio of ice particles to INP concentration) of 80 in wintertime orographic clouds, indicating that throughout most temperature regimes, a factor of 80 more ice particles than INP were observed. Their results agree with many previous studies, as can be seen in Figure 2.2. This excess in ice particle number concentration compared to the concentration of INP is in general explained by SIP.

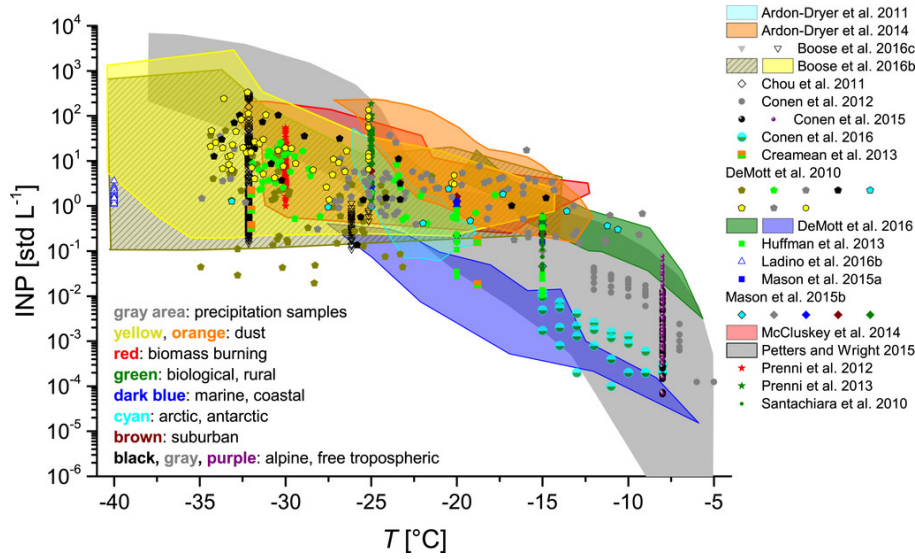


Figure 2.1: Summary of INP concentrations taken from various in-situ field campaigns. This graph is taken from Kanji et al., 2017. ©American Meteorological Society. Used with permission.

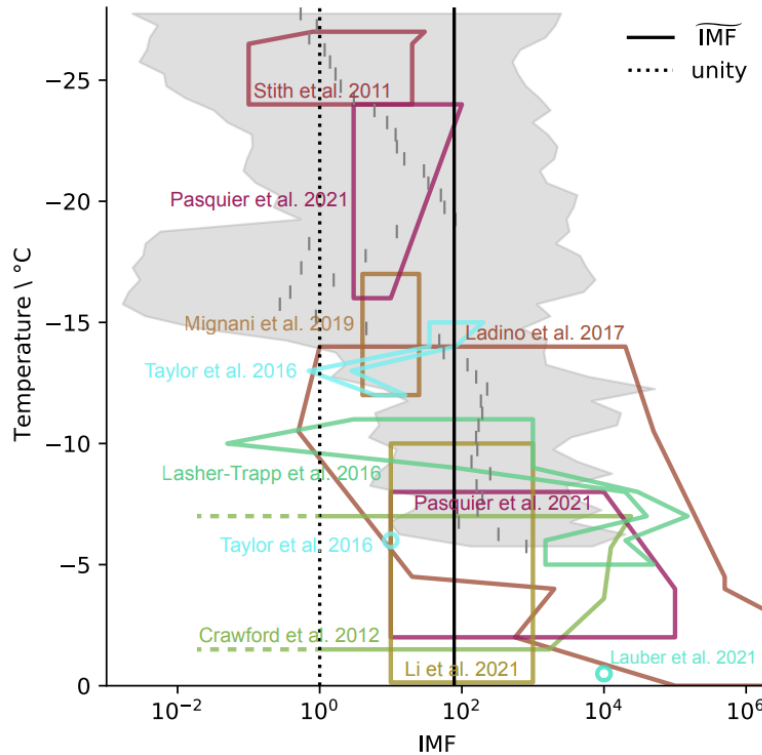


Figure 2.2: Ice multiplication factor (IMF) taken from Wieder et al., 2022. The grey area indicated the 10<sup>th</sup> and 90<sup>th</sup> percentile of the measured distribution, while the vertical, grey lines indicate the median. Their results are compared to the results of previous field observations. The black dashed line indicates unity and the solid black line the median IMF of their study independent of the temperature. This figure was taken from Wieder et al., 2022 and redistributed under the creative commons attribution 4.0 License.

**SIP** are processes, where ice is formed in the atmosphere as a result of processes involving pre-existing ice particles. New ice particles are e.g. formed on the splinters that formed during the freezing of **SLW** droplets. There is a variety of **SIP** that have been hypothesised in theoretical studies and/or observed in laboratory studies, or during in-cloud in-situ observations. In their review of laboratory observations of **SIP**, Korolev and Leisner, 2020 summarised the main **SIP** mechanisms observed during the past 7 decades (Figure 2.3) to droplet fragmentation during freezing, splintering during riming (or Hallett-Mossop process), fragmentation during ice-ice collision, ice fragmentation during thermal shock, fragmentation during sublimation and activation of **INPs** in transient supersaturation.

Fragmentation during freezing (Figure 2.3a) was the first ever proposed **SIP** which might be responsible for enhancing the ice particle number concentration (e.g. Korolev et al., 2020; Mason and Maybank, 1960). Freezing droplets might break when an ice shell is first forming on the outside of the water particle, trapping liquid water inside a shell of ice. Since water expands when freezing, pressure builds up inside the ice shell. This built up in pressure can eventually break the shell and produce ice fragments or cause a spicule to penetrate through the surface of the frozen particle. Summarising a variety of laboratory studies Korolev et al., 2020 concluded that the fragmentation of freezing drops depends on a large number of parameters, including the environmental temperature and pressure, droplet size, fall velocity of the droplet, the kind of crystals forming during freezing (i.e. mono-crystalline or poly-crystalline) among others. Most laboratory studies found fragmentation during freezing to occur at temperatures between  $-30$  and  $0$  °C, making it a suitable candidate for the main source of secondary ice (e.g., Korolev et al., 2004, 2020; Lawson et al., 2017).

The Hallett-Mossop (**HM**)-process was first observed by various laboratory observations (Aufdermaur and Johnson, 1972; Bader et al., 1974; Hobbs and Burrows, 1966; Latham and Mason, 1961; Macklin, 1960). In a series of laboratory experiments, Hallett and Mossop, 1974; Mossop and Hallett, 1974 as well as Mossop, 1978, 1985, they found that splinter production during riming is most active in the temperature region of  $-8^{\circ}\text{C} < T < -3^{\circ}\text{C}$ , with a clear maximum at  $-5^{\circ}\text{C}$  and a drop impact velocity of  $2.5\text{m s}^{-1}$ . One splinter was produced per 250 cloud droplets of diameters  $D < 12\mu\text{m}$  and liquid drops of  $D > 24\mu\text{m}$  that hit the ice particle during the riming process. Due to the quantification of the rime-splintering process in Hallett and Mossop, 1974, various **SIP** parameterisations could be formulated and are used in many numerical simulation of clouds (e.g., Cotton et al., 1986). Another process which might happen during riming is the fragmentation due to thermal shock, when a **SLW** droplet rimes on an ice particle. Parts of the latent heat released during the freezing might be transferred onto the ice particle, causing a thermal shock and possible fragmentation due to the expansion of the ice which is in contact with the droplet (Koenig, 1963; Korolev et al., 2020).

Fragmentation of ice-ice collision was already suggested as a process to potential increase the number of ice particles by Findeisen, 1940. 20 years later, when looking at rime-splintering, Macklin, 1960 noticed the fragility of some low-density rime structures that were easily broken off. Thus-far, fragmentation was only investigated in more detail by three laboratory studies (Griggs and Choularton, 1986; Takahashi et al., 1995; Vardiman, 1978). Airborne in-situ observations have observed fragments of dendrites and stellars (Hobbs and Rangno, 1985, 1990, 1998; Rangno and Hobbs, 2001). Fragmentation during ice-ice collision seems to be the most likely explanation for the presence of



these fragments. Unlike other SIP such as the HM-process, collisional fragmentation could provide an explanation of the discrepancy between INP and ice particle number concentration over a wide temperature range. Vardiman, 1978 observed the number of fragments during ice-ice collisions when natural ice crystals collided with a fixed mesh copper screen. In their observations, they did not find large enough numbers of ice fragments during the collision to explain the high crystal concentration observed in many cold clouds. In a later experimental study, Griggs and Choularton, 1986 tested the mechanical strength of rime and vapour-grown crystals. They concluded that in a collision of rimed particles, there is very likely no fragmentation happening. However, in collisions of rimed particles with ice crystals, especially with dendrites, 1 to 2 fragments per collision occurred. Interestingly, dendrites were also found to break through air drag alone at air velocities of  $2 \text{ m s}^{-1}$ . Focusing only on possible graupel-graupel collisions, Takahashi et al., 1995 collided two ice-spheres. On the surface of the first ice sphere, dendritic structures were grown via depositional growth for 15 minutes at water saturation. The surface of the second ice sphere was rimed during those 15 minutes. After 15 minutes, the two spheres were collided at different speeds. The fragments that broke off during the collisions were collected on a metal plate placed below the chamber in which the collisions were performed. The fragments collected there were then allowed to grow by deposition for an additional 10 minutes and then counted under a magnifying glass. The total number of collected particles on the metal plate was multiplied by 4, since visual observations suggested that fragments were also landing outside of the metal plate range. They found a clear maximum of ejected particles at  $-16^\circ \text{ C}$ , with up to approximately 800 fragments. Even though the estimation of ice fragmentation is approximate, and further laboratory studies are clearly needed to constrain this process further and test different dependencies on e.g. particle types or supersaturation, the studies by Takahashi et al., 1995 and Vardiman, 1978 are the basis of various modelling studies (Phillips et al., 2015; Sullivan et al., 2018; Yano and Phillips, 2011; Yano et al., 2016).

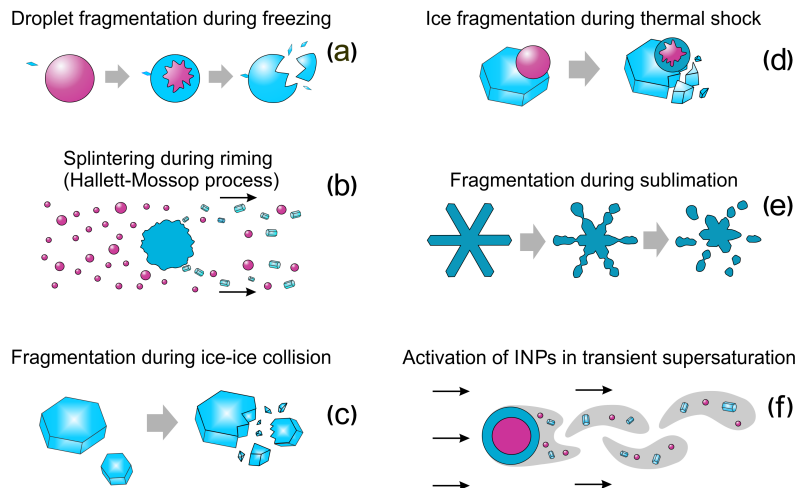


Figure 2.3: Schematics of SIP mechanisms studied in the past decades. This figure was taken from Korolev et al., 2020 and redistributed under the creative commons attribution 4.0 License.

### 2.1.2 Ice crystal growth

Once an ice crystal is formed via primary ice production or [SIP](#), it needs to grow in order to sediment towards the ground as precipitation. In general, an ice particle can grow in two different ways. Either, the particle grows from the vapour phase, where it increases its size molecule by molecule (i.e. depositional growth). Or the particle can grow by collecting other particles while it is moving through the cloud (i.e. aggregation and riming). The ice particles first increase in size via depositional growth of water vapour onto the ice particle ([Section 2.1.2.1](#)). Depending on the temperature and supersaturation, the ice particle grows into a specific shape (habit), such as a dendrite or needle. Once the particle has grown enough to sediment towards the ground, aggregation can happen ([Section 2.1.2.2](#)). There, particles collide and possibly stick together, forming an aggregate. Aggregation is an efficient process in increasing particle size and reducing the total number of ice particles. In the presence of [SLW](#), particles can grow further by the deposition of droplets onto the ice particle. This process is called riming ([Section 2.1.2.3](#)). If particles sediment to temperatures warmer than 0° C, they start to melt. Below the melting layer ([ML](#)), particles can experience further liquid microphysical processes (e.g. diffusional growth, collision-coalescence, droplet break-up). If the particles are large enough, they reach the ground as rain or snow.

#### 2.1.2.1 Depositional growth

Depositional growth happens once the partial vapour pressure around the ice particle exceeds the saturation vapour pressure of the surface of an ice particle. In general, depositional growth happens in three steps. First, water vapour gets transported via diffusion or air flow towards the surface of the particle. Second, the water molecule deposits onto the ice particle and changes the phase. During this phase change, latent heat is released. Further, the concentration of water vapour gets reduced in the vicinity of the ice particle. This reduction in water vapour in turn increases the gradient of water vapour concentration, which increases the diffusional transport of water vapour towards the particle. In a third step, the released latent heat gets transported away from the ice particle by thermal diffusion. The mass growth of an ice particle can be derived from Maxwell's law of mass growth. For the derivation of the mass growth law, the reader is referred to chapter 8, Lamb and Verlinde, [2011](#). Using the formulation from Shima et al., [2020](#), their equation 11 and 12, the mass growth is described by

$$\frac{dm}{dt} = 4\pi CD_v \bar{f} \frac{S_i - 1}{F_k^i + F_d^i} \quad (2.1)$$

with the mass ([m](#)) of the particle, the water vapour diffusivity in air ([D<sub>v</sub>](#)), ambient saturation ratio with respect to ice ([S<sub>i</sub>](#)) (i.e.  $S_i := e_i/e_{s,i}(T_i)$ ), with vapour pressure ([e<sub>i</sub>](#)) and saturation vapour pressure over ice ([e<sub>s,i</sub>](#))(*T*) at temperature *T*, and the particle-average ventilation coefficient ([f̄](#)). [f̄](#) is needed because the particles are falling while growing, increasing the transport of water vapour towards the particle surface. The electrical capacitance of the ice particle ([C](#)). The capacitance is dependent on the size and shape of the particle (see also [Section 3.2](#)). Further,

$$F_k^i = \left( \frac{L_s}{R_v T} - 1 \right) \frac{L_s}{c_a T}, \quad F_d^i = \frac{R_v T}{D_v e_s^i(T)} \quad (2.2)$$



where  $F_k^i$  is the thermodynamic term related to the latent heat release due to the phase change from vapour to ice and the transport of the latent heat away from the particle.  $F_d^i$  is describing the diffusion of water vapour towards the ice particle, with the latent heat of sublimation ( $L_s$ ), the thermal conductivity of moist air ( $c_a$ ) and the gas constant of water vapour ( $R_v$ ).

When growing by deposition, ice crystals can develop distinct shapes, so called ice habits. Already Johannes Kepler was fascinated by the many habits an ice crystal can obtain. In his book "On the six-cornered snowflake", written in 1611 he tried to explain the tetrahedral structure that underlies the ice crystal form. Over the centuries, many scientists have put an effort into studying the details of ice crystal growth from the water vapour to understand the development of ice crystal habits. The ice crystal grows such that the surface energy per volume is minimised (chapter 8.2, Lohmann, 2016). Due to different surface tensions, this minimum surface energy depends on the ambient temperature and ice super-saturation the particle experiences while growing (Bailey and Hallett, 2009; Bailey and Hallett, 2004; Libbrecht, 2017; Lohmann, 2016; Takahashi, 2014, among others). In his Figure 1, Libbrecht, 2017 nicely illustrates this dependency on the temperature and supersaturation (also shown here in Figure 2.4). The habits developed by ice crystals can be grouped into primary and secondary habits (chapter 8, Lamb and Verlinde, 2011). Primary habits are defined by the aspect ratio of the particle and depend on the temperature where the crystal is growing. At a constant super-saturation, between 0 and  $-5^\circ\text{C}$  and  $-10$  and  $-20^\circ\text{C}$  the growth rate of the prism face exceeds the rate of the basal face, thus growing plate-like. When grown in pure water vapour environments and at constant vapour pressure, the growth rate of the prism face has a local maximum close to  $-15^\circ\text{C}$ , where the particles are growing most efficiently into plate-like particles (e.g. Lamb and Scott, 1972). Vice versa, between  $-5$  and  $-10^\circ\text{C}$  the basal face is growing more strongly, resulting in columnar particles. The maximum basal face growth rate in a pure water vapour environment was found at  $-7^\circ\text{C}$  (Lamb and Scott, 1972). In high super-saturation environments, the water vapour deposition onto the crystal is faster than the diffusion of water vapour towards the crystal. Therefore, the water vapour concentration around the crystal is not homogeneous, resulting in shapes that differ from the primary habits. Secondary habits develop, where e.g. a dendrite is formed due to local maxima in the water vapour concentration at the 6 corners of the ice crystal and subsequent branching. Why the particle habit strongly depends on temperature and super-saturation is not completely understood yet. Libbrecht, 2017 summarises the state of the art theories that might explain especially the temperature dependence of the primary habit. The most challenging aspect is understanding the attachment kinetics, i.e. how rapidly water vapour molecules attach to the different basal or prism surfaces of the ice crystal, thus determining if the crystal grows plate-like or columnar.

In contrast to the growth by vapour of a cloud droplet, an ice crystal grows very efficiently through depositional growth and may even reach the surface as a single crystal (chapter 8.3 Lohmann, 2016). Takahashi, 2014, among others has shown that ice crystals can reach sizes of 1.5 mm when grown by deposition at liquid water saturation for 10 minutes. The depositional growth is so efficient, because in general the ice crystal observes a significantly higher super-saturation in clouds as compared to water droplets. While a liquid droplet might be just saturated at 100% relative humidity with respect to water, an ice particle in the same environment will experience a super-saturation of e.g. close to 30% at  $-12^\circ\text{C}$ . This is caused by the smaller saturation vapour pressure of

ice compared to that of water. This difference in saturation vapour pressure reaches a maximum at  $-12^{\circ}\text{C}$ , where the environment is super-saturated with respect to ice of close to 30% at liquid water saturation. If the environment is sub-saturated with respect to water, it can still be super-saturated with respect to ice. In case of a mixed-phase cloud, meaning a cloud where simultaneously *SLW* droplets and ice particles are present, the ice particles can grow through deposition at the expense of the *SLW* droplets. This process is called Wegener-Bergeron-Findeisen process, and is most efficient at an ambient air temperature of  $-15^{\circ}\text{C}$  (Korolev, 2007). The release of latent heat during the depositional growth of ice particles increases the surface temperature of the ice particle, shifting the maximum of the growth rate through the Wegener-Bergeron-Findeisen process to colder ambient air temperatures.

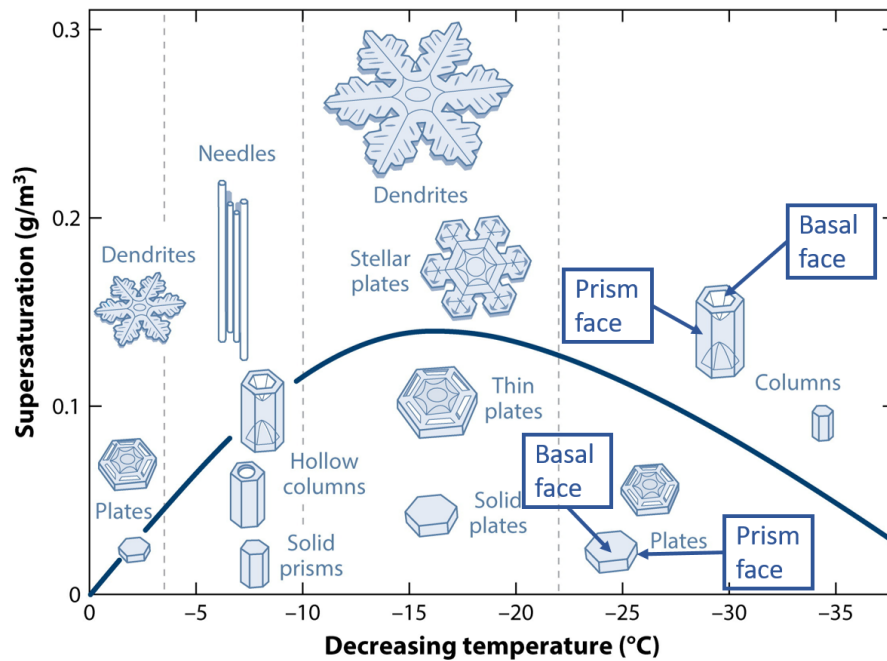


Figure 2.4: Growth regimes of ice crystals dependent on the temperature and super-saturation. the solid blue line represents water saturation. Also, the basal and prism face of the crystals are illustrated. This Figure was taken and adapted from Figure 1, Libbrecht, 2017.

#### 2.1.2.2 Aggregation

It is rare that a snow crystal grown solely by deposition reaches the ground. Most snowfall observed on the ground consists of so-called aggregates. During the aggregation process, two or more ice particle collide and join together, forming an aggregate. During the aggregation process, large particles are formed on the expense of smaller crystals. Aggregation is thus a growth process which most efficiently increases the mean mass of the particle distribution and reduces the total number concentration of particles inside a cloud, without changing the total mass concentration of ice. Aggregation is a process observed at a wide range of temperatures. Many in-situ studies have observed the aggregation process to happen from  $-60^{\circ}\text{C}$  up to close to  $0^{\circ}\text{C}$  (Connolly et al., 2012). However, describing the aggregation process in detail is challenging due to the various

shapes and habits ice particles can exhibit. The shape of ice particles affects their falling behaviour (Karrer et al., 2020), and finding an accurate parameterisation of the collision efficiency of two ice particles is challenging. In general, the change in the particle mass distribution ( $f(m)$ ) due to the aggregation of two particles with masses  $m_i$  and  $m_j$  can be described by the stochastic collection equation (Pruppacher and Klett, 1997):

$$\frac{df(m_i)}{dt} = \int_0^{m_i/2} f(m_j)f(m_i - m_j)K(i, j)dm_j - \int_0^\infty f(m_i)f(m_j)K(i, j)dm_j \quad (2.3)$$

The first term of Equation 2.3 describes the gain of number of particles with  $m_i$  during the collision of particles with mass  $m_j$  and  $m_i - m_j$ . The second term describes the loss of the particles of mass  $m_i$  due to collisions with particles with mass  $m_j$ . The aggregation kernel ( $K_{agg}$ ) (or hydrodynamic kernel)

$$K_{agg}(i, j) = (A_i^{0.5} + A_j^{0.5})^2 |v_i - v_j| E_{agg} \quad (2.4)$$

describes how likely the aggregation between particle  $i$  and  $j$  is.  $A_{i,j}$  describes the projected area ( $A$ ) of the particle  $i$  or  $j$  normal to the fall direction,  $v_{i,j}$  the terminal velocity of particle  $i$  or  $j$  and the  $E_{agg}$ , which is the product of the  $E_c$  and the  $E_s$ .

$E_c$  (between 0 and 1) is needed, since the true collision cross-section is smaller than the  $A$  of the two particles that are colliding (first term in Equation 2.4). The smaller particle that is within the  $A$  of the larger particle might be deflected by the flow, and therefore not get collected by the particle (see Figure 2.5, orange particle).

$E_s$  can be described as a function of temperature (e.g. Connolly et al., 2012). Previous studies (e.g. Mitchell, 1988) have found two maxima of  $E_s$  between  $-30$  and  $0^\circ\text{C}$ . The first maximum in  $E_s$  is within the dendritic growth layer (at temperatures between  $-20$  and  $-10^\circ\text{C}$ ). There, dendritic particles are growing, whose branched arms can mechanically interlock.  $E_s$  is generally increasing with the temperature, reaching a second maximum at  $0^\circ\text{C}$ . For warmer temperatures, the thickness of the quasi-liquid layer (QLL) on the surface of ice particles increases (Slater and Michaelides, 2019), which increases the stickiness. The QLL (or premelting layer) is a layer where the water molecules are not in a fixed structure such as ice crystals. However, the molecules also do not behave exactly like SLW (Li and Somorjai, 2007). The QLL is commonly accepted to start at temperatures close to  $-30^\circ\text{C}$ .

Another possible sticking mechanism, especially at colder temperatures, is the sticking due to electrical charge of ice particles (e.g. Connolly et al., 2005).

### 2.1.2.3 Riming

Although riming was only observed in a small number of cases in the observational dataset it is an important ice growth process and will be explained briefly in this section. Riming is an ice growth process, where SLW droplets are collected by ice particles. The SLW droplet freezes onto the surface of the ice particle, increasing its mass and density (Heymsfield, 1982; Pruppacher and Klett, 1997). Due to this increase in density, the ice particle fall velocity increases (section 9.2 Lamb and Verlinde, 2011). In stratiform clouds graupel with fall velocities of up to  $3\text{ m s}^{-1}$  is generated through riming (e.g. Locatelli and Hobbs, 1974). In convective clouds with high liquid water paths and strong updrafts, riming can even lead to the production of large hail stones (Lamb and Verlinde, 2011).

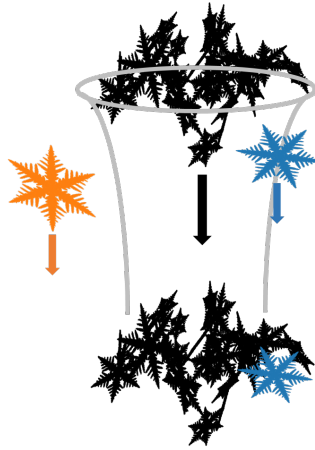


Figure 2.5: Schematic of the aggregation process between an aggregate (black particle) and an ice crystal (blue particle). Since the blue particle is within the swept out volume of the aggregate (grey lines) and it is falling slower than the aggregate (indicated by the arrows below the particles), these particles collide and aggregate. The swept volume of a particle is smaller than its  $A$ , since particles located towards the side of the  $A$  might be deflected by the flow and not collide with the particle (orange ice crystal).

Since riming is a collision and collection process, it can also be described by Equation 2.3. However, certain differences compared to aggregation need to be considered. During riming, an  $E_s$  of 1 can usually be assumed. The liquid water droplet always sticks to the ice particle, since the droplet immediately freezes upon contact with the ice particle (chapter 9, Lamb and Verlinde, 2011). Also, the cloud droplet has a substantially smaller  $v$  and  $m$  than the ice particle. This reduces  $E_c$  significantly, as the cloud droplet can be deflected by the flow around the ice particle. In case of cloud droplets smaller than  $10\text{ }\mu\text{m}$ ,  $E_c$  even approaches zero (e.g., Böhm, 1992a).

## 2.2 OBSERVING ICE MICROPHYSICAL PROCESSES WITH RADAR REMOTE SENSING

Radars have been used to detect the distance and some physical properties of targets since 1904, when a German engineer patented the use of radar to detect ships (Raghavan, 2003). Since then, radars have come a long way. During World War II, radars were rapidly developed and mainly used in air defence. Precipitation was found to clutter the radar signal of the preferred military targets. These first observations of precipitation have kick-started the use of radars for meteorological purposes, with the first symposium on radar use for meteorology being held by the British Physical Society and the Royal Meteorological Society in 1946. Since then, various advances have been made concerning radar observations: the first Doppler radar observations (Section 2.2.3) were made in 1953 by Barratt and Browne, dual-wavelength observations (Section 2.2.4) have been used probably since 1968, when Russian scientist Kostarev investigated hailstorms, and dual-polarisation observations (Section 2.2.5) were made in China in the 1970s. Radars for meteorological use are now operationally assimilated into numerical weather prediction (NWP) models, used in predicting natural disasters, such as thunderstorms, floods or tornadoes, used for nowcasting of precipitation or used to study clouds and precipitation processes.

A radar operates with the echo-sounding principle. An electromagnetic (EM) wave with a frequency within the microwave region (a few MHz up to 110 GHz) gets transmitted and meets an object. Part of the energy of the EM wave gets transmitted through the object, while other parts are scattered in all directions and absorbed by the object. The backscattered radiation is received by the radar receiver, and from the time the radiation travelled, the location of the object can be obtained. The measurement of the received energy or phase, among others, gives information on the physical properties of the object (e.g. the chemical composition, orientation relative to the radar beam, velocity towards the radar, size, shape, etc.). Due to its military origin, the wavelengths at which the radar operates are still named after the corresponding wave bands. These bands will hereafter be used when referring to a radar at a specific wavelength. The most frequently used bands and their applications are summarised in Table 2.1.

Table 2.1: The most commonly used radar bands, frequencies and wavelengths for meteorological applications. This table is adapted from table 1.1 Raghavan, 2003

Band designation	Frequency range	Wavelength range	meteorological application
L	1 – 2 GHz	30 – 15 cm	clear air and precipitation phenomena
S	2 – 4 GHz	15 – 7.5 cm	Precipitation measurement, tropical cyclone observation, local severe storms, radio wave propagation
C	5 – 7 GHz	6 – 4.5 cm	Local severe storms, precipitation measurements, tropical cyclone observation, radio wave propagation, use on aircraft, weather radar network of german weather service DWD
X	9 – 11 GHz	3.3 – 2.7 cm	Thunderstorm and gust front detection, radio wave propagation, use on aircraft
Ku	12 – 18 GHz	2.5 – 1.7 cm	Cloud microphysics and dynamics, air- and space-borne radars, synthetic aperture radars for sea surface studies, precipitation measurement from attenuation, tornado observation
Ka	27 – 40 GHz	1.1 – 0.75 cm	as Ku-Band
W	94 GHz	3.2 mm	Cloud microphysics and dynamics, tornado observations

### 2.2.1 Short introduction into scattering from single particles

When an EM wave propagates through a dielectric object (e.g. hydrometeors, insects), part of the energy carried by the EM wave gets transmitted through the object, part of it is absorbed and part of it is scattered in all directions. The incident electromagnetic

*Note: In the following, matrices will be noted **bold***

field ( $\mathbf{E}^i$ ) can be related to the scattered electromagnetic field ( $\mathbf{E}^s$ ) via the amplitude scattering matrix ( $\mathbf{S}$ ) (chapter 2 Brongi and Chandrasekar, 2001).

$$\begin{bmatrix} \mathbf{E}_h^s \\ \mathbf{E}_v^s \end{bmatrix} = \frac{e^{-jkr}}{r} \begin{bmatrix} S_{hh} & S_{hv} \\ S_{vh} & S_{vv} \end{bmatrix} \begin{bmatrix} \mathbf{E}_h^i \\ \mathbf{E}_v^i \end{bmatrix} \quad (2.5)$$

where  $\mathbf{E}_h^i$  and  $\mathbf{E}_v^i$  are the incident plane waves at horizontal and vertical polarisation. Similarly,  $\mathbf{E}_h^s$  and  $\mathbf{E}_v^s$  are the scattered waves at horizontal and vertical polarisation.  $S_{hh}$  and  $S_{vv}$  are the scattering amplitudes when the incident and scattered wave are horizontally (vertically) polarised, while  $S_{hv}$  and  $S_{vh}$  when the incident wave is horizontally (vertically) polarised and the scattered wave vertically (horizontally), respectively. Further,  $k = 2\pi/\lambda$  is the wavenumber of free space,  $r$  is the distance from the scatterer and imaginary unit  $j$ . For most radar application, the component of the scattered radiation that is directed back towards the radar is most interesting. A common way to describe the backscattered fraction is with the backscattering cross section ( $\sigma_b$ ).  $\sigma_b$  is defined as the ratio of the magnitude of radiation scattered in the direction of the instrument to the magnitude of the incident radiation.  $\sigma_b$  is defined as (chapter 1.4 Brongi and Chandrasekar, 2001)

$$\sigma_b = 4\pi |\mathbf{S}(\pi)|^2 \quad (2.6)$$

To relate the received backscattered radiation to properties of the scatterer (e.g. size, concentration,...), the magnitude of the backscattered field of each scatterer has to be known. Several approximations, that calculate  $\mathbf{S}_b$  are described in more detail in Section 2.4. For spherical (water) particles much smaller than the incident wavelength, the Rayleigh approximation can be used. The Rayleigh approximation is valid when the size parameter ( $X$ )  $X = 2\pi r_{\text{part}}/\lambda$ , with  $r_{\text{part}}$  the radius of the particle, is between 0.002 and 0.2. The amplitude scattering matrix under the Rayleigh approximation simplifies to

$$\mathbf{S}_{\text{ray}} = \begin{bmatrix} S_1 & 0 \\ 0 & S_1 \cos(\Theta) \end{bmatrix} \quad (2.7)$$

with the scattering angle ( $\Theta$ ) and

$$S_1 = \frac{3k^2}{4\pi} KV \quad (2.8)$$

The backscattering cross-section according to the Rayleigh approximation can therefore be written as

$$\sigma_{b,\text{ray}} = \frac{9}{4\pi} k^4 |K|^2 V^2 = \frac{36\pi^3}{\lambda^4} |K|^2 V^2 \quad (2.9)$$

with the volume ( $V$ ) of the scatterer and the dielectric factor ( $|K|^2$ ) of the scatterer.  $|K_\lambda|^2$  accounts for the dielectric properties of the scatterer at wavelength ( $\lambda$ ) and can be calculated from the complex refractive index ( $\epsilon$ ) as

$$|K|^2 = \left| \frac{\epsilon(\lambda)^2 - 1}{\epsilon(\lambda)^2 + 2} \right|^2 \quad (2.10)$$



for spherical particles,  $\sigma_{b,ray}$  is directly related to the 6<sup>th</sup> power of the diameter  $D$

$$\sigma_{b,ray} = \frac{\pi^5}{\lambda^4} |K_\lambda|^2 D^6 \quad (2.11)$$

so larger particles also produce a larger backscattering signal. However, once the particle size and wavelength become comparable, destructive interference inside the particle reduces backscattering cross section ( $\sigma_b$ ) and it can not be described by Rayleigh scattering any longer. This reduction in  $\sigma_b$  when particle size and wavelength become comparable is used in multi-frequency radar setups to infer the particle size when using radar observations at different wavelengths (Section 2.2.4).

### 2.2.2 Radar observations of a distribution of particles

Of course, a meteorological radar rarely observes just a single scatterer. Rather, a population of particles are observed at each time step and range. In general, a population of particles can be described by the PSD ( $N(D)$ ), and the radar observes the received signal integrated over the PSD of the scatterers. In case of ice particles, the PSD is often described with an exponential size distribution Field and Heymsfield, 2003 of the form

$$N(D) = N_0 \exp(-\Lambda D), \quad (2.12)$$

where  $N_0$  is the number of particles at size  $D = 0$  and  $\Lambda$  is the rate coefficient, describing how quickly the number of particles declines towards larger  $D$ . Several in-situ observations rather suggest that the PSD of ice particles is better described by a gamma distribution, where  $\Lambda$  and  $\mu$  describe the shape of the PSD and  $N_0$  is the scaling parameter (e.g. Petty and Huang, 2011)

$$N(D) = N_0 D^\mu \exp(-\Lambda D) \quad (2.13)$$

In case of a distribution of liquid water Rayleigh scatterers, one can define the radar reflectivity factor per unit volume as

$$Z \equiv \int_0^\infty N(D) D^6 dD. \quad (2.14)$$

The radar reflectivity factor ( $Z$ ) is expressed in units of  $\text{mm}^6 \text{m}^{-3}$ .  $Z$  can be obtained from the measured radar equation. The radar equation relates the received power ( $P_r$ ) to several instrument quantities as well as quantities of the scatterer and the atmosphere that the EM wave travels through. According to Raghavan, 2003, the radar equation can be written as:

$$P_r = \frac{\pi^3}{1024 \ln(2)} \frac{P_t h G^2 \theta \Phi}{\lambda^2} \frac{\alpha_{\lambda,r}}{r^2} |K_\lambda|^2 Z \quad (2.15)$$

with the transmitted power ( $P_t$ ), the radar gain ( $G$ ), the pulse width ( $h$ ), the elevation beam width ( $\theta$ ) and azimuth beam width ( $\Phi$ ), the transmitted wavelength  $\lambda$ , the attenuation along the path through the atmosphere at the transmitted wavelength attenuation along the path through the atmosphere at the transmitted wavelength ( $\alpha$ ) and the distance between the radar and scatterer  $r$ . The first term of Equation 2.15 is made up of

constants, the second term describes radar parameters, the third term the transmission of the EM wave through the atmosphere and the last term the properties of the target (scatterer). Equation 2.15 is only valid if all particles are Rayleigh scatterers, spherical, have the same dielectric constant and are randomly distributed within the sampling volume (chapter 3.1 Fabry and Zawadzki, 1995). If all radar parameters, and path properties and  $|K|^2$  are known,  $Z$  can be obtained from the strength of the received power. However, it is impossible to always know which material a target is made of. In the atmosphere there might be e.g. liquid water drops, ice particles or insects present, each with their own dielectric properties. Therefore, the equivalent radar reflectivity factor equivalent radar reflectivity factor ( $Z_e$ ) is defined, such that

$$P_r = \frac{\pi^3}{1024 \ln(2)} \frac{P_t h G^2 \theta \Phi}{\lambda^2} \frac{\alpha_{\lambda,r}}{r^2} |K_{w,\lambda}|^2 Z_e \quad (2.16)$$

with  $|K_{w,\lambda}|^2$  the dielectric constant of water at wavelength  $\lambda$ . In case of Rayleigh scattering and liquid water,  $Z_e = Z$ . In case the target is not made out of liquid water,  $Z_e$  is related to  $\sigma_b$  via

$$Z_e(\lambda) \equiv \frac{\lambda^4}{\pi^5 |K_\lambda|^2} \int_0^\infty N(D) \sigma_b(D, \lambda) dD \quad (2.17)$$

Except for the dielectric properties of the target, also the path properties are difficult to obtain. The attenuation is dependent on  $\lambda$ , the distance travelled through the atmosphere as well as the different concentration of gases and hydrometeors the EM wave encounters. Attenuation refers to the reduction in power of the radiation that is travelling through an object, such as the atmospheric gases or hydrometeors. This reduction in power is caused by the absorption of EM radiation by the object it encounters, or the scattering of the radiation in any direction away from the radar. The atmospheric gases that attenuate the radar signal most are oxygen and water vapour. Also hydrometeors lead to attenuation. While especially liquid water particles attenuate the signal significantly, also a large ice water path can lead to attenuation (see for example table 8.2 Rinehart, 2005). The smaller the radar frequency, the less affected the radar is by attenuation (Rinehart, 2005). At larger frequencies, attenuation needs to be taken into account and corrected for when looking at  $Z_e$  observations (Section 3.1.3.3)

### 2.2.3 Doppler spectra and moments

Doppler radars do not only record the magnitude of the backscattered signal and the time duration between transmitted received radiation, but also the phase shift. From the time shift  $dt$ , the distance between the scatterer and the radar can be calculated (later referred to as the range). As described in Fabry, 2015, the phase shift ( $\phi_i$ ) between transmitted EM wave and received wave is

$$\phi_i = 2\pi f dt = -\frac{4\pi f n r_i}{c} \quad (2.18)$$

The transmitted frequency ( $f$ ) and the refractive index of the atmosphere ( $n$ ) can be assumed constant. Therefore, a phase shift is directly caused by the changes in the range of the scatterer  $r$ . By measuring this phase shift, the radar can gain information about



the velocity of the scatterer perpendicular to the direction of transmission. Therefore, considering the rate of change in time of  $\phi_i$ , Equation 2.18 becomes

$$\frac{d\phi_i}{dt} = -\frac{4\pi f n}{c} \frac{dr}{dt} = -\frac{4\pi f n}{c} v_D \quad (2.19)$$

with Doppler velocity ( $v_D$ ) of the scatterer. With a spectral composition of the received signal at a certain range is made by computing the Fourier transform the power spectrum at that range is obtained, which is the distribution of the total received power as a function of  $v_D$ . Figure 2.6 visualises a possible Doppler spectrum. If there is no vertical air motion and no turbulence present, the Doppler spectrum shows the distribution of the terminal velocities of the scatterers. However, vertical air motions can shift the entire spectrum to slower or faster falling velocities, while turbulence broadens the Doppler spectrum (see Figure 2.6). Due to a dependency of the terminal velocity of a particle on its size

*Note: In the following, negative  $v_D$  indicate a movement towards the radar, while positive away from the radar. In case of vertically pointing radars, negative  $v_D$  therefore indicate that the scatterer is falling towards the ground.*

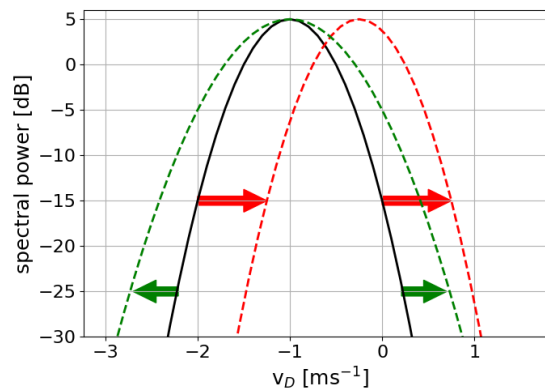


Figure 2.6: Conceptual plot of the spectral power as function of  $v_D$  at one range gate (black line). The effect of turbulence (green line and arrows) as well as upward vertical air motion (red line and arrows) are visualised here.

and shape (for water drops, the size and velocity are easily linked due to the spherical shape of water drops, while for ice particles it is more complicated. See e.g. Karrer et al., 2020), the evolution of particle size distributions (PSDs) and particle populations (e.g. rimed particles, aggregates, SLW droplets) can be studied. The PSD at certain heights can be retrieved using Doppler spectra (Barrett et al., 2019; Moisseev and Chandrasekar, 2007; Mróz et al., 2020; Mróz et al., 2021; Tridon and Battaglia, 2015), however, especially for snow, many assumptions have to be made regarding e.g. the habit and type of snow. Because of their separation of smaller and larger particles, Doppler spectra are also suited to investigate certain IMP. A frequently observed secondary, slow mode is e.g. indicative of SIP and the subsequent depositional growth at that height (e.g. Moisseev et al., 2015; Oue et al., 2018). The Doppler spectrum can be expressed in terms of the PSD as

$$S_\lambda(v_D) = \frac{\lambda^4}{\pi^5 |K|^2} N(D) \sigma_\lambda(D) \frac{dD}{dv_D} \quad (2.20)$$

The Doppler spectra are often not recorded, due to the large memory required to save the data. Also, the Doppler spectra are not operationally used. Rather, moments of the Doppler spectrum, such as Ze, the mean Doppler velocity (MDV) or the spectral

width (*SW*), are calculated and recorded. The  $n^{\text{th}}$ -Moment of the Doppler spectrum is defined as

$$M_n = \int_0^{\infty} (v_d - c)^n S(v_d) dv \quad (2.21)$$

For the lower moments,  $c$  is usually assumed to be 0, for the second and higher moments, the central moment (so the mean) is used as  $c$ .  $Ze$  is the  $0^{\text{th}}$ -Moment of the Doppler spectra:

$$Ze(\lambda) = \int_0^{\infty} v^0 S_{\lambda}(v_d) dv \quad (2.22)$$

The *MDV* represents the mean motion of the particles within the sampled volume and is defined as the  $1^{\text{st}}$ -Moment, normalised with the  $0^{\text{th}}$ :

$$\text{MDV}(\lambda) = \frac{\int_0^{\infty} v^1 S_{\lambda}(v_D) dv}{\int_0^{\infty} S_{\lambda}(v_D) dv} \quad (2.23)$$

and the variance the (normalised)  $2^{\text{nd}}$ -Moment:

$$\text{var}(\lambda) = \frac{\int_0^{\infty} (v - \text{MDV}(\lambda))^2 S_{\lambda}(v_D) dv}{\int_0^{\infty} S_{\lambda}(v_D) dv} \quad (2.24)$$

where the more frequently used *SW* is the square root of the variance:

$$\text{SW}(\lambda) = \left( \frac{\int_0^{\infty} (v - \text{MDV}(\lambda))^2 S_{\lambda}(v_D) dv}{\int_0^{\infty} S_{\lambda}(v_D) dv} \right)^{\frac{1}{2}} \quad (2.25)$$

Due to the large span of values, *Ze* is often used in logarithmic units of dB:  $Ze[\text{dB}] = 10 \log_{10}(Ze)$ . In the following, *Ze* is in dB.

#### 2.2.4 Multi-frequency approach

As was explained in [Section 2.2.1](#), the  $\sigma_b$  increases with increasing size of the scatterer. However, once the wavelength and scatterer size become comparable, the induced dipoles within the particle oscillate out of phase (see schematic in [Figure 2.7](#)), and the resulting destructive interference leads to a reduction of the backscattered signal ( $\sigma_b \lambda^{-4} \pi^{-5}$ ). This behaviour can be seen in [Figure 2.8](#), where the reflectivity for a single particle at X-, Ka- and W-Band are shown in dependency of the particle size. When assuming the same  $|K|^2$  for all wavelengths, *Ze* in the Rayleigh regime is the same for all wavelengths. This is valid for the particle type used in [Figure 2.8a](#) up to a particle maximum dimension ( $D_{\text{max}}$ )



Figure 2.7: Schematic drawing showing a particle smaller than the wavelength (a) and a particle large compared to the wavelength (b). The white spheres in the particles illustrate the dipoles, the green line the EM wave and the arrows the induced field. In (a) all dipoles oscillate in phase with each other, while in panel (b), the dipoles oscillate out of phase, thus reducing the backscattered signal. This graphic is taken from Kumjian, 2018 with permission from Springer Nature under license number 5372471325791

of approximately 1 mm at W-Band. For larger particles, the backscattered signal starts to deviate increasingly from that of the X- and Ka-Band. Similarly, at approximately 3 mm, the backscattered signal from the Ka-Band starts to deviate from the X-Band signal, and the Ka-Band leaves the Rayleigh regime. Only at approximately 2 cm, the X-Band leaves the Rayleigh regime, and destructive interference becomes important. In Figure 2.8a, one can nicely see, that the first Mie-Dip happens, when the particle and the wavelength have the same size. This reduction in the backscattered signal can be used to obtain an information of the size of the particle. The dual-wavelength ratio (DWR) is defined as the difference in  $Ze$  in logarithmic units

$$DWR_{\lambda_1\lambda_2} = Ze_{\lambda_1} - Ze_{\lambda_2} \quad (2.26)$$

where  $\lambda_1$  is the longer wavelength and typically chosen to be in the Rayleigh regime (e.g. Ka-Band), and  $\lambda_2$  is the shorter wavelength (e.g. W-Band) which deviates from the Rayleigh regime. Figure 2.8b shows the DWR at Ka-, W-band ( $DWR_{KaW}$ ) and DWR at X-, Ka-band ( $DWR_{XKa}$ ), in dependency of the median mass diameter  $D_0$ . Since it is

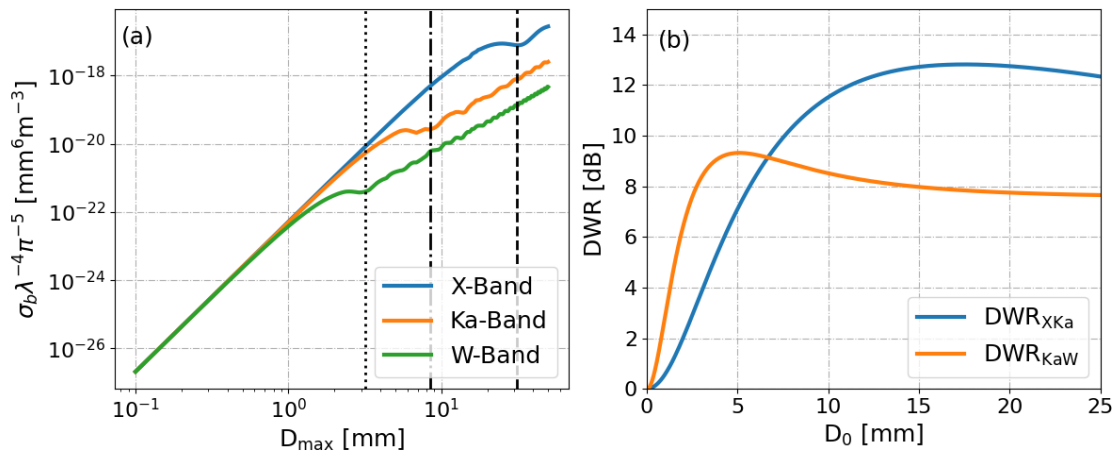


Figure 2.8: Single particle scattering in dependency of the particle diameter  $D_{\max}$  for X-, Ka- and W-Band (a). The dashed line in (a) shows the wavelength of the X-Band, the dash-dotted line of the Ka-Band and the dotted line of the W-Band. The DWR at X-Ka and Ka-W in dependency of the median mass diameter median mass diameter ( $D_0$ ) of an inverse exponential PSD is shown in (b). The scattering properties were calculated with snowScatt (Ori et al., 2021) for aggregates of dendrites (vonTerzi-Dendrite).

the logarithmic difference of the  $Ze$  at two  $\lambda$ , the  $DWR$  is independent of the number concentration of the  $PSD$ . When the  $PSD$  can be described by an inverse exponential distribution, and the particle type (e.g. aggregates of dendrites, rimed particles, crystals) is known, the  $DWR$  depends only on  $D_0$ . However, in clouds also other  $PSD$  shapes are to be expected. Also, rarely the particle type is known and frequently mixtures of different particle types are present. Mason et al., 2019 explored the dependency of the triple-frequency signatures (so the combination of three  $\lambda$ , where e.g. the  $DWR_{KaW}$  is visualised in dependency of the  $DWR_{XKa}$ , see Figure 2.9 for an example) on the  $PSD$  shape and the physical properties of the particles (e.g. density, monomer type,...) in more detail. Continuing the work of Kneifel et al., 2015, they concluded that the triple-frequency signatures vary with the structure of the particles themselves (i.e. the density and homogeneity of the particles) as well as the shape of the  $PSD$ . Figure 2.9b shows the schematics of their findings, where an increase in  $D_0$  increases  $DWR_{KaW}$  and  $DWR_{XKa}$  simultaneously, whereas an increase in density and the shape parameter of the gamma distribution ( $\mu$ ) mostly increases  $DWR_{KaW}$  with only small increases in  $DWR_{XKa}$ . Further, an increase in the fractal dimension of the particle (self-similar Rayleigh-Gans approximation (SSRGA),  $\gamma$ , see Section 2.4) moves the triple-frequency signature towards larger  $DWR_{KaW}$ , while an increase in the fluctuations around the mean particle shape (SSRGA-parameter  $\beta$ ) moves the signatures towards smaller  $DWR_{KaW}$ . Stein et al., 2015 found, that, when assuming an exponential  $PSD$ , the  $DWR$ -saturation in the triple-frequency diagram can be related to the fractal dimension ( $d_f$ ) of the particles. For  $d_f < 3$ ,  $DWR \rightarrow d_f 10 \log_{10}(\lambda_1/\lambda_2)$ . To summarise: knowledge of the structure of the particle as well as the shape of the  $PSD$  are needed in order to relate multi-frequency observations such as  $DWR_{KaW}$  directly to the mean size of the particles present. However, an increase in  $DWR_{KaW}$  (or  $DWR_{XKa}$ ) is frequently interpreted as an increase in particle size through aggregation or riming (e.g. Barrett et al., 2019; Dias Neto et al., 2019; Ori et al., 2020).

$DWR$  also depends on the distribution of mass along the propagation direction (i.e. is mass concentrated in center or outside)

### 2.2.5 Radar polarimetry

While multi-frequency observations are particular useful for retrieving information about the evolution of the mean particle size, polarimetric radar observations are mainly sensitive to a change in aspect ratio (i.e. differential reflectivity ( $ZDR$ )) or concentration of asymmetric particles (i.e. specific differential phase shift ( $KDP$ )). In the case of ice particles, polarimetric radar observations are mainly used to gain information about the shape and concentration of ice crystals. "Conventional", single-polarisation radars transmit  $EM$  radiation that is horizontally polarised and receive horizontally polarised radiation. Some radars are operated in linear depolarisation ratio ( $LDR$ ) mode, meaning that they transmit horizontally and receive both horizontally and vertically polarised radiation. The linear depolarisation ratio  $LDR$  depends on the shape and the dielectric constant of the particle, while it is independent of the particle concentration and attenuation along the path (e.g. Fabry, 2015; Raghavan, 2003). Highly asymmetric hydrometeors, such as needle ice crystals can produce  $LDR$  values as high as  $-10$  dB. Since  $LDR$  is also dependent on the dielectric constant of the particle, it is also enhanced during melting of ice particles, and can thus be used to identify the  $ML$ . Some radars can also be operated

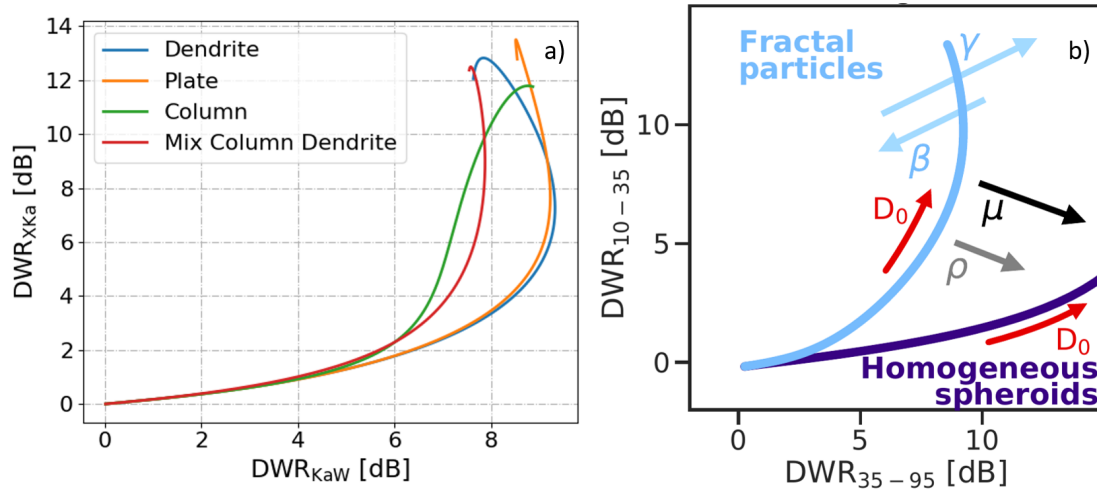


Figure 2.9: Example of triple-frequency signatures of different aggregates consisting of dendrite, plate, or column monomers or a mixture of dendrites and columns (a). The triple-frequency signatures were calculated using snowScatt and an inverse exponential PSD. The effects of the density ( $\rho$ ),  $D_0$ , the shape parameter of the used gamma PSD ( $\mu$ ) as well as the two parameters  $\gamma$  and  $\beta$  of the self-similar Rayleigh-Gans theory (Section 2.4), which represent the effect of the internal aggregate structure on its scattering properties, are shown in b). Panel b) is taken from Mason et al., 2019 and redistributed under the creative commons attribution 4.0 License.

in the STSR-mode, which stands for simultaneous transmit simultaneous receive. The radars are transmitting both horizontally and vertically polarised radiation and are also receiving both polarisations and will thus be referred to as (dual-) polarimetric radars in the following.

#### 2.2.5.1 Differential reflectivity

Asymmetric particles produce a different backscattering cross-section at horizontal and vertical polarisation. Kumjian, 2018 explains the induced horizontally and vertically polarised field in an asymmetric particle. Assume a horizontally aligned plate, consisting of a single layer of dipoles (which are of course also aligned horizontally). Considering the plate is illuminated by a horizontally polarised wave, inducing an EM field inside each dipole that is aligned with the incoming EM field (see Figure 2.10a) top). The dipole fields are not only influenced by the incoming EM field, but also by the induced field in all neighbouring dipoles. Since the EM fields in the neighbours to the right and left are in the same direction, these fields are added constructively (see Figure 2.10a) bottom). This effect is called near-field interactions. The scattered field at horizontal polarisation for a horizontally aligned plate is therefore larger than that of a sphere. Considering now a horizontally aligned plate with an incident vertically polarised electric field (Figure 2.10b)). The induced field in each dipole is now vertically polarised. In contrast to the horizontal example, the electric fields from the neighbouring dipoles now points in the opposite direction as the induced electric field. This leads to destructive interference, with the total electric field being smaller than for an isolated sphere. Therefore, for a horizontally aligned plate,  $\sigma_b$  (and hence also  $Z_e$ ) at horizontal polarisation is larger than that at vertical.

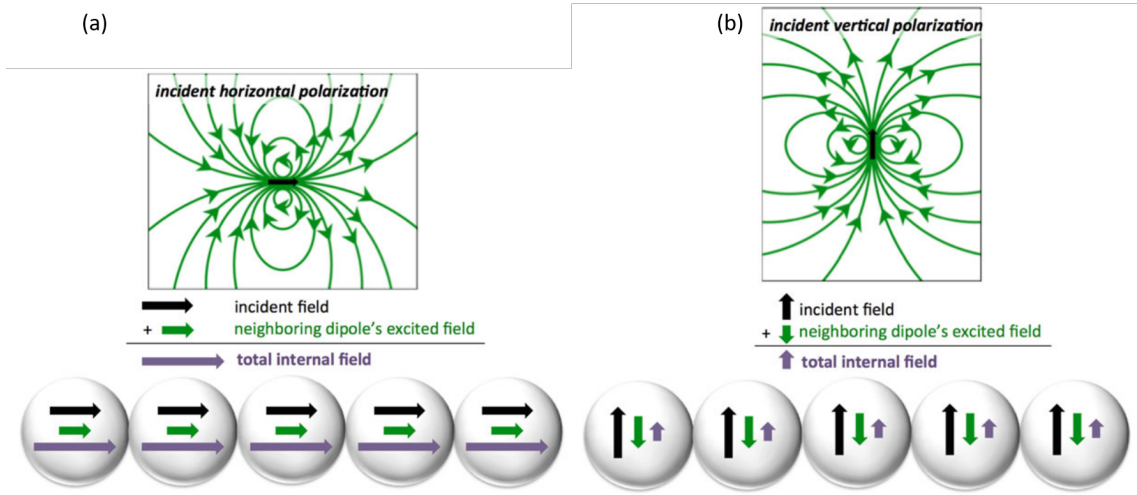


Figure 2.10: Panel a): Top: electric field lines for a horizontally aligned dipole excited by a horizontally polarised incident field. Bottom: Conceptual drawing of a row of dipoles inside the horizontally aligned particle, that are excited by the incident horizontally polarised electric field. The incident field is shown as a black arrow, the field induced by the neighbouring particle in green, and the resulting total internal field in purple. Panel b): similar as for panel a), except for a horizontally aligned particle and vertically polarised incident electric field. This figure was taken and adapted from Kumjian, 2018 with permission from Springer Nature under license number 5372471325791.

This effect is used in the differential reflectivity  $ZDR$  and can be written as:

$$ZDR = 10 \log_{10} \left( \frac{Ze_H}{Ze_V} \right) = Ze_H[dB] - Ze_V[dB] \quad (2.27)$$

$ZDR$  is independent of the concentration of particles. For particles that scatter within the Rayleigh regime,  $ZDR$  is positive for particles whose major axis is aligned horizontally and negative for those with their major axis aligned vertically (Kumjian, 2013).  $ZDR$  also depends on the density of the particle and the physical composition.  $ZDR$  tends to be larger for higher density particles and larger for larger complex refractive indices. Similar to  $LDR$ ,  $ZDR$  is not affected by attenuation or relative miscalibrations, since it is the ratio of  $Ze_H$  to  $Ze_V$ . Similar to the reflectivity Doppler spectrum discussed in Section 2.2.3, also  $ZDR$  can be measured spectrally resolved. This has the advantage that the integrated  $ZDR$  is weighted by  $Ze$ . Therefore, it is mostly affected by the  $ZDR$  signal of the particles that produce the strongest  $Ze$ . In case of large aggregates, the  $ZDR$  signal would be small, since the density of the aggregates is small and their aspect ratio is smaller than that of a plate. The integrated  $ZDR$  would therefore be small, even if small, asymmetric ice crystals are present. Since the small particles are falling slower than the larger particles, their signal is mostly separated in the Doppler spectrum. Therefore, in the spectrally resolved  $ZDR$ , the high- $ZDR$  producing, slow falling crystals are visible even when large aggregates would dominate the integrated signal. The spectrally resolved  $ZDR$  thus enables to study crystal growth and formation (e.g. SIP) processes in more detail as compared to the integrated  $ZDR$ .



### 2.2.5.2 Differential and specific differential phase shift

An EM wave that travels through a dielectric medium such as liquid, ice or air travels slower than in vacuum because the phase speed decreases. The wave that travels through the medium is able to do more of its oscillation compared to the wave in vacuum. Therefore, a phase shift is acquired in the dielectric medium relative to the freely propagating wave travelling the same distance. This is only valid when the medium extends infinitely in the directions orthogonal to the wave propagation direction. However, for particles that are small compared to the wavelength of the EM wave, a similar phenomena is observed (Bohren and Huffman, 1983; Kumjian, 2018). At horizontal and vertical polarisation no difference of the wave propagation speed is expected (Kumjian, 2018). But, since the amplitudes of the scattered waves are different for asymmetric particles, interference between the radar transmitted wave and the scattered wave leads to a different phase shift for horizontally and vertically polarised waves. This effect is illustrated in Figure 2.11. The acquired differential phase shift ( $\phi_{dp}$ ) depends on the size and concentration of the particles within the observed volume.

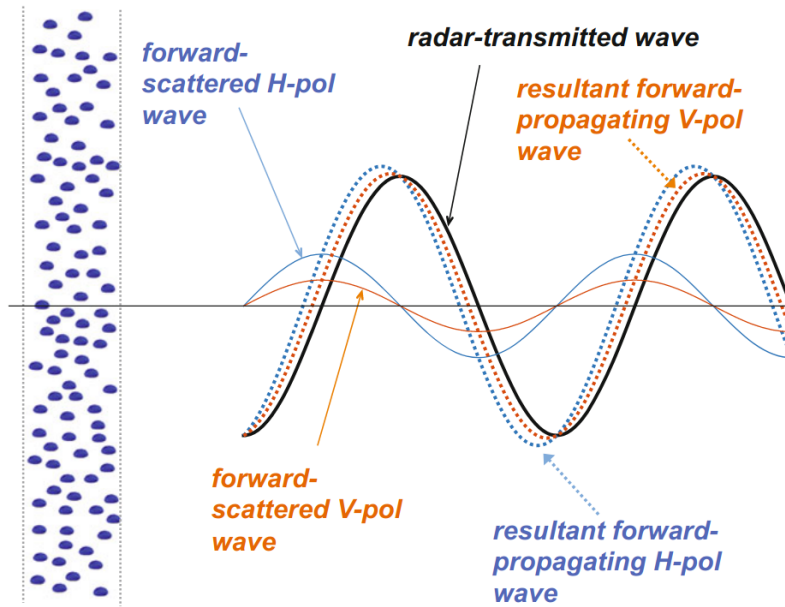


Figure 2.11: Schematic showing the difference in phase shift for a horizontally and vertically polarised EM wave travelling through a volume of identical raindrops that extends infinitely in the direction orthogonal to the propagation direction. All raindrops are oblate with their maximum dimension aligned horizontally. Therefore, the amplitude of the forward scattered horizontally polarised wave is larger than that of the vertically polarised wave. This figure was taken from Kumjian, 2018 with permission from Springer Nature under license number 5372471325791.

More frequently, the KDP is used. KDP is the one half range derivative of  $\phi_{dp}$ , therefore the phase shift per unit radial distance (Kumjian, 2018):

$$\text{KDP} = \frac{\Delta\phi_{dp}}{2 * \Delta r} \quad (2.28)$$

KDP is a measure for the number concentration and/or size of non-spherical particles within the observed volume. Similar to ZDR, KDP and  $\phi_{dp}$  are not affected by attenu-

ation, since they measure the phase difference and not the magnitude of the scattered field.

#### 2.2.5.3 Co-polar correlation coefficient

The co-polar correlation coefficient ( $\rho_{hv}$ ) is the correlation between the received signals at H and V polarisation.  $\rho_{hv}$  is a measure for the diversity of how each particle in the observed volume contributes to the H- and V-Signal (e.g. Kumjian, 2013).  $\rho_{hv}$  is  $< 1$  when a large variety of types (e.g. droplets and ice particles), shapes (e.g. particles with different aspect ratios) and/or orientation of particles are present. For example, drizzle has values close to 1, because all drops are small and thus spherical and they are all liquid water.

#### 2.2.6 Summary of radar remote sensing

As was introduced in the previous sections, radar observations can provide useful information about ice microphysical processes happening in clouds. Especially a combination of different radar approaches can help to shed light on the different aspects of ice microphysics. While the polarimetric radar observations are mainly sensitive to the shape and concentration of ice crystals and small aggregates (Section 2.2.5), the multi-frequency approach can provide information about the evolution of aggregation or riming in the cloud (Section 2.2.4). Further, not only looking at the over the PSD integrated radar moments, but also the spectrally resolved radar variables helps to resolve the signal of large (moment-dominating) ice particles and small ice crystals due to their difference in fall velocity (Section 2.2.3).

### 2.3 MODELLING OF ICE MICROPHYSICAL PROCESSES

Modelling microphysical processes of clouds is extremely challenging due to the large number of particles with varying particle properties and the complex interactions between these particles (Morrison et al., 2020). Also, knowledge gaps of the underlying microphysical processes lead to uncertainties in the microphysical representation in models. Depending on the application, different aspects of the particle properties and interactions are approximated. Traditionally, in numerical weather prediction models the microphysics are approximated in an Eulerian coordinate system. The two Eulerian microphysical models are the bulk and the bin model. The bulk model assumes that the particles follow a predefined PSD, and one or more moments of this PSD are predicted (see for example Khain and Pinsky, 2018; Morrison et al., 2020; Shima et al., 2020). All bulk models predict the mass concentration (1<sup>st</sup>-Moment) while higher-moment models can also predict the number concentration (0<sup>th</sup>-Moment) among others. Bin models represent the particle distribution explicitly and can therefore predict more variables and have more flexibility to evolve the microphysics of the particles (Morrison et al., 2020). However, bin models are computationally expensive, therefore in most numerical weather prediction models, bulk models are used to approximate the microphysics of clouds.

In recent years, Lagrangian particle models have become more popular (e.g. Brdar and Seifert, 2018; Seifert et al., 2019; Shima et al., 2009). In contrast to Eulerian models,



Lagrangian particle models predict the motion of the particles in physical space and the evolution of the particle properties (such as mass, or shape). Therefore, the differential equations describing the evolution of the particle (e.g. the differential equation describing the depositional growth) can be directly calculated. To reduce computational effort, particles with the same attributes (e.g. mass, size, shape) and spatial position are represented by a super-particle. The evolution of the super-particles is then tracked, and the number of ice particles represented by the super-particle is called multiplicity. Since no two particles actually have the same physical properties and spatial position, the super-particle is a representation of an ensemble of particles, where the differences of the particles are too small to be resolved further in actual calculations. Lagrangian particle models have several advantages. The detailed microphysics implemented can show gaps in knowledge of the microphysical processes. It can further help to investigate the impact of microphysical processes on microphysical quantities, processes and observations and it can be used to develop and evaluate new microphysical parameterisations (e.g. Karrer et al., 2021; Kumjian and Ryzhkov, 2010; Seifert, 2008). The bulk model, bin model and Lagrangian model are schematically displayed in Figure 2.12.

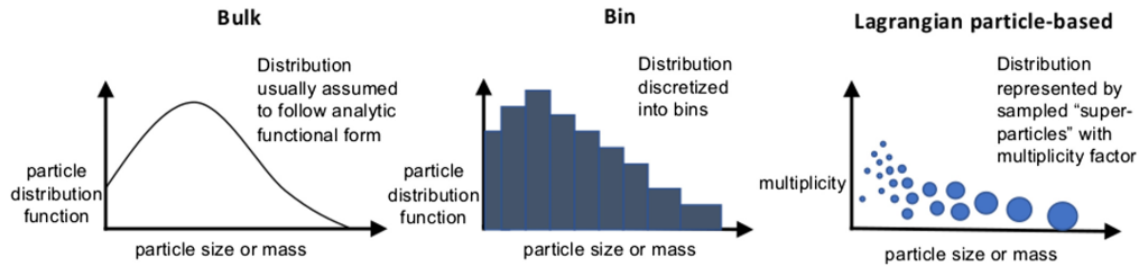


Figure 2.12: Schematic of the different microphysical models. Shown are representations of the particle mass distributions in Bulk models (left), bin models (centre) and Lagrangian models (right). The size of the blue super-particles in the right diagram shows the size or mass of a super-particle. This scheme is taken from Morrison et al., 2020 and permitted to reproduce under the creative commons attribution license.

## 2.4 LINKING MODEL AND OBSERVATIONS BY FORWARD SIMULATIONS

Comparison of model and observations has many advantages: model microphysics can be evaluated, or, if the microphysical model used has well developed imp parameterisations, observational hypothesis can be tested. Two approaches are commonly used to compare modelled and observational data. The observational data can be converted into model variables such as IWC or particle concentration or the modelled data is converted into synthetic observations. The former is also known as retrieval, while the later is known as forward simulation. Since retrievals of ice microphysical quantities is not straight forward, frequently forward simulations of model into observational space are preferred.

### 2.4.1 Short overview of common scattering approximations

#### 2.4.1.1 SSRGA

As was described in Section 2.2.1, the Rayleigh approximation is valid for most applications in the microwave regime. However, at cloud radar frequencies, larger snowflakes

(or water drops) scatter outside of the Rayleigh regime, such that  $\sigma_b$  is smaller compared to Rayleigh scattering. To compensate for this deviation from the Rayleigh regime, Gans introduced the form factor ( $f_{\text{RGA}}$ ) as the integral of the phase of the EM wave over V:

$$f_{\text{RGA}} = \frac{1}{V} \int_V \exp(2jkr) dr \quad (2.29)$$

Under the Rayleigh-Gans approximation (RGA), Equation 2.8 is modified to

$$S_1 = \frac{3k^2}{4\pi} KVf \quad (2.30)$$

The RGA assumes that the scattered wave is only the superposition of the scattering of the single dipoles within a scatterer. The RGA is therefore only valid when interactions between the dipoles in a scatterer are weak enough to be neglected. This is the case when  $|n - 1| \ll 1$  and  $kD|n - 1| \ll 1$ , with the  $n$ . The  $f_{\text{RGA}}$  is given by the Fourier transform of the particle mass distribution along the direction of propagation (Leinonen et al., 2013). Therefore,  $\sigma_{b,\text{RGA}}$  is given by

$$\sigma_{b,\text{RGA}} = \frac{9k^4 |K|^2}{4\pi} \left| \int_{-D/2}^{D/2} A(s) \exp(2jks) ds \right|^2 \quad (2.31)$$

such that the particle lies completely within  $-D/2 \leq s \leq D/2$ . diameter ( $D$ ) is the maximum dimension of the particle along the direction of propagation and  $A(s)$  is the area intersected by a plane at range  $s$  in the particle (Hogan and Westbrook, 2014). In case of aggregates,  $A(s)$  is the area of solid ice intersected by that plane at range  $s$ . The Rayleigh approximation assumes an isotropic distribution of dipoles in all directions, and is therefore only applicable to spheres.  $|K|^2$  as described in Section 2.2.1 is therefore also only valid for spherical particles. Since snow particles are not spherical, the shape (and orientation) has to be taken into account. In the RGA,  $K$  along a primary axis  $x$  (or  $y$  or  $z$ ) of the particle is therefore defined as

$$K_{x,y,z} = \left( \frac{\epsilon - 1}{1 + (\epsilon - 1)L_{x,y,z}} \right) \quad (2.32)$$

where  $L_{x,y,z}$  are geometry factors that characterise the shape of the particle (Hogan et al., 2017). In case of a sphere,  $L_{x,y,z}$  are  $1/3$ . Westbrook, 2014 calculates  $L_{x,y,z}$  of hexagonal plates and columns depending on the aspect ratio ( $\phi$ ) as

$$L_x = L_y = \frac{1}{4} \left( \frac{1 + 0.5\phi^{-0.9}}{1 + 0.5\phi^{-0.9}} + 1 \right); \quad L_z = \frac{1}{2} \left( \frac{1 - 3\phi}{1 + 3\phi} + 1 \right) \quad (2.33)$$

Equation 2.31 is easy to use for single particles, when  $A(s)$  is known. However, there is never just a single particle in the observed volume, and the exact shape of the particles in the observed volume is not known. Therefore, Hogan and Westbrook, 2014 proposed to describe the characteristics of  $A(s)$  statistically for a known ensemble of particles. By considering an ensemble of particles rather than the backscattering of single particles, "extreme" shapes of single particles have less effect on the mean backscattering cross section and can be more robustly applied to e.g. retrievals of the PSD of the unknown

ensemble of particles that the radar is observing. Rather than simply averaging  $\sigma_b$  for an ensemble of particles, they decompose  $A(s)$  of the ensemble into the mean and fluctuations from the mean of a single particle. This is valid for self-similar, or fractal particles such as aggregates, thus this approximation is called **SSRGA**.

$$\underbrace{A(s)}_{A(s) \text{ of ensemble}} = \underbrace{a_0 \left[ \left(1 + \frac{\kappa}{3}\right) \cos\left(\frac{\pi s}{D}\right) + \kappa \cos\left(\frac{3\pi s}{D}\right) \right]}_{\text{mean } A(s)} + \underbrace{\sum_{i=1}^n a'_i \cos\left(\frac{2\pi i s}{D}\right) + a''_i \sin\left(\frac{2\pi i s}{D}\right)}_{\text{fluctuations around the mean}} \quad (2.34)$$

The kurtosis ( $\kappa$ ) describes the mean shape, such that the distribution of mass along  $s$  with a  $\kappa = 0$  is represented by a single cosine, while for a  $\kappa < 0$  the mass is distributed more equally along  $s$  and for a  $\kappa > 0$  the mass is concentrated around the middle. After estimating  $\kappa$  from the mean shape and setting  $a_0 = V\pi/(2D)$ ,  $a'_i$  and  $a''_i$ , a Fourier transformation is performed on the fluctuations around the mean to obtain  $a'_i$  and  $a''_i$ . The resulting power spectrum with  $i$  the index of the wavenumber follows a power law. The slope ( $\gamma$ ) of the power law is related to the fractal dimension ( $d_f$ ) of the aggregates, and the prefactor ( $\beta$ ) represents the amplitude of the fluctuations.  $a'_i$  and  $a''_i$  are then calculated from  $\beta$  and  $\gamma$  by

$$\frac{\langle a'^2_i + a''^2_i \rangle}{\langle a_0^2 \rangle} = \beta (2i)^{-\gamma} \quad (2.35)$$

A scaling factor ( $\zeta_i$ ) was introduced by Hogan et al., 2017 to reduce the amplitude of the power law at the largest scale (so the smallest wavenumber index). The average backscattering cross-section according to the **SSRGA** is calculated as

$$\begin{aligned} \sigma_{b,SSRGA} &= \frac{9}{4\pi} k^4 |K|^2 V^2 \Phi(kD) \\ \Phi(kD) &= \frac{\pi^2}{4} \left[ \cos^2(kD) \left\{ \left(1 + \frac{\kappa}{3}\right) \left( \frac{1}{2kD + \pi} - \frac{1}{2kD - \pi} \right) \right. \right. \\ &\quad \left. \left. - \kappa \left( \frac{1}{2kD + 3\pi} - \frac{1}{2kD - 3\pi} \right) \right\}^2 \right. \\ &\quad \left. + \beta \sin^2(kD) \sum_{i=1}^n \zeta_i (2i)^{-\gamma} \left\{ \frac{1}{(2kD + 2\pi i)^2} + \frac{1}{(2kD - 2\pi i)^2} \right\} \right] \end{aligned} \quad (2.36)$$

The **SSRGA** is an interesting tool, since it describes the scattering of snowflakes in dependency of the internal structure, so the internal distribution of mass. It therefore allows to analyse the scattering properties of snowflakes in dependency of their internal structure. As was described in Section 2.2.4, the triple-frequency saturation value changes when  $\gamma$  or  $\beta$  are changed. Therefore, the distribution of mass along the propagation of the incident wave determines in part the multi-frequency response of an ensemble of particles. A comparison of the **SSRGA** to other scattering approximations such as the T-matrix or discrete dipole approximation (DDA) showed that for aggregates, the scattering

properties are well captured (Hogan et al., 2017; Leinonen et al., 2018; Ori et al., 2021), if the density of the particle increases due to heavy riming, SSRGA underestimates the backscattering cross section, as then the interaction between the dipoles in the scatterer can no longer be neglected. One advantage of the SSRGA is the low computational cost even at particle sizes much larger than the wavelength, where e.g. the computational cost of the Discrete Dipole Approximation (DDA) becomes prohibitive (Hogan et al., 2017). But, due to the assumptions of the RGA of no interactions between dipoles and an isotropic distribution of dipoles in all directions, the SSRGA is unable to estimate the scattering differences at horizontal and vertical polarisation.

#### 2.4.1.2 *T-matrix approach*

The T-matrix method has originally been introduced by Waterman in 1965. Mishchenko et al., 2004 defined the T-matrix method as follows: "In the T-matrix method, the incident and scattered electric fields are expanded in series of suitable vector spherical wave functions, and the relation between the columns of the respective expansion coefficients is established by means of a transition matrix (or T-matrix). This concept can be applied to the entire scatterer as well as to separate parts of a composite scatterer". In case of a homogeneous sphere composed of isotropic materials, the T-matrix method reduces to the popular Mie-approximation (Mishchenko et al., 2002). At the core of the T-Matrix approach stands the transition matrix (T matrix) which relates the incident field expansion coefficients  $a$  and  $b$  to the expanded internal field  $c$  and  $d$  and the scattered field expansion coefficients  $p$  and  $q$ , such that

$$\begin{bmatrix} a \\ b \end{bmatrix} = \begin{bmatrix} Q_{11} & Q_{12} \\ Q_{21} & Q_{22} \end{bmatrix} \begin{bmatrix} c \\ d \end{bmatrix} \quad (2.37)$$

and

$$\begin{bmatrix} p \\ q \end{bmatrix} = - \begin{bmatrix} R_g Q_{11} & R_g Q_{12} \\ R_g Q_{21} & R_g Q_{22} \end{bmatrix} \begin{bmatrix} c \\ d \end{bmatrix} \quad (2.38)$$

where the  $Q$  and  $R_g Q$  matrix elements are integrals over the scatterers surface and depend on its size, shape refractive index and orientation (Mishchenko et al., 1996). The T matrix is then given as

$$\mathbf{T} = -\mathbf{R}_g \mathbf{Q} \mathbf{Q}^{-1} \quad (2.39)$$

A detailed description of the expansion coefficients and the corresponding descriptions of incident and scattered field expressed in vector spherical wave functions is certainly out of the scope of this thesis. Therefore, the reader is referred to chapter 5, Mishchenko et al., 2002. One advantage of the T-matrix approach is that the T matrix only depends on the physical and geometrical properties of the scatterer. It is independent of the propagation directions and polarisation of the incident and scattered fields. Thus, the T matrix needs to be only computed once for a given particle and can then be used to obtain the scattering and extinction properties in all propagational directions and polarisations (Mishchenko et al., 2002). The biggest disadvantage of the T-matrix method is the assumption of an effective medium, i.e. the homogeneous distribution of mass within the particle. However, the description of the mass distribution within the particle plays an important

role for its scattering properties (Sorensen, 2001). The assumption of an effective medium leads to an increasing underestimation of the backscattered signal with increasing  $X$  e.g. Kneifel et al., 2020. Further, the different effective medium approximations, such as the Maxwell-Garnett or Bruggeman effective medium approximation lead to large discrepancies when compared to the DDA (Petty and Huang, 2010).

The T-matrix method is technically not a method to compute the scattering properties of a particle, but rather a formalism describing scattering calculations via a  $\mathbf{T}$  matrix. However, the description T-matrix approximation is commonly used to describe programs that compute the scattering properties of particles with this formalism. The  $\mathbf{T}$  matrix itself can be calculated with various methods such as the null-field method, the generalised point matching method or the extended boundary condition method, which is the standard scheme for computing the  $\mathbf{T}$  matrix (Mishchenko et al., 1996). The most widely used code that computes the  $\mathbf{T}$  matrix and the resulting scattering properties is that by Mishchenko and Travis, 1998. This code is also the basis in the python based PyTmatrix interface (Leinonen, 2013), which is the code used for the T-matrix calculations with McRadar, a forward operator tool used and developed in the course of this thesis.

### 2.4.1.3 DDA

In contrast to the T-matrix method, which calculated the scattering properties by an integral over the surface of the scatterer, the Discrete Dipole Approximation (DDA) is a volume integral method. In the DDA, the scatterer is replaced by a set of point dipoles (hence the name), that interact with the incoming electric field and the fields of the neighbouring dipoles. These interactions give rise to a system of linear equations, which are solved using standard linear algebra to obtain the polarisations of the dipoles (Yurkin and Hoekstra, 2007). From these polarisations, all scattering properties of the scatterer can be calculated. Yurkin and Hoekstra, 2007 describes the DDA as follows. When assuming that the scatterer is dielectric but not magnetic, the electric field inside a scatterer can be described by the general form of the integral equation

$$\mathbf{E}(\mathbf{r}) = \mathbf{E}_{\text{inc}}(\mathbf{r}) + \int_{V/V_0} d^3\mathbf{r}' \bar{\mathbf{G}}(\mathbf{r}, \mathbf{r}') \chi(\mathbf{r}') \mathbf{E}(\mathbf{r}') + \mathbf{M}(V_0, \mathbf{r}) - \bar{\mathbf{L}}(\delta V_0, \mathbf{r}) \chi(\mathbf{r}) \mathbf{E}(\mathbf{r}) \quad (2.40)$$

where  $\mathbf{E}(\mathbf{r})$  and  $\mathbf{E}_{\text{inc}}(\mathbf{r})$  are the total and incident electric field at location  $\mathbf{r}$ .  $\chi(\mathbf{r})$  is the susceptibility of the medium at  $\mathbf{r}$ ,  $V$  is the volume of the particle, and  $V_0$  is a smaller volume, such that  $V_0$  is a subset of  $V$  ( $V_0 \subset V, \mathbf{r} \in V_0/\delta V_0$ ).  $\bar{\mathbf{G}}(\mathbf{r}, \mathbf{r}')$  is the free space Green's function,  $\mathbf{M}$  is an integral describing the finiteness of  $V_0$  and  $\bar{\mathbf{L}}$  is the self-term dyadic. For their definition, the reader is referred to Yurkin and Hoekstra, 2007. When discretizing the scatterer into a finite number of sub-volumes (or dipoles) and assuming that  $\mathbf{E}(\mathbf{r})$  and  $\chi(\mathbf{r})$  are constant inside each sub-volume, Equation 2.40 at point  $\mathbf{r}_i$  for  $n$  sub-volumes can be written as

$$\mathbf{E}_i = \mathbf{E}_i^{\text{inc}} + \sum_{j \neq i}^N \bar{\mathbf{G}}_{ij} V_j \chi_j \mathbf{E}_j + (\bar{\mathbf{M}}_i - \bar{\mathbf{L}}_i) \chi_i \mathbf{E}_i \quad (2.41)$$

After determining the internal electrical fields by solving this system of  $3N$  linear equations using standard techniques of linear algebra, the scattered field can be calculated. The only approximation made in the DDA is the subdivision into sub-volumes, where

the electric field is assumed to be constant. The accuracy of the DDA depends on the number of sub-volumes chosen. However, for larger  $N$ , the number of linear equations that need to be solved increases by 3. Therefore, a compromise between accuracy and computational expense has to be made. When  $kd|m| < 1$  (with  $d$  the size of the sub-volume), the DDA provides reasonable accuracy (Zubko et al., 2010).

Several computer implementations of the DDA exist. The two most frequently ones used are the ADDA (Yurkin and Hoekstra, 2011) and DDASCAT (Draine and Flatau, 2013). The ADDA code was used to calculate the scattering properties of dendritic crystals and aggregates, which are available in McRadar (Section 3.3). Since the DDA is computationally expensive, scattering databases, such as the Liu database (Liu, 2008) were developed that obtain the scattering properties of various ice particles computed with the DDA.

## DATA AND METHODS

---

### 3.1 THE TRIPEX-POL DATASET: DESCRIPTION AND PROCESSING

The Triple-frequency and polarimetric radar experiment for improving process observation of winter precipitation (**TRIPEX-POL**) campaign took place from November 2018 until January 2019 at **JOYCE-CF** (Löhnert et al., 2015) located ca. 40 km west of Cologne, Germany. With a horizontal distance of less than 20 m, vertically pointing X-, Ka-, and W-band radars, as well as a scanning W-band radar were installed on the roof platform of **JOYCE-CF**. The measurement setup is displayed in Figure 1 of von Terzi et al. 2022. Compared to a previous campaign (TRIPEX, Dias Neto et al., 2019), several aspects were improved. First, a set of new radars were installed at **JOYCE-CF**: a new Doppler X-band radar (JOYRAD-10) with higher sensitivity was permanently installed. The Radiometer Physics GmbH (RPG) lent a polarimetric Doppler W-band radar for the duration of the campaign. In cooperation with the University of Granada, Spain, another vertically looking W-band radar was installed temporarily. Second, the vertical resolutions of the radars were adjusted in order to reduce the displacement between the centre of each range gate. Third, the pointing accuracy of the radars was verified by comparing the vertical X- and W-band radars to the Ka-band radar, whose absolute pointing accuracy was evaluated using sun scans.

#### 3.1.1 Description of radars and instruments installed during the TRIPEX-pol campaign

The JOYRAD-10 and JOYRAD-35, hereafter referred to as X-band and Ka-band radar, are pulsed radar systems manufactured by Metek GmbH of the type MIRA-10 and MIRA-35 (Görsdorf et al., 2015; Mróz et al., 2020). Both radars provide high resolution radar Doppler spectra, as well as standard moments such as **Ze**, **MDV** or skewness. In addition, the Ka-band radar provides **LDR** and spectrally resolved **LDR**. The vertically pointing W-band as well as the scanning polarimetric W-band radar are frequency modulated continuous wave (**FMCW**) systems manufactured by Radiometer Physics GmbH (RPG) (Küchler et al., 2017). The vertically pointing W-band radar (hereafter referred to as W-band radar) provides high resolution Doppler spectra observations as well as standard moments similar to the Ka-band radar. The scanning W-band radar (hereafter referred to as polarimetric radar) provides simultaneous transmit simultaneous receive (**STSR**) dual-polarisation observation, including **ZDR**, **KDP** and  $\rho_{hv}$  as well as spectrally resolved **ZDR** (**sZDR**). The polarimetric radar was measuring at 30° constant elevation (**CEL**) towards the west for 5 minute intervals. The **CEL** measurements were interrupted with one range height indicator (**RHI**) scan from 30 to 150° elevation towards the west-east and one plan position indicator (**PPI**) scan at 85° elevation. Detailed information about the setup of each radar is given in Table 3.1.

JOYCE-CF is further equipped with various remote sensing and in-situ instruments such as rain gauges, Doppler wind lidars or microwave radiometers (Löhnert et al., 2015). These instruments were continuously operated during the campaign, providing



additional information about the state of the atmosphere as well as information about the precipitation type, frequency and amount. For example, the Particle Size and Velocity Disdrometer (**PARSIVEL**) (Löffler-Mang and Joss, 2000), which was installed in close proximity to the radars, provided the drop size distribution (**DSD**) which was used to continuously evaluate the calibration of the radar reflectivity as described in Section 3.1.3.2. The additional instruments at **JOYCE-CF** allow for the continuous generation of Cloudnet classification and categorization products (Illingworth et al., 2007). Cloudnet products also incorporate information about the thermodynamic state of the atmosphere and wind information extracted over **JOYCE-CF** from the European Centre for Medium-Range Weather Forecast (**ECMWF**) Integrated Forecast System (**IFS**) model. The IFS model has a horizontal grid resolution of approximately 10 km and 137 height levels.

Table 3.1: From von Terzi et al., 2022: Technical specifications of the four radars that were deployed during the **TRIPEX-POL** campaign. The vertically pointing W-band (in this table denoted as W-band) and the polarimetric W-band radar (in the table denoted as W-band pol) are **FMCW** radars, therefore the range resolution,  $v_D$  resolution and the Nyquist range vary for the different chirps. The values in this table are valid for the lowest chirp region (W-band: 215 – 1475 m, W-band pol: 107 – 715 m). The full chirp tables for both W-band radars are provided in von Terzi et al., 2022.

Specifications	X-band	Ka-band	W-band	W-band pol
Frequency [GHz]	9.4	35.5	94.1	94.0
Polarimetry	single-pol	LDR	LDR	STSR
Number of spectral averages	10	20	13	28
Half-power beam width [°]	1.0	0.6	0.6	0.6
Range resolution [m]	36.0	36.0	36.0	35.8
Temporal resolution [s]	2	2	3	7
Sensitivity at 1 km [dBZ], 2 s integration time	−50	−63	−58	−58
Maximum range [km]	12	15	16	16
$v_D$ resolution [ $\text{m s}^{-1}$ ]	0.038	0.04	0.04	0.05
Nyquist range [ $\text{m s}^{-1}$ ]	$\pm 78$	$\pm 20$	$\pm 10$	$\pm 6$

### 3.1.2 Evaluation of Cloudnet temperature and Humidity profiles

In Section 3.1.3.3 as well as in Chapter 4, the temperature and/or humidity profiles are needed to calculate attenuation profiles (Section 3.1.3.3) and evaluate ice-microphysical processes in dependency of the temperature (Chapter 4). Unfortunately, no temporally and vertically high-resolved temperature and humidity information were available during the **TRIPEX-POL** campaign. Therefore, the temperature and humidity profiles from Cloudnet are used. Dias Neto, 2021 evaluated the temperature and humidity profiles from Cloudnet against 27 radiosondes of type DFM-09, manufactured by GRAW Radiosondes

GmbH & Co. KG, launched during the [TRIPEX-POL](#) campaign. The comparison of radiosondes and Cloudnet profiles showed in general a good agreement. The bias between the Cloudnet temperature and the measured temperature is  $0.2^{\circ}\text{C}$ , with a precision (i.e. the standard deviation of the bias between Cloudnet and Radiosonde temperature) of  $1.1^{\circ}\text{C}$ . The correlation between the two temperatures was found to be 0.9. For the relative humidity over water ( $\text{RH}_w$ ), Dias Neto, [2021](#) found a bias of 1.1%, a precision of 9.2% and a correlation between Cloudnet and Radiosonde ( $\text{RH}_w$ ) of 0.7.

### 3.1.3 Processing of the zenith radar dataset

The following sections describe the processing steps necessary for the statistical analysis of the [TRIPEX-POL](#) dataset, such as removal of artefacts and correction of attenuation and offsets. The zenith dataset was processed in three levels. For the level 0 processing step, the zenith Doppler spectra were regridded to the same time-height grid and cleaned of spectral artefacts ([Section 3.1.3.1](#)). In the level 1 step, the moments were calculated from the level 0 dataset. The level 2 processing follows closely the approach described in Dias Neto et al., [2019](#). The radar moments were corrected for liquid, ice and gas attenuation as well as radar specific calibration offsets ([Section 3.1.3.2](#)). The processing steps will be discussed in more detail in the following sections.

#### 3.1.3.1 Doppler spectra processing

Despite the close matching of the time and range resolutions ([Table 3.1](#)), the Doppler spectra of the three vertically pointing radars were regridded to the same time height grid with a spatial resolution of 36 m and a temporal resolution of 4 s. A total displacement of 17 m and 2 s were allowed. This simplifies the combined statistical analysis of the radar observations. Since the W-band radar was measuring with 4 chirp sequences with different  $v_D$  resolutions,  $v_D$  resolution of chirps 2 – 4 were regridded to  $v_D$  resolution of chirp 1. In order to avoid biases in  $Ze$  due to the interpolation to a common  $v_D$  resolution, the interpolated spectrum was normalised to match the original  $Ze$ .

To avoid interference between the two W-band radars, the frequency of the vertically pointing W-band radar had to be slightly adjusted from 94.00 GHz to 94.12 GHz. Unfortunately, this caused some spectral artefacts visible in [Figure 3.1b](#)) and [Figure 3.2a](#)). The chirp generator of the W-band radar is optimized to the default central frequency of 94.00 GHz. When the radar is operated at this default frequency, the spectral impurities of the chirp generator are low. However, when changing to a slightly different frequency, these spectral impurities increase, leading to the observed spectral artefacts. Since the Ka-band radar has the highest sensitivity of the radars, a similar beam width as the W-band radar and its spectra showed no artefacts, the Ka-band radar was used to develop a spectral mask. For this, we first estimated the noise floor of the Ka-band radar using the method by Hildebrand and Sekhon, [1974](#). We then identified the "true" spectral edges by locating the fastest and slowest spectral bins which exceeded the noise floor by 3 dB. This spectral mask was then applied to the W-band Doppler spectra, by discarding all signals with Doppler velocities outside of the spectral edges. The artefacts outside the spectral mask were successfully removed. However, sometimes the artefacts did not only occupy regions outside the "true" spectral signal, but in some cases it also overlapped with the Doppler signal from real targets. One example of the original, "raw"  $Ze$  and processed

$Ze$  is given in Figure 3.2. The spectral mask was also applied to the X-band Doppler spectra. Some of the X-band spectra were affected by spectral side lobes. These artefacts were observed at Doppler velocities far outside the "true" atmospheric signal, allowing for their entire removal with the spectral mask.

*Note: Due to attenuation in the rain (below 1 km range), the W-band spectra in Figure 3.1 are narrower than the Ka-band spectra. Therefore, the spectral edges derived from the Ka-band radar in this case do not match the edges of the "true" atmospheric signal observed from the W-band radar. In cases with less rain, due to the similar beam widths of the Ka- and W-band, the spectral edges of these radars match more closely. However, in most cases the Ka-band spectral edges were sufficient to remove the spectral artefacts as can be seen here.*

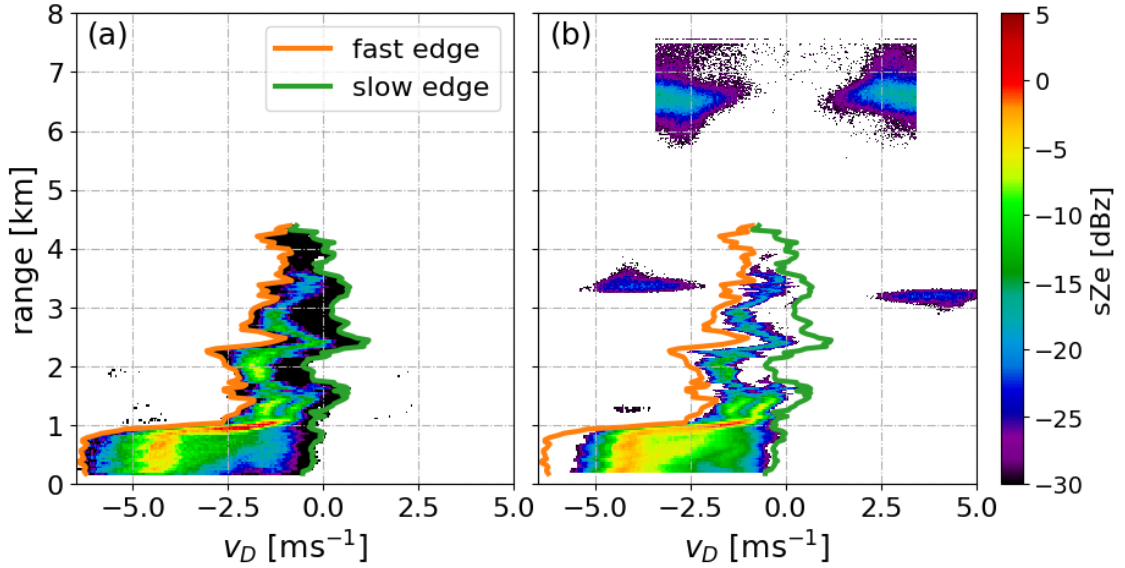


Figure 3.1: Doppler spectra observations from 24<sup>th</sup> November 2018, 08:00:08 UTC. Panel (a) shows the Ka-band Doppler spectra, panel (b) the unprocessed W-band Doppler spectra. The green and orange lines in panel (a) and (b) represent the fast and slow spectral edges used as the spectral mask for the X- and W-band radar.

After the Doppler spectra were regridded to the same time-height grid and the spectral artefacts of the W- and X-band radar were removed with the spectral mask derived from the Ka-band, all standard moments were calculated from the Doppler spectra. The resulting Level 1 dataset includes  $Ze$ ,  $MDV$ , skewness and  $SW$  at horizontal polarisation for the X-, Ka- and W-band. Since the Ka- and W-band radar were transmitting horizontally polarised radiation while receiving horizontally and vertically polarised radiation, all moments are also available at horizontal polarisation, allowing for the calculation of the  $LDR$  and spectrally resolved  $LDR$ .

### 3.1.3.2 Calibration evaluation

The four radars used during the **TRIPEX-POL** campaign have all been calibrated by their respective manufacturers. However, drifts over time of certain radar components (e.g. the radome, antenna,...) might occur. Therefore, the absolute calibration of the radar reflectivity has to be evaluated on a regular basis. There are several possibilities to calibrate different radar components and observables. For example, radars can be calibrated using point targets, such as standard reflectors or spheres, with known scattering properties. This is called end-to-end calibration (Chandrasekar et al., 2015). The point target has to be mounted in the far field of the radar. For cloud radars, this is often not feasible, since this requires the radar to scan in the direction of the point target. Also, the correct range weighting function of the radar has to be known. Cloud radars, such as the X-band radar deployed during the **TRIPEX-POL** campaign do not have a

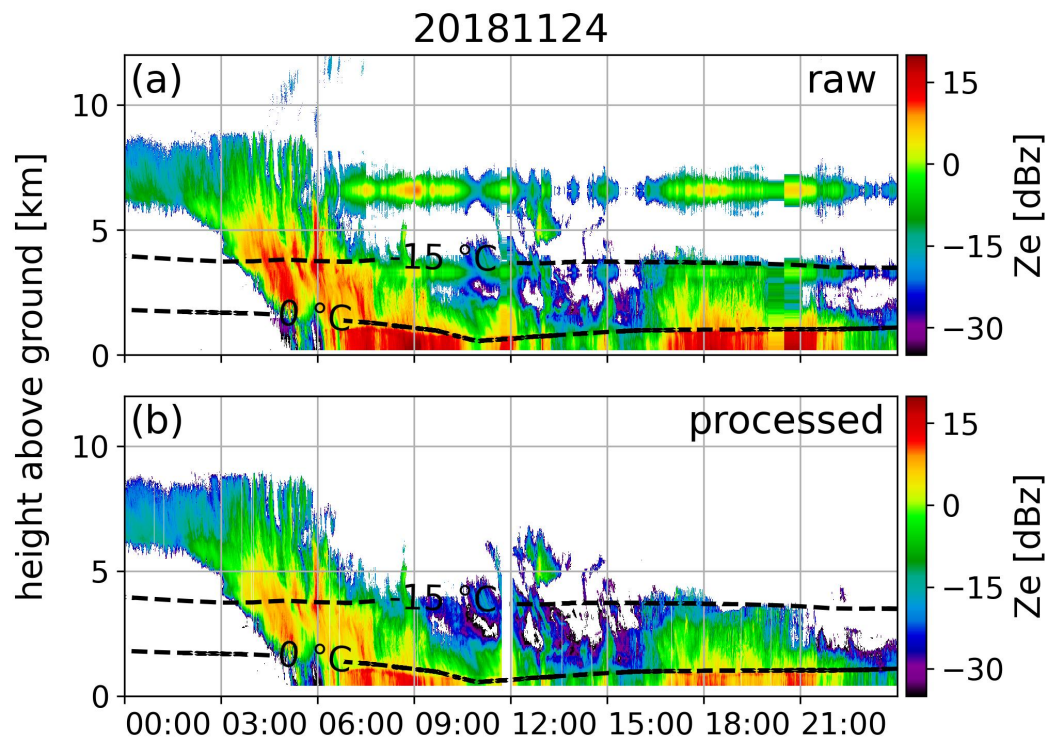


Figure 3.2:  $Z_e$  from the W-band radar from 24<sup>th</sup> November 2018. Panel (a) shows the "raw" data before the spectral filtering was applied. Panel (b) shows the data after the spectral processing. The black line gives the contour of the  $-15^{\circ}\text{C}$  and  $0^{\circ}\text{C}$  isotherm.

scanner and can thus not be calibrated with a point target. Another approach often used is the comparison of the  $Ze$  observations with a calibrated reference system. For this, the space-borne W-band radar CloudSat observations of ice-clouds are often used as the reference, since its reflectivity is regularly calibrated with the known scattering properties of the sea surface (e.g., Protat and Williams, 2011). Unfortunately, CloudSat has a cycle of 16 days and the comparison needs to be done in pure ice, non-precipitating clouds, which makes this method only applicable to long-term calibration monitoring (Kollias et al., 2019). Using natural volume-distributed targets for calibration is a method widely used for cloud radars. For example, a calibration using raindrops has been first applied in 1968 (Atlas, 2002). DSDs derived from disdrometers are often used as reference targets. There, the reflectivity forward simulated from the DSD is compared to the reflectivity of the lowest range gate of the radar. During the TRIPEX-POL campaign, this method was used to evaluate the calibration of the vertically pointing radars (Myagkov et al., 2020). The DSD obtained from the PARSIVEL was used to compare to the  $Ze$  of the radars. The lowest usable range gate was 400 m above the PARSIVEL. Therefore, a constant DSD has to be assumed over this height range in order to compare  $Ze$ s observed with the radar and calculated from the PARSIVEL observations. However, time lags, wind shears and microphysical processes lead to uncertainties in the calibration. Systematic differences can be caused by evaporation of raindrops, drop breakup or growth due to accretion. Therefore, the  $Ze$  distribution of several hours obtained from the radar and forward simulated from the PARSIVEL are compared in a statistical sense. As described in Dias Neto et al., 2019, the scattering properties of the raindrops are obtained using the T-matrix approach, with a drop shape model that follows Thurai et al., 2007, assuming drop canting angles within a Gaussian distribution with a mean of 0 and a standard deviation of  $7^\circ$ . With this method, offsets of 0 dB for the X-band,  $-3$  dB for the Ka-band and 2 dB for the W-band radar have been estimated. An example of the histograms of  $Ze$  of the radars compared to the histogram of  $Ze$  calculated from the PARSIVEL measurements can be seen in Figure 3.3. Over the entire campaign, 21 cases were analysed, which revealed no temporal drift of these calibration offsets. Independently, Myagkov et al., 2020 evaluated the W-band calibration with different methods. Our 2 dB offset lies within their estimated 0.5 to 2.1 dBZ calibration offset. Further, they estimated the calibration offset of the polarimetric W-band radar to be  $-0.7 \pm 0.7$  dBZ.

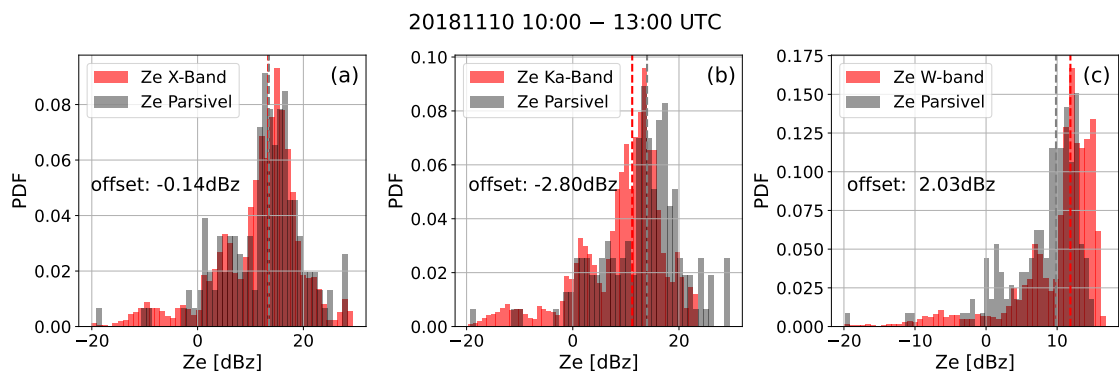


Figure 3.3: Histograms of  $Ze$  from the X-band (a), Ka-band (b) and W-band(c) compared to results from the T-matrix calculations from the DSD of PARSIVEL measurements for a long-lasting rain event on 11<sup>th</sup> November 2018, 10:00 to 13:00 UTC.



### 3.1.3.3 Attenuation correction and DWR calibration

Ice growth processes, such as aggregation and riming, can be well detected in multi-frequency observations. However, not only an increase in size has an influence on the multi-frequency measurements. Also attenuation by gases and hydrometeors, which generally increases with frequency, as well as hardware (instrument) effects such as wet radome or snow on the antenna can cause an increase in [DWR](#) which need to be accounted for. The total [DWR](#) at two wavelengths  $\lambda_1, \lambda_2$  measured at a certain range can therefore be written as the sum

$$\text{DWR}_{\lambda_1, \lambda_2} = \text{DWR}_{\text{scat}} + \text{DWR}_{\text{hard}} + \text{DWR}_{\text{att}} \quad (3.1)$$

In order to recover the "true" microphysical [DWR](#) signal due to differential scattering [DWR](#) due to differential scattering ([DWR<sub>scat</sub>](#)), the [DWR](#) due to hardware offsets [DWR](#) due to hardware offsets ([DWR<sub>hard</sub>](#)) and due to differential attenuation [DWR](#) due to differential attenuation ([DWR<sub>att</sub>](#)) need to be accounted for. The correction applied in this thesis for [DWR<sub>hard</sub>](#) and [DWR<sub>att</sub>](#) follows Dias Neto et al., 2019.

First, the radar profiles were corrected for gas attenuation. The gas attenuation was calculated with the Passive and Active Microwave TRAnsfer model ([PAMTRA](#)) (Mech et al., 2020), which takes into account the attenuation by oxygen, nitrogen and water vapour. As input for [PAMTRA](#), temperature, humidity and pressure profiles from Cloudnet were used.

Second, also attenuation by liquid and ice needs to be taken into account. In the winter mid-latitude, frontal clouds often observed during the [TRIPEX-POL](#) campaign, all three ice-phases can be present at the same height. Frequently, super-cooled liquid water (SLW) layers are embedded into ice dominated regions of the cloud. The largest contributions to attenuation are due to rain, the [ML](#) and SLW layers. However, also ice and snow can contribute to the attenuation, especially at W-band. Tridon et al., 2020 showed, that an ice water path larger then  $1 \text{ kgm}^{-2}$  is needed to cause a two-way attenuation of 1 dB at W-band. In order to estimate the vertical profiles of attenuation due to liquid and ice, accurate profiles of particle size distributions and [m](#) contents are needed. However, this information is challenging to retrieve from the observations and model output available at [JOYCE-CF](#). Since there are no accurate liquid and ice profiles available during the [TRIPEX-POL](#) campaign, the total path integrated attenuation (PIA) is estimated using the relative [DWR](#) calibration approach presented in Dias Neto et al., 2019. In order to estimate [DWR<sub>hard</sub>](#) and [DWR<sub>att</sub>](#), [DWR<sub>scat</sub>](#) needs to be zero. As described in [Section 2.2.4](#), [DWR<sub>scat</sub>](#) is zero if all scatterers are within the Rayleigh regime. This is for example the case for small ice particles. In order to identify regions within the cloud that consist entirely of Rayleigh scatterers, a [Ze](#) threshold can be assumed (Hogan et al., 2000; Tridon et al., 2020). In these cloud regions, [DWR<sub>scat</sub>](#) can be neglected and the observed [DWR<sub>λ<sub>1</sub>, λ<sub>2</sub></sub>](#) can be attributed to the sum of [DWR<sub>hard</sub>](#) and [DWR<sub>att</sub>](#).

Radars at lower frequencies are less affected by attenuation. Therefore, using the X-band [Ze](#) profiles as a reference in the [DWR](#) calibration would be the ideal choice. However, the X-band sensitivity is often too low to capture the signal from small ice crystals at far ranges. Therefore, the Ka-band [Ze](#) profiles corrected for gas attenuation are used to apply the relative [DWR](#) calibration. The Rayleigh regions in clouds are identified using a [Ze](#) threshold of  $-30 \text{ dBz} < \text{Ze}_{\text{Ka}} < -10 \text{ dBz}$  and  $-15 \text{ dBz} < \text{Ze}_{\text{Ka}} < 10 \text{ dBz}$  for the W-Ka and X-Ka [DWR](#) pair, respectively. To exclude partially melted particles,

the cloud regions used for the relative  $DWR$  calibration were further restricted to be at least 1 km above the  $0^\circ$  C isotherm. The  $DWR$  in these cloud regions is then estimated within a moving time window of 15 minutes. The estimated offset due to  $DWR_{hard}$  and  $DWR_{att}$  is then applied to each profile within this 15 minute time window. During the relative  $DWR$  calibration, a set of quality flags are produced. For a detailed description of the quality flags, the reader is referred to Dias Neto et al., 2019. For this dataset, all profiles where the number of measurements used for the  $DWR$  calibration is less than 300 are excluded. Further, profiles where the variance of calculated  $DWR$  exceeds  $2 \text{ dB}^2$  or where the correlation of  $Ze$  pairs is less than 0.7 are excluded.

The largest contribution to the total attenuation is expected from rain and the  $ML$ . However, in case of additional attenuation due to large ice water paths or SLW layers, the attenuation is overestimated at the range gates below the SLW layer or in lower parts of the cloud. Therefore, our processed  $DWR_{scat}$  in the regions below the attenuation layers would be underestimate, even leading to negative  $DWR$ . The calculated  $DWR_{scat}$  is expected to be increasingly underestimated towards the ground, especially for  $DWR_{KaW}$ .

#### 3.1.3.4 Derived radar variables from the vertically pointing radars

In addition to the standard multi-frequency radar moments, i.e.  $Ze$ ,  $MDV$ , skewness,  $SW$ ,  $DWR_{KaW}$  and  $DWR_{XKa}$  also the spectral edge velocities were derived for the statistical analysis in Chapter 4. This analysis aims at investigating ice microphysical processes statistically, based on distinct radar signatures. Several studies have found a new, slow-falling secondary mode in Doppler spectra close to  $-15^\circ$  C and  $-8^\circ$  C, most likely related to the new formation of small, slow falling particles (D. and M., 2004; Field, 2000; Moisseev et al., 2015; Oue et al., 2018; Zawadzki et al., 2001). Looking at the slow falling edge velocity reveals such a secondary mode, since the slow falling edge would be slowed-down. One example can be seen in Figure 3.1a), where the slow edge is slowed down at a range of approximately 1.7 km. At this height, a second mode appears in the Doppler spectra. Similar to the derivation of the spectral mask described in Section 3.1.3.1, the slow and fast falling edge of the Ka-band Doppler spectra were derived. In case of strong atmospheric signals, spectral leakages might shift the fast (slow) edge velocity towards faster (slower) velocities. Therefore, in addition to selecting the slowest and fastest spectral velocity 3 dB above the noise level, spectral lines which are lower than 40 dB with respect to the maximum spectral line are neglected. The derived fast and slow edges of a case study are shown in Figure 3.1. Looking at the fast edge in addition to the slow edge can give information about updrafts, turbulence or particle growth. In case of an updraft, both spectral edges would slow down similarly (see Figure 3.1a), at approximately 2.4 km), while turbulence would broaden the spectrum, slowing down the slow edge and accelerating the fast edge in a similar way. In case of weak turbulence and low vertical velocity,  $v_D$  can be related to the particles terminal fall velocity. It is therefore related to the particles  $m$  and  $A$ , where an increase in  $m$  would increase the fall velocity, whereas an increase in  $A$  would decrease the fall velocity (e.g. Karrer et al., 2020). An acceleration of only the fast edge velocity would therefore indicate an increase in  $m$  of the fastest particles through e.g. aggregation or riming, or a decrease of  $A$  through for example melting. In Figure 3.1a), at 1 km height, the fast edge velocity is accelerating rapidly, since the particles are starting to melt, decreasing the area while the  $m$  is kept constant.



### 3.1.4 Processing of polarimetric dataset

For the analyses presented in Chapter 4, the CEL were used. The CEL measurements were collected for periods of 5 minutes. In contrast to the zenith dataset, no cleaning of the Doppler spectra, attenuation or offset correction was applied to the polarimetric dataset. The polarimetric radar moments and spectra were projected to the height above ground and then regridded to the same time-height grid as the zenith dataset. Since the radar is looking slant,  $v_D$  is impacted by the horizontal and vertical wind velocity as well as the fall velocity of the particles. Since the horizontal wind velocity often exceeds the Nyquist range, especially at higher altitudes, the Doppler spectra were often folded. Therefore, a simple dealiasing algorithm was applied, rotating  $v_D$  vector at each range until the Doppler bins containing only noise are at  $\pm$  the Nyquist range. An example of the non- and dealiased spectra can be found in Figure 3.4. In general, the quality of the polarimetric observations depends strongly on the signal-to-noise ratio (SNR) (e.g. section 6.5 in Bringi and Chandrasekar, 2001). In order to use only high quality data for the analyses presented in this study, only polarimetric data where the SNR (or in case of spectral polarimetry SNR per spectral bin) is above 10 dB are used.

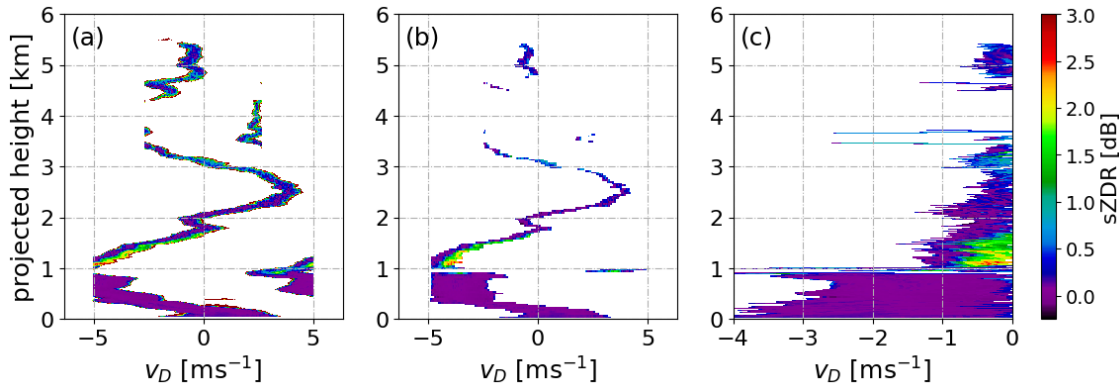


Figure 3.4: Example of spectral  $sZDR$  from 24<sup>th</sup> November 2018, 08:02:30UTC. Panel (a) shows an uncorrected  $sZDR$ , panel (b) the  $sZDR$  after the dealiasing was applied and the spectral bins where the spectral SNR is less than 10 dB were masked. Panel (c) shows the corrected  $sZDR$  with the slowest falling spectral bin moved to 0 m s<sup>-1</sup>. In this way, the effect of the horizontal wind on  $v_D$  is reduced, allows an easier analysis of the microphysical features.

#### 3.1.4.1 Derived radar variables from the polarimetric radar

The Level-1 files produced by the internal software of the polarimetric radar already contained  $Ze$  at horizontal and vertical polarisation,  $MDV$ ,  $ZDR$ ,  $\rho_{hv}$ ,  $\phi_{dp}$ , skewness,  $SW$  and slanted  $LDR$ , among others. In order to reduce the noise in  $\phi_{dp}$  and estimate KDP,  $\phi_{dp}$  was smoothed over 5 range gates (corresponding to 180 m) using a moving window mean and then averaged over 5 minutes. KDP was then calculated as

$$KDP = \frac{\Delta\phi_{dp}}{2 * \Delta r} \quad (3.2)$$

with  $\Delta r$  the range resolution.

As described in Section 2.2.5,  $ZDR$  is reflectivity weighted and thus reduced as soon as large aggregates are observed. Since the larger aggregates are usually falling faster than the smaller  $ZDR$  producing ice crystals, the  $ZDR$  is separated in  $sZDR$ . By looking at the maximum  $sZDR$  ( $sZDR_{max}$ ), high- $ZDR$  producing particles can be observed, even when large aggregates are present and reducing the integrated  $ZDR$ .

### 3.1.5 Matching of polarimetric and zenith dataset

As described in Section 3.1, all radars were installed in close vicinity to each other, in order to enable an optimal volume matching. Further, the vertical and temporal resolutions as well as the beam widths of the vertically pointing radars were chosen such that the difference between the three radars is as small as possible (Table 3.1). However, since the polarimetric W-band was pointing at  $30^\circ$  elevation, the volumes of the vertically pointing and polarimetric radar do not match. At the maximum range of the polarimetric radar (16 km), the maximum horizontal distance between the vertically pointing and the polarimetric radar is  $\cos(30^\circ) \cdot 16 \text{ km} = 13.86 \text{ km}$ . An analysis of the wind direction during the TRIPEX-POL campaign, obtained from Cloudnet, revealed that the main wind direction was between  $235^\circ$  and  $350^\circ$  (south-west to north-west, Figure 3.5 a), close to the chosen azimuth during the CEL measurements. Most cloud systems are therefore advected from the volumes observed by the polarimetric radar over the volumes observed by the vertically pointing radars. The most frequent wind velocity, without discriminating different heights, was found to be approximately  $10 \text{ m s}^{-1}$  (Figure 3.5 b). As expected, the wind velocity increases with increasing height above the radar (decreasing temperature, Figure 3.5 c). The analysis of ice microphysical processes in this study focuses on the region between  $-20$  and  $0^\circ \text{ C}$ . In this region, the median wind velocity lies between  $20$  and  $10 \text{ m s}^{-1}$  at  $-20$  and  $0^\circ \text{ C}$  respectively (white line in Figure 3.5 c). The mean  $2 \text{ m}$  temperature according to Cloudnet during the TRIPEX-POL campaign was  $4.6^\circ \text{ C}$ . Assuming a constant lapse-rate of  $-6^\circ \text{ km}^{-1}$ ,  $-20^\circ \text{ C}$  would be at approximately  $4.1 \text{ km}$  height, leading to a distance of  $7.1 \text{ km}$  between the observed volumes of the polarimetric and vertically pointing radars. At a wind velocity of  $20 \text{ m s}^{-1}$ , the volume observed from the polarimetric radar would be advected over JOYCE-CF in 355 seconds (or 5.9 minutes). Similarly, a volume observed at  $0^\circ \text{ C}$  from the polarimetric radar would be advected over JOYCE-CF in 133 seconds, corresponding to 2.2 minutes. In order to compare the observations from the polarimetric radar to the observations of the vertically pointing radars, all datasets were averaged over 5 minutes to account for the time needed to advect the observed radar volumes from the polarimetric radar over the vertically pointing radars. Of course with this correction, it is implicitly assumed that the vertical distribution of particles and processes does not change or that it can be at least assumed to be in a steady-state condition during the averaging time period.

## 3.2 THE MONTE-CARLO LAGRANGIAN PARTICLE MODEL MCSNOW

The MCSNOW was developed by Brdar and Seifert (Brdar and Seifert, 2018). MCSNOW models the evolution of ice particles via depositional growth, aggregation, riming, melting and warm phase processes. In MCSNOW, ice mass, rime mass and volume, number of monomers and shape of the monomers is tracked for each super-particle. In the course of PROM-IMPRINT, a habit prediction was added to the initial MCSNOW at

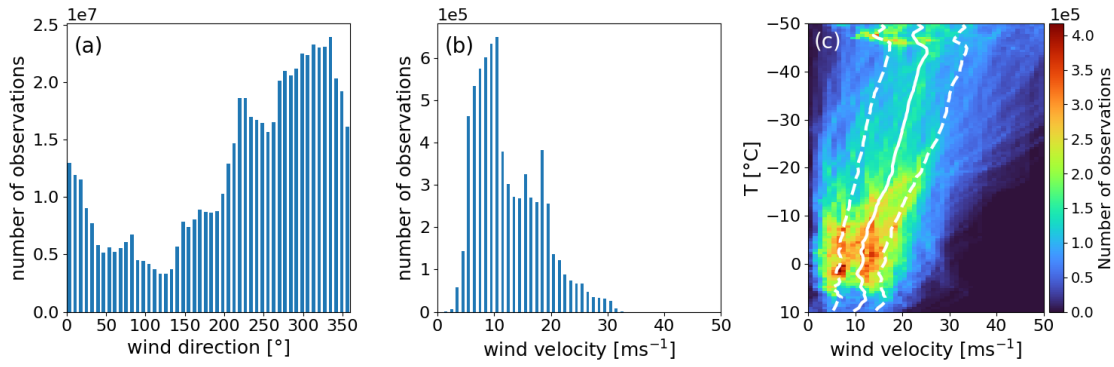


Figure 3.5: Histograms of the wind direction at all heights (a), the wind speed at all heights (b) and the wind speed in dependency of the temperature (c). The white solid line in (c) represents the median of the distribution, the dashed lines the 25<sup>th</sup> and 75<sup>th</sup> percentiles

german weather service (DWD). In the habit prediction, the shape of the particle can be altered by growth processes such as depositional-growth, riming or aggregation. Shape is an important property of ice particles, as it impacts the fall velocity and interaction with other particles. The difference in fall velocity is an important property impacting the collision kernel (Equation 2.4). Further, the shape of the particle also influences the collision kernel by affecting the  $A$ . The shape can also affect  $E_s$ , as e.g. dendritic particles increase  $E_s$  through mechanical interlocking. The shape of the ice particle also tells a story about its motion through the cloud. The habit is temperature and super-saturation dependent and therefore shows where the particle was nucleated and which conditions it experienced while falling towards the ground. So far, only ice crystal experience habit dependent growth in McSnow.

### 3.2.1 Depositional growth

Depositional growth affects the primary and secondary habit of ice particles. As described in Section 2.1.2.1, the primary habit (i.e. aspect ratio) of the ice particle is determined by the temperature that the particle is growing at. The secondary habit depends on the super-saturation during growth and the temperature and effectively reduces the density of the ice particle through branching (plate-like particles) or hollowing (column-like particles).

In McSnow, the particles are modelled as spheroids. Therefore, the aspect ratio ( $\phi$ ) of a particle can be described with the ratio of the a and c-axis of the particle (see spheroids in Figure 3.6):

$$\phi = \frac{c}{a} \quad (3.3)$$

The change of  $\phi$  due depositional growth is then given by

$$\frac{dc}{da} = \frac{\alpha_c}{\alpha_a} \phi \quad (3.4)$$

with deposition coefficient of axis c ( $\alpha_c$ ) and deposition coefficient of axis a ( $\alpha_a$ ). Chen and Lamb, 1994 derived the ratio of the deposition coefficients from laboratory studies.

The resulting, temperature dependent inherent growth function ( $\Gamma$ ) is shown in Figure 3.6. The change of mass due to depositional growth is then calculated with Equation 2.1, where the change in  $\phi$  is incorporated via  $C$ . For spherical particles,  $C$  is equal to one. For oblate (plate-like) particles,  $C$  is given by

$$C = \frac{\alpha \epsilon_o}{\sin^{-1} \epsilon_o} \quad (3.5)$$

with eccentricity of oblates ( $\epsilon_o$ )  $\epsilon_o = \sqrt{1 - \phi^2}$  (Chen and Lamb, 1994). Similarly,  $C$  for prolate (column-like) particles is given by

$$C = \frac{c \epsilon_p}{\ln(1 + \epsilon_p) \phi} \quad (3.6)$$

with eccentricity of prolates ( $\epsilon_p$ )  $\epsilon_p = \sqrt{1 - \phi^{-2}}$  (Chen and Lamb, 1994). As a spheroid can not directly develop a secondary habit (such as the growth of branched arms), the effects of a secondary habit get incorporated as a change in density ( $\rho$ ). For this, the ice volume increase gets amplified relative to the mass increase. Following Jensen and Harrington, 2015,  $V$  of the spheroid is increasing through depositional growth with

$$\frac{dV}{dt} = \frac{1}{\rho_{\text{depo}}} \frac{dm}{dt}. \quad (3.7)$$

The deposition density ( $\rho_{\text{depo}}$ ) is dependent on ambient temperature and super-saturation and proportional to  $\rho_i \Gamma(T)$  for prolate particles and  $\rho_i \Gamma(T)^{-1}$  for oblate particles, with density of solid ice ( $\rho_i$ ). The secondary habit is only assumed to happen once the particle has reached a fall velocity of  $va^2 > \pi D_v C$  (Jensen and Harrington, 2015).

### 3.2.2 Sedimentation

With a complete description of the particles geometry, the terminal velocity of the particle can be calculated. In McSnow, the fall velocity can be calculated using different aerodynamic models, such as the Khvorostyanov and Curry (Khvorostyanov and Curry, 2005), Heymsfield and Westbrook (Heymsfield and Westbrook, 2010) or Böhm model (Böhm, 1992a). In the following, the Böhm model is used to calculate the terminal velocity of the particles simulated in McSnow.

### 3.2.3 Aggregation

As in case of the depositional growth, aggregation is calculated directly from the stochastic collection equation Equation 2.3. The shape of the particle is expected to have an impact on the aggregation through changing the sticking efficiency in case of branched dendrites or changing the fall-velocity difference if there are different habits present at the same height. In McSnow, different collision efficiencies are implemented. In the course of this work, the collision efficiency of Böhm, 1992b is chosen, which considers the shape of the particle. The sticking efficiency ( $E_s$ ) is considered to be a function of the air temperature as described in Brdar and Seifert, 2018.

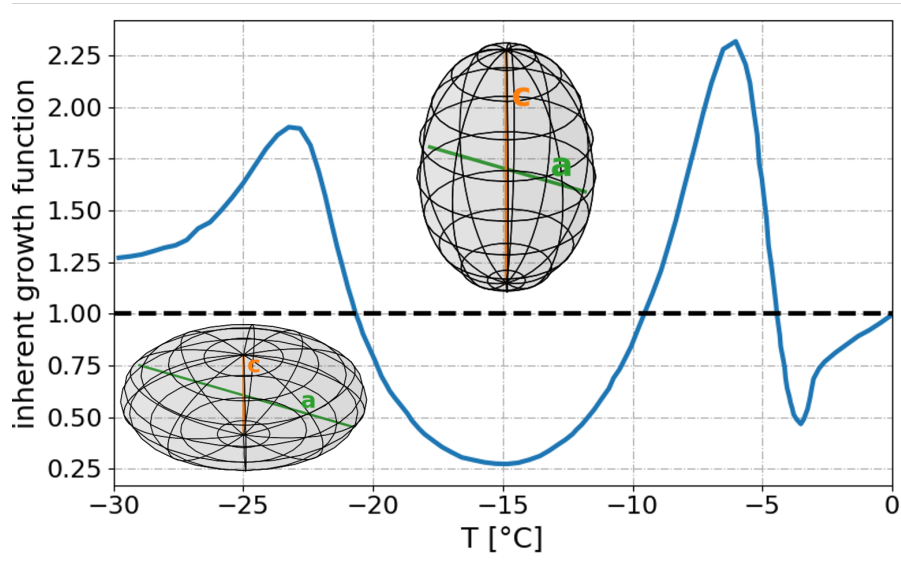


Figure 3.6: Inherent growth function ( $\Gamma$ ), adapted from Chen and Lamb, 1994. The spheroids are illustrating the shape in which the particles are growing for  $\Gamma$  above one (prolate) and below (oblate) one. Further, the a- and c-axis of the spheroid are illustrated (in orange and green respectively).

#### 3.2.4 Riming

If SLW droplets are present, McSnow has the ability to model riming. Two different approaches are implemented in McSnow, a continuous riming model and a stochastic riming model (Brdar and Seifert, 2018; Seifert et al., 2019). As was mentioned in Section 2.1.2.3, the observational dataset consisted of only a few riming cases, therefore, riming is not included in the modelling studies in Chapter 5.

#### 3.2.5 Secondary ice production

McSnow further allows to simulate different SIP, such as the HM-process or fragmentation during ice-ice collision. At DWD, the fragmentation scheme developed by Phillips et al., 2017 was recently implemented into McSnow. Their scheme is based on the laboratory studies conducted by Vardiman, 1978 and Takahashi et al., 1995, and the conservation of energy during the collisions of ice particles. The governing variable in the fragmentation scheme is the collision kinetic energy. The scheme allows fragmentation for collisions of graupel-graupel, hail-hail and snow (crystal or aggregate) with any other ice particle. For the following analysis, the fragmentation scheme is not used. The conducted simulations are based on observations were only little, if any riming occurred. However, the fragmentation scheme is based on the experiments of collisions of two ice-spheres. The collision kinetic energy required for fragmentation calculated from the experiments of Takahashi et al., 1995 is much higher than would be expected in the

collisions between two aggregates or aggregates and crystals. Further, [McSnow](#) is still in a developing stage and collisions and resulting aggregation between ice crystals has proven to be more difficult than expected. The ice crystals need to be initialised with maximum dimension ( $D_{\max}$ )  $\leq 50 \mu\text{m}$  in order to achieve reasonable habit growth. This limits the variability of fall velocities and sizes needed for collisions and subsequent aggregation. In addition, the shape of the fragments generated during collisions is unknown. Therefore, the fragments do not experience habit dependent growth at this developing stage, which limits the ability of forward simulations and polarimetric scattering calculations.

### 3.2.6 1D Model

1D "shaft" models have been used to investigate the impact of microphysical processes and physical parameters on microphysical quantities, processes or observations (e.g. Karrer et al., 2021; Kumjian and Ryzhkov, 2010; Seifert, 2008). The use of a 1D model significantly reduces the complexity compared to a full 3D microphysical simulation, as in the 1D setup, atmospheric parameters are predefined and feedback mechanisms from microphysics to the thermodynamics are neglected. Also, the computational cost is reduced drastically, allowing to test sensitivities, among others, in much more detail. However, 1D models are highly idealised and the neglect of feedback mechanisms between thermodynamics and microphysics might lead to a bias when investigating processes such as aggregation or riming which could be influenced by turbulence. Further, influences of updrafts on depositional growth (i.e. through an increase in residence time in possible depositional growth favouring cloud regions) can not be investigated. Seifert, 2008 investigated the impact of evaporation of raindrops on the [DSD](#) using a 1D model and developed a new parameterisation of the shape of the [DSD](#). Kumjian and Ryzhkov, 2010 studied the impact of evaporation on the polarimetric radar variables in rain using as well a 1D shaft model. The performance of the predicted particle properties ( $P_3$ ) scheme was shown using a 1D model, simulating total ice mass and reflectivity among others. Karrer et al., 2021 used a 1D setup of the Icosahedral Nonhydrostatic Model ([ICON](#)) to investigate sensitivities of aggregation to various parameters such as the width of the PSD or the fall velocity of the particles.

#### 3.2.6.1 Setup of depositional growth study

In this work, two different 1D setups have been chosen. With the first setup, the evolution of ice crystal habit through depositional growth during sedimentation has been investigated ([Section 5.1](#)). For this, a constant lapse rate of  $6 \text{ K km}^{-1}$  and  $0^\circ \text{ C}$  at 0 m height has been assumed. In total, 5 simulations have been performed, for each simulation the relative humidity over ice ( $\text{RH}_i$ ) was kept constant at  $\text{RH}_i = 101\%$  (105%, 110%, 115%, 120%). Ice crystals were initialised every 10 m (so every  $0.06^\circ \text{ C}$ ) between  $-30$  and  $-10^\circ \text{ C}$  with a diameter of  $10 \mu\text{m}$  and an aspect ratio of 1. This resulted in 350 particles. Even if [McSnow](#) is a "super-particle" model, the small number of particles allowed to assume that all particles are real particles. The 1D model contained 300 vertical cells, giving a height resolution of 16.67 m. The thermodynamic properties (i.e. temperature, relative humidity and pressure) were interpolated to the particles' actual position. This setup is illustrated in [Figure 3.7a](#). To simplify the simulations and



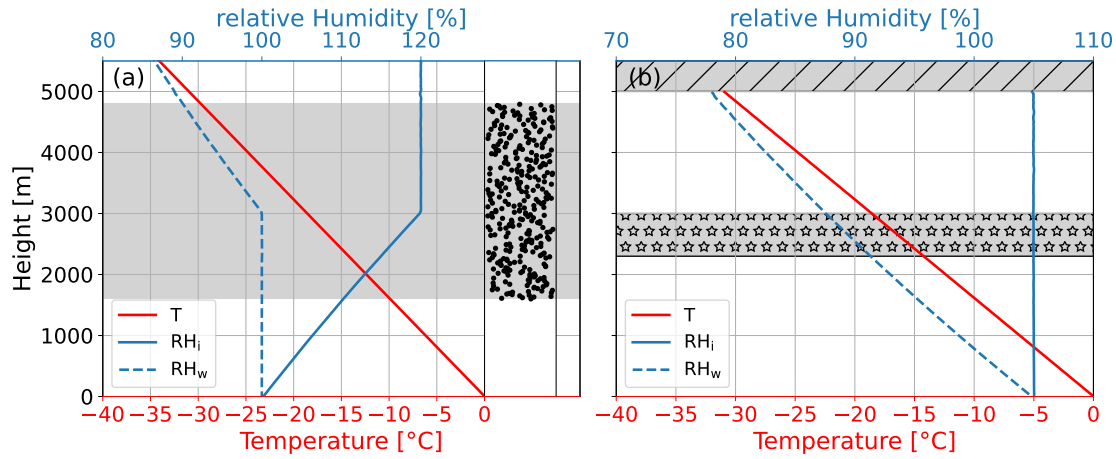


Figure 3.7: Schematic illustration of the setup used for *McSnow* simulations in this thesis. (a) Setup for testing the depositional growth under sedimentation. The red line shows the temperature, the blue dashed line the relative humidity over water ( $RH_w$ ) and the blue solid line the  $RH_i$ . The simulations were performed with  $RH_i = 101, 105, 110, 115$  and  $120\%$ . In this case,  $RH_i = 120\%$  is illustrated. Once  $RH_w = 100\%$  is reached, constant  $RH_w = 100\%$  is assumed (here from  $3000$  m towards the bottom of the domain). The black dots in the right of panel (a) illustrate the ice particles that were initialised in the height region underlined by the grey area. (b) Setup of the secondary mode study. The grey area with slashes at the top of the domain illustrates the top boundary zone, in which aggregates are initialised on three model levels. This creates a constant mass flux into the domain according to the predefined mass distribution (see Brdar and Seifert, 2018). The grey area with stars shows the second nucleation (or initialisation) layer within the DGL. Here, a second mode of ice crystals is nucleated to simulate possible secondary ice processes.



focus only on the depositional growth of ice crystals, aggregation was deactivated. In contrast to observations in the laboratory, where the ice particles are kept at constant super-saturations and temperatures during growth, this setup resembles more realistic conditions, as ice particles are able to develop various habits while falling.

### 3.2.6.2 Setup of secondary mode study

Previous studies have frequently observed a secondary, slow falling mode to appear in the Doppler spectrum close to  $-15^{\circ}\text{C}$  (e.g. D. and M., 2004; Field, 2000; Moisseev et al., 2015, 2009; Oue et al., 2018). This secondary mode of particles is likely linked to the growth of plate-like particles at  $-15^{\circ}\text{C}$ . However, no final conclusion on the origin of these particles has been found in literature. It has been hypothesised in von Terzi et al., 2022 that the secondary mode is related to collisional fragmentation of ice particles during aggregation. The secondary mode of ice particles is often accompanied with an updraft. Zawadzki, 2013 have therefore hypothesised that the updraft enhances the  $\text{RH}_i$  in the vicinity of  $-15^{\circ}\text{C}$ , leading to the new activation of INP and therefore primary nucleation of ice particles. Both hypothesis are investigated in Section 5.3. Further, von Terzi et al., 2022 found that already larger particles and wider PSD that are sedimenting into the DGL are connected to stronger aggregation.

As was described in Section 3.2, the fragmentation scheme implemented in McSNOW has certain caveats. First, the collision kinetic energy needed for fragmentation is much higher than expected for aggregates, as the fragmentation scheme is based on the collision of two solid ice spheres (Takahashi et al., 1995). Therefore, during the collisions of aggregates no fragments are generated. Second, collisions and aggregation between ice crystals in McSNOW is more difficult than expected. In order to simulate the habit growth due to deposition of ice crystals, they need to be nucleated with  $D_{\text{max}} < 50\text{ }\mu\text{m}$ , which limits the variability of sizes and fall velocities required for aggregation to happen. Third, the shape of the fragments are unknown. Therefore the fragments in McSNOW currently do not develop a habit. This affects their interaction with other particles (such as aggregation), and limits the possibility of forward simulations.

Rather, the impact of possible ice fragmentation and primary nucleation due to enhanced  $\text{RH}_i$  on aggregation was investigated by simulating an aggregate mode sedimenting into the DGL and inserting a second initialisation layer at temperatures close to  $-15^{\circ}\text{C}$ . Further, the impact of different PSDs of aggregates sedimenting into the DGL was tested. The simulation setup is described in more detail in the following paragraph and schematically in Figure 3.7b. The simulation domain was setup as in Section 3.2.6.1, and the  $\text{RH}_i$  was assumed to be 105%. As reference simulations, an aggregate mode with a constant flux through the top boundary was simulated. The aggregates were drawn from two different mass distributions, following the generalised gamma distribution

$$N(m) = A_m m^{\nu_m} \exp(-\lambda_m m^{\mu_m}), \quad (3.8)$$

with  $m$  as primary variable.  $A_m$  and  $\lambda_m$  are calculated from the defined ice water content (IWC) and number of real particles ( $n_{rp0}$ )

$$\begin{aligned}\bar{m} &= \frac{IWC}{n_{rp0}}, \\ \lambda_m &= \left( \frac{\Gamma_{n1}}{\Gamma_{n2}\bar{m}} \right)^{-\mu_m}, \\ A_m &= \left( \frac{\mu_m n_{rp0}}{\Gamma_{n1}} \right) \lambda^{\frac{\mu_m+1}{\mu_m}},\end{aligned}\tag{3.9}$$

with  $\Gamma_{n1} = \Gamma(\frac{\mu_m+1}{\mu_m})$  and  $\Gamma_{n2} = \Gamma(\frac{\mu_m+2}{\mu_m})$ . The initialised aggregates follow the  $m$ - $D_{max}$  relationship and area- $D_{max}$  relationship of aggregates of side planes, columns and bullets from Mitchell et al., 1996. While sedimenting towards the ground, the aggregates can further aggregate according to the collection equation Equation 2.3 and with the aggregation efficiency from Connolly et al., 2012. The specific setup of the two distributions is described in Table 3.2. They will hereafter be referred to as the simulation with a wide PSD ( $S_{wi}$ ) and simulation with a narrow PSD ( $S_{na}$ ).  $S_{wi}$  was set up such that the forward simulated  $DWR_{Kaw}$  and  $Ze$  are close to the observed median  $DWR_{Kaw}$  and  $Ze$  of  $DWR_{Kaw}$ -class 3 provided in Chapter 4.

The impact of a secondary mode due to primary nucleation on aggregation was investigated by adding a second initialisation layer between  $-13.8$  and  $-18$  ° C to the simulations  $S_{na}$  and  $S_{wi}$ . In the second initialisation layer, particles with ice density and  $\phi = 1$  are drawn from a gamma distribution in mass with a nucleation rate of 50 super-particles per  $m^3$ . This corresponds to spherical particles with a mean  $D_{max}$  of 20  $\mu m$  and a mean number concentration between 2000 and 5000 particles per  $m^3$ . This nucleation rate was chosen, since the INP concentration at  $-15$  ° C was found to be 1000 to 2000  $m^{-3}$  in DeMott et al., 2010 and mostly below 10000  $m^{-3}$  in Kanji et al., 2017. The complete setup of the simulations with a second mode simulating a secondary mode due to primary nucleation is summarised in Table 3.2. The simulations will hereafter be referred to as simulation with a wide PSD and secondary mode due to primary nucleation ( $S_{w,2nd}$ ), and simulation with a narrow PSD and secondary mode due to primary nucleation ( $S_{n,2nd}$ ).

In a recent Master-Thesis conducted in the cold chamber of the University of Mainu, Grzegorzczuk, 2022 investigated ice fragmentation due to the collisions of two realistically grown graupel particles. Grzegorzczuk, 2022 found that the PSD of fragments produced during the collision of two graupel particles had a maximum at a  $D_{max}$  of 75  $\mu m$ , and all fragments were found to be smaller than 1000  $\mu m$  (see detailed description in Appendix B). This PSD is the basis in the following experiments addressing fragmentation. Similar to  $S_{n,2nd}$  and  $S_{w,2nd}$ , to simulate a secondary mode due to fragmentation, a second initialisation layer was inserted between  $-13.8$  and  $-18$  ° C. The particles in the second initialisation layer were drawn from a gamma distribution in  $D_{max}$  with the parameters provided in Table 3.2. Grzegorzczuk, 2022 further found that  $\phi$  of the fragments are similar to that of dendritic particles. Therefore, the particles were initialised with  $\phi$ - $D_{max}$  relation from Pruppacher and Klett, 1997 for dendritic crystals of type P1e. The mass and volume of the particles were then calculated from the  $D_{max}$  and  $\phi$  obtained. Vardiman, 1978 found that SIP due to ice-ice collisions might enhance the particle number concentration by a factor of 10. To allow for a better comparison to the  $S_{n,2nd}$  and  $S_{w,2nd}$  scenarios, and since the real number of fragments due to collisions of

aggregates is unknown, a nucleation rate of 50 super-particle per  $\text{m}^3$  was also chosen in this setup. The secondary mode due to fragmentation was again simulated with the wide and narrow aggregate PSD from  $S_{wi}$  and  $S_{na}$ . The simulation will hereafter be referred to as simulation with a wide PSD and secondary mode due to fragmentation ( $S_{w,frag}$ ), and simulation with a narrow PSD and secondary mode due to fragmentation ( $S_{n,frag}$ ).

Table 3.2: Initial setup of the particle mass and size distributions of the simulations of aggregation with McSnow.  $\nu_m$  and  $\mu_m$  as well as IWC and  $\text{nrp}_0$  describe the parameters of the generalised gamma distribution used to initialise the aggregate mode. The second mode was nucleated from a gamma distribution described with the scale and shape with a nucleation rate  $\text{ncl}_{\text{rate}}$  given in number of super-particles per s and per  $\text{m}^3$ . In case of  $S_{w,2nd}$  and  $S_{n,2nd}$  the second mode was nucleated with a gamma distribution in mass. The scale was chosen such that the mean mass of the distribution is  $10^{-11}$  kg, corresponding to a mean  $D_{\text{max}}$  of 20  $\mu\text{m}$ . In case of  $S_{w,frag}$  and  $S_{n,frag}$  the second mode was nucleated with a gamma distribution in size. The scale and shape of the distribution were chosen such that the maximum number of particles have a  $D_{\text{max}}$  of 75  $\mu\text{m}$  and all particles are smaller than 1000  $\mu\text{m}$ .

Simulation	$\nu_m$	$\mu_m$	IWC [ $\text{kg m}^{-3}$ ]	$\text{nrp}_0$ [ $\text{m}^{-3}$ ]	$\text{ncl}_{\text{rate}}$ [SP s $^{-1}$ m $^{-3}$ ]	scale	shape
$S_{wi}$	3.5	0.5	$3 \cdot 10^{-5}$	2000	0	0	0
$S_{na}$	10	10	$1 \cdot 10^{-5}$	1000	0	0	0
$S_{w,2nd}$	3.5	0.5	$3 \cdot 10^{-5}$	2000	50	$10^{-11}$ kg	0.64
$S_{n,2nd}$	10	10	$1 \cdot 10^{-5}$	1000	50	$10^{-11}$ kg	0.64
$S_{w,frag}$	3.5	0.5	$3 \cdot 10^{-5}$	2000	50	$10^{-4}$ m	0.5
$S_{n,frag}$	10	10	$1 \cdot 10^{-5}$	1000	50	$10^{-4}$ m	0.5

### 3.3 MCRADAR: A FORWARD SIMULATION TOOL FOR MCSNOW OUTPUT

McRadar is a forward operator that links simulations and observations. McRadar was developed to deal with the complex output of **McSnow**. Especially the predicted shape of the monomers can so far not be forward simulated with more sophisticated forward simulators such as **PAMTRA**. The basic setup of McRadar was originally developed by José Dias-Neto and Davide Ori within the EN OPTIMice working-group. McRadar is based on look-up tables, where the particle properties and corresponding scattering properties are saved. The initial development of McRadar used the T-matrix code from Leinonen, 2013 to calculate the scattering properties of the particles simulated with McSnow. In the course of this thesis, look-up tables based on **DDA** and **SSRGA** were added to McRadar. McRadar was further further extended to calculate the scattering properties using the Rayleigh approximation. As the observed Doppler spectra are affected by turbulence broadening and radar noise, among others, these effects can be added to the Doppler spectra after the scattering properties have been derived. This noise convolution and turbulence broadening is done as in **PAMTRA** and is described in detail in chapter 6, Maahn, 2015

In general, the scattering properties of ice particles are challenging to characterise. The main issues arise from describing the particles physical properties (e.g. the structure,

$m$ , density, aspect ratios) and calculating the scattering properties from those physical properties (Kneifel et al., 2020). Four scattering approaches are available in McRadar. The first approach is the T-matrix method (see Section 2.4). This approach has the advantage that both McSnow and the T-matrix approximate the particles as spheroids. Therefore, the physical properties of the particles do not need to be characterised further. However, since the T-matrix is assuming a homogeneous mixture of ice and air within the particle, the  $m$  distribution within the particle is not described accurately. However, the description of the  $m$  distribution seems to be necessary in order to calculate the scattering properties of particles accurately (Sorensen, 2001). Therefore, the T-matrix has been found to deviate from accurate scattering methods such as DDA (e.g. Kneifel et al., 2020). These discrepancies are especially large in case of large  $X$  (Kim, 2006; Kneifel et al., 2020). Further, in the course of this thesis, it has been found that at W-band, the T-matrix is not converging to a stable solution for particles larger than 5 mm or aspect ratios smaller than  $10^{-2}$ .

Another possibility in McRadar is the use of look-up tables calculated with DDA. The look-up tables are based on the calculations of 50 horizontally aligned dendritic aggregates and 50 horizontally aligned dendritic crystals. The crystals were produced using the aggregation model developed by Leinonen and Moisseev, 2015. There, the crystals are modelled using thickness-diameter relationships from Pruppacher and Klett, 1997. The aggregates have been generated with the same aggregation model and they have been used in previous studies (Karrer et al., 2020; Ori et al., 2021). The DDA was then calculated using the ADDA code (Yurkin and Hoekstra, 2011). The DDA look-up tables can so far not be used to forward simulate the scattering properties based on the physical properties of the particles simulated with McSnow. The DDA calculations have to be done on particles where the structure (i.e. the position of each dipole) is known. However, McSnow approximates the particles using spheroids, where the actual structure of the particle (i.e. the  $m$  distribution within the particle) is unknown. The particle structure is dependent on the growth history, and choosing an accurate particle type (e.g. dendrite vs. broad-branched sector vs. stellar crystal) only having the information about the  $\phi$  and  $\rho$  of the particle is challenging. Especially since the complex growth history can result in a large variety in  $\phi$ ,  $\rho$  and  $m$ . The look-up tables with the scattering properties need to be able to represent this large variety of physical properties. So far the physical properties of the crystals and aggregates used to calculate the DDA do not match the physical properties of the particles in McSnow well, as especially the aspect ratio and density in McSnow is much more variable than that of the dendritic crystals available (see Figure 3.8).

To allow a fast and accurate calculation of the multi-frequency scattering properties of aggregates, also look-up tables based on SSRGA are available in McRadar. As has been described in Section 2.4, SSRGA calculates the scattering properties of an ensemble of particles, where the structure of each particle does not need to be known. The scattering properties with the SSRGA were calculated using the snowScatt tool (Ori et al., 2021). So far, the scattering properties of dendritic aggregates (type vonTerzi\_dendrite) are available in McRadar. The SSRGA is only valid for self-similar, low-density particles such as aggregates (see Section 2.4.1.1). When particles are heavily rimed or single crystals, this assumption is no longer valid (Leinonen et al., 2018). Therefore, when calculating multi-frequency variables in McRadar, ice crystals can be assumed to be Rayleigh-scatterers, or approximated by the T-matrix.

*snowScatt: python package that provides the scattering and physical properties of aggregates and rimed particles. The scattering properties in snowScatt are approximated using the SSRGA.*

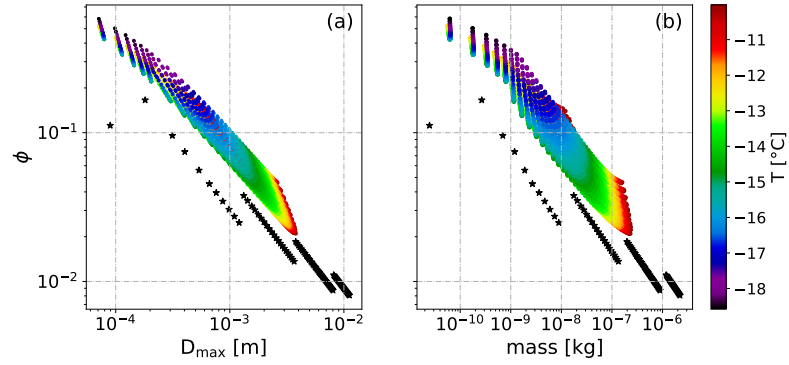


Figure 3.8: Comparison of the physical properties of the dendritic crystals used to calculate the scattering properties with DDA (black crosses) and the particle properties obtained from McSnow simulations. The particles in McSnow were grown at water saturation while sedimenting towards the ground. Shown is a comparison of the aspect ratio ( $\phi$ ) - maximum dimension ( $D_{\max}$ ) (a) and aspect ratio -  $m$  (b) of the particles. The colouring denotes the temperature at which the particles are growing.

### 3.3.1 McRadar setup

McRadar was used to forward simulate the [McSnow](#) output. The simulations conducted to investigate the depositional growth ([Section 3.2.6.1](#)) were forward simulated using the T-matrix approximation.

The McSnow simulations investigating the influence of a secondary spectral mode were forward simulated using the look-up tables of [SSRGA](#) scattering properties for aggregates. The scattering properties of the monomers were calculated with the Rayleigh-approximation. Further, noise and turbulence was convoluted on the Doppler spectra. The setup of the forward simulations is described in detail in [Table 3.3](#). The setup was chosen to follow the specifications of the Ka-band radar used in the radar observations.

Table 3.3: Setup of the forward simulations with McRadar.

Parameter	Setup
Scattering approximation	SSRGA, Rayleigh
Range resolution	36 m
Elevation	90°
Frequency	9.6, 35.5, 94.0 GHz
Number of FFTs	512
Nyquist range	$\pm 3 \text{ m s}^{-1}$
Doppler resolution	$0.012 \text{ m s}^{-1}$
Integration time	2.0 s
Number of spectral averages	20
Half-power beam width	0.6°
Noise Power	−40 dB
Eddy-Dissipation rate	$10^{-6}$
Horizontal wind velocity	$10 \text{ m s}^{-1}$





The **DGL** is a fascinating temperature region in clouds, as various ice microphysical processes have been observed to take place there. The plate-like particle growth between  $-20$  and  $-10^{\circ}\text{C}$  leads to a maximum in the depositional growth rate at  $-15^{\circ}\text{C}$  (Pruppacher and Klett, 1997). Further, the difference in water vapour saturation pressure between ice and liquid is largest at  $-12^{\circ}\text{C}$ , which favours the depositional growth of ice through the Wegener-Bergeron-Findeisen process (Korolev, 2007). The plate-like particles are known to produce distinct dendritic secondary habits at temperatures between  $-16$  and  $-12^{\circ}\text{C}$ . These dendritic particles grow fragile branched arms, which have been found to break off during collisions (Griggs and Choulaton, 1986; Takahashi, 1993; Takahashi et al., 1995; Vardiman, 1978). Collisional fragmentation might explain the increase in ice crystal number concentration found in in-situ and radar observations (e.g. Hobbs and Rangno, 1985, 1990, 1998). These dendritic particles are also known to favour aggregation, through interlocking the branched arms upon collision (Connolly et al., 2012).

Even though the **DGL** is an important region for ice growth processes and therefore also for precipitation development, the interplay between plate-like growth, secondary ice processes and aggregation have not been fully understood. In von Terzi et al., 2022, aggregation and its connection to depositional growth and SIP, as well as the slow-down in **MDV** is investigated in detail by analysing vertically pointing triple-frequency Doppler radar observations combined with spectrally resolved dual-polarimetric radar observations. This unique setup enables a simultaneous look at the aggregate size, as well as ice crystal shape and concentration. Therefore, the increase of aggregation and ice crystal size and concentration can be investigated in more detail. Further, most previous studies have focused their investigations of the **DGL** on case studies which revealed strong polarimetric and multi-frequency signatures. It is unclear however, how frequent and important these signatures are in mid-latitude winter clouds. von Terzi et al., 2022 analyses these signatures and their relation to aggregation statistically.

This study has been published in

**von Terzi, L., Dias Neto, J., Ori, D., Myagkov, A., and Kneifel, S. (2022): Ice microphysical processes in the dendritic growth layer: a statistical analysis combining multi-frequency and polarimetric Doppler cloud radar observations, Atmos. Chem. Phys., 22, 11795–11821, <https://doi.org/10.5194/acp-22-11795-2022>**

The article was published by Copernicus Publications and is reproduced here under the Creative Commons Attribution License 4.0.



# Ice microphysical processes in the dendritic growth layer: a statistical analysis combining multi-frequency and polarimetric Doppler cloud radar observations

Leonie von Terzi<sup>1</sup>, José Dias Neto<sup>2</sup>, Davide Ori<sup>1</sup>, Alexander Myagkov<sup>3</sup>, and Stefan Kneifel<sup>1,4</sup>

<sup>1</sup>Institute of Geophysics and Meteorology, University of Cologne, Cologne, Germany

<sup>2</sup>Department of Geosciences and Remote Sensing, Delft University of Technology, Delft, the Netherlands

<sup>3</sup>Radiometer Physics GmbH, Meckenheim, Germany

<sup>4</sup>Meteorological Institute, Ludwig-Maximilians University Munich, Germany

**Correspondence:** Leonie von Terzi (lterzi@uni-koeln.de)

Received: 7 April 2022 – Discussion started: 11 April 2022

Revised: 24 August 2022 – Accepted: 25 August 2022 – Published: 13 September 2022

**Abstract.** The dendritic growth layer (DGL), defined as the temperature region between  $-20$  and  $-10$  °C, plays an important role for ice depositional growth, aggregation and potentially secondary ice processes. The DGL has been found in the past to exhibit specific observational signatures in polarimetric and vertically pointing radar observations. However, consistent conclusions about their physical interpretation have often not been reached.

In this study, we exploit a unique 3-months dataset of mid-latitude winter clouds observed with vertically pointing triple-frequency (X-, Ka-, W-band) and polarimetric W-band Doppler radars. In addition to standard radar moments, we also analyse the multi-wavelength and polarimetric Doppler spectra. New variables, such as the maximum of the spectral differential reflectivity (ZDR) ( $sZDR_{max}$ ), allows us to analyse the ZDR signal of asymmetric ice particles independent of the presence of low ZDR producing aggregates. This unique dataset enables us to investigate correlations between enhanced aggregation and evolution of small ice particles in the DGL. For this, the multi-frequency observations are used to classify all profiles according to their maximum average aggregate size within the DGL. The strong correlation between aggregate class and specific differential phase shift (KDP) confirms the expected link between ice particle concentration and aggregation. Interestingly, no correlation between aggregation class and  $sZDR_{max}$  is visible. This indicates that aggregation is rather independent of the aspect ratio and density of ice crystals. A distinct reduction of mean Doppler velocity in the DGL is found to be strongest for cases with largest aggregate sizes. Analyses of spectral edge velocities suggest that the reduction is the combined result of the formation of new ice particles with low fall velocity and a weak updraft. It appears most likely that this updraft is the result of latent heat released by enhanced depositional growth. Clearly, the strongest correlations of aggregate class with other variables are found inside the DGL. Surprisingly, no correlation between aggregate class and concentration or aspect ratio of particles falling from above into the DGL could be found. Only a weak correlation between the mean particle size falling into the DGL and maximum aggregate size within the DGL is apparent. In addition to the correlation analysis, the dataset also allows study of the evolution of radar variables as a function of temperature. We find the ice particle concentration continuously increasing from  $-18$  °C towards the bottom of the DGL. Aggregation increases more rapidly from  $-15$  °C towards warmer temperatures. Surprisingly, KDP and  $sZDR_{max}$  are not reduced by the intensifying aggregation below  $-15$  °C but rather reach their maximum values in the lower half of the DGL. Also below the DGL, KDP and  $sZDR_{max}$  remain enhanced until  $-4$  °C. Only there, additional aggregation appears to deplete ice crystals and therefore reduce KDP and  $sZDR_{max}$ .

The simultaneous increase of aggregation and particle concentration inside the DGL necessitates a source mechanism for new ice crystals. As primary ice nucleation is expected to decrease towards warmer temperatures,

secondary ice processes are a likely explanation for the increase in ice particle concentration. Previous laboratory experiments strongly point towards ice collisional fragmentation as a possible mechanism for new particle generation. The presence of an updraft in the temperature region of maximum depositional growth might also suggest an important positive feedback mechanism between ice microphysics and dynamics which might further enhance ice particle growth in the DGL.

## 1 Introduction

Recent space-borne analyses underline once more the importance of understanding ice growth processes in clouds as more than 70 % of global precipitation is found to be generated via the ice phase (Heymsfield et al., 2020; Field and Heymsfield, 2015; Mülmenstädt et al., 2015). The dendritic growth layer (DGL), usually located between  $-20$  and  $-10^{\circ}\text{C}$ , is known to play an important role for the growth and evolution of ice and snow in clouds. The reasons for its importance are manifold: the difference in saturation vapour pressure between ice and liquid reaches a maximum at  $-12^{\circ}\text{C}$  which favours depositional growth by the Wegener–Bergeron–Findeisen (WBF) process (Korolev, 2007). In addition, the particular plate-like shapes that particles grow into in the DGL lead to a distinct maximum in the depositional growth rate at  $-15^{\circ}\text{C}$ , where dendritic particles can exceed 1.5 mm in size within 10 min growth time at liquid water saturation (Takahashi, 2014). The fragile structure of those particles has also been found by airborne in situ observations (Schwarzenboeck et al., 2009; Hobbs and Rangno, 1998, 1990, 1985) and laboratory experiments (Takahashi et al., 1995; Griggs and Choulaton, 1986; Vardiman, 1978) to favour collisional breakup. This secondary ice process (SIP) gains increasing attention by the scientific community (e.g. Georgakaki et al., 2022; Phillips et al., 2018) as an important process which could explain the discrepancy between number of ice nucleating particles (INPs) and ice particle number concentration (IPNC) (Kanji et al., 2017). Unlike for example the Hallett–Mossop rime splintering process (Field et al., 2017; Hallett and Mossop, 1974), ice collisional fragmentation could provide new secondary ice particles over a wide temperature range. Finally, ice particles which are multiplied in number by SIP and grow rapidly in the DGL have been found to also aggregate very efficiently in the DGL (Lamb and Verlinde, 2011). Especially the branched structure of dendrites appears to be responsible for enhancing the stickiness of the crystals and thus favouring the formation of aggregates (Connolly et al., 2012). The various ice growth signatures in the DGL which can be observed for example with radars could be linked to the intensity of surface precipitation (Trömel et al., 2019, and references therein). This highlights again the importance to properly understand the interplay of microphysical processes in the DGL in order to accurately model surface precipitation.

Dual-polarisation radar observations are a powerful tool to observe the result of several of the aforementioned growth processes in the DGL. The abundance of plate-like particles in the DGL leads to vertically distinct layers of enhanced differential reflectivity (ZDR) and propagational differential phase shift (KDP) close to the  $-15^{\circ}\text{C}$  region (Griffin et al., 2018; Schrom and Kumjian, 2016; Schrom et al., 2015; Moisseev et al., 2015; Thompson et al., 2014; Becchini et al., 2013; Andrić et al., 2013; Kennedy and Rutledge, 2011; Trapp et al., 2001, among others). Interestingly, the ZDR layer appears at slightly higher altitudes as the KDP enhancement. ZDR is independent of the particle concentration but increases strongly with particle density and aspect ratio (Kumjian, 2013). However, the formation of aggregates leads to a decrease of ZDR despite the presence of asymmetric crystals which explains its layered structure. KDP is strongly related to particle concentration and, in contrast to ZDR, is not reflectivity-weighted, and thus not strongly influenced by the presence of large aggregates. While the general connection of ZDR and KDP layers, and intensive plate-like growth and subsequent aggregation is widely accepted, a definite conclusion on the reasons for the distinct vertical structure has not yet been reached (e.g. Schrom and Kumjian, 2016; Schrom et al., 2015; Moisseev et al., 2015).

Polarimetric information from the DGL is mostly lacking in vertically pointing radar observations. Similar to slant measuring radars, vertically pointing radars commonly observe a rapid increase in the radar reflectivity factor ( $Z_e$ , henceforth called reflectivity) in the DGL, in particular at  $-15^{\circ}\text{C}$  (e.g. Schrom and Kumjian, 2016; Zawadzki, 2013). The Doppler spectra collected with zenith-pointing radars revealed two distinct features in the DGL: first, the Doppler spectra often reveal an additional slow secondary mode in the DGL. In case of low turbulence and weak vertical air motions, the Doppler velocities can be related to the particles' terminal fall velocity. Apparently, the second spectral mode indicates the formation of new ice particles that often increase in fall speed and eventually merge with the main aggregate mode falling from higher altitudes. Second, the mean Doppler velocity (MDV) often reveals a slight but temporally very persistent reduction in the DGL. Various explanations for those features have been presented in the literature (see for example discussion presented in Schrom and Kumjian, 2016; Schrom et al., 2015). Zawadzki (2013) argues that vertical air motion at  $-15^{\circ}\text{C}$  is necessary to enhance supersaturation which enables the nucleation and subsequent growth

of plate-like particles. Other authors assign the MDV reduction simply to the evolution of a new secondary mode in the spectrum (e.g. Oue et al., 2018; Moiseev et al., 2015, 2009; Shupe et al., 2004; Zawadzki et al., 2001; Field, 2000, and references therein). The explanations for the origin of a new, slow ice particle mode include sedimentation of ice particles into the DGL from higher altitudes (Moiseev et al., 2015), enhanced primary nucleation due to upward air motion (Zawadzki, 2013) and secondary ice particle formation (e.g. Kennedy and Rutledge, 2011). Also, buoyancy-driven upward motion due to latent heat release of rapidly growing ice particles by water vapour deposition has been discussed as a potential reason for the decrease of MDV (Schrom and Kumjian, 2016).

An increasing number of ground-based sites are equipped with polarimetric and multi-frequency cloud radars. The use of higher frequencies does not only substantially increase the backscattered signal, especially of small ice particles scattering in the Rayleigh regime, but it also reduces observational limitations in some polarimetric variables. KDP is the range derivative of the differential phase shift and generally affected by high measurement noise. As KDP is inversely proportional to the wavelength, it can be more reliably estimated at shorter wavelength, also for small concentrations of asymmetric ice particles (Brangi et al., 2001). Moreover, even particles whose reflectivity values are below the radar detection level will cause some differential phase shift. Hence, KDP is sensitive also to the presence of extremely small, asymmetric ice crystals such as those expected to be produced by SIP (secondary ice process). The elevation-dependence of polarimetric cloud radar observations allows to infer shape, orientation and apparent density of ice crystals (e.g. Myagkov et al., 2016a; Matrosov et al., 2012). In addition, most polarimetric cloud radars provide polarimetric Doppler spectra which allow assigning of the polarimetric signatures to specific Doppler velocities. Most previous studies used linear depolarisation ratio (LDR) spectra from vertically pointing radar observations to investigate the evolution of columnar and needle particles between  $-10$  and  $0^{\circ}\text{C}$  (e.g. Giangrande et al., 2016; Oue et al., 2015). Spectral ZDR from an S-band radar system has been used by Spek et al. (2008) to retrieve particle size distribution of aggregates and plates. Pfitzenmaier et al. (2018) analysed spectral LDR from a zenith-pointing Ka-band and spectral ZDR from a slant-viewing S-band radar to study ice particle growth along fall streaks.

Aggregation in the DGL can be only indirectly detected by radar polarimetry as a reduction of for example ZDR and concurrent increase of radar reflectivity (Kumjian, 2013). In contrast, the increase in mean particle size can be well observed as an increasing reflectivity difference in multi-frequency cloud radar observations (e.g. Kneifel et al., 2011; Liao et al., 2008, 2005; Matrosov, 1992). Ice particles increasing in size begin to scatter less radiation back relative to particles that can be still approximated by Rayleigh scattering (usually valid if particles size  $\ll$  wavelength). As this de-

viation happens first at the shorter wavelength, the logarithmic reflectivity difference (also called dual wavelength ratio, DWR) increases with the mean size of the particle size distribution (PSD). Also, DWR can be resolved spectrally, which allows to constrain particle scattering models (Kneifel et al., 2016), to retrieve the particle size distribution (Mróz et al., 2021; Barrett et al., 2019) or to separate attenuation and differential scattering effects (e.g. Li and Moiseev, 2019; Tridon and Battaglia, 2015).

The majority of previous radar studies on the DGL focus their analysis on a number of case studies. A more statistical investigation is presented by Trömel et al. (2019), where X-band radar observations of 52 stratiform precipitation cases obtained close to Bonn, Germany, were analysed using quasi-vertical profiles (QVP, Ryzhkov et al., 2016). They found a correlation of KDP and Ze in the DGL, and were able to link signatures in the DGL to surface precipitation. Similarly, in a statistical analysis of 27 d of C-band observations close to the city of Turin, northern Italy, Bechini et al. (2013) linked enhanced KDP in the DGL to an enhanced Ze at the surface. Schneebeli et al. (2013) analysed a dataset of polarimetric X-band radar observations of clouds ranging in temperature between  $-30$  to  $0^{\circ}\text{C}$  collected in the Swiss Alps. Interestingly, they were unable to find a distinct KDP maximum in the DGL but rather a continuous increase of KDP and Ze towards warmer temperatures related to a general increase of the ice water content (IWC).

Only a few studies attempted to combine different radar approaches for studying the DGL. Oue et al. (2018) used vertically pointing and slant-viewing polarimetric cloud radars to study the DGL in Arctic clouds. By combining Doppler spectra of a vertically pointing Ka-band radar with slant polarimetric observations, they were able to assign the increasing ZDR signatures in the DGL with the slow, secondary mode in the reflectivity Doppler spectra. A similar correlation of spectral bi-modalities and polarimetric signatures in the DGL have also been identified in mid-latitude clouds (Moiseev et al., 2015).

In this study, we present an in-depth analysis of vertically pointing triple-frequency (X-, Ka-, W-band) Doppler spectra combined with spectral polarimetric observations from a W-band cloud radar operated at a fixed  $30^{\circ}$  elevation angle. To our knowledge, such a combined multi-frequency analysis including spectral polarimetric observations obtained at W-band with a simultaneous transmit simultaneous receive (STSR) mode radar have not been presented so far. The 3-months dataset of winter clouds observed at a mid-latitude European site close to Cologne, Germany, are described in Sect. 2.1. A combined view with the various radar observables on the DGL is illustrated for a case study in Sect. 3. The case study description provides an overview of typical radar signatures which have been observed in the DGL in previous studies, and an introduction to new observables based on spectral polarimetry and multi-frequency observations. In Sect. 4, a statistical analysis is presented, which aims



to connect polarimetric and spectral signatures dominated by newly generated ice crystals to the maximum aggregate size reached in the DGL. The section also includes a spectral analysis aimed to disentangle the contributions of upward air motion and secondary ice particle mode on the MDV reduction observed in the DGL. In Sect. 5.1, we summarise the vertical evolution of the various radar variables with a special focus on the temperature level where changes in the different variables are most pronounced. Profiles from laboratory experiments are added to this conceptual picture to allow an in-depth discussion of the most likely evolution of microphysical processes in the DGL. In Sect. 5.2, the role of sedimenting particles from higher altitudes and especially cloud top temperature on the signatures in the DGL are briefly discussed. The main findings of our statistical analysis are summarised in Sect. 6.

## 2 Data and methods

### 2.1 TRIPEX-pol campaign

The results presented in this study are based on a multi-month dataset obtained during the campaign “TRIPEX-frequency and Polarimetric radar Experiment for improving process observation of winter precipitation” (TRIPEX-pol). The campaign took place from November 2018 until January 2019 at the Jülich Observatory for Cloud Evolution Core Facility (JOYCE-CF, Löhnert et al., 2015, 50°54′31″N, 6°24′49″E; 111 m a.s.l.) located ca. 40 km west of Cologne, Germany. Similar to a previous winter campaign (TRIPEX, Dias Neto et al., 2019), radar Doppler spectra and moments were continuously collected from a combination of vertically pointing triple-frequency (X-, Ka- and W-band) radars. The main difference from the earlier TRIPEX campaign is an extension of the observational capabilities by two additional radars: a new X-band radar with better sensitivity and the possibility to record Doppler spectra, and a scanning polarimetric Doppler W-band radar (Table 1). The vertically pointing and the scanning W-band radars are both frequency modulated continuous wave (FMCW) systems manufactured by Radiometer Physics GmbH (Myagkov et al., 2020; Küchler et al., 2017). The X- and Ka-band systems are pulsed radar systems manufactured by Metek GmbH (Mróz et al., 2021; Görsdorf et al., 2015). All four radar systems were installed at the same roof platform within horizontal distances of less than 20 m. The resolution in range and time were adjusted to allow a very close radar volume matching (Table 1). The polarimetric W-band radar was measuring at 30° constant elevation (CEL) for intervals of 5 min towards West. In between the CEL measurements, the radar was performing single range height indicator (RHI, from 30 to 150° elevation) and plan position indicator (PPI, at 85° elevation) scans intended for wind profiling. Auxiliary instruments at JOYCE including rain gauges, microwave radiometers and Doppler wind lidars provide additional information about the

atmospheric state and precipitation on the surface (for further details, see Löhnert et al., 2015). The combination of various remote-sensing instruments also allows the continuous generation of Cloudnet classification and categorisation products (Illingworth et al., 2007). Besides in situ and remote-sensing observations, Cloudnet products also incorporate thermodynamic and wind information for JOYCE-CF extracted from analysis fields provided by the European Centre for Medium-Range Weather Forecasts (ECMWF) Integrated Forecast System (IFS) model.

### 2.2 Processing of the vertically pointing radar data

The dataset from the three vertically pointing radars was processed in three levels. Level 0 contains the regridded and cleaned Doppler spectra. Level 1 contains the radar moments calculated from the level 0 dataset (Sect. 2.2.1). The level 2 processing follows closely the method presented in Dias Neto et al. (2019). It includes corrections for radar-specific calibration offsets and gas, liquid and ice attenuation (Sects. 2.2.2 and 2.2.3). Key methods of the processing steps will be discussed in the following subsections.

#### 2.2.1 Doppler spectra processing

Despite the similarity of the radar resolutions in space and time (see Table 1), the measured Doppler spectra of each radar had to be regridded to a reference time–height grid. For the reference grid, we chose a temporal resolution of 4 s and a range resolution of 36 m. The original data were matched to the reference grid using the method of nearest neighbours but only considering data points with a maximum displacement of  $\pm 17$  m in range and  $\pm 2$  s in time.

The centre frequency of the vertically pointing W-band radar had to be slightly changed from 94.00 to 94.12 GHz in order to avoid interference with the W-band polarimetric radar. This change caused some spectral artefacts which are caused by the spectral impurities of the used chirp generator. The level of impurities is considerably lower when the radar operates at the default centre frequency. Also, some weak “side lobes” appeared in the X-band Doppler spectra when stronger signals were present close to the ground.

In order to identify the spectral region with “true” atmospheric signal, we selected the Ka-band radar as reference. The Ka-band radar provides the highest sensitivity of all radars, and its Doppler spectra showed no artefacts. Due to the different heights of the lowest usable range gates of the radars, return signals below 400 m altitude were omitted. The Ka-band Doppler spectra were used to derive a spectral mask for each range gate and time step. For this, we first identified the spectral edges by subtracting the noise floor using the common method by Hildebrand and Sekhon (1974) and then locating the outermost spectral bins which exceed the noise level by 3 dB. Our spectral mask is defined by the Doppler velocity bins identified by this method to contain real sig-

**Table 1.** Technical specifications of the four radars that were deployed during the TRIPEX-pol campaign. The W-band and the W-band pol radar are FMCW radars, therefore the range resolution, Doppler velocity resolution and the Nyquist range vary for the different chirps. The values in this table are valid for the lowest chirp region (W-band: 215–1475 m, W-band pol: 107–715 m). The full chirp tables for both W-band radars are provided in Appendix A.

Specifications	X-band	Ka-band	W-band	W-band pol
Frequency [GHz]	9.4	35.5	94.1	94.0
Polarimetry	single-pol	LDR	LDR	STSR
Number of spectral averages	10	20	13	28
Half-power beam width [°]	1.0	0.6	0.6	0.6
Range resolution [m]	36.0	36.0	36.0	35.8
Temporal resolution [s]	2	2	3	7
Sensitivity at 1 km [dBz], 2 s integration time	−50	−63	−58	−58
Maximum range [km]	12	15	16	16
Doppler velocity resolution [ $\text{m s}^{-1}$ ]	0.038	0.04	0.04	0.05
Nyquist range [ $\text{m s}^{-1}$ ]	$\pm 78$	$\pm 20$	$\pm 10$	$\pm 6$

nal. This spectral mask was then applied to filter the Doppler spectra of the other two vertically pointing radars. This filtering could unfortunately not remove all artefacts, as the W-band artefacts did also sometimes overlap with the Doppler spectrum from real atmospheric targets.

From the regridded and filtered Doppler spectra, the common radar moments are derived including equivalent radar reflectivity factor ( $Z_e$ ), mean Doppler velocity (MDV), spectrum width and skewness. The Ka-band spectra were also used to derive the fast-falling edge and slow-falling edge of the Doppler velocity of each spectrum. Those spectral edge velocities were derived in a similar way as the spectral mask. In case of strong atmospheric signals, spectral leakages might cause biases in the spectral edge velocity estimate. We mitigate this effect by neglecting all spectral lines which are lower than 40 dBz with respect to the maximum spectral line. Examples of the derived spectral edge velocities are shown in Fig. 3d where they are overlaid to the original spectra.

### 2.2.2 Evaluation of radar reflectivity calibration and antenna pointing

The reflectivity calibration of all four radars was evaluated using the drop size distributions (DSDs) measured during rainfall periods by the PARSIVEL optical disdrometer (Löffler-Mang and Joss, 2000) which was installed at JOYCE-CF in close vicinity to the radars (Fig. 1). The method is identical to the approach described in Dias Neto et al. (2019). The DSDs are used to calculate the  $Z_e$  distribution for each radar frequency and rainfall event. This distribution is then compared to the measured  $Z_e$  distribution at the lowest usable range gate (more details and discussion of uncertainties are provided in Dias Neto et al., 2019). The offsets estimated with this method for the three radars are 0 dBz for the X-band, an underestimation of 3 dBz for Ka-band and an overestimation of 2 dBz for the W-band. We applied the

disdrometer-based method to 21 rainfall cases and found no systematic temporal drifts of the estimated offsets. The W-band radar data obtained during the TRIPEX-pol campaign have also been used in Myagkov et al. (2020) to evaluate different calibration methods including also disdrometer-based methods. Our estimated bias of 2 dBz lies within their estimated values of 0.5 to 2.1 dBz for the vertically pointing W-band radar. For the polarimetric W-band radar, they found an underestimation of  $0.7 \pm 0.7$  dBz.

Accurate zenith pointing is crucial for the analysis of Doppler spectra and MDV in order to avoid velocity biases induced by horizontal wind. The absolute pointing of the Ka-band radar has been evaluated using sun-tracking scans (e.g. Muth et al., 2012). The pointing accuracy during the campaign was found to be better than  $\pm 0.1^\circ$  in elevation and azimuth. For the non-scanning X- and W-band radar, the pointing could only be evaluated relative to the absolute calibrated Ka-band radar. Following the approach shown in Kneifel et al. (2016), the pointing of the X- and W-band radars has been evaluated in relation to the Ka-band radar. For this, the difference in mean Doppler velocity (MDV) between X- and Ka-band (Ka- and W-band) has been analysed in dependency of the horizontal wind speed and direction obtained from Cloudnet. The analysis of the MDV differences obtained during TRIPEX-pol indicated that the misalignment between X- and Ka-band as well as W- and Ka-band did not exceed  $0.1^\circ$ .

### 2.2.3 Attenuation correction and relative DWR calibration

At cloud radar frequencies, atmospheric gases and hydrometeors cause attenuation which generally increases with frequency. Similar to Dias Neto et al. (2019), we first corrected the  $Z_e$  profiles for the estimated attenuation by gases. The gas attenuation profiles were calculated with the Passive and Active Microwave TRAnsfer model (PAMTRA, Mech

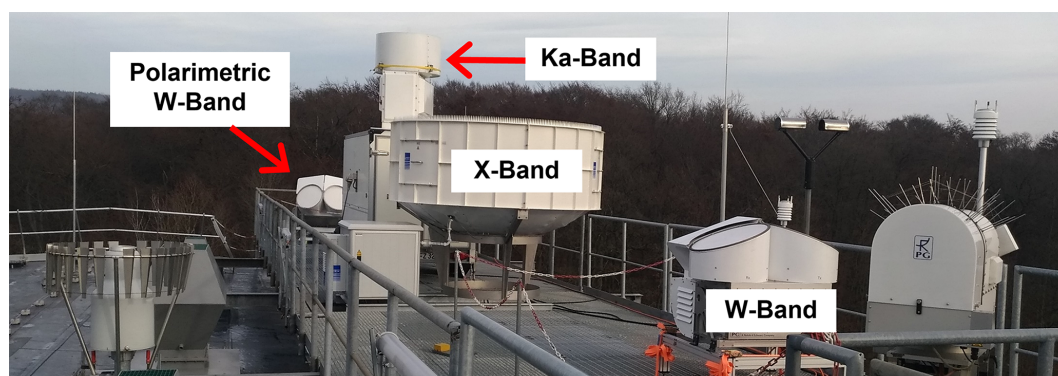


**Figure 1.** Measurement setup on the roof platform of JOYCE-CF in Jülich, western Germany (Löhnert et al., 2015). The four radars measuring during the TRIPEX-pol campaign were mounted in close vicinity to ensure optimal volume matching. A description of the radar setup can be found in Table 1 and Sect. 2. The radar measurement setup is complemented with a microwave radiometer HATPRO (in front of the W-band radar at the far right of the picture), a PARSIVEL (behind the W-band radar) and a Pluvio precipitation gauge on the far left of the picture. Information about further instrumentation on the JOYCE-CF roof platform is given in Sect. 2 and in Löhnert et al. (2015).

et al., 2020) which takes into account contributions by nitrogen, oxygen and water vapour. Profiles of temperature, humidity and pressure provided by Cloudnet were used as input for PAMTRA. Estimating the vertical profile of attenuation by liquid and frozen hydrometeors is challenging as accurate profiles of hydrometeor mass content and size distributions are required. As profile information of liquid and ice are unavailable, we only estimate the total path integrated attenuation following the approach presented in Dias Neto et al. (2019).

This method leverages on the fact that small ice particles can be assumed to be Rayleigh scatterers for which the radar reflectivity factor,

$$Ze(\lambda) = \frac{\lambda^4}{\pi^5 |K_\lambda|^2} \int \sigma_\lambda(D) N(D) dD, \quad (1)$$

is independent of the wavelength  $\lambda$ , if we assume a constant dielectric factor  $|K_\lambda|^2$  (e.g. Kneifel et al., 2015; Hogan et al., 2000).  $\sigma_\lambda(D)$  is the backscattering cross section of a particle with maximum size  $D$  and  $N(D)$  is the particle size distribution. The dual-wavelength ratio,

$$DWR_{\lambda_1, \lambda_2} = Ze_{\lambda_1} - Ze_{\lambda_2}, \quad (2)$$

is the difference in reflectivity in logarithmic units at two wavelengths  $\lambda_1, \lambda_2$  (usually with  $\lambda_1 > \lambda_2$ ). With the particle size getting closer to the wavelength, the backscattering cross section increases less than expected from the Rayleigh approximation due to the destructive interference of electromagnetic waves scattered by various parts of the particle (see Fig. C1a). This deviation from the Rayleigh scattering behaviour starts first at the smallest wavelength. As a result, increasing DWRs can be attributed to larger mean particle sizes in the radar volume. If the mean particle size becomes large enough, also the largest wavelength would transition to the non-Rayleigh regime and the DWR will increase slower, eventually reaching a saturation point (Mason et al., 2019).

The total DWR measured under real conditions at a certain range can be written as the sum,

$$DWR_{\lambda_1, \lambda_2} = DWR_{\text{scat}} + DWR_{\text{hard}} + DWR_{\text{att}}. \quad (3)$$

$DWR_{\text{scat}}$  is due to differential scattering of particles. Constant hardware-related offset  $DWR_{\text{hard}}$  might originate for example from radar miscalibration or differential radome attenuation. Differential attenuation causes a propagational component  $DWR_{\text{att}}$  which accumulates with increasing range. The major contributions to total attenuation are due to rain, the melting layer and supercooled liquid water. Ice and snow also contribute to W-band attenuation but as shown by Tridon et al. (2020), an ice water path larger than  $1 \text{ kg m}^{-2}$  is needed to cause 1 dBz two-way attenuation.

As proposed originally by Hogan et al. (2000) and recently evaluated by Tridon et al. (2020), a reflectivity threshold can be used to identify cloud regions where  $DWR_{\text{scat}}$  is negligible. The remaining DWR can then be attributed to the sum of  $DWR_{\text{att}}$  and  $DWR_{\text{hard}}$ . The X-band profiles would be least affected by attenuation but the X-band sensitivity is often too low to capture Rayleigh regions at high altitudes. Therefore, we use Ze profiles from the Ka-band radar as our reference which have been corrected for gas attenuation. Ka-band reflectivities between  $-30 \text{ dBz} < Ze_{\text{Ka}} < -10 \text{ dBz}$  and between  $-15 \text{ dBz} < Ze_{\text{Ka}} < 0 \text{ dBz}$  are used for estimating the non-scattering DWR components for W-Ka and X-Ka, respectively. To exclude partially melted particles, we additionally restricted the cloud regions used for the relative DWR calibration to be at least 1 km above the melting layer. Following the approach in Dias Neto et al. (2019), we also exclude profiles where the number of valid measurements within a 15 min time window is less than 300. Further, regions for which the variance of the DWRs exceeds  $2 \text{ dB}^2$ , or where the correlation between Ze measurements from the reference radar (Ka) and one of the other radars (X, W) is



less than 0.7, are discarded. The estimated relative DWR offset for a moving time window of 15 min is then applied to the entire profile. As we expect the major contributions to the total attenuation from the rain part and the melting layer, this approach appears to be justified for the ice part of the cloud. In case of additional attenuation in the ice part, for example due to layers of supercooled liquid, our approach would cause an overestimation of the true attenuation, and hence our processed  $DWR_{\text{scat}}$  values would underestimate the real  $DWR_{\text{scat}}$  below the attenuation layer (even returning negative values). For convenience, in the following, we use the radar bands (X, Ka, W) instead of the wavelengths as indices (e.g.  $DWR_{\text{KaW}}$ ). The DWRs have also been derived spectrally (sDWRs) by calculating the difference of the logarithmic power in each Doppler spectral bin. Identical corrections and relative calibrations as used for the DWR are applied for sDWR.

### 2.3 Processing of the polarimetric radar data

The polarimetric W-band radar observations were collected at constant  $30^\circ$  elevation and a fixed azimuth angle of  $235^\circ$  for 5 min time periods. The azimuth direction is close to the main wind direction where most cloud systems have been advected from during the campaign (south–west to north–west according to wind information from Cloudnet). In order to minimise time-lag differences related to different observation volumes of the slanted polarimetric radar and vertically pointed systems, we average all measurements over 5 min.

The polarimetric radar moments and the polarimetric Doppler spectra have been projected to the height above ground, and then regridded to the same observations. At a maximum range of the polarimetric radar of 16 km (see also Table 1), the height above ground is 8 km, and the maximum horizontal distance between the vertically pointing radar and the polarimetric radar is  $\cos(30^\circ) \times 16 \text{ km} = 13.86 \text{ km}$ . In order to reduce the noise of the specific differential phase shift (KDP), we first smoothed the differential phase shift  $\phi_{\text{dp}}$  over five range gates (corresponding to 180 m) using a moving window mean and then averaged it over 5 min before calculating KDP as half of the discrete range derivative of  $\phi_{\text{dp}}$ :

$$\text{KDP} = \frac{\Delta\phi_{\text{dp}}}{2 \times \Delta r}, \quad (4)$$

with  $\Delta r$  being the distance between the range gates.

The ZDR is defined as

$$\text{ZDR} = 10 \log_{10} \left( \frac{Z_{\text{eH}}}{Z_{\text{eV}}} \right), \quad (5)$$

with the radar reflectivity at horizontal polarisation ( $Z_{\text{eH}}$ ) and vertical polarisation ( $Z_{\text{eV}}$ ). The ZDR values are dominated by the particles contributing largest to the reflectivity. In addition to ZDR, we also derived the spectral ZDR (sZDR) as the logarithmic difference of horizontal and vertical power in each Doppler spectral bin. The maximum in

sZDR called  $s\text{ZDR}_{\text{max}}$  indicates the presence of high ZDR producing ice particles within the radar volume even in cases where the ZDR is for example lowered by the presence of low ZDR producing aggregates. The quality of polarimetric measurements strongly depends on the signal-to-noise ratio (SNR). Variance in ZDR,  $\phi_{\text{dp}}$  and  $\rho_{\text{hv}}$  drastically increases at very low SNR (Eq. 6.122 and Sect. 6.5 in Bringi and Chandrasekar, 2001). Therefore, in order to use only high quality data for the following analysis, we omit all polarimetric observations when SNR (or in case of sZDR, spectral SNR in a spectral bin) is less than 10 dB.

### 2.4 Evaluation of the temperature information from Cloudnet

In Sects. 4 and 5.2, we statistically analyse different radar variables with respect to their temperature-dependent behaviour. As no regular radio soundings are available at JOYCE-CF, we use the temperature information included in the Cloudnet products. We evaluated the temperature information from Cloudnet with the temperature measured by 27 radiosondes which were launched throughout the course of the TRIPEX–pol campaign for all heights below 8 km (see Chap. 3.3 in Dias Neto, 2021). The analysis showed a good agreement between the temperature information from Cloudnet and the measured temperature from the radiosondes. The mean difference between the Cloudnet and radiosonde is  $0.2^\circ\text{C}$ , with a standard deviation of the mean difference of  $1.1^\circ\text{C}$ . The correlation between the Cloudnet temperature and measured temperature is 0.9. Further, the root mean square difference was found to be  $\text{RMSD} \approx 1.1^\circ\text{C}$ .

### 2.5 Description of the dataset

Most clouds and precipitation events that occurred during the 89 d of the campaign were caused by mid-latitude frontal systems which are common during wintertime at JOYCE-CF. According to the Cloudnet classification, ice and mixed phase clouds were present 46.6 % of the time (1029 h). Rainfall was observed during 9.2 % (202.8 h) of the time causing a total accumulation of 152.7 mm of rainfall measured by the Pluvio weighing gauge installed at JOYCE-CF. On three days, snowfall was reaching the ground. A total of 18.6 h of snowfall produced a total liquid equivalent accumulation of 10.8 mm. The coldest temperature of  $-7.0^\circ\text{C}$  was observed on 24 January 2019, one of the three days with snowfall on the ground. The warmest temperature, reaching  $16.7^\circ\text{C}$ , during the campaign was observed on 24 November 2018.

## 3 Snowfall case study: 30 January 2019

With the following snowfall case study, we aim to provide an impression of the data quality and illustrate the complementary information in spectral multi-frequency and polarimetric observations. Common observational features of the

DGL visible in standard radar moments and in new spectral variables will be discussed. The case study selected shows more pronounced signals than the average profiles discussed later in the statistical analysis. However, the case is not an exceptional event and similar profiles of radar variables can be found frequently at JOYCE-CF during similar winter cases.

On 30 January 2019, a frontal system passed over JOYCE-CF and caused snowfall reaching the surface with a liquid equivalent accumulation of 6.6 mm. During the entire day, temperatures at the surface remained below freezing, ranging between  $-2.4$  and  $-0.4$  °C. The various radar observables from zenith pointing and slant polarimetric observations are displayed in Fig. 2. The cloud system produced snowfall reaching the ground mainly between 05:00 and 19:00 UTC. The overall cloud structure observed in zenith is very similar to the radar measurements at 30° elevation. This similarity was regularly observed for the 3-months time period probably due to the predominantly large-scale structure of the winter precipitation observed during the campaign.

The MDV (Fig. 2b) throughout the case are found to be larger than  $-1.5 \text{ m s}^{-1}$  which indicates unrimed or only slightly rimed particles (Kneifel and Moisseev, 2020). Here we use the convention that negative (MDV) velocities correspond to motion towards the ground. Faster falling particles therefore have smaller (more negative) values than slower falling particles. When plotting the DWR in the triple-frequency space ( $\text{DWR}_{\text{KaW}}$  against  $\text{DWR}_{\text{XKa}}$ , not shown), we also find a “hook shape” which has been previously found to indicate predominance of unrimed aggregates (Kneifel et al., 2015). Certainly, the particles observed on the surface are not necessarily representative for the particles sampled with the radars due to impacts of advection and further growth processes during sedimentation towards the surface. Still, the snowfall reaching the ground was mostly comprised of unrimed or only slightly rimed crystals and aggregates. Visual observation on the ground at the site between 09:00 and 10:00 UTC (Fig. B1) reveals the presence of stellar and dendritic crystals reaching up to 4 mm in size mixed with unrimed aggregates with maximum sizes up to 10 mm.

The combined radar observations reveal several features which have been reported and discussed in previous literature related to the DGL (Ori et al., 2020; Barrett et al., 2019; Griffin et al., 2018; Oue et al., 2018; Schrom et al., 2015; Moisseev et al., 2015; Andrić et al., 2013; Bechini et al., 2013, among others). The Ze values (Fig. 2a) rapidly increase at the  $-15$  °C temperature level most likely due to an increase in the mean particle size as indicated by  $\text{DWR}_{\text{KaW}}$  (Fig. 2c). A layer of enhanced  $s\text{ZDR}_{\text{max}}$  (Fig. 2d) values up to 4 dB at  $-15$  °C indicates a rapid generation of asymmetric particles. Note that at 30° elevation, ZDR is expected to be in general smaller than ZDR measured at lower elevation angles which have often been used in previous studies where data from lower frequency scanning radar systems have been analysed. According to Myagkov et al. (2016b), such values of differential reflectivity at these temperatures correspond to

horizontally aligned strongly oblate (plate-like) ice particles. For the following analysis, we define the aspect ratio similar to Takahashi et al. (1991) as the ratio of the  $a$  and  $c$  axis of an ice crystal. Plate-like particles for example then have aspect ratios larger than 1.

The decrease of  $s\text{ZDR}_{\text{max}}$  from 4 to 2 dB towards lower layers indicates a change in particle properties (i.e. aspect ratios become closer to unity and/or apparent ice density becomes smaller) of the strong ZDR producing particles found at  $-15$  °C. Also the KDP (Fig. 2e) shows an immediate increase at  $-15$  °C with values of up to  $3$  °  $\text{km}^{-1}$ . Interestingly, both KDP and  $s\text{ZDR}_{\text{max}}$  remain enhanced down to the surface despite the ongoing aggregation indicated by increasing  $\text{DWR}_{\text{KaW}}$  towards the ground.

Additional insights into the vertical evolution of particle populations and their contribution to radar moments can be gained from the analysis of vertical profiles of Doppler spectra (Fig. 3d–f). The first aggregates which produce a noticeable  $\text{DWR}_{\text{KaW}}$  signal (see Fig. 3e) appear at  $-18$  °C on the fast edge of the Doppler spectra (ca.  $-1$  to  $-1.2 \text{ m s}^{-1}$ ). Interestingly, the spectral velocity where we find the largest  $s\text{Ze}$  values at this temperature is at slightly lower velocities ( $-0.8$  to  $-1 \text{ m s}^{-1}$ ). This could indicate that the number concentration of the aggregates producing the enhanced  $s\text{DWR}_{\text{KaW}}$  region is still low. At around the same temperature level, we also find a secondary mode in  $s\text{Ze}$  and a broadening of  $s\text{DWR}_{\text{KaW}}$  (indicated by magenta square in Fig. 3d, e). At its first appearance, the secondary mode shows initial spectral velocities close to  $-0.3 \text{ m s}^{-1}$  which indicates small ice particles rather than supercooled liquid droplets which typically produce a narrow spectral mode around  $0 \text{ m s}^{-1}$  (e.g. Kalesse et al., 2016; Shupe et al., 2004). The spectral asymmetry introduced by the secondary mode leads to a rapid change in the Doppler spectral skewness (Fig. 3b). Starting at  $-18$  °C, the skewness increases from values close to unity (symmetrical spectra) to 1.4 at  $-17$  °C (Doppler spectra are skewed towards the slower falling side). The secondary mode appears alongside polarimetric signatures. KDP starts to increase at  $-20$  °C, reaching a maximum of  $2.1$  °  $\text{km}^{-1}$  at  $-15$  °C, correlating well with the increase and the maximum of  $s\text{ZDR}$  of around 4 dB. The enhanced KDP and  $s\text{ZDR}$  values indicate an increase in concentration and aspect ratio of small ice crystals.

For temperatures warmer than  $-15$  °C, the fall velocities,  $s\text{Ze}$  and  $s\text{DWR}_{\text{KaW}}$  of the secondary mode increase until they merge with the main mode at around  $-12$  °C. Interestingly, at this temperature we also see a distinct slow-down of the MDV from approx.  $-0.9 \text{ m s}^{-1}$  at  $-17$  °C to  $-0.6 \text{ m s}^{-1}$  at  $-12$  °C. Looking at the spectrogram for this particular time, it appears as if the slow-down in MDV is the result of the new mode and a general shift of the entire spectrum towards larger values. The latter is compatible with the effect of upward air motion. This slow-down of the entire Ze spectrum is illustrated in Fig. B2a) which presents a zoomed view into the temperature region  $-16$  to  $-10$  °C. The main mode con-

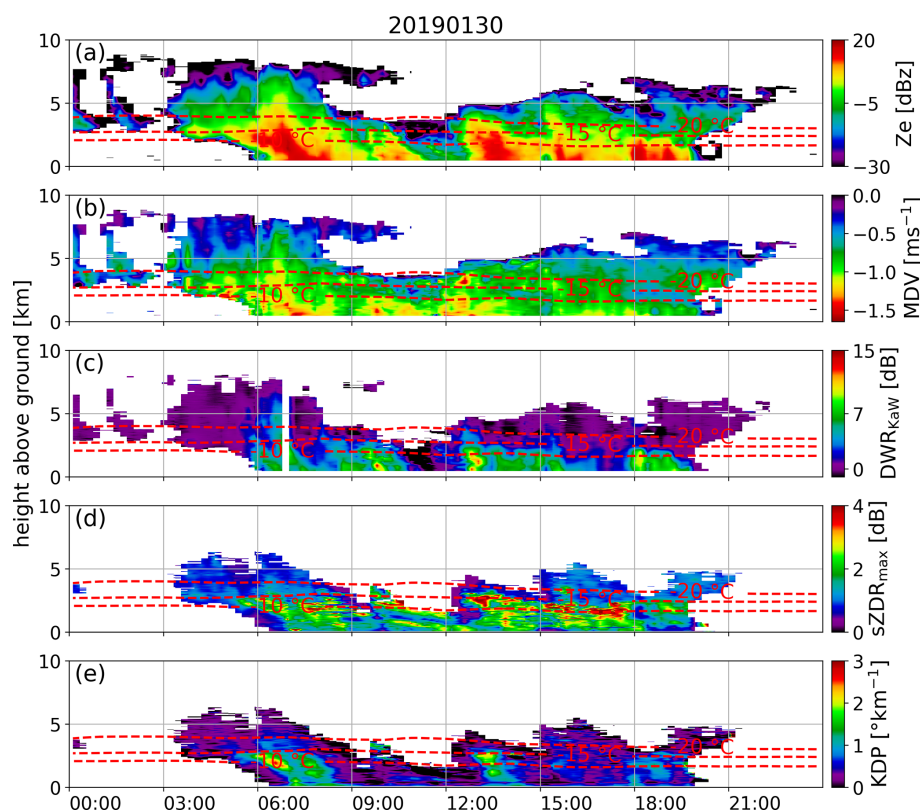


**Figure 2.** Snowfall event occurring on 30 January 2019 at JOYCE. From the vertically pointing radars, the (a) Ze and (b) MDV at Ka-band, and the (c)  $DWR_{KaW}$  are shown as time–height plots. From polarimetric observations at W-band and  $30^\circ$  elevation angle (mapped to height above ground), the (d) maximum spectral ZDR  $sZDR_{max}$  and (e) KDP are presented. In (a–e), the dashed red lines depict the  $-20$ ,  $-15$  and  $-10^\circ\text{C}$  isotherms. Impressions of dendrites and aggregates sampled on the ground between 09:00 and 10:00 UTC are provided in Fig. B1.

tributes more power to the spectrum than the newly formed secondary mode. Therefore, shifts of the main mode towards slower or faster velocities dominate changes in MDV. Hence, the slow-down of the main spectral mode at  $-12.5^\circ\text{C}$  reduces the MDV at this temperature.

Just slightly below the temperature level where the secondary mode merges with the main mode, we find the largest  $sDWR_{KaW}$  values of up to 10 dB at spectral velocity bins between  $-1$  and  $-1.5\text{ m s}^{-1}$ . At temperatures around  $-10^\circ\text{C}$ , the  $sZDR_{max}$  values increase again. The maximum in  $sZDR_{max}$  at around  $-8^\circ\text{C}$  roughly coincides with the appearance of a weak secondary mode in the  $sZe$  and an increase in KDP. The new particle mode as well as the enhanced  $sZDR_{max}$  and KDP values mostly disappear at temperatures higher than  $-5^\circ\text{C}$  while  $sZe$  and  $sDWR_{KaW}$  remain enhanced.

The signatures found in this case study are largely in agreement with radar signatures reported in previous studies about particle growth and aggregation in the DGL (Griffin et al., 2018; Schrom and Kumjian, 2016; Moisseev et al., 2015; Schrom et al., 2015; Andrić et al., 2013; Bechini et al., 2013, among others). However, some differences are also found, especially when comparing our results to studies that

analysed lower frequency polarimetric radar observations. Those observations frequently revealed layers of enhanced KDP and ZDR at the  $-15^\circ\text{C}$  level. One reason for the less layered appearance of KDP and ZDR in our case could be related to the higher frequency used for polarimetric observations in this study. As KDP is inversely proportional to the radar wavelength (e.g. Bringi et al., 2001), we are able to observe KDP signals from relatively small particle concentrations which are difficult to detect by low-frequency polarimetric radars. For example, a KDP signal of  $1^\circ\text{ km}^{-1}$  observed at W-band would only be  $0.1^\circ\text{ km}^{-1}$  at X-band. Also, the SNR is much higher for cloud radars since the maximum distance measured is smaller than for typical weather radars. As a result, only the maximum of the KDP enhancement close to the  $-15^\circ\text{C}$  level might be detectable by low-frequency radars and regions with enhanced particle concentrations, but KDP values below the detection limit might be missed. Another reason for the less layered appearance of KDP and ZDR might be an underrepresentation of cases with strong forcing conditions during TRIPEX-pol. More intense vertical air motions are expected to result in a larger concentration of particles and abundance of dendrites, that is expected to lead to stronger aggregation and more intense de-

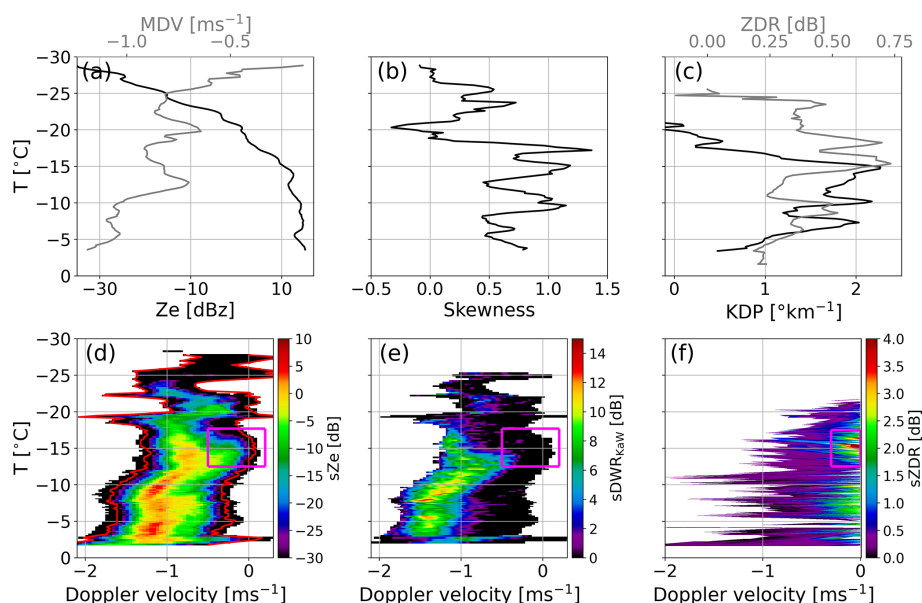


**Figure 3.** Radar profiles and spectrograms from the snowfall event occurring on 30 January 2019 at JOYCE at 13:30 UTC. Vertical profiles of (a) Ze and MDV, (b) skewness from the Ka-band radar, and (c) KDP and ZDR from the W-band radar are shown. Spectrograms (i.e. vertical evolution of Doppler spectra) of (d) Ze from the Ka-band are shown together with the derived spectral edge velocities (red lines). Panel (e) shows spectrograms of  $DWR_{KaW}$  and (f) ZDR from the W-band radar. The magenta squares in (d–f) depict the region where a secondary spectral mode is visible. An example of a single Doppler spectrum, where the second mode is visible, is also provided in Fig. B2.

pletion of ice crystals (e.g. Moisseev et al., 2015; Schrom et al., 2015). Radars operating at longer wavelengths can clearly detect these cases with large concentrations of ice crystals at  $-15^{\circ}\text{C}$  but might miss cases with weaker forcing due to sensitivity limits. The differences in sensitivity between W-band and lower frequency radars might cause a selection bias of low-frequency radars with respect to stronger depositional growth and aggregation cases. A more detailed discussion of the expected similarities and differences of ZDR and KDP at X-band and W-band is provided in Appendix C.

In the following sections, we will apply our analysis to all ice-containing clouds included in our dataset. As this case study illustrated, the combination of observations from the slant (Fig. 2d–e) and the zenith direction (Fig. 2a–c) appears to be reasonable, especially when applying an additional temporal averaging over 5 min to the profiles. This will allow us to link polarimetric and multi-frequency zenith observations in order to better understand which radar variables are connected to different intensities of aggregation in the DGL.

#### 4 Profile classification by the mean aggregate size in the DGL using $DWR_{KaW}$

Aggregation becomes particularly active in the DGL, causing rapid changes in radar quantities sensitive to the mean size, such as Ze or DWR (see also Fig. 2). As a growing aggre-

gate will deviate from Rayleigh scattering first at the shortest wavelength, we use  $DWR_{KaW}$  as our most sensitive measure for the onset of aggregation. In order to exclude multi-layer or sublimation cases, we require the radar profiles to be continuous within the DGL. Following the approach presented in Dias Neto (2021), these profiles were sorted into three classes according to their maximum  $DWR_{KaW}$  value reached within the DGL (Table 2). Assuming inverse exponential PSDs combined with particle and scattering properties of dendritic aggregates (Ori et al., 2021), we find the three  $DWR_{KaW}$  classes representing mean mass diameters ( $D_0$ ) ranging from 1 to 6 mm. However, the  $D_0$  estimation likely represents only a lower limit, especially for  $DWR_{KaW}$  class 3. As is shown in Mason et al. (2019), the shape of the PSD influences the shape of the triple-frequency signatures, and by extension also the DWR measurements. A narrow PSD with a large  $D_0$  might account for the same  $DWR_{KaW}$  as a more wide PSD with a smaller  $D_0$ . The  $DWR_{KaW}$  classes were chosen such that there is a similar number of profiles within each  $DWR_{KaW}$  class. All profiles with  $DWR_{KaW}$  values exceeding 9.5 dB are excluded as they are most likely related to partially rimed aggregates or due to an insufficient correction of W-band attenuation.



**Table 2.** Definition of maximum  $\text{DWR}_{\text{KaW}}$  intervals within the DGL (i.e. temperature region between  $-20$  and  $-10^\circ\text{C}$ ) used to classify radar profiles according to the particles' maximum mean mass diameters  $D_0$  in the DGL. The last column denotes the number of available radar profiles with continuous observations within the DGL.

max ( $\text{DWR}_{\text{KaW}}$ ) [dB]	class number	approx. $D_0$ [mm]	number of profiles
0–1.5	1	$< 0.75$	222
1.5–4.0	2	0.75–1.5	223
4.0–9.5	3	1.5–6	190

#### 4.1 Relation of vertically pointing radar variables to the mean aggregate size in the DGL

After classifying all vertically pointing profiles according to their maximum  $\text{DWR}_{\text{KaW}}$  in the DGL, we can now investigate how other radar moments evolve as a function of temperature for the different classes (Fig. 4). The profiles of  $\text{DWR}_{\text{KaW}}$  (Fig. 4b) reveal that the maximum  $D_0$  is reached at the lower end of the DGL ( $-10^\circ\text{C}$ ) with the strongest  $\text{DWR}_{\text{KaW}}$  increase found at temperatures warmer than  $-15^\circ\text{C}$ . This is also the temperature where we find  $\text{DWR}_{\text{XKa}}$  (Fig. 4c) to rapidly increase reaching values of 2 dB at  $-10^\circ\text{C}$  for the highest  $\text{DWR}_{\text{KaW}}$  class. Both DWRs only slightly change from  $-10$  to  $-5^\circ\text{C}$ . From  $-5^\circ\text{C}$  towards the melting layer we find an additional increase in the DWRs, especially in  $\text{DWR}_{\text{XKa}}$ . This is in agreement with previous DWR studies (Ori et al., 2020; Dias Neto et al., 2019) and in situ observations (Lawson et al., 1998). The most common explanation for this second aggregation layer is an increasing thickness of the quasi-liquid layer of the ice surface causing the sticking efficiency to rapidly increase at  $T > -5^\circ\text{C}$  coupled with enhanced depositional growth at around  $-5^\circ\text{C}$  (Lamb and Verlinde, 2011).

Interestingly, small differences in the Ze median and quantile profiles between the aggregation classes are already visible at temperatures lower than  $-20^\circ\text{C}$  (Fig. 4a). At the top of the DGL, we find a 3 dB difference in Ka-band reflectivity medians between the different aggregation classes which increase up to 10 dBz at the bottom of the DGL. Between  $-20$  and  $-15^\circ\text{C}$ , the slopes of the Ze medians are relatively similar. From  $-15^\circ\text{C}$  to the bottom of the DGL, we find a relatively constant Ze for class 1, an unchanged linear increase for class 2 and a more rapidly increasing Ze curve for class 3. Unlike the DWRs, the Ze medians remain relatively constant or even decrease for temperatures between  $-10$  and  $0^\circ\text{C}$ . This behaviour might be related to non-Rayleigh scattering effects at Ka-band (also indicated by increasing  $\text{DWR}_{\text{XKa}}$ ) and/or a result of microphysics. For example, a simultaneous increase in mean particle size and a decreasing number concentration caused by aggregation might have a compensating effect on Ze. The quantiles of the distribution in general fol-

low the Ze median throughout the shown temperature range. At the top of the DGL, the spread between the 25th and 75th percentile is 11 dB (10, 12.2 dB) for aggregation classes 1 (2, 3). This spread remains similar throughout the DGL. Only at warmer temperatures the spread increases, reaching 16.6 dB (24.4, 30 dB) at  $0^\circ\text{C}$ .

The most intriguing signature, however, is found for the MDV in the DGL (Fig. 4d). The magnitude of MDV increases (in an absolute sense) from ca.  $-0.6\text{ m s}^{-1}$  at  $-30^\circ\text{C}$  to  $-0.9\text{ m s}^{-1}$  at  $-18^\circ\text{C}$ . This continuous increase is expected due to evolving particle size related to depositional growth and aggregation. Unlike Ze and  $\text{DWR}_{\text{KaW}}$ , the MDVs are only slightly more negative for the larger  $\text{DWR}_{\text{KaW}}$  classes. Also, the quantiles of the distributions reveal a larger overlap in most regions. When the temperature increases above  $-16^\circ\text{C}$ , the largest  $\text{DWR}_{\text{KaW}}$  class shows a pronounced reduction of the MDV reaching a local minimum of  $-0.8\text{ m s}^{-1}$  at  $-13^\circ\text{C}$ . This slow-down is also visible in the vertical evolution of the quantiles. The lower (upper) quantile is reduced from  $-1.1\text{ m s}^{-1}$  ( $-0.83\text{ m s}^{-1}$ ) at  $-16^\circ\text{C}$  to  $-1.03\text{ m s}^{-1}$  ( $-0.63\text{ m s}^{-1}$ ) at  $-13^\circ\text{C}$ , resulting in a slow-down of  $0.075\text{ m s}^{-1}$  ( $0.15\text{ m s}^{-1}$ ). At the bottom of the DGL, the MDV values increase to only slightly larger values ( $-0.8$  to  $-1.1\text{ m s}^{-1}$ ) as compared to the top of the DGL. This “slow-down” of the MDV in the DGL appears to increase with  $\text{DWR}_{\text{KaW}}$  class. Different explanations for this slow-down in the DGL have been discussed in literature. A common explanation for this effect is the occurrence of a new and slower ice mode in the Doppler spectrum (similar to the mode shown in Fig. 2f) which would cause a reduction in the MDV (e.g. Schrom and Kumjian, 2016). An alternative explanation proposes the existence of a frequently occurring updraft at  $-15^\circ\text{C}$  produced by large-scale lifting (Zawadzki, 2013). A third explanation assumes that the latent heat released by enhanced depositional growth of ice particles in the DGL will locally increase buoyancy and eventually cause upward air motion (Schrom and Kumjian, 2016; Zawadzki, 2013). Obviously, if only the MDV is considered, it is impossible to disentangle vertical air motion and microphysical effects. In the following section, we will extend the analysis to the Doppler spectra in order to better estimate the relative contributions of microphysics and upward motion on the observed MDV slow-down in the DGL.

#### 4.2 Estimating the contribution of vertical air motion and new particle mode to the MDV reduction in the DGL

The observed slow-down of the MDV in the DGL could be solely caused by the appearance of a slow, secondary particle mode or entirely due to an upward air motion. Both effects might even be connected to each other, for example if a large-scale updraft is locally enhancing relative humidity which might then trigger nucleation of new ice particles. Alternatively, rapid depositional growth of ice particles

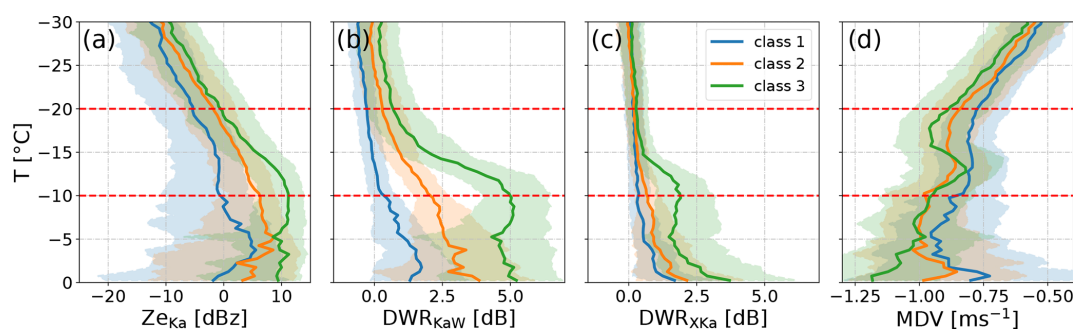


**Figure 4.** Median (solid line) and quantiles (shading) of (a) Ze at Ka-band, (b) DWR<sub>KaW</sub>, (c) DWR<sub>XKa</sub> and (d) MDV (Ka-band) profiles stratified with temperature and classified into classes of maximum DWR<sub>KaW</sub> in the DGL (see class definition in Table 2). The temperature region of the DGL is indicated by the dashed red lines. Only profiles which are continuous in the DGL are considered.

in the DGL might release latent heat which could cause a buoyancy-driven upward air motion.

Vertical air motion can be derived from Doppler spectra if the terminal velocity of a spectral mode or distinct spectral feature is well-known. In mixed-phase clouds, the presence of a narrow spectral peak due to small supercooled liquid water droplets can sometimes be used to infer vertical air motion, assuming that the terminal velocity of the droplets is negligible (e.g. Zhu et al., 2021; Shupe et al., 2004). Unfortunately, a supercooled liquid peak does not appear in all ice clouds and is often only occurring in a relatively narrow height region of the cloud. However, vertical air motion is commonly assumed to impact all particles in the radar volume in the same way. As a result, the spectrum will be shifted to higher or lower Doppler velocities but without changing its shape. In contrast, a new particle mode will only affect the slow edge of the spectrum while the fast-falling particles will be mostly unaffected. This slow-down effect due to new particle formation will be detectable as soon as the new mode overcomes the noise threshold even if no distinct secondary peak can be identified. Therefore, if the MDV slow-down is solely an effect of vertical air motion, we expect the slow and the fast spectral edge to show an identical reduction in Doppler velocity. If the slow-down is caused by new particles only, the slow edge should decrease while the fast edge should remain constant or increase.

The median and quantile profiles of slow and fast spectral edges separated for the three DWR<sub>KaW</sub> classes are shown in Fig. 5. We can clearly see that the slow-down on the slow edge is larger than on the fast edge for all classes. This implies that the MDV slow-down is indeed a combination of vertical air motion and the formation of a new, slower spectral mode. The reduction on the fast edge is almost only visible for the largest DWR<sub>KaW</sub> class while the reduction on the slow edge is also noticeable for the lower DWR<sub>KaW</sub> classes. On the fast edge, the differences in the median velocity profiles between class 1 and 3 are around 0.2 to 0.3 m s<sup>-1</sup> throughout the entire temperature region, while on the slow edge the differences are negligibly small. When focusing on

the largest DWR<sub>KaW</sub> class and zooming into the temperature region of the DGL (Fig. 5b), we can roughly estimate the velocity reduction at the two spectral edges. We assume that the spectral edges without new particle mode or updraft would remain constant or increase towards warmer temperatures. For each spectral edge profile, we search for the level where we find the velocities indicating the onset of a slow-down (vertical red lines in Fig. 5b). If we subtract the velocities at this level from the values of the strongest reduction found in the DGL, we obtain a lower limit estimate of the real slow-down. For the slow edge, we find a reduction of 0.28 m s<sup>-1</sup> between -18 and -14 °C. On the fast edge, the reduction is almost a factor of 3 smaller with a reduction of 0.1 m s<sup>-1</sup> between -16 and -14 °C. The total slow-down in the MDV is 0.18 m s<sup>-1</sup> between -16 and -14 °C, which is less than for the slow edge simply due to the stronger contribution of the larger (faster) particles to the MDV. A Kolmogorov–Smirnov two-sample test revealed that the slow-down on the slow-falling edge is statistically significant, while it is not significant for the fast edge.

In case of no updraft, we would expect the fast edge velocity to continuously increase, similarly as for temperatures colder than -16 °C. So even if the Kolmogorov–Smirnov test indicates that the slow-down on the fast edge is not statistically significant, we argue that the persistent stagnation of the fall velocities over the temperature range from between -16 and -14 °C strongly points towards the presence of an updraft. The presence of an updraft can also be detected at the slow edge velocities. The median values reduce at -14 °C to almost 0 m s<sup>-1</sup>; the quantiles indicated by the shaded areas in Fig. 5b show even upward (positive) velocities which strongly indicates an upward air motion. The presence of an updraft was also found by Dias Neto (2021) for a similar winter dataset collected at JOYCE-CF. Our estimated updraft velocity represents, however, only a lower boundary of the true updraft speed as the terminal velocity of the particles at the spectral edges are unknown.

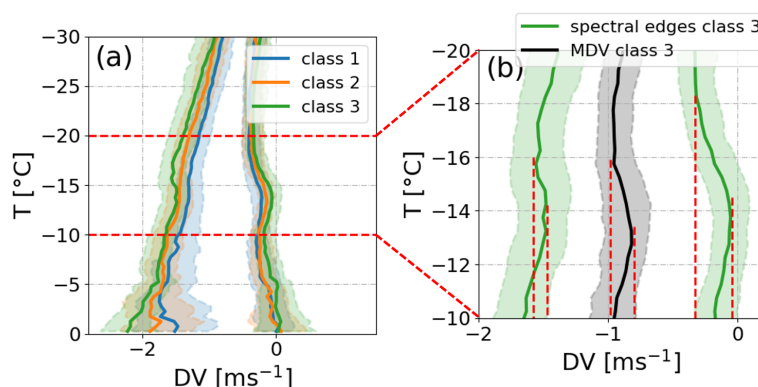


**Figure 5.** (a) Derived Doppler velocities of the spectral edges classified into  $\text{DWR}_{\text{KaW}}$  classes (see also Table 2). Solid lines indicate the median and the shading denotes the quantiles of the distribution. The dashed red lines indicate the location of the DGL. (b) Zoomed view into the DGL region but only including the spectral edge velocities (green) and MDV (black) of class 3. The vertical dashed red lines in (b) visualise the points in the spectral edges and MDV which have been used to estimate the maximum velocity reduction (see details in the text).

### 4.3 Investigation of the small particle mode

The spectral analysis in the previous section clearly indicated the formation of a new, slow falling ice particle mode in the DGL. As polarimetric variables are known to be particularly sensitive to newly formed ice crystals with asymmetric shape, we also sort the polarimetric profiles according to the  $\text{DWR}_{\text{KaW}}$  classification in order to analyse their relation to the aggregate class.

Interestingly, the median ZDR profiles do not reveal a clear maximum of ZDR at  $-15^{\circ}\text{C}$  (Fig. 6a) despite the expected presence of dendrites with very low aspect ratios. Between  $-30$  and  $0^{\circ}\text{C}$  we find the ZDR profiles to be increasingly shifted to smaller values for higher aggregate class. The spread between the quantiles is rather large compared to the relative difference between the aggregate classes. The differences between the lower and upper quantile varies between 0.3 and 0.5 dB, with a similar magnitude for all classes and throughout the entire analysed temperature region. This indicates that even if the medians and quantiles are shifted towards smaller values for higher aggregate class, there is a large variability within each class. From the ZDR profiles alone it is very difficult to tell whether the shift towards small values is caused by a change of small ice particle properties or by varying number, size or density of aggregates.

As already illustrated in the case study analysis (Fig. 2h), the high ZDR producing particles usually populate at lower Doppler velocities and are thus well separated from larger, low ZDR producing aggregates. As a result, the  $s\text{ZDR}_{\text{max}}$  (Fig. 6b) is mostly unaffected by the presence of aggregates and shows the ZDR signature of the most ZDR producing particles present in the radar volume. Increasing first at  $-18^{\circ}\text{C}$  from 1.0 dB,  $s\text{ZDR}_{\text{max}}$  of aggregate class 2 and 3 reaches a maximum within the bottom half of the DGL (1.5 and 1.7 dB for class 2 and 3, respectively). Below the DGL,  $s\text{ZDR}_{\text{max}}$  remains relatively constant between 1 and 1.5 dB

down to  $-3^{\circ}\text{C}$ . Further down,  $s\text{ZDR}_{\text{max}}$  drops to values of 0.8 to 1 dB, which are similar to the values found at temperatures colder than  $-20^{\circ}\text{C}$ . Overall, the  $s\text{ZDR}_{\text{max}}$  in the DGL is only weakly dependent on aggregate class, with only slightly larger values (ca. 0.5 dB) for aggregate class 2 and 3 compared to class 1. This seems to indicate that the properties impacting ZDR, such as aspect ratio or ice density of the dendrites and other plate-like particles growing in the DGL, are overall relatively similar for aggregate classes 2 and 3. However, the position of the maxima within the DGL of aggregate class 2 and 3 differs. Class 3 reaches its maximum slightly below  $-15^{\circ}\text{C}$ , while class 2 reaches its maximum at the bottom of the DGL. This might indicate that the  $s\text{ZDR}_{\text{max}}$  producing particles of class 2 continue to grow and increase their aspect ratio and/or density throughout the entire DGL, while the particles in class 3 reach their largest aspect ratio already slightly below  $-15^{\circ}\text{C}$ .

Most notably, when comparing ZDR and  $s\text{ZDR}_{\text{max}}$ , the  $s\text{ZDR}_{\text{max}}$  profiles lack the shift towards higher values with lower aggregate class. As both variables are independent of particle concentration, it appears most likely that the ZDR shift is related to on average larger aggregates throughout the profile rather than less ZDR producing ice crystals. This interpretation is consistent with the  $\text{DWR}_{\text{KaW}}$  profiles in Fig. 4b which show overall larger mean aggregate sizes between  $-30$  and  $0^{\circ}\text{C}$  for increasing aggregate classes. The maximum size of aggregates in the DGL appears to be correlated with the mean size of particles above the DGL. For temperatures colder than  $-18^{\circ}\text{C}$ , the spread between the lower and upper quantile of all classes is approximately 1 dB. At  $-18^{\circ}\text{C}$ , which is the temperature level where the medians of class 2 and 3 start to increase, we also find an increasing spread between the quantiles of class 2 and 3 reaching values up to 3.5 dB (4 dB) for class 3 (class 2) in the lower half of the DGL. Below the DGL, the spread slightly reduces again, un-



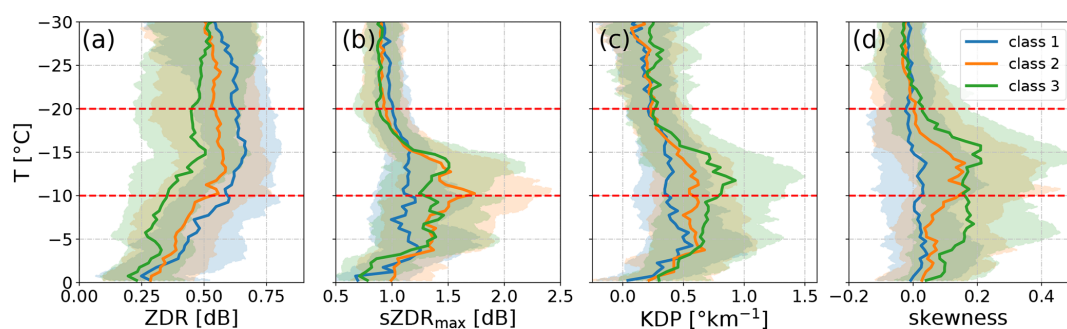


**Figure 6.** Same as in Fig. 4, but showing profiles of W-band (a) ZDR, (b)  $sZDR_{\max}$ , (c) KDP and (d) Ka-band skewness (for interpretation of the skewness sign, see text). Note that the polarimetric variables have been obtained at  $30^\circ$  elevation and the skewness from the zenith Doppler spectra.

til approximately 1.5 dB at  $0^\circ\text{C}$ . In general, the upper quantile follows the course of the median. This large spread of the quantiles within the DGL indicates that many profiles included in the dataset show only a rather weak or completely absent increase in  $sZDR_{\max}$  within the DGL. This is most likely also the explanation why the median of  $sZDR_{\max}$  is substantially smaller than the  $sZDR_{\max}$  profile presented in Fig. 3.

Similar to  $sZDR_{\max}$ , the median KDP profiles (Fig. 6c) above the DGL show only low values ( $0.25^\circ\text{km}^{-1}$ ) and no clear difference between the aggregate classes. This implies that the particles falling from aloft into the DGL are not only similar in terms of their properties impacting ZDR, but also in terms of average concentration. All median KDP profiles start to increase at  $-18^\circ\text{C}$  which is again very similar to the behaviour of  $sZDR_{\max}$ . The KDP values within the DGL show a stronger increase for larger aggregate classes as observed for  $sZDR_{\max}$ . Interestingly, the KDP profile observed for aggregate class 3 is on average not peaking directly at  $-15^\circ\text{C}$ , but rather linearly increasing from  $-18^\circ\text{C}$  towards  $-12^\circ\text{C}$  where it reaches a maximum of  $0.7^\circ\text{km}^{-1}$ . The KDP profiles remain enhanced from the bottom of the DGL down to  $-3^\circ\text{C}$  where their values suddenly drop to nearly  $0^\circ\text{km}^{-1}$ . The rapid decrease of KDP and  $sZDR_{\max}$  at temperatures larger than  $-3^\circ\text{C}$  is correlated with the increase of  $DWR_{\text{Ka}}$  (Fig. 4c) in this region. It appears to be quite likely that the second intensified aggregation zone close to  $0^\circ\text{C}$  is mainly responsible for the reduction of high ZDR producing ice particles. Similar to  $sZDR_{\max}$ , the spread between the upper and lower quantile is small (within  $0.5^\circ\text{km}^{-1}$ ) above the DGL. At  $-18^\circ\text{C}$  the spread especially of class 3 increases to  $1.1^\circ\text{km}^{-1}$  at  $-12^\circ\text{C}$ . The spread reduces again at temperatures warmer than  $-5^\circ\text{C}$  to  $0.65^\circ\text{km}^{-1}$  at  $0^\circ\text{C}$ . Again, the distributions show a large overlap between the different classes. Also for the largest aggregate class, we find profiles with very weak increase of KDP. On the other side, the upper quantiles also clearly reveal a higher likelihood for extreme KDP and  $sZDR_{\max}$  values for higher aggregate classes.

In order to complement the picture of the small particle evolution, in Fig. 6d we also included the skewness of the non-polarimetric Ka-band Doppler spectra recorded in zenith. Asymmetric broadening of the spectra on the fast edge (negative skewness) or on the slow edge (positive skewness) can be very well detected in the skewness profile (see also example profile in Fig. 3). The formation of new, small ice particles can be expected to result in positive skewness values even if the spectra do not reveal a separated spectral mode. Above the DGL, all median skewness profiles are close to 0 indicating on average symmetrical spectra. Similar to KDP, the skewness values increase most rapidly at  $-18^\circ\text{C}$ . We also find clearly larger skewness values (up to 0.2) for higher aggregate classes. For the largest aggregate class, the skewness values also remain close to 0.2 down to the  $-5^\circ\text{C}$  level. This similarity to the signature found in KDP is even more surprising as we can expect processes such as riming (broadening on fast spectral edge) to decrease skewness, and hence potentially masking the signature of the small particle mode. Also, when looking at the 75th percentiles (shaded areas), we find, similar to  $sZDR_{\max}$  and KDP, distinct maxima at  $-15$  and  $-5^\circ\text{C}$ .

Comparing the results of the statistical analysis to the case study presented in Sect. 3, we note the smaller values of KDP,  $sZDR_{\max}$  and skewness found in the statistics. In the case study,  $sZDR_{\max}$  values of up to 4 dB at around  $-15^\circ\text{C}$  were reached, alongside a maximum KDP of approx.  $2^\circ\text{km}^{-1}$  and a skewness of 1.3. However, in the statistics we classify the profiles with the maximum  $DWR_{\text{KaW}}$ . In Fig. 2, one can see that we do not always find an increase in KDP or  $sZDR_{\max}$  for increasing  $DWR_{\text{KaW}}$ . For example, at 06:30 UTC, a strong increase in KDP below  $-15^\circ\text{C}$  coincides with an enhanced  $sZDR_{\max}$  and  $DWR_{\text{KaW}}$ . At later periods of the day, for example at 18:00 UTC, we see enhanced  $DWR_{\text{KaW}}$  without enhanced KDP and  $sZDR_{\max}$ . Those examples explain why the medians in our statistical analysis are shifted to smaller values.

Summarising the results of this section, we can say that our statistics reveal that the aggregation in the DGL is corre-

lated to growth and evolution of asymmetric particles within the DGL. Aggregation in the DGL appears to be stronger if larger aggregates fall already from higher levels into the DGL. Most notably, signatures related to crystal growth or aggregation that evolved in the DGL appear to persist to lower layers until  $-5^{\circ}\text{C}$  is reached. In the following section, we will discuss our main findings together with laboratory results, and attempt a physical interpretation of the potentially involved processes.

## 5 Discussion

### 5.1 Interpretation of the temperature dependence of ice particles, aggregates and vertical air motion in the DGL

The most striking features visible in the radar data of the DGL are rapid changes of vertical gradients within a relatively small temperature range, and distinct maxima at specific temperatures. In order to simplify their interpretation, we schematically show the radar profiles for the highest aggregation class in Fig. 7, together with related results from previous laboratory studies. Although we are lacking in situ observations from inside the cloud for our dataset, we base our interpretation on well-established relations between microphysical processes and distinct radar signatures. For example, aggregation can be clearly associated with an increase in DWR (e.g. Ori et al., 2020; Barrett et al., 2019; Dias Neto et al., 2019; Mason et al., 2019), whereas plate-like particle growth is strongly linked to enhanced ZDR and KDP (e.g. Moisseev et al., 2015; Schrom et al., 2015).

According to Takahashi (2014), hereafter “TKH14”, the increase in mass and size of plate-like particles is strongest between  $-16$  and  $-13^{\circ}\text{C}$  with a local maximum at  $-15^{\circ}\text{C}$  for stellar particles. When growing at constant temperature and high supersaturation, they develop distinct habits ranging from sectors (SEC), broad branched particles (BB), stellars (STEL), dendrites (DEN) and fern-like dendrites (FERN) (indicated on the left in Fig. 7). This shape dependency on temperature was also confirmed by airborne in situ observations (Bailey and Hallett, 2009). As mentioned in (Bailey and Hallett, 2009, among others), the shape of the particles does not only depend on temperature, but also on the supersaturation that the particle experiences during growth. During the TRIPEX-pol campaign, we did not have sufficient relative humidity information. In the following, we therefore only focus our interpretation on the observed temperature-dependent growth of ice particles.

The plate-like particle growth connected to increasing  $s\text{ZDR}_{\text{max}}$  values seems to start at  $-20^{\circ}\text{C}$ . This temperature roughly coincides with the temperature level where the aspect ratio of crystals observed in the laboratory starts to deviate from unity (see Fig. 2 in Takahashi et al., 1991, hereafter TKH91). Initially, the increase in  $s\text{ZDR}_{\text{max}}$  is relatively moderate down to  $-15^{\circ}\text{C}$ . At this temperature level,

$s\text{ZDR}_{\text{max}}$  strongly increases reaching its maximum values between  $-13$  and  $-14^{\circ}\text{C}$ . As long as the particles grow in the plate-like growth regime, we can expect a certain correlation of aspect ratio and size. Regions showing enhanced  $s\text{ZDR}_{\text{max}}$  values are also likely connected to larger sized crystals. Interestingly, the maximum in  $s\text{ZDR}_{\text{max}}$  is found at slightly warmer temperatures than  $-15^{\circ}\text{C}$  where the maximum size and aspect ratio is found in TKH14 and TKH91. A simple explanation might be the fact that unlike the particles grown in the experiments by TKH14 and TKH91, particles in real clouds are sedimenting into different temperature regions while growing. Once the sedimenting particles reach the  $-15^{\circ}\text{C}$  level, they grow most efficiently by vapour deposition as indicated by the strong gradient found in the  $s\text{ZDR}_{\text{max}}$  profile. The most favourable growth region (indicated in the curve of maximum particle size found in TKH14) extends from  $-15^{\circ}\text{C}$  to almost  $-13^{\circ}\text{C}$  which is the location where  $s\text{ZDR}_{\text{max}}$  indicates the largest particles with most extreme aspect ratios. But why are  $s\text{ZDR}_{\text{max}}$  values not increasing further towards the bottom of the DGL? Scattering calculations (Myagkov et al., 2016b; Hogan et al., 2000) indicate that ZDR is only slowly increasing once a certain aspect ratio is reached (see also Fig. C1b). The  $s\text{ZDR}_{\text{max}}$  values can therefore be expected to reach a certain saturation value once the particle grew into a shape with very low aspect ratio. Further, in case of dendritic growth, the effective density of the particle decreases with size, leading to a saturation of ZDR. With increasing size, also the particles' cross sectional area strongly increases which makes it more likely for the particle to collide with another crystal or aggregate. At a certain point, increasing aggregation (more likely for larger crystals) might counteract the general increase in crystal size leading to the observed slight decrease in  $s\text{ZDR}_{\text{max}}$  towards  $-10^{\circ}\text{C}$ . The increasing  $\text{DWR}_{\text{KaW}}$  values in the DGL appear to be consistent with this interpretation. The  $s\text{ZDR}_{\text{max}}$  and  $\text{DWR}_{\text{KaW}}$  most rapidly increase both at  $-15^{\circ}\text{C}$  but unlike  $s\text{ZDR}_{\text{max}}$ , the  $\text{DWR}_{\text{KaW}}$  continues to rise throughout the DGL. This effect might also be responsible for the different vertical location of the maximum in  $s\text{ZDR}_{\text{max}}$  for aggregate class 2 and 3 (Fig. 6b). More intense aggregation (class 3) might consume the largest dendrites earlier, which results in a  $s\text{ZDR}_{\text{max}}$  maximum closer to the  $-15^{\circ}\text{C}$  level.

The temperature region of maximum crystal growth found in TKH14 also roughly coincides with the temperature region where the upward air motion is found to be largest. This indicates that the weak upward air motion might indeed be a result of the latent heat released by the intensified depositional growth. If we look again at the spectral edge velocities in Fig. 5b, we see that the slow edge velocity begins to decrease already at a temperature of  $-18^{\circ}\text{C}$  which is almost  $2^{\circ}\text{C}$  colder than the temperature where the fast edge is affected by the updraft. At  $-18^{\circ}\text{C}$ , the number of new particles appears to increase, which can be also seen in the KDP profile. The latent heat release due to the increasing number and more favourable growth conditions starting at  $-16^{\circ}\text{C}$

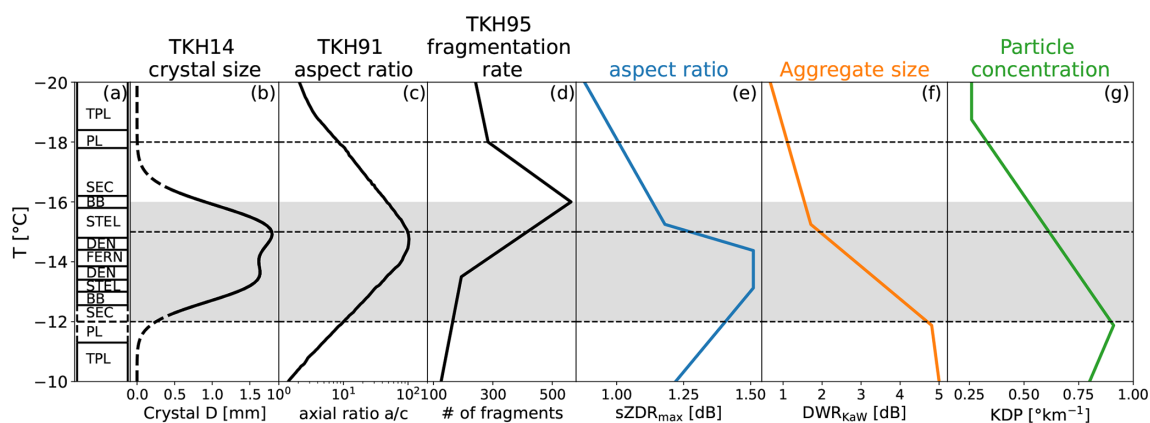


**Figure 7.** Schematic plot combining the main features found in the radar profile statistics (coloured lines) discussed in Sect. 4 and results from laboratory experiments (black lines) in the DGL. The leftmost column denotes temperature regions where specific crystal types are growing (according to TKH91 and TKH14). The abbreviations used in this study and the ones according to the classification of Kikuchi et al. (2013) used in TKH14 denote thick hexagonal plates (TPL, P1b), hexagonal plates (PL, P1a), sectors (SEC, P2a), broad branched (BB, P2b), stellars (STEL, P3a), dendrites (DEN, P3b) and fern-like dendrites (FERN, P3c). **(a)** The maximum crystal size and **(b)** aspect ratio (defined as ratio of the maximum dimensions along the  $a$  and  $c$  axis) which is reached in the experiments by TKH14 (their Table 1) and TKH91 (their Fig. 2) at constant temperature and liquid water saturation after 10 min growth time. The solid line indicates the temperature region in which the experiment was conducted and the dashed line shows the interpolation to warmer/colder temperatures which the fitted function to the measurement predicts. **(c)** Number of fragments collected after the collision of two ice spheres at different temperatures (fit to values shown in Fig. 14 in TKH95). Median profiles of observed **(d)**  $sZDR_{\max}$  (blue), **(e)**  $DWR_{KaW}$  (orange) and **(f)** KDP (green) for the largest aggregate class shown in Figs. 4 and 6. Note that the original profiles have been reduced to the main features such as maximum/minimum or strongest vertical change in order to simplify the discussion. The grey shaded area denotes the temperature region where the spectral edge analysis (Sect. 4.2) indicated upward air motion possibly related to latent heat release. The titles in **(d–f)** indicate the most common particle properties to which the polarimetric variables are related (a more detailed discussion is provided in the text).

might finally be sufficient to also increase buoyancy enough to sustain upward air motion. The updraft might even cause a positive feedback, as its presence enables the particles to grow in the favourable growth region longer. This would further enhance their mass uptake by deposition and increase the latent heat release.

The reverse explanation that an updraft produces local enhancement of supersaturation leading to subsequent nucleation and depositional growth can not be entirely ruled out by the observations. However, it appears rather unlikely that a synoptic or small-scale dynamical feature would be statistically prevalent in this narrow temperature region, despite the large number and variety of cloud and weather conditions included in our statistics. We speculate that one reason why such a latent heat-driven updraft has not been detected so far in numerical weather prediction models might be simply related to the fact that most models do not include an explicit habit prediction scheme which is probably needed to reproduce the intensive growth rate found in the laboratory. However, when simulating a heavy rainfall case, Lee and Baik (2018) found that simulations with a bin microphysics schemes reveal intense latent heat release due to depositional growth. This latent heat release is sufficient to cause an updraft and a positive feedback mechanism. The latent heat release in bulk schemes was found to be substantially weaker.

The profile of KDP, with its sudden increase at  $-18^{\circ}\text{C}$  and its nearly linear increase towards  $-12^{\circ}\text{C}$ , appears to be more challenging to be explained by updraft and depositional growth features. If depositional growth alone was responsible for the increase in KDP, we would expect the profile to have a similar shape as  $sZDR_{\max}$ . KDP is well-known to be closely related to the concentration of asymmetric particles (Kumjian, 2013). Primary ice nucleation appears to be rather unlikely as an explanation for increasing KDP in the DGL. The activation of INPs is expected to decrease with warmer temperatures (Kanji et al., 2017) which is opposite to the KDP signature found in our dataset. The increase of KDP towards the bottom of the DGL is even more surprising as ongoing aggregation (increasing  $DWR_{KaW}$  values) should reduce the number concentration of KDP producing particles, therefore reducing KDP or at the least keeping KDP constant.

Single scattering computations for realistically shaped crystals and aggregates show that KDP is by approximately a factor of 3 larger for dendrites than for same-sized aggregates (Appendix C). Therefore, the contribution of aggregates to total KDP can not be completely neglected. A simple calculation example for the bottom of the DGL using DWR, Ze and KDP values for class 3 revealed that aggregates might contribute 1/3 to the total KDP (Appendix C). KDP at W-band can be interpreted in a similar way as commonly done

for lower frequency radars. Unlike for Ze and ZDR, KDP seems to not be affected by non-Rayleigh scattering effects. It should be noted that this behaviour is expected to change for increasing size parameters (e.g. at radar frequencies higher than W-band).

Secondary ice processes (SIP, Korolev and Leisner, 2020; Field et al., 2017) appear to be a more likely explanation for the observed increase in particle concentration. Several in situ studies (e.g. Rangno and Hobbs, 2001; Hobbs and Rangno, 1998, 1990, 1985) have reported fragments of stellar and dendrites in the DGL. The most likely SIP explaining this effect appears to be fragmentation of ice particles when colliding with each other. Unfortunately, this process has so far only been studied in three laboratory studies (Takahashi et al., 1995; Griggs and Choulaton, 1986; Vardiman, 1978). The number of fragments ejected when colliding two ice spheres at constant temperature and water saturation has been found by Takahashi et al. (1995), hereafter TKH95, to be particularly enhanced inside the DGL between  $-18$  and  $-12$  °C. Although the collisional energy from two cm-sized ice spheres used in TKH95 is quite unrealistic for the scenarios observed in our cases, the rapid growth of fragile dendritic arms on the ice spheres observed by TKH95 indicates that such structures are likely to also grow on aggregates which we found to be sedimenting from above into the DGL. It appears quite probable that collision or even touching of two aggregates might already cause fragmentation of the delicate structures growing on their surfaces. Griggs and Choulaton (1986) also reports that dendrite crystals can fragment without collisions simply due to air drag. Recent modelling studies suggest that ice collisional fragmentation can elevate the ice number concentration by three orders of magnitude (Georgakaki et al., 2022).

Clearly, more insights into the competing effects of aggregation and potential particle generation by ice fragmentation need to be explored, for example using model simulations which include habit-dependent growth and also recent formulations of ice fragmentation (Phillips et al., 2018). Also, new laboratory studies constraining the physical basis of ice fragmentation are clearly needed. Future measurement campaigns should combine in-cloud in situ measurements with multi-frequency and polarimetric radar observations in order to further constrain the hypothesised ice microphysical processes.

## 5.2 Dependency of DWR and polarimetric quantities on cloud top temperature

Previous studies (Trömel et al., 2019; Griffin et al., 2018; Oue et al., 2018) found evidence that the cloud top temperature (CTT) is correlated with polarimetric radar features within the DGL. Griffin et al. (2018) analysed five winter storms at S-band and found an increase of the 80th percentile of KDP values inside the DGL with colder CTT. Similar dependencies were also found for a large set of mid-latitude

clouds (Trömel et al., 2019) and case studies of Arctic mixed-phase clouds (Oue et al., 2018). Griffin et al. (2018) explained the high KDP in the DGL with a high number of irregular crystals or nearly isometric aggregates falling from cloud top. At colder CTT, the primary ice production can be expected to be larger due to the temperature dependence of INP activation (DeMott et al., 2010; Kanji et al., 2017). At  $T < -37$  °C, also homogeneous ice nucleation can further increase the number of ice particles. Although we found no clear correlation of aggregation in the DGL with particle concentration or habit of particles sedimenting from aloft in Sect. 4.3, we sorted our profiles with respect to CTT in order to allow a direct comparison with previous studies.

We determined cloud top height using the Ka-band radar because it is the most sensitive radar and it is less affected by signal attenuation compared to the W-band. The temperature information is taken again from the model analysis implemented in Cloudnet. All profiles with continuous values from cloud top down to  $-10$  °C level (to avoid multi-layer cloud cases) were sorted into three 10 °C-wide CTT regimes ranging from  $-60$  to  $-30$  °C (Fig. 8).

Focusing first on the region above the DGL ( $-30$  to  $-20$  °C), the  $DWR_{KaW}$  profiles for the different CTT (Fig. 8b) show rather similar values around 0 dB. Also, KDP values for different CTT are relatively similar above the DGL, varying between  $0.1$  and  $0.4$  °km $^{-1}$ , and showing maximum differences between the CTT regimes of less than  $0.2$  °km $^{-1}$  (Fig. 8e). A slightly larger separation with CTT regime can be found for  $sZDR_{max}$  and ZDR (Fig. 8f, d). Colder CTT seem to be connected to slightly larger ZDR values. The maximum differences in ZDR and  $sZDR_{max}$  for the three CTT regimes are both around 0.25 dB. Also Ze at Ka-band (Fig. 8a) shows larger values for colder CTT. KDP, Ze and ZDR show a larger spread between the lower and upper quantile. For Ze, the spread between the quantiles of class 1 (2, 3) reaches approximately 8.75 dB (11.25, 13.7 dB). The quantiles of all classes show large overlap. Similarly, the quantiles of KDP are mostly overlapping and spreading  $1.2$  °km $^{-1}$ . ZDR shows the largest spread relative to the magnitude of the median of 0.5 dB (0.7, 0.8 dB) above the DGL. However, the upper and lower quantiles of the classes differ similar to the medians.

From these observations, we can conclude that the concentration of particles (KDP) and average size of aggregates or polycrystals ( $DWR_{KaW}$ ) above the DGL does not substantially vary for different CTT. The similarity of the CTT dependency in ZDR and  $sZDR_{max}$  rather indicates that the three CTT regimes lead to different shapes of ZDR producing crystals. This might simply be related to different habits that the particles grow into after being nucleated at different CTT. Particles falling from lower CTT have also had more time to grow by deposition, and can hence reach larger sizes and potentially more asymmetric shapes.

Considering that the analysis was performed for the same cases as analysed in Sect. 4, the median profiles appear to



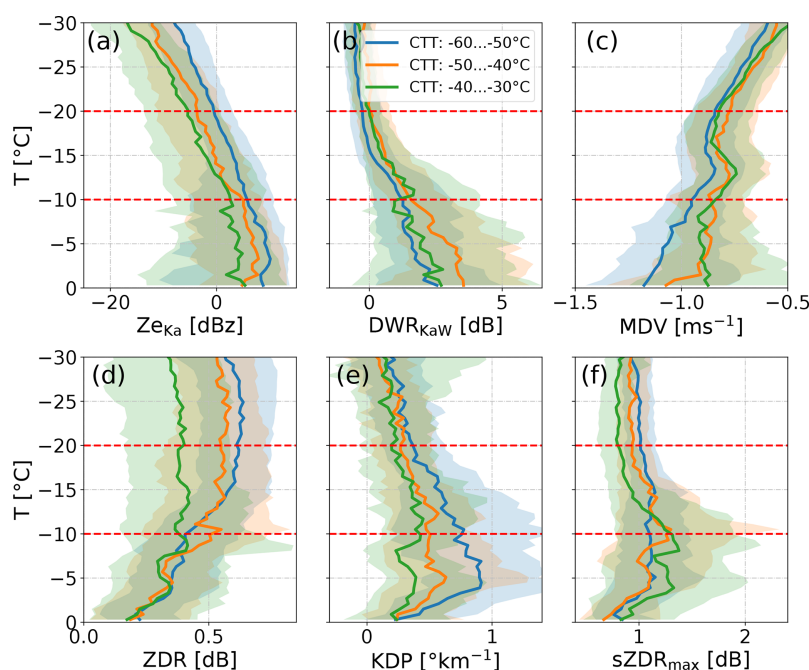


**Figure 8.** Dependency of (a)  $Z_e$ , (b)  $DWR_{KaW}$ , (c) MDV, (d) ZDR (e) KDP and (f)  $sZDR_{max}$  on cloud top temperature (CTT). The profiles of each radar observable were stratified with temperature and classified into CTT classes. As in Fig. 4, the solid lines depict the median of the distribution in each CTT class. The shaded area indicates the quantiles of the distribution.

be much less dependent on CTT as compared to sorting them with respect to the maximum  $DWR_{KaW}$  in the DGL. Except for a clear slow-down in MDV, the signatures inside the DGL, for example the steep increase in  $sZDR_{max}$  at  $-15^\circ\text{C}$ , are much less pronounced or completely absent. Still, certain weak dependencies on CTT can be found in some variables shown in Fig. 8. The total ZDR for profiles starting at colder CTT decreases in the DGL. For the coldest CTT class, ZDR decreases from 0.6 dB at  $-20^\circ\text{C}$  to 0.4 dB at  $-10^\circ\text{C}$ . In contrast, for the warmest CTT class, the ZDR profile stays rather constant at 0.4 dB. The KDP values increase stronger for colder CTT regimes. For CTT between  $-60$  and  $-50^\circ\text{C}$ , KDP increases from around  $0.4^\circ\text{km}^{-1}$  at  $-20^\circ\text{C}$  to  $0.7^\circ\text{km}^{-1}$  at  $-10^\circ\text{C}$ . In contrast, for the warmest CTT class, KDP increases only from  $0.2^\circ\text{km}^{-1}$  at  $-20^\circ\text{C}$  to  $0.35^\circ\text{km}^{-1}$  at  $-10^\circ\text{C}$ . The MDV slow-down is less pronounced for colder CTT ( $0.03\text{ m s}^{-1}$  for the coldest,  $0.11\text{ m s}^{-1}$  for the warmest CTT class). Below  $-15^\circ\text{C}$ , the particles fall faster for colder CTT ( $-0.97\text{ m s}^{-1}$  for the coldest CTT class,  $-0.85\text{ m s}^{-1}$  for the warmer CTT classes). Interestingly, the  $DWR_{KaW}$  profiles show no evidence of a strong dependence of aggregation in the DGL on CTT regime. They only increase from 0 dB at  $-20^\circ\text{C}$  to 1–1.5 dB at  $-10^\circ\text{C}$ . Interestingly, also  $sZDR_{max}$  lacks a clear maximum in the DGL and increases much less than when sorting the profiles with maximum  $DWR_{KaW}$ . Only the median profile of the warmest CTT class increases slightly from 0.95 dB at  $-20^\circ\text{C}$  to 1.3 dB at  $-10^\circ\text{C}$ . The upper quantile of the

distribution, however, shows a stronger increase for the two warmest CTT classes, reaching 2.29 and 1.88 dB at the bottom of the DGL for class 2 and 3, respectively.

The results obtained by sorting the profiles according to their CTT reveal, similar to Sect. 4, that the main changes of particle concentration, crystal shape and aggregate size take place within the DGL. The role of particles sedimenting from upper layers appear to be small regardless of whether we sort by CTT or maximum  $DWR_{KaW}$ . This is in agreement with Dias Neto (2021), who found no clear dependency of aggregation strength on CTT. However, why do we still find larger KDP values for colder CTT if the influence of particles sedimenting from above is weak? Deeper clouds might simply overall provide a more favourable environment (for example larger updrafts, larger super-saturation) for ice particle growth. This might also lead to higher super-saturation inside the DGL. As a result, we expect primary ice nucleation and secondary ice processes to be more enhanced in such an environment. A more intense depositional growth of delicate dendritic structures will most likely also impact number and size of fragments caused by ice collisional fragmentation. As discussed in the previous section, there is growing evidence that fragmentation is a potential source for enhancing particle number concentration in the DGL. The dependence of KDP on CTT found in our study and in previous work might therefore be less related to the larger nucleation rates expected for colder CTT. The sorting by CTT might simply result into a separation of cloud regimes with more or less favourable

growth conditions. This aspect should be further investigated with future campaign datasets that include a large number of reliable humidity profiles (e.g. from frequent radio soundings).

## 6 Summary and conclusions

A statistical analysis of 3 months of ground-based, triple-frequency (X-, Ka-, W-band) Doppler radar observations combined with polarimetric Doppler W-band observations was conducted at the JOYCE-CF site in order to better understand growth signatures and related processes in the DGL. Similar to previous studies, we find rapid aggregation taking place in the DGL in combination with the formation of a new ice particle mode, most likely associated to dendritic particles.

After classifying the profiles with respect to their maximum average particle size (maximum  $DWR_{KaW}$ ), we found a substantial reduction of the MDV in the DGL, which is strongest for the highest aggregate class. An analysis of the spectral edge velocities revealed that part of the reduction is due to a new mode of slow falling ice particles, that first appears in the spectra at  $-18^{\circ}\text{C}$ . In addition, an updraft in the order of  $0.1\text{ m s}^{-1}$  is revealed by the fast spectral edge velocity with a maximum reached at  $-14^{\circ}\text{C}$ . As suggested by previous studies, it appears most likely that the updraft is a result of latent heat release due to enhanced depositional growth in the DGL.

Clearly, processes in the DGL are strongly tied to temperature. After combining the main signatures revealed by spectral multi-frequency and polarimetric observations with recent laboratory experiments, we derived the following interpretation of particle evolution within the DGL:

- The concentration of particles indicated by KDP continuously increases from  $-18$  to  $-12^{\circ}\text{C}$ . This increase in concentration seems not to be strongly affected by the particle concentration falling from above. Only for the 75 % percentile we find a distinct maximum of KDP at  $-12^{\circ}\text{C}$ , similar to previous studies using lower frequency radars. The temperature where KDP first increases roughly coincides with the temperature where laboratory studies found an increase in the numbers of fragments ejected due to particle collisions. Such an SIP could potentially compensate the loss of particles due to aggregation within the DGL and hence explain the continuous increase of KDP.
- The maximum spectral ZDR ( $sZDR_{\text{max}}$ ) indicates that the aspect ratio of dendritic particles strongly increases at  $-15^{\circ}\text{C}$ , coinciding with the temperature of maximum growth rate and aspect ratio measured in the laboratory. Slight temperature shifts between the radar observations and laboratory results can be most likely assigned to particle sedimentation while growing. Similar

as for KDP, no strong difference is found in  $sZDR_{\text{max}}$  for particles sedimenting into the DGL from above. However,  $DWR_{KaW}$  and ZDR indicate that aggregates sedimenting from higher altitudes into the DGL are larger for cases with enhanced aggregation in the DGL.

- The temperature region where the analysis of the spectral edge velocity indicated an updraft coincides with the region of strongest depositional growth and increase in mean aggregate size. This updraft, potentially connected to latent heat release, might cause a positive feedback as it would enhance the residence time of small particles in the favourable growth zone.

Sorting the profiles with respect to cloud top temperature revealed only slight differences in ice particle shape but nearly negligible differences in concentration or mean size for particles entering the DGL from above. The strongest change in concentration, aspect ratio and mean aggregate size is again observed within the DGL. This highlights the importance of processes taking place inside the DGL for evolution of particle concentration and size. Larger aspect ratios and sizes of ice particles falling from above into the DGL and the generally stronger increase of KDP in the DGL for colder CTT might be simply explained by the overall more favourable growth conditions expected for deeper cloud systems, such as higher super-saturation.

Our statistical analysis further revealed that KDP and  $sZDR_{\text{max}}$  values remain enhanced after leaving the DGL down to  $-3^{\circ}\text{C}$  where their values rapidly decrease towards the melting layer. Other SIP being active at warmer temperatures might be a potential source for new ice particles that maintain the high KDP values. Intensified aggregation at temperatures warmer than  $-3^{\circ}\text{C}$  is the most likely explanation for the rapid decrease of polarimetric variables with concurrent increase of DWR. This increase in aggregation might be explained by the strongly increasing thickness of a quasi-liquid layer (QLL) on ice surfaces, which is expected to increase the sticking efficiency of all ice particles.

This study clearly demonstrates the added value of combining different radar approaches including Doppler spectral analysis, high-frequency radar polarimetry and multi-frequency observations for ice microphysical studies. A statistical analysis as presented in this work can provide robust estimates of potential correlations between different radar variables and their specific temperature dependency. Unlike case studies, such a statistical approach also provides an estimation of the natural variability of observables involved. Statistically-based observational process signatures are very useful for evaluating and improving microphysical schemes in weather prediction models (e.g. Karrer et al., 2021; Ori et al., 2020). They are also urgently needed as constraint for recent model developments such as habit-dependent growth (Jensen et al., 2017; Sulia and Kumjian, 2017; Harrington et al., 2013; Hashino and Tripoli, 2007) and Lagrangian Monte Carlo models where the particle history can be traced

(Grabowski et al., 2019; Brdar and Seifert, 2018). Signatures in remote-sensing datasets can also guide new laboratory studies which are inevitably needed to improve our process understanding and microphysical parameterisations in models. Such laboratory studies in addition to in situ measurements or Monte Carlo modelling studies could also provide unique opportunities to validate our findings and the hypothesised ice microphysical processes of this study.

#### Appendix A: Chirp tables of the vertically pointing W-band and slant polarimetric W-band radar.

The range resolution, number of spectral averages, Doppler velocity resolution and Nyquist range vary with range for the two FMCW W-band radars. This is due to different chirp settings being defined for different range gate regions. The details of the chirp settings applied during TRIPEX-pol are summarised in Tables A1 and A2.

**Table A1.** Chirp table for the vertical W-band radar installed during the TRIPEX-pol campaign.

Specifications	Chirp 1	Chirp 2	Chirp 3	Chirp 4
Range [m]	215–1475	1482–3986	3999–8151	8165–11998
Range resolution [m]	36.0	12.8	12.8	12.8
Number of spectral averages	13	13	15	11
Doppler velocity resolution [ $\text{m s}^{-1}$ ]	0.04	0.027	0.028	0.029
Nyquist range [ $\text{m s}^{-1}$ ]	$\pm 10.26$	$\pm 6.85$	$\pm 3.41$	$\pm 1.81$

**Table A2.** Chirp table for the polarimetric W-band radar installed during the TRIPEX-pol campaign.

Specifications	Chirp 1	Chirp 2	Chirp 3
Range [m]	107–715	751–5902	5938–17994
Range resolution [m]	35.8	35.8	35.8
Number of spectral averages	28	56	104
Doppler velocity resolution [ $\text{m s}^{-1}$ ]	0.05	0.042	0.039
Nyquist range [ $\text{m s}^{-1}$ ]	$\pm 6.35$	$\pm 4.98$	$\pm 2.66$



## Appendix B: Snow particle observations on the surface and zoomed view on Doppler spectra observed on 30 January 2019 at JOYCE-CF

On 30 January 2018, snowfall was observed on the ground at JOYCE-CF. Between 09:00 and 10:00 UTC, large dendritic crystals and aggregates could be photographed (Fig. B1). The pictures are meant to complement the remote-sensing observations from the case study presented in Sect. 3.

For a better visibility of the second spectral mode described in Sect. 3, we show a zoomed view of the spectral Ze in the DGL (Fig. B2a) and a single Doppler spectrum extracted close to the  $-14^{\circ}\text{C}$  level where the second, slow falling mode can be recognised (Fig. B2b).

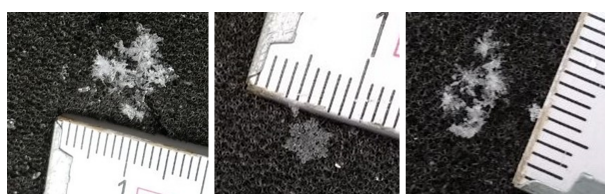


**Figure B1.** Example photographs of dendritic crystals and aggregates reaching the surface during the snowfall event occurring on 30 January 2019 at JOYCE. The sample pictures were taken at 09:00 UTC. The long ticks on the scale denote 1 cm while the short ticks denote 1 mm.

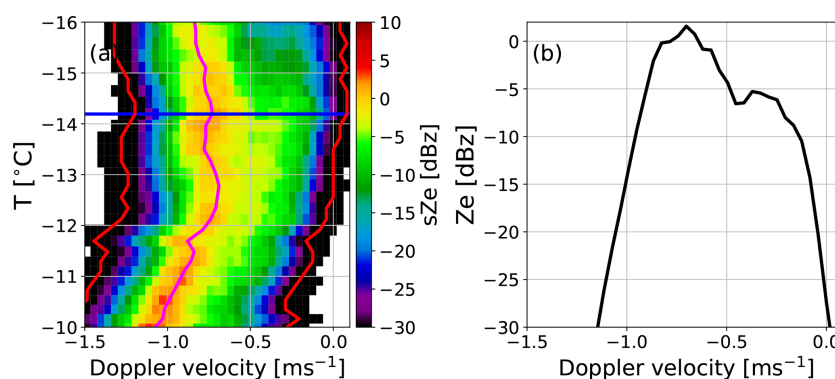


**Figure B2.** Zoom into the spectrogram shown in Fig. 3: (a) spectral Ze from the Ka-band radar, the magenta line depicts the position of the maximum of the main spectral mode. As in Fig. 3d, the red lines indicate the derived spectral edge velocities. The blue line in (a) shows the temperature from which the single spectrum in (b) was taken.

### Appendix C: Comparability of W-band and X-band polarimetric observations and estimation of the contribution of aggregates to KDP

The majority of polarimetric observations in the DGL have been obtained by lower frequency systems (e.g. S-, C-, X-band). Only during recent years, an increasing number of higher frequency polarimetric cloud radars (mainly Ka- and W-band) became available. The use of higher frequencies has a number of advantages, such as larger KDP (increasing with  $\lambda^{-1}$ ) for a given particle population. However, also non-Rayleigh scattering effects become increasingly important at higher frequencies which can make the interpretation of high-frequency polarimetric observations more challenging.

Certainly, an in-depth discussion of the differences in polarimetric observations at various frequencies is out of the scope of this study. However, a comparison of the size and frequency dependence of some key radar variables, such as Ze, ZDR and KDP, for single particles can help to understand which variables are more or less affected by non-Rayleigh scattering effects. Figure C1 shows those three variables which were derived using a recent scattering database by Lu et al. (2016) which also contains scattering properties needed for polarimetric quantities. As our focus in this study is on the DGL, we focused on horizontally aligned branched planar crystals and aggregates of stellars (HD-P1d) at an elevation angle of 30° (consistent with our observations during Tripex-pol). In addition to W-band, values are calculated for X-band as this is the lowest frequency included in the database.

Up to 1 mm particle size, the single-particle Ze at X- and W-band are almost identical as expected from Rayleigh theory (Fig. C1a). The slight differences between crystals and aggregates are most likely due to their different mass–size relations. No specific resonance effects are visible at X-band up to 10 mm size, while at W-band we find the first distinct minimum at 3 mm which is close to the wavelength (3.3 mm). As a result, the Ze at W-band is lower than at X-band for particles larger than 1 mm which is the reason for increasing DWR at larger mean size.

Similar resonance phenomena can also be found in ZDR at very similar particle sizes (Fig. C1b). ZDR at X- and W-band are very similar up to 1 mm size with larger values (3 dB) for crystals and smaller values (1.3 dB) for aggregates owing to their lower density and less extreme aspect ratio. The ZDR values at X-band remain relatively constant over the entire size range. At W-band we find, in addition to a strong minimum at 3 mm, two distinct maxima at 2 and 4–5 mm. Similar but overall less extreme resonance phenomena can also be found for the aggregates at W-band. The ZDR at W-band from the aggregates seems also to increase with particle size.

Despite the large values in ZDR, which can be reached at specific diameters due to resonance phenomena at W-band (between 0 and 9 dB), the differences in total ZDR between

X- and W-band can be expected to be relatively small as the extreme values are likely to cancel out when integrating over a PSD (Matrosov, 2021). Even for spectrally resolved ZDR, resonance effects might be difficult to detect as various ice particle sizes are likely to fall into the same Doppler velocity bin due to natural variability in particle shape and orientation. Matrosov (2021) measured ZDR at W- and Ka-band in Arctic clouds and found that the ZDR differences are slightly increasing with ZDR but, on average, the differences are found to be less than 0.5 dB.

Most interesting for the interpretation of the results of our study is the comparison of single-particle KDP shown in Fig. C1c. One can see that after scaling KDP with  $\lambda$ , there are only very small differences found between X- and W-band. Especially, no resonance phenomena as observed for Ze and ZDR can be found for KDP at any size and for both particle types. This is in agreement with Lu et al. (2015), who showed that simulated KDP at cloud radar wavelengths does not exhibit resonance phenomena. Also, measured KDP values at Ka- and W-band reveal only the expected wavelength scaling (Matrosov, 2021). Also the strong increase of KDP with particle size is remarkably similar at X- and W-band (Fig. C1c). As expected, the KDP for crystals is much larger (up to 1 order of magnitude at 4 mm) than for aggregates. However, as shown in the following simple calculation, the contribution of aggregates to the total KDP can usually not be neglected.

In the observational statistics (Fig. 7), we saw that KDP and DWR continuously increase towards the bottom of the DGL. Can those enhanced KDP values maybe entirely be explained by the contribution from aggregates as for example suggested by Moisseev et al. (2015)? We try to shed light on this question with the following simple calculation.

For simplicity, we assume an inverse exponential size distribution for the aggregates of the form,

$$N(D) = N_0 \cdot \exp(-\Lambda D), \quad (\text{C1})$$

with the slope parameter  $\Lambda$  in  $\text{m}^{-1}$ , the intercept parameter  $N_0$  in  $\text{m}^{-4}$  and the particle size  $D$ . It appears reasonable to assume that at the bottom of the DGL,  $\text{DWR}_{\text{KaW}}$  and Ze are dominated by the contributions from the aggregates. Using the scattering properties shown in Fig. C1, we can directly estimate  $\Lambda$  to be  $(2.25 \times 10^{-3})^{-1} \text{m}^{-1}$  for the maximum  $\text{DWR}_{\text{KaW}}$  of 4.3 dB observed at  $-12^\circ\text{C}$  for the largest aggregate class. With this  $\Lambda$ , we need to assume  $N_0$  to be  $5.6 \times 10^4 \text{m}^{-4}$  in order to match the Ka-band Ze of 10.2 dBz at  $-12^\circ\text{C}$ .

The W-band KDP caused by this aggregate distribution is  $0.28^\circ \text{km}^{-1}$  which is roughly one-third of the observed KDP. If we repeat the same calculation with the 75th percentile of the radar variables measured at  $-12^\circ\text{C}$ , we obtain for a  $\text{DWR}_{\text{KaW}}$  of 6 dB, and Ze of 13 dBz, a KDP of  $1.5^\circ \text{km}^{-1}$ . The aggregates contribute still  $0.32^\circ \text{km}^{-1}$  (20 %) to the total KDP. This high contribution of aggregates to the observed KDP is most likely an upper limit, since we assume the

aggregates to be perfectly horizontally aligned. The naturally occurring tumbling and fluttering of the particles within clouds would reduce the KDP (and ZDR) produced by aggregates.

Unfortunately, we have less constraints on the PSD for the small, presumably dendritic particles at the  $-12^{\circ}\text{C}$  level. For the case study shown in Fig. 2, we observed on-the-ground dendrites reaching up to 5 mm size (see example in Fig. B1). Cloud chamber experiments by TH14 show that particle sizes of 1–1.5 mm are reached in the DGL temperature regime after a growth time of 10 min. In order to produce the remaining KDP signal for the median KDP value at  $-12^{\circ}\text{C}$ , a concentration of 2500 dendrites per  $\text{m}^3$  with 1 mm or  $120\text{ m}^{-3}$  with a size of 5 mm would be needed. For the 75th percentile of the KDP observed at  $-12^{\circ}\text{C}$ , the concentration would increase to 4150 and  $200\text{ m}^{-3}$ , respectively. For comparison, the expected number of ice nucleating particles at  $-12^{\circ}\text{C}$  ranges between 1000 and  $2000\text{ m}^{-3}$  (e.g. DeMott et al., 2010).

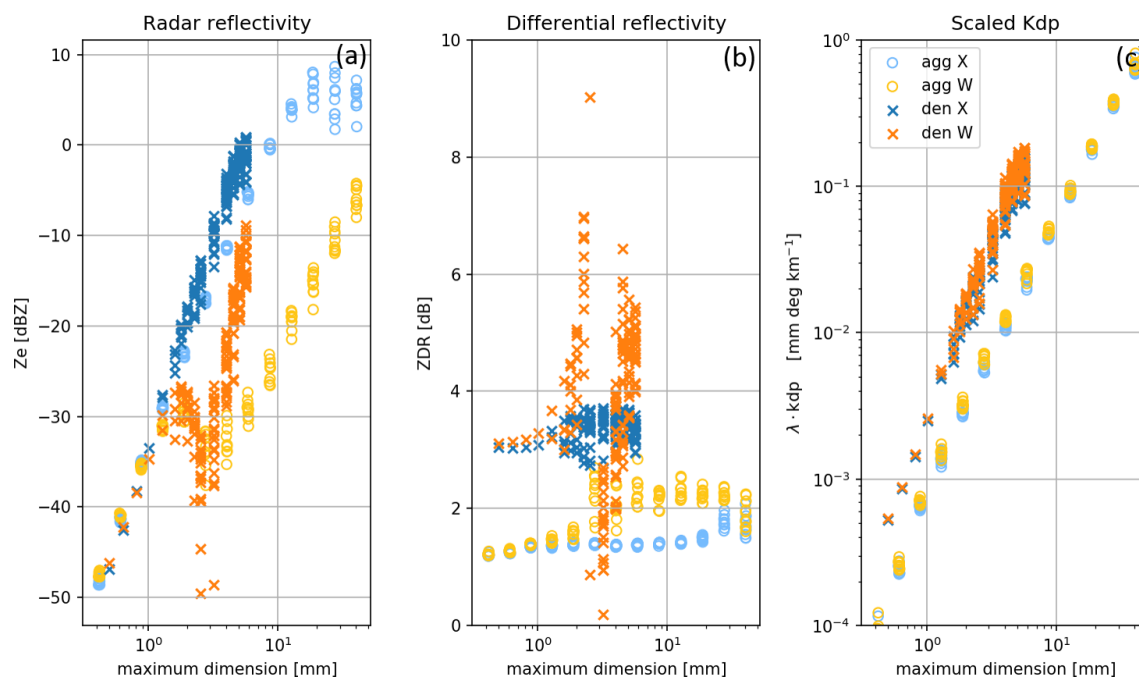


**Figure C1.** Scattering properties of single particles for X- and W-band calculated with dendrites (branched planar crystals, blue and orange crosses) and aggregates of stellar crystals (HD-P1d, light blue and yellow circles) from the scattering database presented in Lu et al. (2016). The calculation of vertically pointing Ze for a single particle at X- and W-band is shown in (a), the ZDR at X- and W-band and  $30^{\circ}$  elevation in (b), and the single particle KDP at X- and W-band in (c). KDP was scaled with the wavelength  $\lambda$  to allow a better comparison of the diameter-dependent behaviour at X- and W-band.

**Code and data availability.** The quality processed level 2 dataset is available on Zenodo under the <https://doi.org/10.5281/zenodo.5025636>, (von Terzi, 2021). The dataset that was used for this statistical analysis (5 min temporal average containing all polarimetric variables and the zenith variables, and variables derived from the Doppler spectra) is available under <https://doi.org/10.5281/zenodo.5025636>, (von Terzi, 2021). Due to the large size, the full level-0 dataset, containing the Doppler spectra of the four radars, is only available on request. The code used to reprocess, classify and plot is available in <https://doi.org/10.5281/zenodo.7050251>, (von Terzi, 2022).

**Author contributions.** Data analysis, post-processing and generation of figures was performed by LvT with contributions from JDN and AM. LvT and SK conceptualised the methods and interpretation. LvT and DO performed the scattering calculations. LvT and SK prepared the paper with contributions from all co-authors.

**Competing interests.** The contact author has declared that none of the authors has any competing interests.

**Disclaimer.** Publisher's note: Copernicus Publications remains neutral with regard to jurisdictional claims in published maps and institutional affiliations.

**Special issue statement.** This article is part of the special issue "Fusion of radar polarimetry and numerical atmospheric modelling towards an improved understanding of cloud and precipitation processes (ACP/AMT/GMD inter-journal SI)". It is not associated with a conference.

**Acknowledgements.** Contributions by José Dias Neto, Davide Ori and Stefan Kneifel were funded by the Deutsche Forschungsgemeinschaft (DFG, German Research Foundation) under grant KN 1112/2-1 and KN 1112/2-2 as part of the Emmy-Noether Group "Optimal combination of Polarimetric and Triple Frequency radar techniques for Improving Microphysical process understanding of cold clouds" (OPTIMIce). The TRIPEX-pol campaign and work provided by Leonie von Terzi have been supported by the DFG Priority Program SPP2115 "Fusion of Radar Polarimetry and Numerical Atmospheric Modelling Towards an Improved Understanding of Cloud and Precipitation Processes" (PROM) under grant PROM-IMPRINT (project number 408011764). We thank the Regional Computing Center of the University of Cologne (RRZK) for providing computing time on the DFG-funded (Funding number: INST 216/512/IFUGG) High Performance Computing (HPC) system CHEOPS as well as their support. Leonie von Terzi and José Dias Neto also acknowledge support from the Graduate School of Geosciences of the University of Cologne. The authors are indebted to staff of the University of Cologne, research center Jülich, and RPG, especially Birger Bohn, Rainer Haseneder-Lind, Pavel Krobot, Bernhard Pospichal, Avdulah Saljihi, and Kai Schmidt for their help with the installation of the W-band radars, and

Kai Schmidt for the preparation of the scanning polarimetric W-band radar for the TRIPEX-pol campaign.

**Financial support.** This research has been supported by the Deutsche Forschungsgemeinschaft (grant nos. 408011764, KN 1112/2-1, and KN 1112/2-2).

**Review statement.** This paper was edited by Matthew Lebsock and reviewed by two anonymous referees.

## References

- Andrić, J., Kumjian, M. R., Zrnić, D. S., Straka, J. M., and Melnikov, V. M.: Polarimetric signatures above the melting layer in winter storms: An observational and modeling study, *J. Appl. Meteorol. Clim.*, 52, 682–700, 2013.
- Bailey, M. P. and Hallett, J.: A comprehensive habit diagram for atmospheric ice crystals: Confirmation from the laboratory, AIRS II, and other field studies, *J. Atmos. Sci.*, 66, 2888–2899, 2009.
- Barrett, A. I., Westbrook, C. D., Nicol, J. C., and Stein, T. H. M.: Rapid ice aggregation process revealed through triple-wavelength Doppler spectrum radar analysis, *Atmos. Chem. Phys.*, 19, 5753–5769, <https://doi.org/10.5194/acp-19-5753-2019>, 2019.
- Bechini, R., Baldini, L., and Chandrasekar, V.: Polarimetric radar observations in the ice region of precipitating clouds at C-band and X-band radar frequencies, *J. Appl. Meteorol. Clim.*, 52, 1147–1169, 2013.
- Brdar, S. and Seifert, A.: McSnow: A Monte-Carlo particle model for riming and aggregation of ice particles in a multidimensional microphysical phase space, *J. Adv. Model. Earth Sy.*, 10, 187–206, 2018.
- Bringi, V. N. and Chandrasekar, V.: *Polarimetric Doppler Weather Radar*, Cambridge University Press, ISBN: 0-521-62384-7, 2001.
- Bringi, V. N., Keenan, T., and Chandrasekar, V.: Correcting C-band radar reflectivity and differential reflectivity data for rain attenuation: A self-consistent method with constraints, *IEEE T. Geosci. Remote*, 39, 1906–1915, 2001.
- Connolly, P. J., Emersic, C., and Field, P. R.: A laboratory investigation into the aggregation efficiency of small ice crystals, *Atmos. Chem. Phys.*, 12, 2055–2076, <https://doi.org/10.5194/acp-12-2055-2012>, 2012.
- DeMott, P. J., Prenni, A. J., Liu, X., Kreidenweis, S. M., Peters, M. D., Twohy, C. H., Richardson, M., Eidhammer, T., and Rogers, D.: Predicting global atmospheric ice nuclei distributions and their impacts on climate, *P. Natl. Acad. Sci. USA*, 107, 11217–11222, 2010.
- Dias Neto, J.: Investigating aggregation in ice and snow clouds using novel combination of triple-frequency cloud radars and radar Doppler spectra, Ph.D. thesis, Universität zu Köln, Cologne, <https://kups.ub.uni-koeln.de/53405/> (last access: 6 September 2022), 2021.
- Dias Neto, J., Kneifel, S., Ori, D., Trömel, S., Handwerker, J., Bohn, B., Hermes, N., Mühlbauer, K., Lenefer, M., and Simmer, C.: The TRIPEX-frequency and Polarimetric radar Experi-

- ment for improving process observations of winter precipitation, *Earth Syst. Sci. Data*, 11, 845–863, <https://doi.org/10.5194/essd-11-845-2019>, 2019.
- Field, P. R.: Bimodal ice spectra in frontal clouds, *Q. J. Roy. Meteor. Soc.*, 126, 379–392, 2000.
- Field, P. R. and Heymsfield, A.: Importance of snow to global precipitation, *Geophys. Res. Lett.*, 42, 9512–9520, 2015.
- Field, P. R., Lawson, R. P., Brown, P. R., Lloyd, G., Westbrook, C., Moisseev, D., Miltenberger, A., Nenes, A., Blyth, A., Choulaton, T., Connolly, P., Buehl, J., Crosier, J., Cui, Z., Dearden, C., DeMott, P., Flossmann, A., Heymsfield, A., Huang, Y., Kalesse, H., Kanji, Z. A., Korolev, A., Kirchgassner, A., Lasher-Trapp, S., Leisner, T., McFarquhar, G., Philips, V., Stith, J., and Sullivan, S.: Secondary ice production: Current state of the science and recommendations for the future, *Meteor. Mon.*, 58, 7–1, 2017.
- Georgakaki, P., Sotiropoulou, G., Vignon, É., Billault-Roux, A.-C., Berne, A., and Nenes, A.: Secondary ice production processes in wintertime alpine mixed-phase clouds, *Atmos. Chem. Phys.*, 22, 1965–1988, <https://doi.org/10.5194/acp-22-1965-2022>, 2022.
- Giangrande, S. E., Toto, T., Bansemer, A., Kumjian, M. R., Mishra, S., and Ryzhkov, A. V.: Insights into riming and aggregation processes as revealed by aircraft, radar, and disdrometer observations for a 27 April 2011 widespread precipitation event, *J. Geophys. Res.-Atmos.*, 121, 5846–5863, 2016.
- Görsdorf, U., Lehmann, V., Bauer-Pfundstein, M., Peters, G., Vavriv, D., Vinogradov, V., and Volkov, V.: A 35-GHz polarimetric Doppler radar for long-term observations of cloud parameters – Description of system and data processing, *J. Atmos. Ocean. Tech.*, 32, 675–690, 2015.
- Grabowski, W. W., Morrison, H., Shima, S.-I., Abade, G. C., Dziekan, P., and Pawlowska, H.: Modeling of cloud microphysics: Can we do better?, *B. Am. Meteorol. Soc.*, 100, 655–672, 2019.
- Griffin, E. M., Schuur, T. J., and Ryzhkov, A. V.: A polarimetric analysis of ice microphysical processes in snow, using quasi-vertical profiles, *J. Appl. Meteorol. Clim.*, 57, 31–50, 2018.
- Griggs, D. and Choulaton, T.: A laboratory study of secondary ice particle production by the fragmentation of rime and vapour-grown ice crystals, *Q. J. Roy. Meteor. Soc.*, 112, 149–163, 1986.
- Hallett, J. and Mossop, S.: Production of secondary ice particles during the riming process, *Nature*, 249, 26–28, 1974.
- Harrington, J. Y., Sulia, K., and Morrison, H.: A method for adaptive habit prediction in bulk microphysical models. Part I: Theoretical development, *J. Atmos. Sci.*, 70, 349–364, 2013.
- Hashino, T. and Tripoli, G.: The Spectral Ice Habit Prediction System (SHIPS). Part I: Model description and simulation of the vapor deposition process, *J. Atmos. Sci.*, 64, 2210–2237, 2007.
- Heymsfield, A. J., Schmitt, C., Bansemer, A., Gettelman, A., Field, P. R., and Liu, C.: Contributions of the liquid and ice phases to global surface precipitation: Observations and global climate modeling, *J. Atmos. Sci.*, 77, 2629–2648, 2020.
- Hildebrand, P. H. and Sekhon, R.: Objective determination of the noise level in Doppler spectra, *J. Appl. Meteorol.*, 13, 808–811, 1974.
- Hobbs, P. V. and Rangno, A. L.: Ice particle concentrations in clouds, *J. Atmos. Sci.*, 42, 2523–2549, 1985.
- Hobbs, P. V. and Rangno, A. L.: Rapid development of high ice particle concentrations in small polar maritime cumuliform clouds, *J. Atmos. Sci.*, 47, 2710–2722, 1990.
- Hobbs, P. V. and Rangno, A. L.: Microstructures of low and middle-level clouds over the Beaufort Sea, *Q. J. Roy. Meteor. Soc.*, 124, 2035–2071, 1998.
- Hogan, R. J., Illingworth, A. J., and Sauvageot, H.: Measuring crystal size in cirrus using 35-and 94-GHz radars, *J. Atmos. Ocean. Tech.*, 17, 27–37, 2000.
- Illingworth, A., Hogan, R., O’connor, E., Bouniol, D., Brooks, M., Delanoë, J., Donovan, D., Eastment, J., Gaussiat, N., Goddard, J. W. F., Haeffelin, M., Klein Baltin, H., Krasnov, O. A., Pelon, J., Pirou, J.-M., Protat, A., Russchenberg, J., Seifert, A., Tompkins, A. M., van Zadelhoff, G.-J., Vinit, F., Willén, U., Wilson, D. R., and Wrench, C. L.: Cloudnet: Continuous evaluation of cloud profiles in seven operational models using ground-based observations, *B. Am. Meteorol. Soc.*, 88, 883–898, 2007.
- Jensen, A. A., Harrington, J. Y., Morrison, H., and Milbrandt, J. A.: Predicting ice shape evolution in a bulk microphysics model, *J. Atmos. Sci.*, 74, 2081–2104, 2017.
- Kalesse, H., Szyrmer, W., Kneifel, S., Kollias, P., and Luke, E.: Fingerprints of a riming event on cloud radar Doppler spectra: observations and modeling, *Atmos. Chem. Phys.*, 16, 2997–3012, <https://doi.org/10.5194/acp-16-2997-2016>, 2016.
- Kanji, Z. A., Ladino, L. A., Wex, H., Boose, Y., Burkert-Kohn, M., Cziczo, D. J., and Krämer, M.: Overview of ice nucleating particles, *Meteor. Mon.*, 58, 1–1, 2017.
- Karrer, M., Seifert, A., Ori, D., and Kneifel, S.: Improving the representation of aggregation in a two-moment microphysical scheme with statistics of multi-frequency Doppler radar observations, *Atmos. Chem. Phys.*, 21, 17133–17166, <https://doi.org/10.5194/acp-21-17133-2021>, 2021.
- Kennedy, P. C. and Rutledge, S. A.: S-band dual-polarization radar observations of winter storms, *J. Appl. Meteorol. Clim.*, 50, 844–858, 2011.
- Kikuchi, K., Kameda, T., Higuchi, K., and Yamashita, A.: A global classification of snow crystals, ice crystals, and solid precipitation based on observations from middle latitudes to polar regions, *Atmos. Res.*, 132, 460–472, 2013.
- Kneifel, S. and Moisseev, D.: Long-term statistics of riming in nonconvective clouds derived from ground-based Doppler cloud radar observations, *J. Atmos. Sci.*, 77, 3495–3508, 2020.
- Kneifel, S., Kulie, M., and Bennartz, R.: A triple-frequency approach to retrieve microphysical snowfall parameters, *J. Geophys. Res.-Atmos.*, 116, D11203, <https://doi.org/10.1029/2010JD015430>, 2011.
- Kneifel, S., von Lerber, A., Tiira, J., Moisseev, D., Kollias, P., and Leinonen, J.: Observed relations between snowfall microphysics and triple-frequency radar measurements, *J. Geophys. Res.-Atmos.*, 120, 6034–6055, 2015.
- Kneifel, S., Kollias, P., Battaglia, A., Leinonen, J., Maahn, M., Kalesse, H., and Tridon, F.: First observations of triple-frequency radar Doppler spectra in snowfall: Interpretation and applications, *Geophys. Res. Lett.*, 43, 2225–2233, 2016.
- Korolev, A.: Limitations of the Wegener–Bergeron–Findeisen mechanism in the evolution of mixed-phase clouds, *J. Atmos. Sci.*, 64, 3372–3375, 2007.
- Korolev, A. and Leisner, T.: Review of experimental studies of secondary ice production, *Atmos. Chem. Phys.*, 20, 11767–11797, <https://doi.org/10.5194/acp-20-11767-2020>, 2020.
- Küchler, N., Kneifel, S., Löhnert, U., Kollias, P., Czekala, H., and Rose, T.: A W-band radar–radiometer system for accurate and



- continuous monitoring of clouds and precipitation, *J. Atmos. Ocean. Tech.*, 34, 2375–2392, 2017.
- Kumjian, M. R.: Principles and Applications of Dual-Polarization Weather Radar. Part I: Description of the Polarimetric Radar Variables., *Journal of Operational Meteorology*, 1, 226–242, <https://doi.org/10.15191/nwajom.2013.0119>, 2013.
- Lamb, D. and Verlinde, J.: Physics and chemistry of clouds, Cambridge University Press, ISBN: 9780511976377, 2011.
- Lawson, R. P., Stewart, R. E., and Angus, L. J.: Observations and numerical simulations of the origin and development of very large snowflakes, *J. Atmos. Sci.*, 55, 3209–3229, 1998.
- Lee, H. and Baik, J.-J.: A comparative study of bin and bulk cloud microphysics schemes in simulating a heavy precipitation case, *Atmosphere*, 9, 475, <https://doi.org/10.1175/JTECH1808.1>, 2018.
- Liao, L., Meneghini, R., Iguchi, T., and Detwiler, A.: Use of dual-wavelength radar for snow parameter estimates, *J. Atmos. Ocean. Tech.*, 22, 1494–1506, 2005.
- Liao, L., Meneghini, R., Tian, L., and Heymsfield, G. M.: Retrieval of snow and rain from combined X-and W-band airborne radar measurements, *IEEE T. Geosci. Remote*, 46, 1514–1524, 2008.
- Li, H. and Moiseev, D.: Melting layer attenuation at Ka-and W-bands as derived from multifrequency radar Doppler spectra observations, *J. Geophys. Res.-Atmos.*, 124, 9520–9533, 2019.
- Löffler-Mang, M. and Joss, J.: An optical disdrometer for measuring size and velocity of hydrometeors, *J. Atmos. Ocean. Techn.*, 17, 130–139, 2000.
- Löhnert, U., Schween, J., Acquistapace, C., Ebell, K., Maahn, M., Barrera-Verdejo, M., Hirsikko, A., Bohn, B., Knaps, A., O’connor, E., Simmer, C., Wahner, A., and Crewell, S.: JOYCE: Jülich observatory for cloud evolution, *B. Am. Meteorol. Soc.*, 96, 1157–1174, 2015.
- Lu, Y., Aydin, K., Clothiaux, E. E., and Verlinde, J.: Retrieving cloud ice water content using millimeter-and centimeter-wavelength radar polarimetric observables, *J. Appl. Meteorol. Clim.*, 54, 596–604, 2015.
- Lu, Y., Jiang, Z., Aydin, K., Verlinde, J., Clothiaux, E. E., and Botta, G.: A polarimetric scattering database for non-spherical ice particles at microwave wavelengths, *Atmos. Meas. Tech.*, 9, 5119–5134, <https://doi.org/10.5194/amt-9-5119-2016>, 2016.
- Mason, S. L., Hogan, R. J., Westbrook, C. D., Kneifel, S., Moiseev, D., and von Terzi, L.: The importance of particle size distribution and internal structure for triple-frequency radar retrievals of the morphology of snow, *Atmos. Meas. Tech.*, 12, 4993–5018, <https://doi.org/10.5194/amt-12-4993-2019>, 2019.
- Matrosov, S. Y.: Radar reflectivity in snowfall, *IEEE T. Geosci. Remote*, 30, 454–461, 1992.
- Matrosov, S. Y., Mace, G. G., Marchand, R., Shupe, M. D., Hallar, A. G., and McCubbin, I. B.: Observations of ice crystal habits with a scanning polarimetric W-band radar at slant linear depolarization ratio mode, *J. Atmos. Ocean. Tech.*, 29, 989–1008, 2012.
- Matrosov, S. Y.: Polarimetric radar variables in snowfall at Ka-and W-band frequency bands: A comparative analysis, *J. Atmos. Ocean. Techn.*, 38, 91–101, 2021.
- Mech, M., Maahn, M., Kneifel, S., Ori, D., Orlandi, E., Kollias, P., Schemann, V., and Crewell, S.: PAMTRA 1.0: the Passive and Active Microwave radiative TRANSfer tool for simulating radiometer and radar measurements of the cloudy atmosphere, *Geosci. Model Dev.*, 13, 4229–4251, <https://doi.org/10.5194/gmd-13-4229-2020>, 2020.
- Moiseev, D., Saltikoff, E., and Leskinen, M.: Dual-polarization weather radar observations of snow growth processes, in: 34th Conference on Radar Meteorology, Williamsburg, VA, 5–9 October 2009, 13B.2, [https://ams.confex.com/ams/34Radar/techprogram/paper\\_156123.htm](https://ams.confex.com/ams/34Radar/techprogram/paper_156123.htm) (last access: 5 September 2020), 2009.
- Moiseev, D. N., Lautaportti, S., Tyynela, J., and Lim, S.: Dual-polarization radar signatures in snowstorms: Role of snowflake aggregation, *J. Geophys. Res.-Atmos.*, 120, 12644–12655, 2015.
- Mróz, K., Battaglia, A., Kneifel, S., von Terzi, L., Karrer, M., and Ori, D.: Linking rain into ice microphysics across the melting layer in stratiform rain: a closure study, *Atmos. Meas. Tech.*, 14, 511–529, <https://doi.org/10.5194/amt-14-511-2021>, 2021.
- Mülmenstädt, J., Sourdeval, O., Delanoë, J., and Quaas, J.: Frequency of occurrence of rain from liquid-, mixed-, and ice-phase clouds derived from A-Train satellite retrievals, *Geophys. Res. Lett.*, 42, 6502–6509, 2015.
- Muth, X., Schneebeli, M., and Berne, A.: A sun-tracking method to improve the pointing accuracy of weather radar, *Atmos. Meas. Tech.*, 5, 547–555, <https://doi.org/10.5194/amt-5-547-2012>, 2012.
- Myagkov, A., Seifert, P., Bauer-Pfundstein, M., and Wandinger, U.: Cloud radar with hybrid mode towards estimation of shape and orientation of ice crystals, *Atmos. Meas. Tech.*, 9, 469–489, <https://doi.org/10.5194/amt-9-469-2016>, 2016a.
- Myagkov, A., Seifert, P., Wandinger, U., Bühl, J., and Engelmann, R.: Relationship between temperature and apparent shape of pristine ice crystals derived from polarimetric cloud radar observations during the ACCEPT campaign, *Atmos. Meas. Tech.*, 9, 3739–3754, <https://doi.org/10.5194/amt-9-3739-2016>, 2016b.
- Myagkov, A., Kneifel, S., and Rose, T.: Evaluation of the reflectivity calibration of W-band radars based on observations in rain, *Atmos. Meas. Tech.*, 13, 5799–5825, <https://doi.org/10.5194/amt-13-5799-2020>, 2020.
- Ori, D., Schemann, V., Karrer, M., Dias Neto, J., von Terzi, L., Seifert, A., and Kneifel, S.: Evaluation of ice particle growth in ICON using statistics of multi-frequency Doppler cloud radar observations, *Q. J. Roy. Meteor. Soc.*, 146, 3830–3849, 2020.
- Ori, D., von Terzi, L., Karrer, M., and Kneifel, S.: snowScatt 1.0: consistent model of microphysical and scattering properties of rimed and unrimed snowflakes based on the self-similar Rayleigh–Gans approximation, *Geosci. Model Dev.*, 14, 1511–1531, <https://doi.org/10.5194/gmd-14-1511-2021>, 2021.
- Oue, M., Kumjian, M. R., Lu, Y., Verlinde, J., Aydin, K., and Clothiaux, E. E.: Linear depolarization ratios of columnar ice crystals in a deep precipitating system over the Arctic observed by zenith-pointing Ka-band Doppler radar, *J. Appl. Meteorol. Clim.*, 54, 1060–1068, 2015.
- Oue, M., Kollias, P., Ryzhkov, A., and Luke, E. P.: Toward exploring the synergy between cloud radar polarimetry and Doppler spectral analysis in deep cold precipitating systems in the Arctic, *J. Geophys. Res.-Atmos.*, 123, 2797–2815, 2018.
- Pfizenmaier, L., Unal, C. M. H., Dufournet, Y., and Russchenberg, H. W. J.: Observing ice particle growth along fall streaks in mixed-phase clouds using spectral polarimetric radar data, *Atmos. Chem. Phys.*, 18, 7843–7862, <https://doi.org/10.5194/acp-18-7843-2018>, 2018.

- Phillips, V. T., Patade, S., Gutierrez, J., and Bansemer, A.: Secondary ice production by fragmentation of freezing drops: Formulation and theory, *J. Atmos. Sci.*, 75, 3031–3070, 2018.
- Rangno, A. L. and Hobbs, P. V.: Ice particles in stratiform clouds in the Arctic and possible mechanisms for the production of high ice concentrations, *J. Geophys. Res.-Atmos.*, 106, 15065–15075, 2001.
- Ryzhkov, A., Zhang, P., Reeves, H., Kumjian, M., Tschallener, T., Trömel, S., and Simmer, C.: Quasi-vertical profiles—A new way to look at polarimetric radar data, *J. Atmos. Ocean. Tech.*, 33, 551–562, 2016.
- Schneebeli, M., Dawes, N., Lehning, M., and Berne, A.: High-resolution vertical profiles of X-band polarimetric radar observables during snowfall in the Swiss Alps, *J. Appl. Meteorol. Clim.*, 52, 378–394, 2013.
- Schrom, R. S. and Kumjian, M. R.: Connecting microphysical processes in Colorado winter storms with vertical profiles of radar observations, *J. Appl. Meteorol. Clim.*, 55, 1771–1787, 2016.
- Schrom, R. S., Kumjian, M. R., and Lu, Y.: Polarimetric radar signatures of dendritic growth zones within Colorado winter storms, *J. Appl. Meteorol. Clim.*, 54, 2365–2388, 2015.
- Schwarzenboeck, A., Shcherbakov, V., Lefevre, R., Gayet, J.-F., Pointin, Y., and Duroure, C.: Indications for stellar-crystal fragmentation in Arctic clouds, *Atmos. Res.*, 92, 220–228, 2009.
- Shupe, M. D., Kollias, P., Matrosov, S. Y., and Schneider, T. L.: Deriving mixed-phase cloud properties from Doppler radar spectra, *J. Atmos. Ocean. Tech.*, 21, 660–670, 2004.
- Spek, A., Unal, C., Moiseev, D., Russchenberg, H., Chandrasekar, V., and Dufournet, Y.: A new technique to categorize and retrieve the microphysical properties of ice particles above the melting layer using radar dual-polarization spectral analysis, *J. Atmos. Ocean. Tech.*, 25, 482–497, 2008.
- Sulia, K. J. and Kumjian, M. R.: Simulated polarimetric fields of ice vapor growth using the adaptive habit model. Part I: Large-eddy simulations, *Mon. Weather Rev.*, 145, 2281–2302, 2017.
- Takahashi, T.: Influence of liquid water content and temperature on the form and growth of branched planar snow crystals in a cloud, *J. Atmos. Sci.*, 71, 4127–4142, 2014.
- Takahashi, T., Endoh, T., Wakahama, G., and Fukuta, N.: Vapor diffusional growth of free-falling snow crystals between  $-3$  and  $-23^{\circ}\text{C}$ , *J. Meteorol. Soc. Jpn.*, 69, 15–30, 1991.
- Takahashi, T., Nagao, Y., and Kushiya, Y.: Possible high ice particle production during graupel–graupel collisions, *J. Atmos. Sci.*, 52, 4523–4527, 1995.
- Thompson, E. J., Rutledge, S. A., Dolan, B., Chandrasekar, V., and Cheong, B. L.: A dual-polarization radar hydrometeor classification algorithm for winter precipitation, *J. Atmos. Ocean. Tech.*, 31, 1457–1481, 2014.
- Trapp, R. J., Schultz, D. M., Ryzhkov, A. V., and Holle, R. L.: Multiscale structure and evolution of an Oklahoma winter precipitation event, *Mon. Weather Rev.*, 129, 486–501, 2001.
- Tridon, F. and Battaglia, A.: Dual-frequency radar Doppler spectral retrieval of rain drop size distributions and entangled dynamics variables, *J. Geophys. Res.-Atmos.*, 120, 5585–5601, 2015.
- Tridon, F., Battaglia, A., and Kneifel, S.: Estimating total attenuation using Rayleigh targets at cloud top: applications in multilayer and mixed-phase clouds observed by ground-based multifrequency radars, *Atmos. Meas. Tech.*, 13, 5065–5085, <https://doi.org/10.5194/amt-13-5065-2020>, 2020.
- Trömel, S., Ryzhkov, A. V., Hickman, B., Mühlbauer, K., and Simmer, C.: Polarimetric radar variables in the layers of melting and dendritic growth at X band – Implications for a nowcasting strategy in stratiform rain, *J. Appl. Meteorol. Clim.*, 58, 2497–2522, 2019.
- Vardiman, L.: The generation of secondary ice particles in clouds by crystal–crystal collision, *J. Atmos. Sci.*, 35, 2168–2180, 1978.
- von Terzi, L.: TRIPEX-pol level-2 data (Version LV2), Zenodo [dataset], <https://doi.org/10.5281/zenodo.5025636>, 2021.
- von Terzi, L.: OPTIMICE-team/DGL-analysis-ACP-2022: Analysis of the dendritic growth layer for von Terzi et al. ACP, 2022 (v1.0), Zenodo [code], <https://doi.org/10.5281/zenodo.7050251>, 2022.
- Zawadzki, I.: Observations of snow growth by a vertically pointing radar, in: 36th Conference on Radar Meteorology, Breckenridge Colorado, 16–20 September 2013, 11A.6, <https://ams.confex.com/ams/36Radar/webprogram/Paper229071.html> (last access: 9 September 2022) 2013.
- Zawadzki, I., Fabry, F., and Szyrmer, W.: Observations of supercooled water and secondary ice generation by a vertically pointing X-band Doppler radar, *Atmos. Res.*, 59, 343–359, 2001.
- Zhu, Z., Kollias, P., Yang, F., and Luke, E.: On the Estimation of In-Cloud Vertical Air Motion Using Radar Doppler Spectra, *Geophys. Res. Lett.*, 48, e2020GL090682, <https://doi.org/10.1029/2020GL090682>, 2021.



## 4.1 THE MDV SLOW-DOWN: AN UPDRAFT IN THE DGL?

In von Terzi et al., 2022 as well as several previous studies, a slow-down in MDV and spectral edges was found in the vicinity of  $-15^{\circ}\text{C}$ . It is unclear whether this slow-down is caused by large-scale lifting, the growth of a new mode of ice crystals that have slower fall velocities and thus shift the MDV towards smaller values or the release of latent heat and concurrent buoyancy during enhanced depositional growth of ice crystals at  $-15^{\circ}\text{C}$ . The analysis in von Terzi et al., 2022 indicated that the slow-down is a combination of the growth of a new particle mode and an updraft. The updraft velocity was roughly estimated to be  $0.1\text{ m s}^{-1}$ . However, this reduction was found to be not statistically significant due to the large inter-profile variability. Further, the origin of a possible updraft is unknown. While the hypothesis of latent heat release and concurrent buoyancy is consistent with the enhanced plate-like growth revealed by the polarimetric radar observations, it is unclear if this hypothesis is valid.

The  $v_D$  measured by vertically-pointing radars is a super-position of the hydrometeor fall velocity and the vertical wind velocity. Therefore, if the fall velocity of the hydrometeors is known, the vertical wind velocity can be obtained. As the MDV is an integrated variable, it combines the fall velocities of many hydrometeors, for which the exact shape and size and therefore fall velocities is unknown. In Doppler spectra the particles are binned by their fall velocities, separating different hydrometeor species that have different fall velocities. The faster falling aggregates occupy different Doppler bins than the slow falling ice crystals or super-cooled liquid water droplets. Previous studies have shown that super-cooled liquid water droplets can be assumed to have a negligible fall velocity (e.g. D. and M., 2004). Therefore, super-cooled liquid water droplets can be used as a tracer for vertical wind velocity. Unfortunately, during the TRIPEX-pol campaign a super-cooled liquid water peak was observed only rarely in the vicinity of  $-15^{\circ}\text{C}$ . As was described in von Terzi et al., 2022, the upward air motion affects all hydrometeors similarly. Therefore, an updraft should be shifting the fast and slow falling spectral edge towards smaller fall velocities (see also Figure 2.6). Statistically, the slow-down can then be investigated by either looking at the slow-down of the median of the spectral edges, as was done in von Terzi et al., 2022, or by estimating the slow down directly from each Doppler spectrum in the dataset and estimating the median from that. The updraft was calculated as follows from each Doppler spectra:

1. The spectral edges were estimated as described in von Terzi et al., 2022. They were then smoothed by calculating a rolling mean over 10 range gates. This corresponds to 360 m. (Figure 4.1 (1))
2. In general, the particles are increasing their fall velocity towards the ground, as they are growing via aggregation or riming. Therefore, the derivative of the spectral edge velocity is expected to be positive. Unfortunately, the rate of increase of fall velocity of particles at the fast falling edge is unknown. The fast edge velocity is only expected to be slowed down in case of an updraft, or if the particles are reducing their size through e.g. sublimation. Further, if an updraft is present, both the fast and slow falling edge should be slowed down. To estimate the slow down due to an updraft, the derivative over the range was calculated for each spectral edge. In case of an updraft, both the fast and slow falling edge have a negative derivative at a certain range gate. If only the fast edge has a negative derivative,

while the slow edge stays constant or has a positive derivative, it is assumed that turbulence is broadening the spectrum. If only the slow edge shows a slow down (so negative derivative), it is assumed that a secondary mode is present (Figure 4.1 (2), see also explanation in von Terzi et al., 2022 and Section 2.2.3)

3. The updraft is then the integral in regions of negative derivative. It is integrated from the point where the derivative first crosses zero down to the current range. This way only the strength of the updraft in the upper region of the slowed down spectrum can be calculated. Once the spectral edge increases its fall velocity again, the derivative becomes positive and the updraft in this region can not be detected further. Therefore, only the updraft velocities from the top of the updraft down to the top of the updraft velocity can be detected (Figure 4.1 (3)).

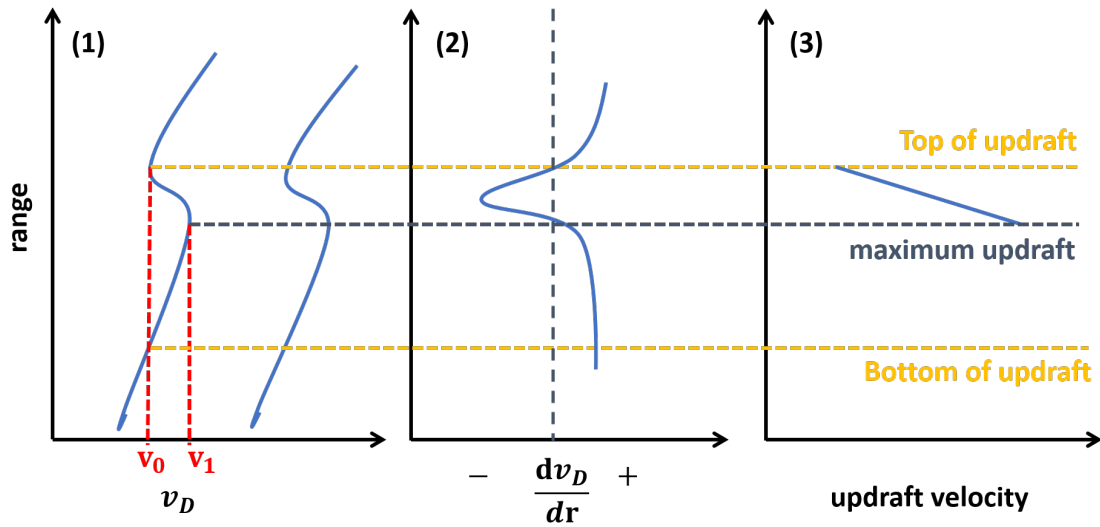


Figure 4.1: Schematic illustrating how the updraft was calculated from the fast spectral edge. (1) shows the first step in calculating the updraft. Drawn is a schematic of spectral edges. The fast falling edge is the left blue curve, the slow falling edge the right blue curve. The bottom and top of the updraft are indicated in yellow. The  $v_D$  that the fast falling particles have before they fall into the region of the updraft is marked with  $v_0$ . The velocity where the updraft is strongest, hence slowing down the particles the strongest is marked with  $v_1$  and the horizontal grey line. (2) shows the second step in the calculation, where the range derivative ( $\frac{dv}{dr}$ ) of the fast and slow spectral edges are calculated. For simplicity, here only the derivative of the fast edge is shown schematically. If both the fast and the slow edge have a negative derivative, an updraft is detected. The updraft is then calculated in the third step by integrating the derivative from the top of the updraft to the current range. As a result, the blue curve in (3) is obtained.

In Figure 4.1 the calculation of the updraft is shown schematically. Unfortunately, the derived updraft velocity could not be tested against other techniques to estimate the vertical wind velocity. In most cases, if super-cooled liquid water droplets were present, it was usually located in regions slightly above where the updraft was detected. Therefore, the velocity of the droplets could not be used to verify the retrieved updraft velocities. Further, the derived updraft is expected to be a lower estimate of the real updraft velocities, as the particles on the fast falling edge are expected to continuously

grow, and therefore also increase their fall velocity towards the ground. As the updraft strength is estimated by integrating from the highest range gate where the beginning of the updraft was detected to the current range gate, the increase in fall velocity is not considered. An example of a detected updraft is provided in Figure 4.2. The fast and slow spectral edge (Figure 4.2 (1)) are found to be first slowed down at a height of 4700 m. Towards the ground, the slow down increases, reaching a maximum at 4100 m. At lower altitudes, the velocity at both spectral edges starts to increase again. The maximum updraft estimated at 4100 m is  $1.0 \text{ m s}^{-1}$ .

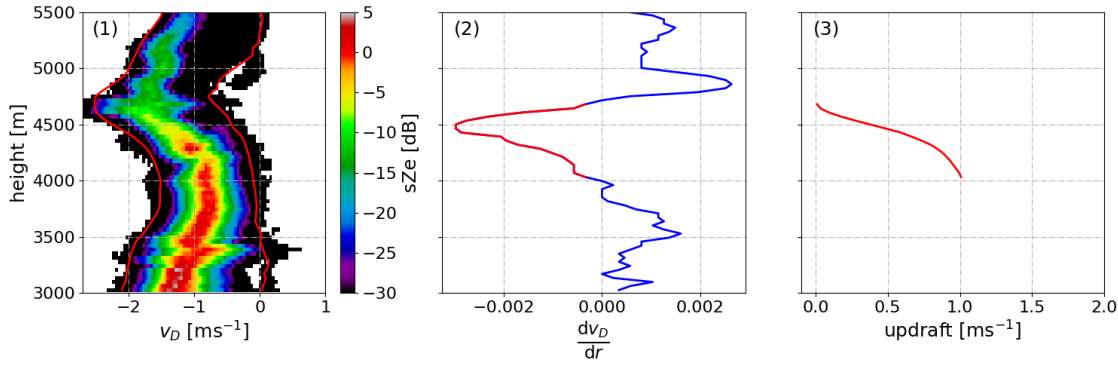


Figure 4.2: Example of a detected updraft obtained on 19<sup>th</sup> December 2018, 02 : 47 : 24 UTC. (1) shows an example of spectral Ze. The red lines in panel (1) indicate the spectral edges. Panel (2) shows the range derivative of the fast spectral edge. Red indicates the region where both the fast and slow falling edge have negative derivatives. In this region, an updraft is detected. Panel (3) shows the calculated updraft.

The classification of the updraft into  $DWR_{K_{aW}}$ -classes revealed that the median updraft of the largest  $DWR_{K_{aW}}$  class first starts to increase at  $-18^\circ \text{C}$ , reaching a maximum at  $-15^\circ \text{C}$  of  $0.8 \text{ m s}^{-1}$  (see Figure 4.3). At  $-15^\circ \text{C}$  also the 25<sup>th</sup> and 75<sup>th</sup> percentiles show an updraft. At temperatures warmer than  $-15^\circ \text{C}$ , the updraft strength reduces, reaching values of  $0.05 \text{ m s}^{-1}$ . The updraft strength of  $DWR_{K_{aW}}$  class 1 and 2 does not have a maximum at  $-15^\circ \text{C}$ . Rather,  $DWR_{K_{aW}}$  class 1 increases from  $-15$  to  $-10^\circ \text{C}$  from  $0.04$  to  $0.075 \text{ m s}^{-1}$ . The updraft strength of  $DWR_{K_{aW}}$  class 2 does not increase within the DGL. At temperatures warmer than  $-5^\circ \text{C}$ , the updraft strength of all  $DWR_{K_{aW}}$  classes increases, reaching a maximum at the melting layer of  $0.125$  to  $0.14 \text{ m s}^{-1}$ .

The maximum updraft velocity obtained with this method is similar to the one obtained in von Terzi et al., 2022, where an updraft of approximately  $0.1 \text{ m s}^{-1}$  was estimated. Both methods derive the updraft from the spectral edges, so a similar updraft velocity was expected. As in von Terzi et al., 2022 it was found that also the updraft found with this analysis is not statistically significant. Therefore, since the results from both methods is similar, this more complicated analysis of the updraft was not included in von Terzi et al., 2022. However, for single case studies where a clear updraft is visible in the Doppler spectra, this method might provide a tool to provide a lower estimate of the updraft velocity. Further analyses are required, focusing on the origin of the updraft and its strength. Modelling studies can help estimate the latent heat released during depositional growth at  $-15^\circ \text{C}$  and the concurrent buoyancy. For example, Lagrangian super-particle models with habit prediction and implemented fragmentation and other

SIP can predict the number of plate-like particles generated through SIP in the DGL, their depositional growth and concurrent latent heat release.

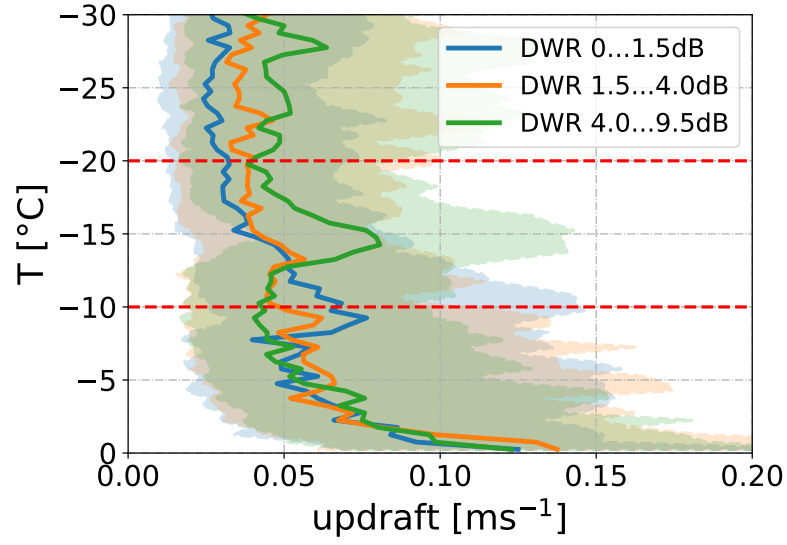


Figure 4.3: Updraft calculated from each spectrum classified into  $DWR_{K_{aw}}$ -classes. Here, positive velocities indicate upward motions.

## INVESTIGATING ICE MICROPHYSICAL PROCESSES IN THE DGL WITH MCSNOW

The statistical analysis of radar observations in [Chapter 4](#) in the [DGL](#) revealed a maximum in  $sZDR_{max}$  at  $-15^{\circ}\text{C}$ . It was hypothesised that this maximum is caused by the depositional growth of plate-like particles in the vicinity of  $-15^{\circ}\text{C}$ . The maximum in  $sZDR_{max}$  was found to frequently occur alongside a secondary, slow-falling spectral mode. Further, a continuous increase of  $KDP$  within the [DGL](#) was observed, indicating an increase in concentration of ice particles. This increase seemed to be correlated to enhanced aggregation in the [DGL](#). It is unclear, where the plate-like particles responsible for these radar signatures are originating from and how the ice particle concentration can increase even though an increase in aggregation should reduce the total particle concentration. Previous studies have suggested that the increase in  $ZDR$  and  $KDP$  in the [DGL](#) is related to small particles sedimenting into the [DGL](#), which are growing into plate-like particles in the vicinity of  $-15^{\circ}\text{C}$  (e.g. Griffin et al., 2018). Other studies have concluded that new ice particles might be growing at  $-15^{\circ}\text{C}$ . These particles might stem from primary nucleation, since the updraft found at  $-15^{\circ}\text{C}$  might enhance  $RH_i$  and therefore activate new  $INP$  or from secondary ice processes (Bechini et al., 2013; Kennedy and Rutledge, 2011; Moisseev et al., 2015, 2009; Oue et al., 2018; Schrom and Kumjian, 2016; Zawadzki et al., 2001, among others). Since the enhanced  $KDP$  seems to be correlated to enhanced aggregation, it was hypothesised in [Chapter 4](#) that the plate-like particles are generated through fragmentation during the collisions of aggregates. In-situ and laboratory studies have suggested that dendritic particles, growing at temperatures close to  $-15^{\circ}\text{C}$  have a fragile structure and are thus subject to collisional fragmentation (Griggs and Choulaton, 1986; Hobbs and Rangno, 1985, 1990, 1998; Schwarzenboeck et al., 2009; Takahashi et al., 1995; Vardiman, 1978).

Radars are not able to directly observe the different IMP hypothesised to happen in the [DGL](#). Only the effect of these processes on certain aspects of the particle distribution can be observed. For example, the presence of asymmetric particles increases  $ZDR$ , however the formation of these particles can not be observed. Therefore, the provided radar observations do not allow to close the questions regarding the origin of plate-like particles within the [DGL](#) and their connection to enhanced aggregation. The newly developed Monte-Carlo Lagrangian particle model ([McSnow](#)) (Brdar and Seifert, 2018, see [Section 3.2](#)) can be used to further evaluate the particle growth signatures found in the statistical analysis of the [DGL](#) provided in [Chapter 4](#). [McSnow](#) explicitly predicts the particle evolution by applying the different growth equations directly to the super-particles, enabling a detailed investigation of depositional growth of particles and aggregation within the [DGL](#), as well as their interaction. [McSnow](#) further allows to track the growth history of particles, enabling a detailed view of the [IMP](#) that the simulated particles experienced. It further provides detailed information about the simulated hydrometeors (e.g.  $m$ , size, shape, fall velocity), enabling straightforward forward simulations without additional and often inconsistent assumptions of particle properties. In the following sections, three hypothesis are investigated in more detail:

1. Small particles nucleated at lower temperatures are sedimenting into the DGL. Due to enhanced depositional growth in the vicinity of  $-15^{\circ}\text{C}$  they grow into plate-like particles. This causes a maximum in  $sZDR_{\text{max}}$  and KDP within the DGL and a secondary spectral mode (Section 5.1 and Section 5.2).
2. The updraft found at  $-15^{\circ}\text{C}$  enhances  $RH_i$  locally and leads to the activation of INP. The newly formed ice particles are then growing into plate-like particles, hence enhancing KDP and  $sZDR_{\text{max}}$  and forming a secondary spectral mode (Section 5.3).
3. The collisions of ice particles during aggregation leads to fragmentation of fragile parts of aggregates or other ice particles. Since these fragments are smaller than the main particles, a secondary, slow falling spectral mode emerges. The fragments have a plate-like aspect ratio, hence enhancing  $sZDR_{\text{max}}$ . An increase in number concentration of these fragments leads to an increase in KDP and might even enhance aggregation further (Section 5.3).

The conducted McSnow simulations are forward simulated into the radar space. The forward simulations allow to compare simulations and observations and evaluate the influence of depositional growth, aggregation and fragmentation on the radar observables. The forward simulations are conducted with McRadar. McRadar, as well as the scattering approximations used are described in detail in Section 3.3.

## 5.1 HABIT GROWTH DEPENDING ON THE NUCLEATION TEMPERATURE

Previous studies have explained the increase in ZDR and KDP at  $-15^{\circ}\text{C}$  with small particles sedimenting into the DGL from above and then growing into a plate-like shape, therefore increasing ZDR (e.g. Griffin et al., 2018). Similarly, other studies have found correlations between the cloud top temperature (CTT) and polarimetric radar features (Griffin et al., 2018; Oue et al., 2018; Trömel et al., 2019). The dependencies of polarimetric and multi-frequency radar signatures on CTT found in Chapter 4 are much weaker than when sorting profiles with respect to the DWR in the DGL. Only the number concentration of asymmetric particles (revealed by KDP) seems to be slightly larger for colder CTT, and therefore deeper cloud systems. It was argued that by sorting the profiles with respect to their CTT, they are also sorted into different cloud regimes. Clouds with colder cloud top are likely deeper systems which might simply favour particle growth by providing for example larger super-saturations with respect to ice also in the DGL (von Terzi et al., 2022).

To test the first hypothesis, which states "particles that sediment from above into the DGL grow into plate-like particles in the vicinity of  $-15^{\circ}\text{C}$  and explain the enhanced KDP and ZDR", the particle evolution through depositional growth was simulated McSnow. The simulation setup is described in detail in Section 3.2 and Figure 3.7. In short: starting at a height of 4800 m ( $-31^{\circ}\text{C}$ ), every 10 m (every  $0.06^{\circ}\text{C}$ ) towards the ground, an ice particle with a diameter of  $10\text{ }\mu\text{m}$  is initialised. While sedimenting, the particles are grown through deposition at 101%, 105%, 110%, 115% and 120%  $RH_i$ . The growth of the particles into plate-like particles within the DGL is analysed by looking at the  $D_{\text{max}}$ ,  $m$  (m),  $\rho$  and aspect ratio  $\phi$  that a particle has at  $-10^{\circ}\text{C}$  in dependency of its initialisation temperature (see Figure 5.1). Looking first at  $\phi$  in Figure 5.1c, one



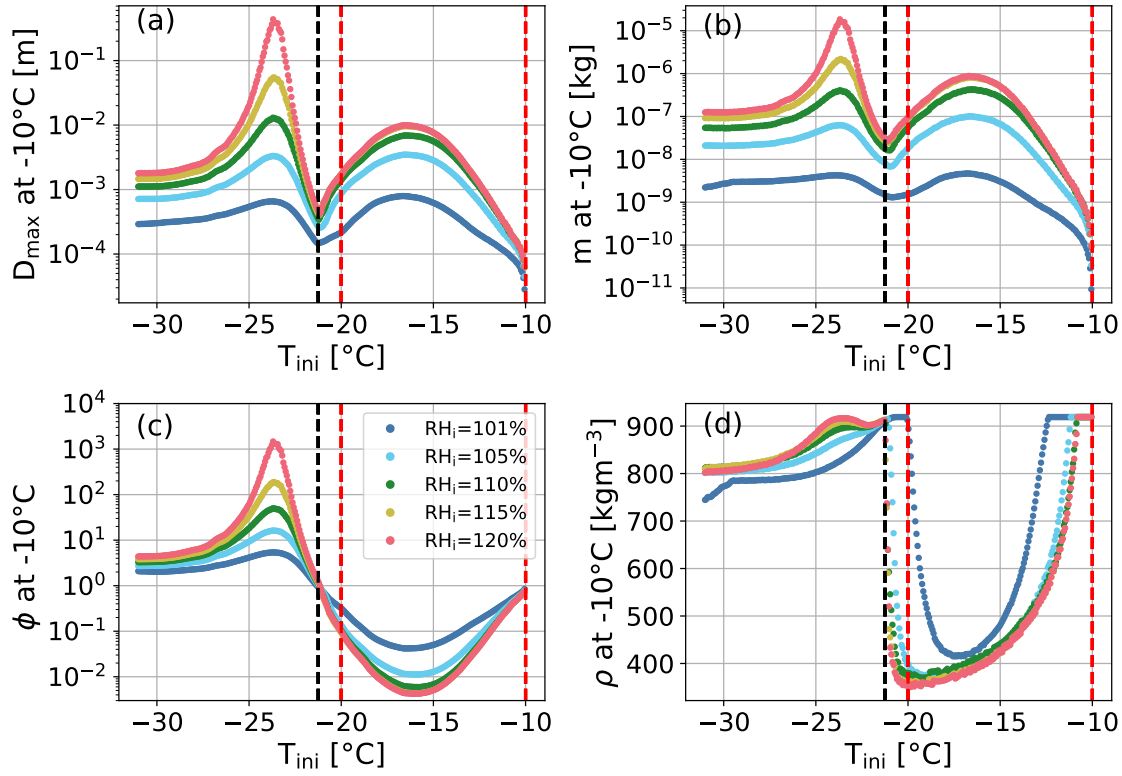


Figure 5.1: Particle size (a),  $m$  (b), aspect ratio (c) and density (d) at  $-10^{\circ}\text{C}$  depending on the temperature where the particle was nucleated. The particles were grown at 1%, 5%, 10%, 15% and 20% super-saturations with respect to ice. The red dashed lines indicate the temperature region of the DGL. For better visibility, the black dashed line separates the temperature regime where particles need to be nucleated to develop a columnar (colder than  $-21^{\circ}\text{C}$ ) or plate-like (warmer than  $-21^{\circ}\text{C}$ ) habit in the DGL.

can see that particles nucleated at temperatures colder than  $-21^{\circ}\text{C}$  develop a distinct column-like habit ( $\phi$  larger than 1). Particles nucleated at this temperature are unable to grow into plate-like particles, independent of the  $\text{RH}_i$ . Only when a particle is nucleated at temperatures between  $-21$  and  $-10^{\circ}\text{C}$ , an  $\phi$  smaller than 1 is reached. This is in agreement with the modelling study conducted in Chen and Lamb, 1994. Particles nucleated between  $-17$  and  $-15^{\circ}\text{C}$  experience the strongest plate-like growth and develop the smallest  $\phi$ . These particles also have the largest  $m$  (Figure 5.1b) and  $D_{\max}$  (Figure 5.1a) compared to particles nucleated within the DGL. As described in Section 3.2, branching reduces  $\rho$  of plate-like particles. The  $\rho$  is reduced most when the particle is nucleated between  $-21$  and  $-15^{\circ}\text{C}$  (see Figure 5.1d). These particles are sedimenting through the region between  $-16$  and  $-13^{\circ}\text{C}$ , where the most branching is expected.

In general, with larger  $\text{RH}_i$ , the particles gain more  $m$  and grow to larger  $D_{\max}$ , both inside and outside of the DGL. The largest  $D_{\max}$  and  $m$ es are reached for particles nucleated at  $-16^{\circ}\text{C}$  and  $-23^{\circ}\text{C}$  at a saturation of 120%. These particles reach  $D_{\max}$  of  $0.01\text{ m}$  ( $0.5\text{ m}$ ) and  $m$ es of  $10^{-6}\text{ kg}$  ( $2 \cdot 10^{-6}\text{ kg}$ ). At a saturation of 101%, particles reach  $D_{\max}$  of  $9 \cdot 10^{-4}\text{ m}$  ( $5 \cdot 10^{-4}\text{ m}$ ) and  $m$ es of  $4 \cdot 10^{-9}\text{ kg}$  ( $4 \cdot 10^{-9}\text{ kg}$ ) when nucleated at  $-16^{\circ}\text{C}$  ( $-23^{\circ}\text{C}$ ). Similarly,  $\phi$  is getting smaller (larger) for plate-like (column-like) particles with larger  $\text{RH}_i$ . The primary habit (which influences the development of  $\phi$ ) only depends on temperature and not the super-saturation (see Section 2.1.2.1). Therefore, the temperature at which the most extreme  $\phi$  are reached do not depend on the  $\text{RH}_i$ . The most extreme  $\phi$  of  $4 \cdot 10^{-3}$  ( $2 \cdot 10^3$ ) are reached for particles nucleated at  $-16^{\circ}\text{C}$  ( $-23^{\circ}\text{C}$ ) at 120% saturation. For the same nucleation temperature, particles reach  $\phi$  of  $6 \cdot 10^{-2}$  (5) at a saturation of 101%. The secondary habit of ice particles is not only dependent on temperature but also on the ambient super-saturation. At 101%, particles develop the smallest  $\rho$  of  $400\text{ kg m}^{-3}$  when nucleated at  $-18^{\circ}\text{C}$ . For higher  $\text{RH}_i$ , the particles nucleated between  $-21$  and  $-20^{\circ}\text{C}$  develop the smallest  $\rho$ . The smallest  $\rho$  of approximately  $350\text{ kg m}^{-3}$  is reached at 120% saturation and a nucleation temperature of  $-21^{\circ}\text{C}$ .

The  $D_{\max}$ ,  $m$  and  $\phi$  reached by particles nucleated at  $-23^{\circ}\text{C}$  at a  $\text{RH}_i$  of 120% are unrealistically large. This behaviour was also observed by Shima et al., 2020. To avoid this behaviour, particles are only allowed to develop a habit at  $D_{\max} > 10\text{ }\mu\text{m}$  (Section 3.2). However, at these large  $\text{RH}_i$ , such unrealistically large  $D_{\max}$  can still be observed. During the TRIPEX-scan campaign,  $\text{RH}_i$  was found to be around 105% in temperature regions between  $-5$  and  $-30^{\circ}\text{C}$  (see Appendix A).

In-situ as well as laboratory studies have found that no specific habit can be associated to temperatures colder than  $-20^{\circ}\text{C}$ . Rather, mixtures of plates, columns and poly-crystals have been found in Bailey and Hallett, 2009; Connolly et al., 2012, and references therein (see also Figure 2.4 and Section 3.2.1). It is therefore difficult to develop an inherent growth function, which describes the primary habit of particles in this temperature regime. The inherent growth function implemented in MCSNOW assumes columnar growth at temperatures colder than  $-20^{\circ}\text{C}$  (see Figure 3.6). However, this does not capture the variety of particles there, making also the investigation of particles sedimenting into the DGL difficult.

To summarise, independent of the  $\text{RH}_i$ , particles nucleated between  $-17$  and  $-15^{\circ}\text{C}$  are growing most efficiently into plate-like particles, reaching  $\phi$  as small as  $4 \cdot 10^{-3}$  when grown at  $\text{RH}_i = 120\%$ . Particles that are nucleated at temperatures colder than  $-21^{\circ}\text{C}$  are not able to develop a plate-like habit. Therefore, it is likely that the particles responsible

TRIPEX-scan:  
successor campaign of  
the TRIPEX-pol  
campaign, which took  
place between  
December 2021 and  
February 2022 at  
JOYCE-CF.

for the  $sZDR_{max}$  and  $KDP$  increase in the DGL are nucleated locally and this signal is not produced by particles sedimenting into the DGL from colder temperatures. This is only valid if the particles growing at temperatures colder than  $-20^\circ\text{C}$  have not grown plate-like, but rather developed a columnar shape. Further, it can not be excluded that particles might sediment through a layer that is sub-saturated with respect to ice, thus sublimating and entering the DGL with small  $D_{max}$ , thus enabling plate-like growth.

## 5.2 FORWARD SIMULATIONS OF PARTICLE DEPOSITIONAL GROWTH IN THE DGL

ZDR is increasing with an increase in aspect ratio, up to a certain saturation value (Hogan et al., 2000; Myagkov et al., 2016). However, ZDR is decreasing with decreasing  $\rho$ . Since in the DGL, the plate-like particles first increase their aspect ratio and then branching sets in and reduces the  $\rho$ , both processes need to be considered to predict the evolution of ZDR in the DGL. It is therefore difficult to retrieve the particle properties based only on observations of ZDR. Vice versa, when the particle properties are known, ZDR can be calculated for these particles. By forward simulating McSnow simulation output, the evolution of ZDR in the DGL can be better understood and the competing effects of increase in aspect ratio and decrease in  $\rho$  can be quantified. Further, different hypothesis explaining the increase of ZDR and KDP in the DGL can be tested. As was observed in von Terzi et al., 2022,  $sZDR_{max}$  increases in the DGL, reaching a maximum at  $-14^\circ\text{C}$  of 1.5 dB. Further, KDP is found to continuously increase within the DGL, reaching a maximum at  $-12^\circ\text{C}$  of  $0.7^\circ\text{km}^{-1}$ . It was hypothesised that the increase in  $sZDR_{max}$  exhibits the increase in  $\phi$  and  $D_{max}$  of plate-like particles, which are growing in the DGL through depositional growth. It is unclear where and how these particles are originating. One hypothesis stated in von Terzi et al., 2022 was the new nucleation of ice particles through SIP. Another explanation would be the seeding of small, plate-like particles into the DGL, which grow efficiently by deposition at  $-15^\circ\text{C}$  and therefore increase  $sZDR_{max}$ . In Section 5.1 it has already been shown that for particles to develop a plate-like shape they most likely need to be initiated within the DGL. The plate-like shape of these particles would indicate an increase of ZDR within the DGL. However, the particles also experience intensive branching, reducing the  $\rho$  to as small as  $350\text{ kg m}^{-3}$ . Forward simulations will reveal which effect dominates ZDR and how the ZDR signal looks like for the 350 particles from the experiment in Section 5.1. For the forward simulations the McSnow simulation with  $RH_i = 105\%$  was chosen (see Section 5.1), since an analysis of the  $RH_i$  of radiosonde launches during the TRIPEX-scan campaign revealed that there is a median  $RH_i$  of approximately 105% in clouds at all temperature levels (see Appendix A). The particle properties were forward simulated using McRadar and the T-matrix method for simulating their scattering properties (see Section 3.3 for a detailed description).

### 5.2.1 Description of particle evolution

The evolution of  $D_{max}$ ,  $m$ ,  $\phi$  and  $\rho$  are illustrated in Figure 5.2. All particles are nucleated as solid ice spheres with  $\phi = 1$ ,  $D_{max} = 10\text{ }\mu\text{m}$ ,  $m = 4.81 \cdot 10^{-13}\text{ kg}$  and  $\rho = 918\text{ kg m}^{-3}$ . The description of the evolution of the physical properties will focus on four particles, nucleated at  $-30.5^\circ\text{C}$  (particle A),  $-25^\circ\text{C}$  (particle B),  $-20^\circ\text{C}$  (particle C) and  $-16^\circ\text{C}$  (particle D), as they represent the main changes in  $D_{max}$ ,  $m$ ,  $\phi$  and  $\rho$ .

Particles A and B were nucleated at temperatures colder than  $-21^{\circ}\text{C}$ , therefore developing a columnar shape. As expected, particles A and B increase their  $D_{\text{max}}$ ,  $m$  and  $\phi$  significantly above the DGL to 0.6 mm and 1.5 mm, reaching a  $m$  of  $7 \cdot 10^{-9}$  kg and  $10^{-8}$  kg and  $\phi$  of 2 and 10 respectively. While  $m$  is continuously increasing within the DGL,  $D_{\text{max}}$  and  $\phi$  are found to stay constant. Within the DGL, the depositional growth happens preferred at the prism face and not the basal face of the crystal, keeping  $\phi$  constant while the c-axis is larger than the a-axis. Since the c-axis is found to remain larger and  $D_{\text{max}}$  is defined by the size of the larger axis, a growth on the prism face of the particle does not increase  $D_{\text{max}}$ . Only in the second columnar growth regime between  $-10$  and  $-5^{\circ}\text{C}$ ,  $D_{\text{max}}$  increases again, finally reaching 1.1 and 5 mm at  $0^{\circ}\text{C}$  with  $\phi$  of 3.5 and 20 respectively. As expected, hollowing reduces  $\rho$  to a minimum of  $578 \text{ kg m}^{-3}$  and  $500 \text{ kg m}^{-3}$  at  $-23^{\circ}\text{C}$  for particles A and B respectively. Within the DGL,  $\rho$  is found to continuously increase, reaching a maximum of  $813 \text{ kg m}^{-3}$  and  $839 \text{ kg m}^{-3}$  at  $-9^{\circ}\text{C}$ .

Particles C and D were nucleated within the DGL, they therefore develop a plate-like habit and increase their  $m$  along the prism face. As expected,  $D_{\text{max}}$ ,  $m$  and  $\phi$  of particles C and D increase (decrease in case of  $\phi$ ) strongly within the DGL. At  $-10^{\circ}\text{C}$ ,  $D_{\text{max}}$  of 1 and 3.5 mm,  $m$  of  $2 \cdot 10^{-8}$  and  $10^{-7}$  kg and  $\phi$  of 0.11 and 0.01 are reached. Similar as for the columnar particles in the DGL,  $D_{\text{max}}$  and  $\phi$  do not increase (decrease) further at temperatures warmer than  $-10^{\circ}\text{C}$ . Only  $m$  of particle D continuous to increase to  $4 \cdot 10^{-7}$  kg at  $0^{\circ}\text{C}$ . As expected, the strong branching at temperatures close to  $-15^{\circ}\text{C}$  reduces  $\rho$  of particles C and D. Both reach minima at temperature just warmer than  $-15^{\circ}\text{C}$  of  $326 \text{ kg m}^{-3}$  and  $256 \text{ kg m}^{-3}$ , respectively. At warmer temperatures,  $\phi$  increases again, causing a local maximum at  $-8^{\circ}\text{C}$ .

### 5.2.2 Forward simulations

Forward simulations were performed for each particle with McRadar using T-matrix. Unfortunately, the T-matrix was found to not converge at W-band for particles with  $D_{\text{max}} > 5 \text{ mm}$  and  $\phi < 10^{-2}$ . Similarly, at Ka-band the T-matrix only converged for particles with  $\phi > 10^{-2}$ . If  $10^{-2} < \phi < 3 \cdot 10^{-2}$ , the T-matrix only converged for particles with  $D_{\text{max}} < 7.5 \text{ mm}$ . At X-band, most particles that were simulated with MCSNOW could be forward simulated using the T-matrix. However, even at X-band, the T-matrix did not converge for particles with  $\phi < 10^{-2}$  (see e.g. temperature region warmer than  $-5^{\circ}\text{C}$  in Figure 5.3). As was shown in the DDA scattering simulations in von Terzi et al., 2022, ZDR does not depend strongly on frequency. However, KDP at X-band is expected to be a factor of 10 smaller than at W-band, as KDP is inversely proportional to the radar wavelength (e.g. Bringi and Chandrasekar, 2001). To investigate the effect of depositional growth on KDP and ZDR, the temperature evolution of the single particle ZDR ( $\text{ZDR}_{\text{particle}}$ ) and KDP ( $\text{KDP}_{\text{particle}}$ ) has been calculated for all 350 particles (Figure 5.3). As in Section 5.2.1, the evolution of  $\text{ZDR}_{\text{particle}}$  and  $\text{KDP}_{\text{particle}}$  is summarised for the four exemplary particles A (initialised at  $-30.5^{\circ}\text{C}$ ), B (initialised at  $-25^{\circ}\text{C}$ ), C (initialised at  $-20^{\circ}\text{C}$ ) and D (initialised at  $-16^{\circ}\text{C}$ ).

For both particles A and B,  $\text{ZDR}_{\text{particle}}$  increases continuously towards warmer temperatures (Figure 5.3a). Particle A increases its  $\text{ZDR}_{\text{particle}}$  from 0.4 dB at  $-30.5^{\circ}\text{C}$  to 1.5 dB at  $0^{\circ}\text{C}$ . Particle B shows a strong increase of  $\text{ZDR}_{\text{particle}}$  above the DGL, where it increases from 0.5 to 4 dB. Towards warmer temperatures,  $\text{ZDR}_{\text{particle}}$  continuous to

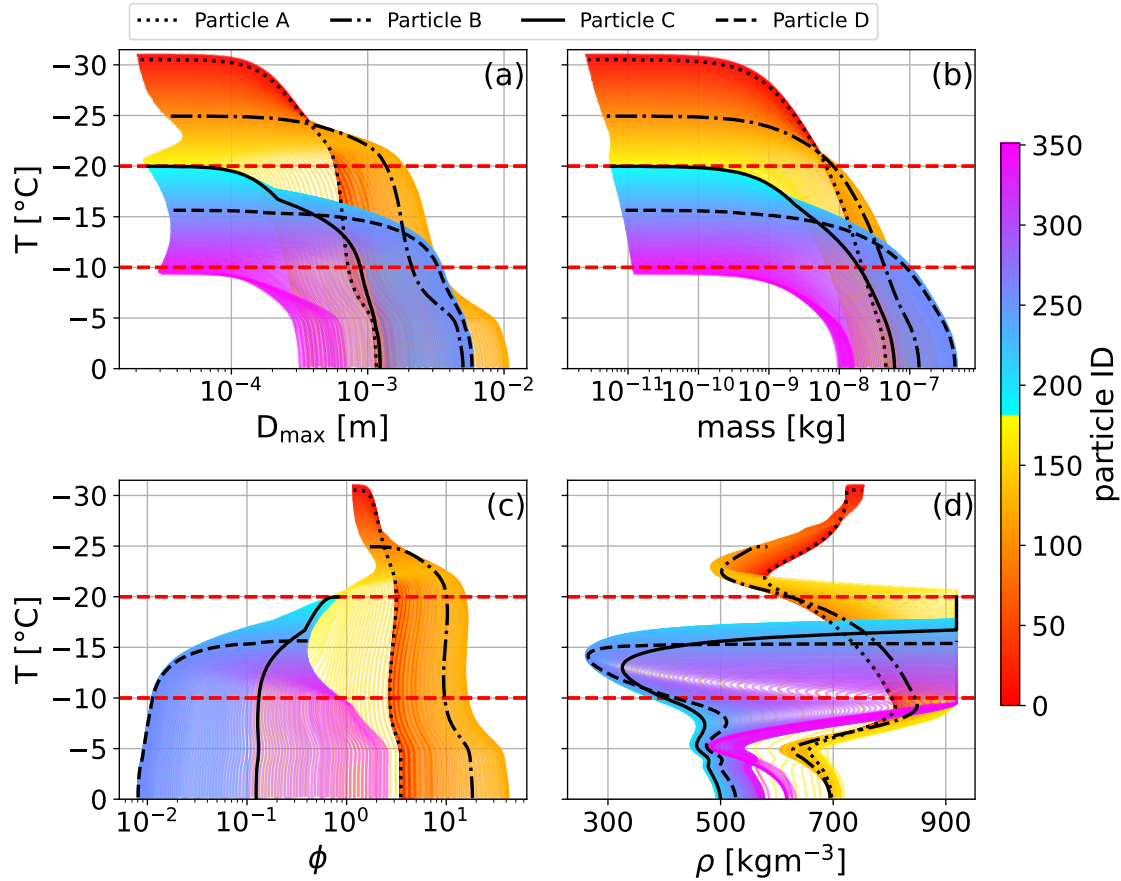


Figure 5.2: Evolution of the particle  $D_{\max}$  (a),  $m$  (b),  $\phi$  (c) and  $\rho$  (d) through depositional growth as a function of temperature. The particles were nucleated at  $D_{\max} = 10 \mu\text{m}$  and  $\phi = 1$  at different temperatures and grown at  $RH_i = 105\%$  while sedimenting. The blue colours show the evolution of physical properties of particles nucleated warmer than  $-20^\circ\text{C}$ , the red colours for particles nucleated colder than  $-20^\circ\text{C}$ . The black lines show the physical properties of four single particles for better visibility. Chosen are the particles with ID 10 (dotted line), 100 (dash-dotted line), 180 (solid line) and 250 (dashed line). The temperature region of the DGL is indicated by the red dashed lines.



increase, reaching a maximum of 6.5 dB at  $-10^{\circ}\text{C}$ . Unfortunately, at this temperature the T-matrix does not converge for particle B, as its  $\phi$  and  $m$  have grown too large. Looking at the evolution of  $\phi$ ,  $m$  and  $\rho$  of particle B at temperatures warmer than  $-10^{\circ}\text{C}$ , it might be possible that  $\text{ZDR}$  saturates there, as strong hollowing is reducing the  $\rho$ , while the  $m$  and  $\phi$  only slightly increase. The effect of the hollowing on  $\text{ZDR}_{\text{particle}}$  can be seen at temperatures between  $-25$  and  $-23^{\circ}\text{C}$ , where the  $\rho$  of the particle is reduced drastically and  $\text{ZDR}_{\text{particle}}$  saturates.  $\text{KDP}_{\text{particle}}$  of particle A remains small for all temperatures, however, it increases slightly from  $10^{-9}^{\circ}\text{km}^{-1}$  at  $-30.5^{\circ}\text{C}$  to  $10^{-2}^{\circ}\text{km}^{-1}$  at  $0^{\circ}\text{C}$  (Figure 5.3b). In contrast to that,  $\text{KDP}_{\text{particle}}$  of particle B increases strongly, from  $10^{-8}^{\circ}\text{km}^{-1}$  at  $-25^{\circ}\text{C}$  to  $0.2^{\circ}\text{km}^{-1}$  at  $-20^{\circ}\text{C}$ . It further increases to  $1^{\circ}\text{km}^{-1}$  at  $-10^{\circ}\text{C}$ . At warmer temperatures no scattering simulations are available as the T-matrix did not converge there.

The maximum values of  $\text{ZDR}_{\text{particle}}$  for particles C and D reach similar magnitudes as for particles A and B.  $\text{ZDR}_{\text{particle}}$  of particle C starts at 0.6 dB at  $-20^{\circ}\text{C}$  and increases to 3 dB at  $-16.5^{\circ}\text{C}$ . As the temperature continuous to increase, branching reduces the  $\rho$  of the particle. Therefore,  $\text{ZDR}_{\text{particle}}$  shows a strong reduction and reaches a minimum of 1.8 dB at  $-13.5^{\circ}\text{C}$ . For warmer temperatures,  $\text{ZDR}_{\text{particle}}$  increases again, until it reaches a value of 3 dB at  $0^{\circ}\text{C}$ . The increase in  $\text{KDP}_{\text{particle}}$  is much smaller than that calculated for particle B. However, it still increases to  $2 \cdot 10^{-4}^{\circ}\text{km}^{-1}$  at  $0^{\circ}\text{C}$ . Particle D already grows a large amount within the first time step, which is not output by McSnow. Therefore,  $\text{ZDR}_{\text{particle}}$  starts already at 3 dB at  $-16^{\circ}\text{C}$ . The particle continuous to grow rapidly, increasing its  $\text{ZDR}_{\text{particle}}$  to 5 dB at  $-15.5^{\circ}\text{C}$ . Then, branching sets in and reduces  $\rho$  and coherently also  $\text{ZDR}_{\text{particle}}$ . A minimum of 2 dB is reached at  $-14.4^{\circ}\text{C}$ . For warmer temperatures,  $\text{ZDR}_{\text{particle}}$  increases continuously, reaching a second maximum at  $-7^{\circ}\text{C}$  of 3.8 dB. Unfortunately, at temperatures warmer than  $-5^{\circ}\text{C}$ , the T-matrix becomes unstable, producing large wiggles in  $\text{ZDR}_{\text{particle}}$  (and also  $\text{KDP}_{\text{particle}}$ ).  $\text{KDP}_{\text{particle}}$  of particle D increases continuously towards warmer temperatures, with the increase getting stronger the warmer the temperature. The rapid increase starts at  $-12^{\circ}\text{C}$  and continuous until  $-5^{\circ}\text{C}$ , where the T-matrix becomes unstable. At  $-5^{\circ}\text{C}$ , a  $\text{KDP}_{\text{particle}}$  of  $0.001^{\circ}\text{km}^{-1}$  is reached.

In general one can say that particles nucleated at temperatures around  $-23^{\circ}\text{C}$  can already produce strong  $\text{ZDR}$ . This is caused by the distinct columnar shape the particles are growing into at this temperature. Particles nucleated at colder temperatures do not produce large  $\text{ZDR}$  values, compared to the maximum  $\text{ZDR}$  reached of plate-like particles or columnar particles. Rather, the  $\text{ZDR}$  of these particles stays constantly small towards warmer temperatures. Assuming particles nucleated at temperatures colder than  $-20^{\circ}\text{C}$  grow columnar, they are not responsible for the increase of  $\text{ZDR}$  and  $s\text{ZDR}_{\text{max}}$  seen at  $-15^{\circ}\text{C}$  in the observations in Chapter 4. Assuming further that the particles grow plate-like at colder temperatures, then they are most likely also not responsible for the peak at  $-15^{\circ}\text{C}$ , as branching in this temperature region would reduce the  $\rho$  and therefore also  $\text{ZDR}$  significantly. This can be seen when looking at  $\text{ZDR}_{\text{particle}}$  of particle C. Particle C reaches a maximum  $\text{ZDR}$  already at  $-16.5^{\circ}\text{C}$ . Particles seeding into the DGL with a plate-like habit might exhibit a similar behaviour. Due to the extensive branching at  $-15^{\circ}\text{C}$ , particles need to be continuously nucleated in this temperature region in order to produce a maximum in  $\text{ZDR}$  or  $s\text{ZDR}_{\text{max}}$  at this temperature.  $\text{KDP}_{\text{particle}}$  increases continuously towards warmer temperatures due to an increase in  $m$ . Particles nucleated at temperatures colder than  $-20^{\circ}\text{C}$  already lead to an increase of  $\text{KDP}$  at



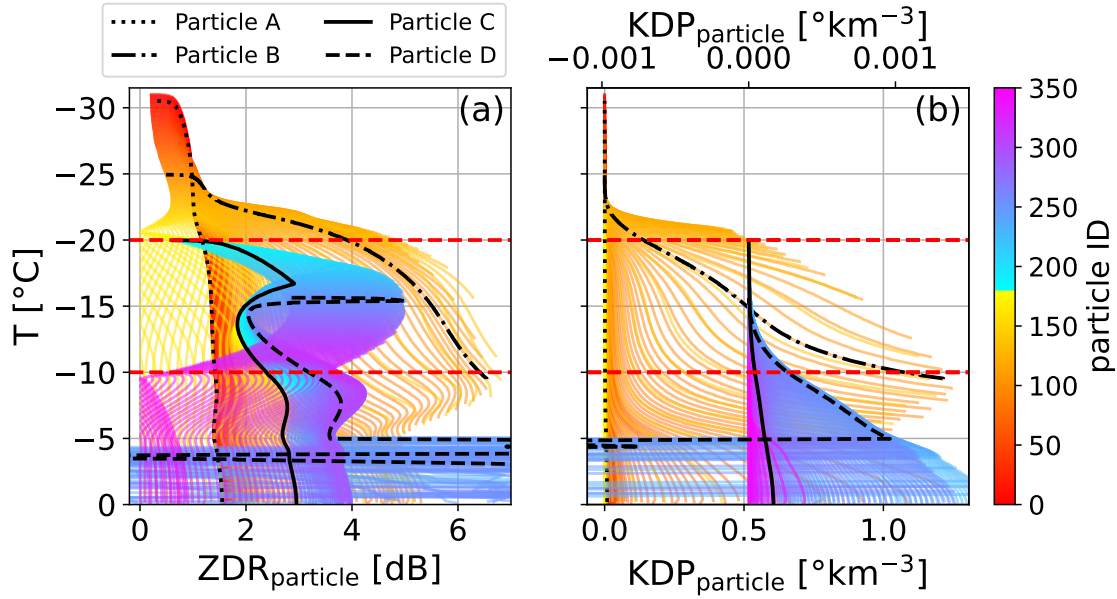


Figure 5.3: Single particle scattering calculations using McRadar and the T-matrix approach. Shown are forward simulations of single particle **ZDR** ( $ZDR_{particle}$ , (a)) and single particle **KDP** ( $KDP_{particle}$ , (b)) of **McSnow** simulations. The particles were grown at  $RH_i = 105\%$ . For a description of the **McSnow** setup and evolution of the particle physical properties see Section 3.2 and Figure 5.2. As in Figure 5.2, the blue colours show the evolution of **ZDR** and **KDP** of particles nucleated warmer than  $-20^\circ\text{C}$ , the red colours for particles nucleated colder than  $-20^\circ\text{C}$ . The top x-axis in panel (b) shows  $KDP_{particle}$  for all blue particles, while the bottom x-axis shows  $KDP_{particle}$  for all red particles. The black lines show the **sZDR** and **KDP** of four single particles for better visibility. Chosen are the particles with ID 10 (dotted line), 100 (dash-dotted line), 180 (solid line) and 250 (dashed line). The temperature region of the **DGL** is indicated by the red dashed lines.

temperatures colder than  $-20^{\circ}\text{C}$ . This is in contrast to what is observed in Chapter 4, where  $\text{KDP}$  is found to first increase at  $-18^{\circ}\text{C}$ , followed by a continuous, almost linear increase towards the bottom of the DGL. Similarly, for particles nucleated within the DGL,  $\text{KDP}_{\text{particle}}$  increases towards the bottom of the DGL. At the bottom of the DGL, a median  $\text{KDP}$  of  $1^{\circ}\text{km}^{-1}$  at W-band is observed (Figure 6 in von Terzi et al., 2022), which corresponds to  $0.1^{\circ}\text{km}^{-1}$  at X-band. 385 particles per  $\text{m}^3$  of type D would be needed to explain the  $\text{KDP}$  signal at this temperature or 1428 per  $\text{m}^3$  particles of type C. As there is very little constrain on the PSD of ice crystals at these temperatures from the observations, it is difficult to further compare the simulated  $\text{KDP}$  to the observed  $\text{KDP}$ .

To better compare the results of this idealised study to the results of the observations, the  $\text{sZDR}_{\text{max}}$  and  $\text{ZDR}$  that these particles would produce are calculated, assuming they are all present in the same volume at the same time (Figure 5.4). This comparison is possible since  $\text{ZDR}$  and  $\text{sZDR}_{\text{max}}$  are independent of the concentration of particles.  $\text{ZDR}$  and  $\text{sZDR}_{\text{max}}$  are calculated separately for particles nucleated in the DGL, particles nucleated at temperatures colder than  $-25^{\circ}\text{C}$  and particles nucleated at all temperatures between  $-10$  and  $-30^{\circ}\text{C}$ . By this separation, one can see the  $\text{ZDR}$  that particles which are newly nucleated in the DGL would produce, as well as the signal of particles sedimenting from above, and the combination of both.

Focusing first on  $\text{ZDR}$  and  $\text{sZDR}_{\text{max}}$  from all particles nucleated at temperatures colder than  $-25^{\circ}\text{C}$  (blue colours in Figure 5.4), one can see that  $\text{ZDR}$  (and  $\text{sZDR}_{\text{max}}$ ) already increases at temperatures colder than  $-20^{\circ}\text{C}$ . At  $-18^{\circ}\text{C}$ , a  $\text{ZDR}$  (and  $\text{sZDR}_{\text{max}}$ ) of 2.5 to 2.8 dB is reached. Throughout the DGL, the values do not increase drastically. Only at temperatures warmer than  $-10^{\circ}\text{C}$ , both  $\text{ZDR}$  and  $\text{sZDR}_{\text{max}}$  are increasing. However, as can be seen in Figure 5.3, at temperatures warmer than  $-5^{\circ}\text{C}$  the T-matrix becomes unstable, making the results there not trustworthy.

Continuing now with the  $\text{ZDR}$  and  $\text{sZDR}_{\text{max}}$  of all particles (green lines in Figure 5.4), one can see that  $\text{ZDR}$  and  $\text{sZDR}_{\text{max}}$  already increase rapidly at  $-23^{\circ}\text{C}$ , where the strongest columnar growth is simulated. At the top of the DGL, a  $\text{ZDR}$  of 4.2 and a  $\text{sZDR}_{\text{max}}$  of 4.7 dB is reached. Both quantities only increase slightly within the DGL, reaching values of 5.4 to 5.6 at  $-10^{\circ}\text{C}$ . At warmer temperatures the result is again not trustworthy, as the T-matrix did not converge for the largest columnar particles. Interestingly, the smaller  $\text{ZDR}$  of the plate-like particles in the DGL does not influence the integrated  $\text{ZDR}$  strongly, however, it is slightly moved towards smaller values compared to  $\text{sZDR}_{\text{max}}$ .

In contrast to the  $\text{ZDR}$  and  $\text{sZDR}_{\text{max}}$  of particles nucleated at temperatures colder than  $-25^{\circ}\text{C}$  and of all particles, the  $\text{ZDR}$  and  $\text{sZDR}_{\text{max}}$  of particles nucleated within the DGL (red lines in Figure 5.4) differ significantly. Between  $-20$  and  $-17.5^{\circ}\text{C}$ , both  $\text{ZDR}$  and  $\text{sZDR}_{\text{max}}$  increase in a similar way. However, at  $-17.5^{\circ}\text{C}$ ,  $\text{ZDR}$  decreases rapidly, reaching a minimum at  $-14.7^{\circ}\text{C}$  of 2 dB, while  $\text{sZDR}_{\text{max}}$  continues to increase, reaching a maximum at  $-15^{\circ}\text{C}$  of 4.95 dB. Branching reduces the  $\rho$  drastically at temperatures between  $-17$  and  $-12^{\circ}\text{C}$ . Therefore,  $\text{ZDR}$  also reduces rapidly there. In contrast, branching does not affect  $\text{sZDR}_{\text{max}}$ , as long as particles with low  $\phi$  and high  $\rho$ , and therefore high  $\text{ZDR}_{\text{particle}}$  are present at the same height. Since branching is only happening once a particle has reached a certain fall velocity (see Section 3.2.1, Jensen and Harrington, 2015; Mason, 1953) they initially increase their  $m$  at  $\rho$  of pure ice, also increasing the  $\text{ZDR}$  of the particle rapidly at temperatures in the vicinity of  $-15^{\circ}\text{C}$ . At  $-15^{\circ}\text{C}$  the smallest aspect ratios are observed at  $\rho$  or pure ice, causing the maximum

in  $sZDR_{max}$ . At temperatures warmer than  $-15^{\circ}\text{C}$ , the particles do not grow into such extreme aspect ratios, therefore  $sZDR_{max}$  is decreasing. In contrast,  $ZDR$ , which seems to be strongly influenced by the  $\rho$  evolution of the largest particles, increases continuously at temperatures warmer than  $-15^{\circ}\text{C}$  and reaches a second maximum at  $-8^{\circ}\text{C}$ . This second maximum is also seen in  $sZDR_{max}$ , which appears to be connected to the increase in  $\rho$  as well.

It is very interesting that the  $ZDR$  of plate-like particles follows so closely the  $\rho$  of the largest particles, which reduces  $ZDR$  rapidly within the DGL, even leading to a minimum at  $-15^{\circ}\text{C}$ . This would indicate that in order to have a maximum  $ZDR$  at  $-15^{\circ}\text{C}$ , as observed in many case studies (Griffin et al., 2018; Moisseev et al., 2015; Schrom and Kumjian, 2016; Schrom et al., 2015, among others), plate-like particles can not have formed at colder temperatures and seeded into the region close to  $-15^{\circ}\text{C}$ . Rather, the particles need to be nucleated in close proximity to  $-15^{\circ}\text{C}$ . It further implies that the formation of aggregates might not be the only reason for a reduction of  $ZDR$  at temperatures slightly warmer than  $-15^{\circ}\text{C}$ . The reduction of  $\rho$  due to branching might reduce  $ZDR$  at these temperatures regions as well.

To compare  $sZDR_{max}$  with the observations, the median  $sZDR_{max}$  of  $DWR_{KaW}$ -class 3 from Chapter 4 (Figure 6 in von Terzi et al., 2022) is also included in Figure 5.4. During the TRIPEX-pol campaign,  $sZDR_{max}$  was frequently observed to coincide with regions of large  $DWR_{KaW}$ . However, there have also been regions of large  $DWR_{KaW}$  without enhanced  $sZDR_{max}$ . By classifying all  $sZDR_{max}$  profiles with the maximum  $DWR_{KaW}$ , cases with large  $sZDR_{max}$  and low  $sZDR_{max}$  are grouped together. Therefore, the median of  $sZDR_{max}$  of  $DWR_{KaW}$ -class 3 is shifted towards smaller values than  $sZDR_{max}$  observed in case studies with large  $sZDR_{max}$  (see also case study in Chapter 4, Figure 2 in von Terzi et al., 2022). Further, the simulations are highly idealised, as the particles grow at constant  $RH_i$  and aggregation does not consume the largest crystals. In real clouds there is also an abundance of various different hydrometeors present, which might reduce  $sZDR_{max}$  further. For example, in a Doppler spectrum, various particles with similar fall velocities are observed in one Doppler bin. Particles with small aspect ratios might fall in the same Doppler bin as particles with slightly larger aspect ratios, reducing  $sZDR_{max}$ . Therefore,  $sZDR_{max}$  and  $ZDR$  of the simulations is expected to be larger than those of the median observations. Still, the observations and simulations can be compared when focusing not on the magnitude, but on the qualitative evolution of  $sZDR_{max}$  with temperature.

The observed  $sZDR_{max}$  ( $sZDR_{max,obs}$ ) increases first at  $-18^{\circ}\text{C}$ , reaching a maximum of 1.5 dB at  $-14^{\circ}\text{C}$ . Towards the bottom of the DGL,  $sZDR_{max,obs}$  reduces slightly, reaching a minimum of 1.25 dB at  $-10^{\circ}\text{C}$ . At temperatures between  $-10$  and  $-5^{\circ}\text{C}$ ,  $sZDR_{max,obs}$  has a second maximum of approximately 1.49 dB. Towards the melting layer,  $sZDR_{max,obs}$  continuously decreases. This evolution with temperature in the bottom half of the DGL and towards warmer temperatures is very similar to that of the simulated  $sZDR_{max}$  ( $sZDR_{max,sim}$ ). This indicates that in these temperature regions,  $sZDR_{max,obs}$  could be explained by the continuous nucleation and subsequent depositional growth of plate-like particles. At colder temperatures (between  $-20$  and  $-15^{\circ}\text{C}$ ),  $sZDR_{max,sim}$  increases faster than  $sZDR_{max,obs}$ . Possibly, plate-like particles do not become nucleated that frequently at these temperatures. It is also possible that at  $-15^{\circ}\text{C}$  the super-saturation is larger compared to at colder temperatures, leading to an enhanced growth at this temperature. However, the median  $RH_i$  of the radiosondes

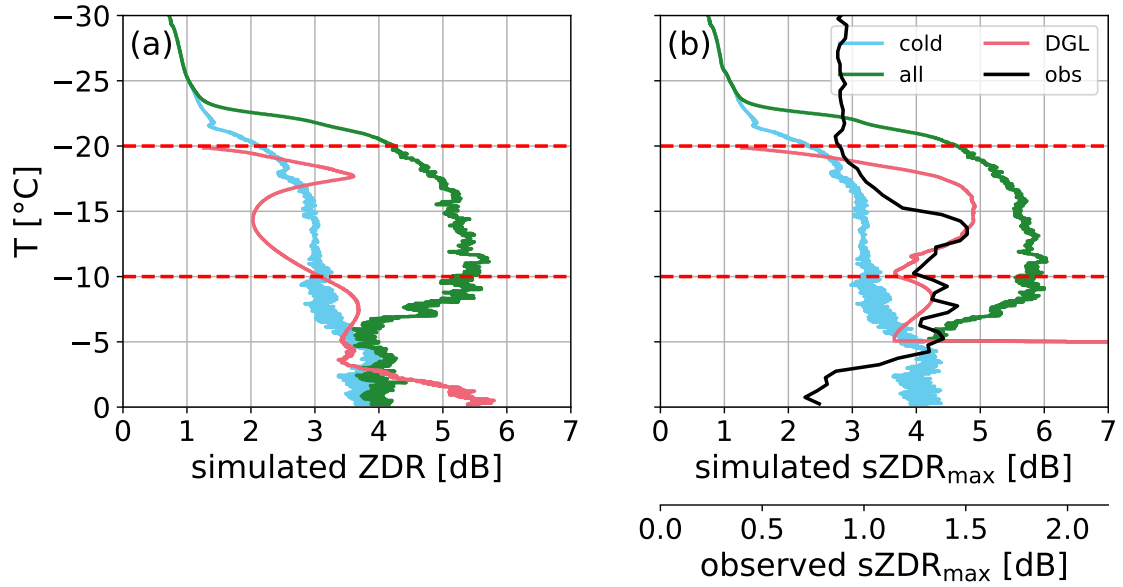


Figure 5.4: Integrated  $ZDR$  (a) and  $sZDR_{max}$  (b) calculated for all particles in Figure 5.3 (green), for all particles nucleated within the DGL (red) and for particles nucleated at temperatures colder than  $-25$  °C (blue). For better comparability, also the observed  $sZDR_{max}$  is plotted (black line and bottom x-axis in panel (b)). The temperature region of the DGL is indicated by the red dashed lines.

launched during the TRIPEX-scan campaign revealed that the  $RH_i$  stays close to 105% at all temperatures, rather increasing slightly with colder temperatures. There is no clear maximum of  $RH_i$  at  $-15$  °C visible. Another possibility is that  $\Gamma$  overestimated the plate-like growth in the top half of the DGL. It has been found by Connolly et al., 2012 that  $\phi$  measured in their laboratory at  $-20$  °C was smaller than that predicted by  $\Gamma$ . Also, Takahashi, 2014 has shown that the  $m$  gain predicted by  $\Gamma$  is too small at temperatures between  $-15$  and  $-16$  °C. Takahashi, 2014 does not provide information about the temperature region colder than  $-16$  °C. These laboratory studies rather suggest that the plate-like growth at the top half of the DGL is underestimated by  $\Gamma$ , indicating that  $sZDR_{max}$  due to plate-like growth could increase even faster between  $-20$  and  $-15$  °C.

To summarise, the MCSNOW simulations indicate that particles nucleated at temperatures colder than  $-20$  °C increase  $ZDR$ ,  $sZDR_{max}$  and  $KDP$  already drastically at temperatures colder than  $-20$  °C. Even if plate-like particles are nucleated within the DGL, the large  $ZDR$ ,  $sZDR_{max}$  and  $KDP$  of the particles nucleation at colder temperatures dominates the signal. It was further shown that if particles are nucleated at all temperatures within the DGL, a maximum  $ZDR$  is reached already at  $-18.5$  °C. Branching even leads to a minimum of  $ZDR$  at  $-15$  °C. This indicates that in order to have a maximum in  $ZDR$  at  $-15$  °C, particles need to be nucleated close to  $-15$  °C, without having plate-like particles sedimenting into the temperature region around  $-15$  °C from colder temperatures. Looking at  $sZDR_{max}$  of all particles nucleated within the DGL, a maximum was found at  $-15$  °C. Interestingly, at temperatures warmer than  $-15$  °C, the  $sZDR_{max,sim}$  follows the evolution of the  $sZDR_{max,obs}$  qualitatively. However, the  $sZDR_{max,sim}$  is found to increase stronger at temperatures colder than  $-15$  °C compared to the  $sZDR_{max,obs}$ . This might indicate that in order to have a maximum of  $sZDR_{max}$  and  $ZDR$  at  $-15$  °C, the particles need to be continuously

nucleated close to  $-15^{\circ}\text{C}$  but can not be nucleated at colder temperatures and sediment in the temperature region around  $-15^{\circ}\text{C}$ . Clearly, the conducted simulations are highly idealised, as particles are grown at constant water saturation and no aggregation can deplete the largest crystals. It is therefore not expected that the forward simulations fit the observations perfectly.

### 5.3 INVESTIGATING SECONDARY SPECTRAL MODES AND THEIR IMPACT ON AGGREGATION

In Chapter 4 it was shown that enhanced aggregation in the DGL is often accompanied by a secondary Doppler spectra mode in the vicinity of  $-15^{\circ}\text{C}$ . This mode is most likely linked to the growth of plate-like particles nucleated close to  $-15^{\circ}\text{C}$  and growing efficiently by deposition. However, with radar observations it is not possible to identify the origin of these particles. It has been hypothesised in Chapter 4 that the particles responsible for the second mode (as well as enhanced  $sZDR_{max}$  and KDP) might be the product of ice fragmentation. Other studies have speculated that an updraft found in the vicinity of  $-15^{\circ}\text{C}$  enhances  $RH_i$  and therefore activates the INP present at this temperature. This could subsequently lead to a new growth of plate-like particles. It was further shown in Chapter 4, that a wider PSD with already slightly larger particles is observed for the largest  $DWR_{KaW}$ -class, indicating that larger particles and a wider PSD sedimenting into the DGL are favourable for stronger aggregation.

As the parameters impacting fragmentation have not been investigated in great detail (see Section 3.2.5), the fragmentation scheme as it is currently implemented in McSNOW is not used to simulate fragmentation. Rather, the impact of a secondary mode of particles on aggregation is investigated with a sensitivity study. The simulation setups are described in detail in Section 3.2.6. In short: An aggregate mode with a wide ( $S_{wi}$ ) and narrow ( $S_{na}$ ) PSD is sedimenting into the DGL. Between  $-13.8$  and  $-18^{\circ}\text{C}$  a secondary mode of particles is simulated. This secondary mode is either setup to resemble possible primary ice nucleation ( $S_{w,2nd}$ ,  $S_{n,2nd}$ ) or fragmentation ( $S_{w,frag}$ ,  $S_{n,frag}$ ). To compare with the observations, the McSNOW simulations are forward simulated with McRadar. A description is provided in Section 3.3.1.

#### 5.3.1 Impact of PSD on aggregation

In general, in  $S_{wi}$  the number concentration of particles decreases towards warmer temperatures, as aggregation reduces the total number of particles, while increasing the particle size (Figure 5.5a,b,c). Particles reach  $D_{max}$  up to 7 to 10 mm. These particles also contain more than 50 monomers, indicating that they could aggregate very efficiently. The strong aggregation can also be seen in the  $DWR_{KaW}$  and  $DWR_{XKa}$  (Figure 5.5e).  $DWR_{KaW}$  increases strongly in the DGL, from 2.5 dB at the top of the DGL to 8 dB at the bottom. This is most likely caused by the maximum in  $E_s$  at  $-15^{\circ}\text{C}$ , which causes enhanced aggregation. At warmer temperatures  $DWR_{KaW}$  does not increase further, as the Ka-band is now also scattering in the Mie-regime and the difference in backscattered signal between Ka and W approaches a constant value.  $DWR_{XKa}$  first starts to increase rapidly at  $-15^{\circ}\text{C}$ , reaching 3 dB at  $-10^{\circ}\text{C}$ . This is in close agreement with the median observations of the largest  $DWR_{KaW}$ -class in Chapter 4. However, in the observations both  $DWR_{KaW}$  and  $DWR_{XKa}$  were found to not increase



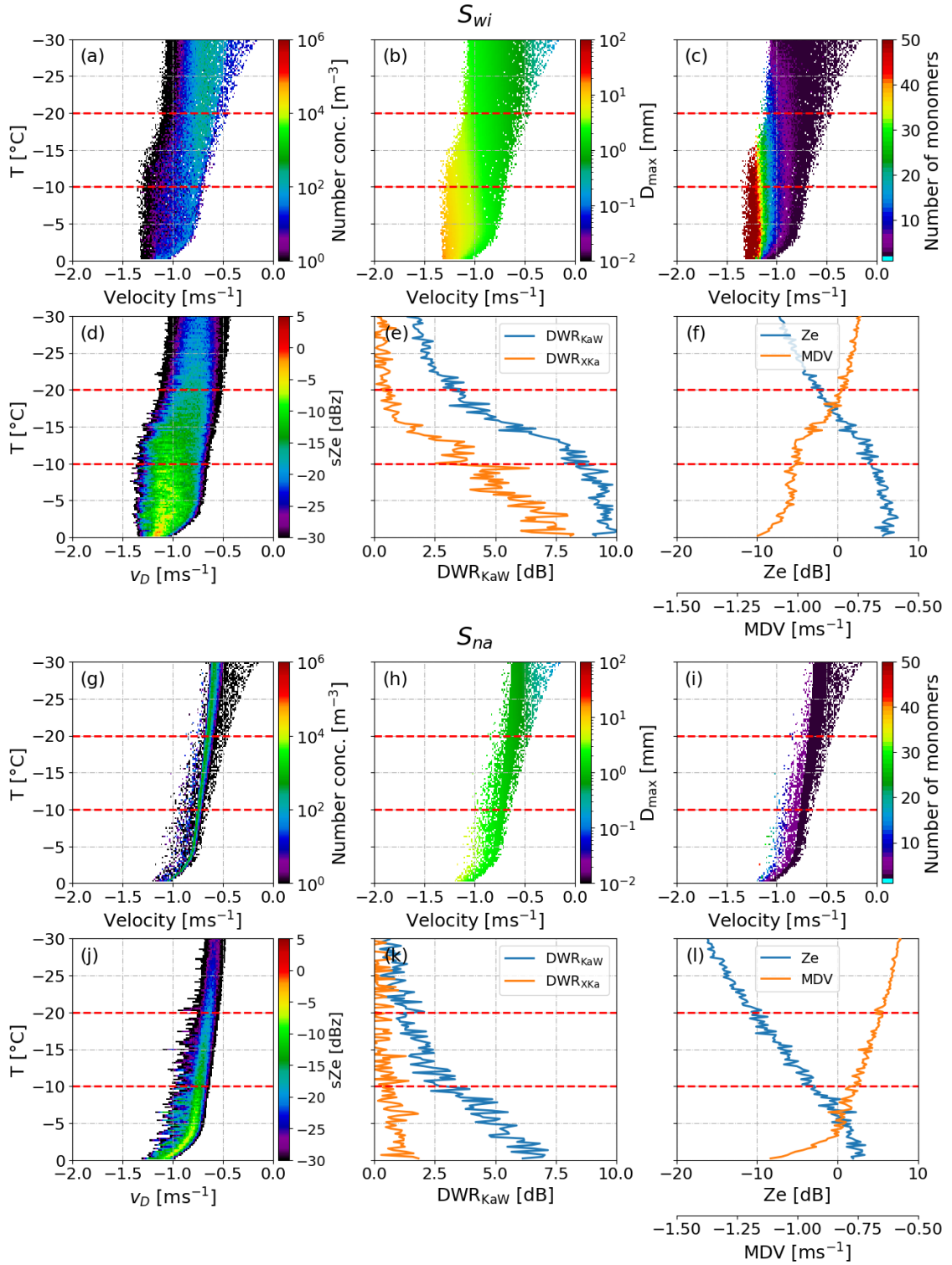


Figure 5.5: Particle properties and forward simulation of the  $S_{wi}$  (top two rows) and  $S_{na}$  (bottom two rows) McSnow simulations. Shown are the number concentration (a, g), the  $D_{\max}$  (b, h), number of monomers per particle (c, i), the forward simulated spectral reflectivity ( $sZe$ ) (d, j), the  $DWR_{KaW}$  and  $DWR_{XKa}$  (e, k) and equivalent radar reflectivity factor at Ka-band ( $Ze_{Ka}$ ) and mean Doppler velocity at Ka-band ( $MDV_{Ka}$ ) (f, l). The forward simulations were conducted with McRadars, using SSRGA for all aggregates and the Rayleigh approximation for monomers (see Table 3.3). The red dashed lines indicate the temperature region of the DGL.



further towards warmer temperatures. In  $S_{wi}$ ,  $DWR_{\chi Ka}$  continuous to increase towards warmer temperatures, reaching a maximum at  $0^\circ \text{C}$  of 7.5 dB. The continuous increase towards warmer temperatures shows the strong continuous aggregation also at warmer temperature regions below the DGL. In contrast to the observations, no second layer of enhanced aggregation close to the melting layer is found. The  $E_{agg}$  parameterisation from Connolly et al., 2012, which is used in these simulations, does not provide any values for temperatures warmer than  $-5^\circ \text{C}$ . Therefore,  $E_{agg}$  is extrapolated towards warmer temperatures, reaching 0.14 at  $0^\circ \text{C}$ , and no maximum in  $E_{agg}$  is assumed close to the melting layer. Due to the increase in size and monomer number, the  $MDV_{Ka}$  is found to continuously increase from  $-30$  to  $-15^\circ \text{C}$ . At temperatures warmer than  $-15^\circ \text{C}$  the  $MDV_{Ka}$  is found to saturate. This saturation of fall velocity of aggregate particle was also found in e.g. Karrer et al., 2020.  $Ze_{Ka}$  is found to continuously increase from  $-8$  dB at  $-30^\circ \text{C}$  to  $5$  dB at  $-10^\circ \text{C}$ . Since the number concentration of particles reduces towards warmer temperatures, this increase in  $Ze_{Ka}$  is due to an increase in size of particles. At temperatures warmer than  $-10^\circ \text{C}$ ,  $Ze_{Ka}$  is found to saturate at values close to  $5$  dB. As was seen in the saturation of  $DWR_{KaW}$ , the particles scatter already out of the Rayleigh regime, thus a further increase in size does not increase  $Ze_{Ka}$  as strongly. The increase in  $Ze_{Ka}$  in  $S_{wi}$  is not as strong as the increase in the median  $Ze_{Ka}$  of the largest  $DWR_{KaW}$  class in the observations. There,  $Ze_{Ka}$  also starts at  $-8$  dB at  $-30^\circ \text{C}$ . However, it is found to increase much stronger, reaching  $10$  dB at  $-10^\circ \text{C}$ . Towards warmer temperatures,  $Ze_{Ka}$  in the observations is also found to saturate. As the  $DWR_{KaW}$  in  $S_{wi}$  is already larger at  $-30^\circ \text{C}$ , most likely the chosen PSD at the top boundary of the domain has too large particles with a total concentration of particles that is smaller than in the observations. The general behaviour of the increase of  $DWR_{KaW}$  and  $DWR_{\chi Ka}$  in the DGL is however well captured by the simulations.

In contrast to  $S_{wi}$ , the particles in  $S_{na}$  are distributed much narrower. The main concentration is peaked at fall velocities in the vicinity of  $-0.6 \text{ m s}^{-1}$  at the top of the domain. Since the difference in fall velocity and size is small between the particles, aggregation does not occur as efficiently as in the  $S_{na}$  case. The size of particles only increases to  $0.3 \text{ mm}$  and the maximum number of monomers per aggregates is less than  $20$ . Therefore,  $DWR_{KaW}$  does not increase as rapidly in the DGL. The strongest increase is found for temperatures warmer than  $-10^\circ \text{C}$ , where  $DWR_{KaW}$  increases from  $2.5$  to  $7$  dB at  $0^\circ \text{C}$ .  $DWR_{\chi Ka}$  does not increase in the simulated temperature regions. The smaller increase in particle size due to aggregation can also be seen in  $Ze_{Ka}$  and  $MDV_{Ka}$ , as they are generally smaller (falling slower). This suggest that if the PSD of particles sedimenting into the DGL is too narrow, even the maximum in  $E_s$  at  $-15^\circ \text{C}$  does not lead to aggregation. Rather, the difference in terminal velocity and  $A$  of the particles (or lack thereof) is driving the aggregation kernel (Equation 2.4) in this case.

The differences between the two reference simulations are illustrated in the first row of Figure 5.6 (panels a to d). Negative values indicate the  $S_{wi}$  has larger values than  $S_{na}$ . As expected,  $D_{max}$ , especially at the fast falling edge, is up to  $5 \text{ mm}$  larger in the  $S_{wi}$  setup than in the  $S_{na}$  setup. Similarly, the largest aggregates in  $S_{wi}$  have more than  $50$  monomers more per aggregate than in  $S_{na}$ . The strongest difference in  $DWR_{KaW}$  can be found in the DGL, where the strong increase in  $DWR_{KaW}$  found in  $S_{wi}$  is not happening in  $S_{na}$ . At the bottom of the DGL  $DWR_{KaW}$  of  $S_{wi}$  is up to  $6$  dB larger than  $S_{na}$ . Towards warmer temperatures, the difference decreases as  $DWR_{KaW}$  of  $S_{wi}$  is

already saturated at these temperatures and does not increase further, while  $DWR_{KaW}$  of  $S_{na}$  increases towards  $0^\circ\text{C}$ .

The statistical analysis of the spectral edges,  $Ze_{Ka}$  and  $DWR_{KaW}$  in Chapter 4 revealed that larger  $DWR_{KaW}$  is associated with already larger particles and wider PSDs sedimenting into the DGL. Although the PSDs of  $S_{wi}$  and  $S_{na}$  are rather extreme assumptions, this behaviour could also be seen in the simulations. Only in cases with a wide PSD, which provides enough variability in fall velocity and size of particles, strong aggregation in the DGL and towards warmer temperatures is observed.

### 5.3.2 Influence of a second mode on aggregation and corresponding radar observables

Interestingly, a secondary mode assumed to originate from primary ice nucleation does not influence  $D_{max}$  or the radar moments when a wide PSD is sedimenting into the DGL ( $S_{w,2nd}$ ). The largest changes are found for the number of monomers in an aggregate, which increases by more than 50 (Figure 5.6e-h). Due to the large velocity difference, the small particles of the secondary mode seem to aggregate with the large aggregates of the aggregate mode already quickly after they were nucleated. Since they have a small  $m$  compared to the already large aggregate, they increase the number of monomers in the aggregate but only weakly the aggregate  $m$  or  $D_{max}$ . Therefore, also  $Ze_{Ka}$  and  $DWR_{KaW}$  is not increased by the secondary mode. Unexpectedly,  $DWR_{KaW}$  seems to be slightly smaller in the case with secondary mode, especially for temperatures warmer than  $-10^\circ\text{C}$ . Most likely the small particles generate more small aggregates, shifting the median  $m$  diameter towards smaller values. Interestingly, although aggregation seems to reduce the number concentration of the small particles, there is constant secondary mode of monomers next to the aggregate mode all the way towards the ground.

The secondary mode has a larger impact on the physical properties and radar observables if a narrow aggregate PSD is sedimenting into the DGL ( $S_{n,2nd}$ , Figure 5.6i-l). In  $S_{n,2nd}$  the number of monomers of aggregates at the fast falling spectral edge as well as their size increases by at least 50 monomers and 4 mm, respectively. The appearance of the second mode leads to a strong increase in  $Ze_{Ka}$  in the vicinity of  $-15^\circ\text{C}$ . This is caused by the large increase in concentration of particles at this height. Interestingly, similar to  $S_{w,2nd}$ , in case of a secondary mode  $DWR_{KaW}$  is smaller for temperatures warmer than  $-10^\circ\text{C}$ , even though the size of the aggregates at the fast falling edge increases. Similar as in  $S_{w,2nd}$ , the second mode does not disappear completely. Rather, a large concentration of monomers coexists with the aggregate mode. Looking at the spectral  $Ze_{Ka}$  in Figure B.3j, it can be seen that the reflectivity of the second mode is comparable to that of the aggregate mode at temperatures warmer than  $-10^\circ\text{C}$ . Since  $DWR_{KaW}$  is reflectivity weighted, it is shifted to smaller values if a large concentration of small ice particles is present.

Similarly to the simulation in  $S_{w,2nd}$ , a secondary mode consisting of larger fragments with lower  $\phi$  does not influence the  $D_{max}$  or radar observables strongly, compared to the reference simulation  $S_{wi}$  (Figure 5.6m-p). The largest change is visible in the increase in number of monomers of the aggregates with the fastest fall velocities. These particles increase their number of monomers by more than 50. Since  $D_{max}$  of the particles does not change significantly, the monomers aggregated to the aggregates need to have small  $D_{max}$ . In contrast to the  $S_{w,2nd}$  simulation, the secondary mode here aggregates very efficiently and already at a few Kelvin warmer than the fragmentation layer, all fragments

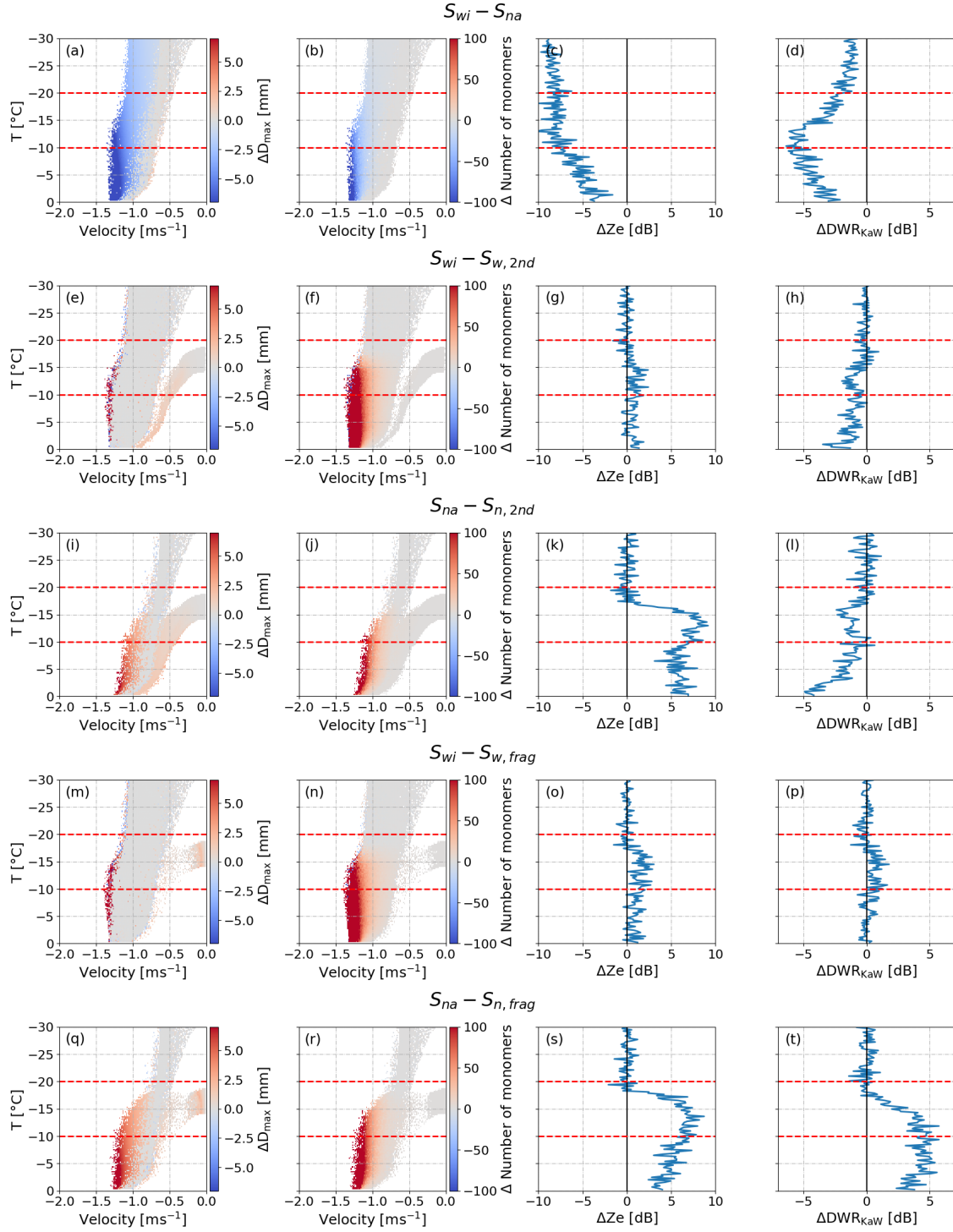


Figure 5.6: Difference in particle properties and radar observables between  $S_{wi}$  and  $S_{na}$  (a to d),  $S_{wi}$  and  $S_{w,2nd}$  (e to h),  $S_{na}$  and  $S_{n,2nd}$  (i-l),  $S_{wi}$  and  $S_{w,frag}$  (m to p) and  $S_{na}$  and  $S_{n,frag}$  (q-t). Shown are the differences in  $D_{max}$  (first column), number of monomers (second column),  $Ze_{Ka}$  (third column) and  $DWR_{KaW}$  (fourth column). Positive values indicate that the reference run had smaller values (e.g.  $D_{max}$  of  $S_{wi}$  is smaller than that of  $S_{w,2nd}$ ), while negative values indicate that the reference run had larger values. The red dashed lines indicate the temperature region of the DGL.

are depleted. The particles in the secondary mode are thus not growing strongly by depositional and are only producing very small  $sZe$  below  $-30$  dB. This is in contrast to  $S_{w,2nd}$ , where not all particles aggregate and thus have time to grow by deposition, enhancing  $sZe$  and their fall velocity.

The biggest change in particle  $D_{max}$  and the radar observables can be seen when comparing  $S_{na}$  and  $S_{n,frag}$  (Figure 5.6q-t). The addition of a secondary mode increases  $D_{max}$  significantly on the fast falling spectral edge by more than 5 mm. Single particles can even reach  $D_{max}$  that are 10 mm larger than those of  $S_{na}$ . These particles also increase their number of monomers by more than 50 (in some cases even more than 500). This large increase in  $D_{max}$  also increases  $Ze_{Ka}$  and  $DWR_{KaW}$  significantly. Within the DGL,  $DWR_{KaW}$  increases rapidly once the second mode is inserted. At  $-10$  °C the largest difference in  $DWR_{KaW}$  of 5 dB is found. At warmer temperatures, the difference in  $DWR_{KaW}$  between  $S_{n,frag}$  and  $S_{na}$  reduces slightly, since the  $DWR_{KaW}$  of  $S_{n,frag}$  is already saturated, while a slight increase in particle size found in  $S_{na}$  at temperatures warmer than  $-10$  °C increases  $DWR_{KaW}$  of  $S_{na}$ . Similarly,  $Ze_{Ka}$  increases rapidly once the second mode is present. The maximum difference between  $S_{n,frag}$  and  $S_{na}$  is found at  $-12$  °C of 7.5 dB. Similarly to the difference in  $DWR_{KaW}$ , at warmer temperatures, the difference in  $Ze_{Ka}$  reduces slightly. In contrast to  $S_{n,2nd}$ , all monomers from the secondary mode aggregate very efficiently with the aggregates and with themselves. The secondary mode is again completely depleted at temperatures only slightly warmer than the second nucleation zone.

It is interesting that the secondary modes due to primary ice nucleation ( $S_{w,2nd}$ ,  $S_{n,2nd}$ ) aggregates much less efficiently than the secondary mode due to fragmentation ( $S_{w,frag}$ ,  $S_{n,frag}$ ). Apparently, the plate-like shape that the particles in  $S_{w,frag}$  and  $S_{n,frag}$  have already appears to strongly enhance their ability to aggregate. Plate-like particles have a larger cross-sectional area than particles with aspect ratios close to one. Since the aggregation kernel (Equation 2.4) depends on the overlapping area between the two interacting particles, a larger cross-sectional area of the monomers increases this area. Even though the particles in  $S_{w,2nd}$  and  $S_{n,2nd}$  also grow into plate-like particles, the decrease of aspect ratio is not fast enough. Especially the particles nucleated at  $-15$  °C or warmer quickly fall out of the favourable depositional growth zone. These particles are found to not aggregate and form the constant secondary mode. In the observations, the secondary mode is found to quickly merge with the main (aggregate) mode within a few Kelvin after it first appeared. Figure 3d-f in von Terzi et al., 2022 shows that a secondary mode first appears at  $-16$  °C. At temperatures close to  $-12$  °C, the secondary mode has merged completely with the main mode. The reduction of  $sZDR$  at this temperature at the slow falling side reveals that the asymmetric ice particles have indeed aggregated, as further below they do not produce a  $sZDR$  signal anymore. This might indicate that the scenario in  $S_{w,frag}$  and  $S_{n,frag}$  might be more realistic. However, compared to the observations, the secondary mode in  $S_{w,frag}$  and  $S_{n,frag}$  is depleted too quickly. In the observations, the secondary mode first increases its reflectivity, possibly through depositional growth of plate-like particles, or in general the presence of larger plate-like particles, and then it merges with the main mode. In  $S_{w,frag}$  and  $S_{n,frag}$ , the secondary mode is depleted through aggregation before the particles can grow through deposition and increase  $sZe$ . Perhaps, a combination between primary nucleation and fragmentation might lead to more realistic signatures.

Clearly, the eight scenarios presented here are very idealised experiments, so a complete agreement with the observations is not expected. A change in radar observable can be caused by an entanglement of changes of different particle properties. Retrieving the influence of a change of these properties on IMP just from the observations is therefore rather difficult. The simulations presented here are useful to test sensitivities of IMP to changes in PSD and particle properties.

## 5.4 CONCLUSIONS

Polarimetric and Doppler radar observations have shown an increase of ice particle concentration and enhanced growth of plate-like particles in the DGL (Chapter 4). Since the increase in concentration of ice particles is correlated with enhanced aggregation within the DGL, fragmentation due to ice-ice collisions was suggested as a possible source of plate-like particles in the DGL. Previous studies have also suggested that the increase of ZDR and KDP in the vicinity of  $-15^{\circ}\text{C}$  might be caused by small ice crystals sedimenting into the DGL and strongly growing there by deposition. McSNOW provides a unique opportunity to investigate these hypothesis in detail.

An analysis of the depositional growth of particles nucleated within and above the DGL revealed that particles nucleated between  $-15$  and  $-17^{\circ}\text{C}$  grow most efficiently into plate-like particles. The in McSNOW implemented inherent growth function predicts column-like growth at temperatures colder than  $-20^{\circ}\text{C}$ . These particles are found to being unable to grow into plate-like particles in the DGL.

Forward simulations of particle evolution due to depositional growth further show that if particles are nucleated continuously within the DGL, ZDR is reduced strongly through branching, leading to a minimum at  $-15^{\circ}\text{C}$ . Further, sZDR<sub>max</sub> starts to increase at temperatures colder than observed in Chapter 4. This suggests that in order to explain the observed maximum of sZDR<sub>max</sub> and ZDR at  $-15^{\circ}\text{C}$ , particles have to be nucleated close to this temperature.

Answering hypothesis 1: The McSNOW simulations suggest that the observed polarimetric signatures are caused by particles nucleated in the vicinity of  $-15^{\circ}\text{C}$ . If there is not a strong sublimation layer at temperatures slightly colder than  $-15^{\circ}\text{C}$ , it appears rather unlikely that particles sedimenting into the DGL from above cause the maximum in sZDR<sub>max</sub> at  $-15^{\circ}\text{C}$ .

To investigate hypothesis 2 and 3, simulations with an aggregate mode sedimenting into the DGL and a second initialisation layer at temperatures between  $-13.8$  and  $-18^{\circ}\text{C}$  were conducted. It was found that

- The impact of the PSD on aggregation appears to be larger than that of a second mode. If a wide PSD of aggregates sediments into the DGL, a secondary mode does not affect  $D_{\text{max}}$ ,  $DWR_{\text{KaW}}$  or  $Ze_{\text{Ka}}$  significantly.
- Interestingly, the aggregation efficiency and interaction of the secondary mode with the aggregate mode seems to depend strongly on the physical properties of the particles in the secondary mode. A secondary mode due to fragmentation is found to aggregate very strongly and is already depleted a few Kelvin warmer than the fragmentation layer. In contrast, the secondary mode due to primary nucleation aggregates much less and constantly exists next to the aggregate mode.



Answering hypothesis 2 and 3: [McSnow](#) simulations suggest that the secondary mode observed in [Chapter 4](#) is more likely caused by fragmentation. However, as the secondary mode due to fragmentation has been found to aggregate too fast, perhaps a combination of both produce realistic signatures.

The simulations presented in this chapter are highly idealised and therefore it is not expected that they agree completely with the observations. Rather, these simulations are a unique and useful tool to test sensitivities of aggregation, plate-like particle growth and their interplay to different environmental and microphysical settings. It can be used to better understand different radar signatures and which particle properties are likely responsible for them. Clearly, more investigations into the shape growth at temperatures colder than  $-20^{\circ}\text{C}$  and an adjustment of the inherent growth function are needed in order to investigate the influence of particles sedimenting into the [DGL](#) on the enhanced aggregation and plate-like particle growth observed there. Further, fragmentation has thus-far only been investigated by a handful of laboratory studies. More insights are needed on the collisional fragmentation of more realistic ice particles in order to constrain the possible number of fragments produced, their dependency on environmental factors and particle types. These results could be used to improve fragmentation schemes such as the one provided by Phillips et al., [2017](#).



## CONCLUSIONS AND OUTLOOK

---

The **DGL**, usually located between  $-20$  and  $-10$  °C, plays an important role in ice particle evolution and precipitation generation in clouds. Various physical and ice microphysical processes (**IMP**) have been found to coexist in the **DGL**. The ice crystals in the **DGL** develop a plate-like shape when growing through depositional growth. This leads to a maximum in the depositional growth rate at  $-15$  °C. The depositional growth is further enhanced if liquid particles are present, since the difference in saturation vapour pressure over ice and liquid is largest at  $-12$  °C. Therefore, depositional growth of ice is favoured via the Wegener-Bergeron-Findeisen process. At  $-15$  °C, the plate-like particles develop a distinct dendritic secondary habit. On the one hand, these dendritic particles have been found to be fragile and fragment upon collisions with other ice particles, which might increase the number concentration of small ice particles. On the other hand, dendritic particles are known to aggregate very efficiently through mechanically interlocking. This increase in particle size due to aggregation is an important process in precipitation formation.

This work aims to improve the understanding of the various **IMP** in the **DGL**, especially the correlation between enhanced aggregation, plate-like particle growth and secondary ice processes. The combination of multi-frequency and polarimetric Doppler radar observations provides a unique and novel opportunity to investigate aggregation and ice crystal growth. The three month **TRIPEX-pol** dataset further allows a statistical analysis, which provides robust estimates of correlations between different radar variables and the **IMP** they are connected to, as well as an estimate of the natural variability of these **IMP**. The statistical analysis can also provide useful constraints for model developments and can be further used to evaluate microphysics schemes and representations of **IMP**.

Lagrangian particle models, such as **McSNOW** provide a unique opportunity to validate the findings in the observational study as well as testing hypothesis of **IMP** developed with the observations. Since **McSNOW** explicitly predicts ice growth processes, aggregation, plate-like growth and **SIP** can be investigated in more detail. The model and observations are combined with the innovative forward simulation tool **McRadar**, where the advantages of various scattering approximations are combined.

The observations and models building the pillars of this dissertation are schematically shown in **Figure 6.1**. There, the studies that comprise this dissertation or are strongly linked to it are illustrated.

The combination of radar observations and modelling can provide useful insights in knowledge gaps.

### 6.1 STUDY I: STATISTICAL ANALYSIS OF ICE MICROPHYSICAL PROCESSES IN THE DGL

von Terzi et al., 2022 investigated the correlation between aggregation, plate-like particle growth and **SIP** in the **DGL**. Presented was the reprocessed and quality controlled three month dataset, collected during the **TRIPEX-pol** campaign at **JOYCE-cf**. The dataset

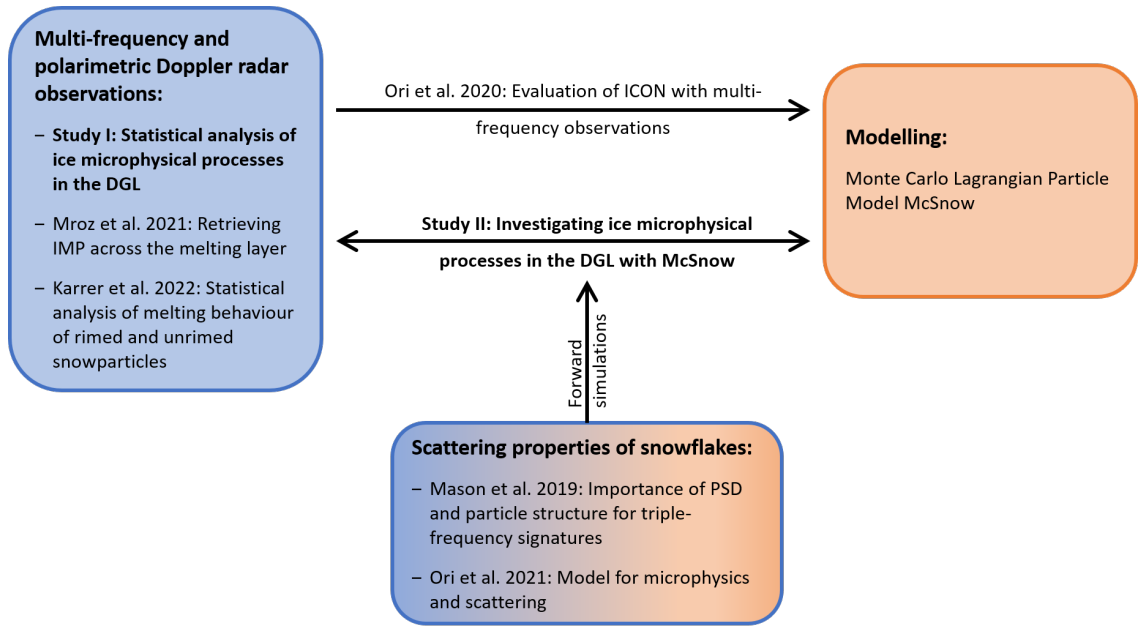


Figure 6.1: Overview of the observational and modelling setup and their usage in this dissertation. Further studies that are strongly connected to this dissertation are also included.

contains data from the vertically pointing X-, Ka- and W-band radars, as well as from the polarimetric W-band radar at 30° elevation. This novel setup allows to combine the advantages of the triple frequency approach (e.g. sensitivity to aggregation, riming processes) with the advantages of polarimetric radar observations (sensitivity to e.g. presence and number concentration of asymmetric ice particles). Similar to previous studies, a case study analysis revealed rapid aggregation within the **DGL**, which was found to coincide with a secondary spectral mode, as well as enhanced  $sZDR_{max}$  and **KDP**. The secondary mode and enhanced  $sZDR_{max}$  and **KDP** are most likely related to the new formation and growth of plate-like particles.

To investigate the relation of different radar variables to the strength of aggregation at and in the vicinity of enhanced aggregation statistically, the dataset was classified by the maximum  $DWR_{KaW}$  present in the **DGL**. The MDV was found to be slowed down for all  $DWR_{KaW}$  classes at temperatures slightly warmer than  $-15^\circ\text{C}$ . An analysis of the spectral edge velocity revealed that this slow-down is most likely caused by the formation of a new particle mode accompanied by an updraft. It was hypothesised that the updraft might be the result of enhanced depositional growth at  $-15^\circ\text{C}$  and concurrent latent heat release.

The new particle mode was looked at in more detail by sorting  $sZDR_{max}$  and **KDP** into  $DWR_{KaW}$  classes.  $sZDR_{max}$  and **KDP** start to increase at  $-18^\circ\text{C}$ , reaching maxima at just below  $-15^\circ\text{C}$  and at the bottom of the **DGL**, respectively. While  $sZDR_{max}$  does not seem to be correlated strongly to the aggregate size, **KDP** is increasing stronger the larger the aggregates are in the **DGL**. The following hypothesis of particle evolution within the **DGL** was derived: The maximum of  $sZDR_{max}$  at  $-15^\circ\text{C}$  revealed a maximum in  $\phi$  at this temperature level. This maximum was found to coincide with the maximum growth rates and  $\phi$ s of plate-like particles found in laboratory studies. Further the MDV slow-down and spectral edge analysis revealed an updraft in the vicinity of  $-15^\circ\text{C}$ . This updraft might be related to latent heat release of the enhanced depositional growth found

at these temperatures. This updraft might even cause a positive feedback, as it increases the residence time of ice particles in the temperature region which favours depositional growth. The continuous increase in  $KDP$  in the  $DGL$  indicates a continuous increase in concentration of ice particles from  $-18$  to  $-12$  °C. Laboratory studies have found that fragments of dendritic arms are ejected during ice-ice collisions. These fragments are found to be first produced at  $-18$  °C, which coincides with the temperature where  $KDP$  is found to increase first. This might indicate that  $SIP$  due to ice-ice collisions might counteract the depletion of ice particles during aggregation.

In previous studies (e.g. Griffin et al., 2018; Oue et al., 2018; Trömel et al., 2019), it was shown that  $IMP$  within the  $DGL$  might depend on cloud top temperature ( $CTT$ ) and the properties of particles aloft. In the presented statistical analysis, it was found that  $DWR_{K_{aW}}$  is already slightly larger above the  $DGL$ , if  $DWR_{K_{aW}}$  is enhanced within the  $DGL$ . This suggests that enhanced aggregation is correlated to already larger sized ice particles aloft. Further, as expected, the spectral edges are further apart for larger  $DWR_{K_{aW}}$  class, indicating that a wider  $PSD$  is sedimenting into the  $DGL$  when stronger aggregation is observed there. Aggregation is depending on the difference in fall velocity and size (Equation 2.4). A wider  $PSD$  enables more variability in fall velocity and size and therefore increases the chance of collisions. Interestingly,  $KDP$  and  $sZDR_{max}$  are found to be similar for all  $DWR_{K_{aW}}$  classes above the  $DGL$ , indicating that the physical properties and concentration of ice crystals above the  $DGL$  might not influence the increase in concentration and  $\phi$  within the  $DGL$ .

To further investigate the influence of particles sedimenting into the  $DGL$ , the radar profiles were sorted into  $CTT$  classes. The analysis revealed that the concentration ( $KDP$ ) and mean size of particles ( $DWR_{K_{aW}}$ ) sedimenting into the  $DGL$  does not depend on the  $CTT$ . Only slight differences in particle shape ( $ZDR$  and  $sZDR_{max}$ ) were found for different  $CTT$ . The strongest increase in  $DWR_{K_{aW}}$  and  $KDP$  were again found within the  $DGL$ . This indicates the importance of the  $IMP$  happening within the  $DGL$ .

Even-though this study was focused on the  $DGL$ , the analysis further revealed that  $sZDR_{max}$  and  $KDP$  stayed constantly enhanced until  $-4$  °C.  $SIP$ , such as the HM around  $-7$  °C might be responsible for the enhanced polarimetric variables. Enhanced aggregation close to the melting layer might deplete the ice crystals at temperature warmer than  $-4$  °C.

It was shown that a statistical analysis can provide estimates of the correlation between different radar variables. Also, it can provide an estimate of the variability of these radar observables and the  $IMP$  that influence the radar observations. The combination of multi-frequency and dual-polarisation Doppler radar observations can provide useful insights into  $IMP$ , as it enables a combined view of particle evolution through depositional growth, aggregation and  $SIP$ . A statistical analysis as presented in von Terzi et al., 2022 can further be used to evaluate and improve ice microphysical schemes in numerical weather prediction models (e.g. Karrer et al., 2021; Ori et al., 2020). Further, the statistical analysis can be used as a constrain of new model developments such as the habit prediction implemented in  $McSNOW$  or new  $SIP$  schemes such as the one presented in Phillips et al., 2018. At the same time, models with a detailed representation of  $IMP$  can help to validate the findings of this study, including the hypothesised particle evolution in the  $DGL$ .

## 6.2 STUDY II: INVESTIGATING ICE MICROPHYSICAL PROCESSES IN THE DGL WITH MCSNOW

The multi-frequency and polarimetric radar observation have shown an increase in ice particle concentration as well as the growth of plate-like particles that is correlated to an enhanced aggregation in the DGL. Based on these observations and previous studies, three hypothesis of the origin of these plate-like particles and their connection to enhanced aggregation have been formulated:

1. Particles are sedimenting from higher altitudes into the DGL. Due to enhanced depositional growth in the vicinity of  $-15^{\circ}\text{C}$  they grow into plate-like particles. This causes a maximum in  $sZDR_{\max}$  and KDP within the DGL.
2. The updraft found at  $-15^{\circ}\text{C}$  enhances  $RH_i$  locally and leads to the new activation of INP. The newly formed ice particles are then growing into plate-like particles, hence enhancing KDP and  $sZDR_{\max}$ .
3. The collisions of ice particles during aggregation leads to fragmentation of fragile parts of aggregates or other ice particles. These fragments have a plate-like  $\phi$ , hence enhancing  $sZDR_{\max}$ . An increase in number concentration of these fragments leads to an increase in KDP and might even enhance aggregation further.

McSnow allows the implementation of the current knowledge of IMP, as well as the tracking of the growth history of particles. The recently implemented habit prediction allows the detailed investigation of ice crystal growth due to deposition. The polarimetric radar observables are highly sensitive to the development of the particles asphericity and  $\rho$ . Linking McSnow with a forward simulator can increase the understanding of the influence of depositional growth on the radar observables. Investigating the depositional growth signatures of particles nucleated within the DGL and aloft might shed light on where particles need to be nucleated in order to produce the increase in  $sZDR_{\max}$  and ZDR observed in the DGL.

An analysis of the depositional growth of ice particles revealed that particles develop the strongest plate-like shape when nucleated between  $-17$  and  $-15^{\circ}\text{C}$ . Particles sedimenting from temperatures colder than  $-21^{\circ}\text{C}$  into the DGL do not develop a plate-like habit. The inherent growth function assumed in McSnow predicts columnar growth at temperatures colder than  $-20^{\circ}\text{C}$ . Recent laboratory as well as in-situ studies have shown that this assumption is not valid. Rather, particles develop a variety of shapes at temperatures colder than  $-20^{\circ}\text{C}$  such as columnar, plate-like or poly-crystalline. With the provided analysis it can therefore not be excluded that plate-like particles might sediment into the DGL and increase ZDR, KDP and  $sZDR_{\max}$  in the vicinity of  $-15^{\circ}\text{C}$ . Forward simulations of these depositional growth signatures revealed that in order to have a maximum of ZDR and  $sZDR_{\max}$  at  $-15^{\circ}\text{C}$ , the particles need to be nucleated in close vicinity to  $-15^{\circ}\text{C}$ . If particles are nucleated throughout the entire DGL, ZDR already has a maximum at  $-17.5^{\circ}\text{C}$  and a minimum at  $-15^{\circ}\text{C}$ . This maximum at  $-17.5$  and minimum at  $-15^{\circ}\text{C}$  are caused by the initial increase in  $\phi$  at colder temperatures (increase in ZDR), followed by the reduction of  $\rho$  due to branching (reduction in ZDR). Branching reduces the  $\rho$  of the particles to a minimum at  $-15^{\circ}\text{C}$ , causing the minimum in ZDR.  $sZDR_{\max}$  is found to increase too fast at temperatures colder than  $-17.5^{\circ}\text{C}$ . In the observations,  $sZDR_{\max}$  is found to first increase slightly

at  $-18^{\circ}\text{C}$ , followed by a stronger increase at  $-15^{\circ}\text{C}$ . These findings strongly indicate that the particles responsible for the  $sZDR_{\max}$  and  $ZDR$  maximum at  $-15^{\circ}\text{C}$  are not nucleated at temperatures much colder than  $-15^{\circ}\text{C}$  and are thus not sedimenting into the DGL from aloft. However, these simulations are highly idealised, as particles are growing at constant  $RH_i$  and aggregation is disabled. Aggregation might be a sink for plate-like particles at colder temperature, depleting the largest particles and thus keeping  $ZDR$  and  $sZDR_{\max}$  lower at temperatures colder than  $-15^{\circ}\text{C}$ .

The second simulation setup was aimed at investigating hypothesis two and three. The following results were obtained:

- A wide PSD of aggregates sedimenting into the DGL shows strong aggregation in the DGL. Similar as in the observations,  $DWR_{K_{aW}}$  was enhanced strongly at  $-15^{\circ}\text{C}$ . In contrast, a narrow PSD sedimenting into the DGL aggregated less efficiently. The strongest increase in  $DWR_{K_{aW}}$  was found at temperatures warmer than  $-10^{\circ}\text{C}$ .
- Introducing a second nucleation layer between  $-18$  and  $-13.8^{\circ}\text{C}$  has a negligible effect on aggregation in case a wide PSD of aggregates sediments into the DGL. However, if a narrow PSD of aggregates is present a secondary mode enhances aggregation and increases the size of the aggregates.
- The interaction between the secondary mode and the aggregate mode depends not only on the PSD of aggregates, but also on the physical properties of the particles of the second mode. If the secondary mode is set up such that it follows a PSD of fragments found in Grzegorzczuk, 2022 and the fragments have  $\phi$ s of dendritic particles, aggregation is very efficient. All particles aggregate quickly and the second mode is already depleted at temperatures only slightly warmer than  $-13.8^{\circ}\text{C}$ . If the secondary mode is however setup to resemble possible primary ice nucleation, such that particles are nucleated with a mean  $D_{\max}$  of  $20\text{ }\mu\text{m}$  and an  $\phi$  of 1, the secondary mode is found to interact much less with the aggregate mode. Both in case of a narrow and wide aggregate mode, the secondary mode is found to coexist with the aggregate mode and persist until the ground. Since the particles in the secondary mode grow by deposition, its  $Ze$  increases continuously, even leading to a reduction of  $DWR_{K_{aW}}$  compared to the simulation without a secondary mode.

Comparing the forward simulated Doppler spectra with the observations, the scenario with a wide aggregate PSD from aloft and a secondary mode due to fragmentation seems the more plausible explanation. The secondary mode in the observations is found to merge quickly with the aggregate mode. However, in the simulations the secondary mode is depleted quickly, rather leading to a disappearance of the second mode than a merging of the two. Perhaps, in reality, the secondary mode could be caused by a combination of fragmentation and primary nucleation.

Answering the three hypothesis stated in this study:

1. It is unlikely that particles sedimenting from colder temperatures into the region in the vicinity of  $-15^{\circ}\text{C}$  are responsible for the observed  $ZDR$  and  $sZDR_{\max}$  signatures. When nucleated at temperatures colder than  $-20^{\circ}\text{C}$ , particles are found to develop a columnar shape and do not grow into plate-like particles



within the DGL. Further, when nucleated close to  $-20^{\circ}\text{C}$ , the particles produce a maximum of ZDR already at  $-18^{\circ}\text{C}$ . At warmer temperatures, branching reduces the  $\rho$  of the particle, leading to a minimum of ZDR at  $-15^{\circ}\text{C}$ .

2. In the statistical analysis of the  $\text{RH}_i$  measured from radiosondes, no distinct maximum in  $\text{RH}_i$  at  $-15^{\circ}\text{C}$  was found. Therefore, the new activation of INP seems to be unlikely. Further, simulating a secondary mode due to primary nucleation does not compare well to the observed Doppler spectra and moments. Rather, the particles in the second mode do not aggregate and a large concentration of ice crystals is continuously present until the ground.
3. A second mode due to fragmentation aggregates fast with the already present aggregate mode. Comparing to the observations, this seems to be a likely explanation. However, in the simulations the secondary mode is depleted too quickly compared to the observations. In the observations the second mode is found to merge with the aggregate mode rather than disappear due to depletion of particles as was found in the simulations. Perhaps, the combination of primary nucleation and fragmentation might provide more realistic signatures.

The conducted simulations provide useful insights into the sensitivities of the depositional growth of ice crystals and the growth of a secondary spectral mode. However, these simulations are highly idealised. The implemented habit prediction scheme needs to be adjusted to better represent recent laboratory and in situ observations of plate-like and poly-crystalline ice particles at temperatures colder than  $-20^{\circ}\text{C}$ . Further, to investigate ice fragmentation and its impact on aggregation and ice particle growth further, more laboratory studies with realistic ice particles are needed in order to develop and improve parameterisations such as Phillips et al., 2018.

### 6.3 OUTLOOK

In the statistical analysis of radar observations provided in Chapter 4 the polarimetric W-band radar looking at  $30^{\circ}$  elevation and the vertically pointing X-, Ka- and W-band radar were not observing the same volume. Therefore, the assumption was made that the observed clouds are stratiform. It was assumed that by considering the advection of the observed volume from the polarimetric W-band radar to the vertically pointing radars and averaging over five minutes, the effects of different observation volumes is small. However, in the TRIPEX-scan campaign, both the Ka-band radar and the polarimetric W-band radar were performing the same scan pattern. Observations of seven minutes at  $30^{\circ}$  elevation will provide DWR and the polarimetric observables from the same volume. Further, collocated RHI scans were performed, allowing to retrieve an elevation dependent DWR. Since the DWR increases with increasing  $m$  along the path of the transmitted electromagnetic wave, the DWR of asymmetric particles is dependent on the elevation angle. This additional information might help constrain the observed PSD further. The TRIPEX-scan campaign further provides more detailed thermodynamical observations. During the campaign, 47 radiosondes were launched, providing profiles of relative humidity, temperature, pressure and vertical wind velocity and direction. In the observational study it was found that enhanced KDP in the DGL correlated with enhanced DWR. However, a large spread was observed, as single case studies revealed



that **KDP** is not always enhanced within the **DGL**. One possible explanation for the variation of **KDP** within the **DGL** is a dependency of fragmentation on the relative humidity. With larger  $RH_i$ , the growth of a secondary habit is stronger. This might indicate that with larger  $RH_i$ , also more, or larger dendritic arms might be growing on ice surfaces, which are then easier fragmented. Larger fragments in turn should also increase **KDP** stronger than smaller fragments. Further, the observed increase in **KDP** and **DWR** in the **DGL** might also depend on the specific weather condition, as e.g. stronger wind shear might further enhance the collisions between particles and therefore aggregation and fragmentation. Within PROM-FRAGILE, these dependencies will be investigated in more detail.

The observed polarimetric and multi-frequency signatures presented in **Chapter 4** might indicate **SIP** within the **DGL**. One possible **SIP** discussed is fragmentation during ice-ice collision. However, the presented analyses do not provide sufficient evidence of fragmentation during collisions. During PROM-FRAGILE, laboratory studies will be undertaken to constrain ice fragmentation and develop parameterisations that can be used in **McSnow**. Model-observation sensitivity and closure studies as presented in **Chapter 5** can then help answering if fragmentation is needed in order to explain the observed radar signatures and they can provide information on the importance of fragmentation on precipitation formation. For this, specific case studies which show the polarimetric and multi-frequency signatures observed in the statistics should be selected. **ICON-LEM** simulations might be used to initialise **McSnow** as they provide hydrometeor distributions and thermodynamic profiles. Comparison between the simulations and observations might then highlight which processes are needed to explain the radar observations as well as possible adjustments needed in **McSnow**.

It is difficult to determine if a possible mismatch in observations and simulations are due to wrongly represented ice microphysics or due to the assumptions made during the forward simulations. To get the best possible match between **McSnow** simulations and observations, the scattering properties of the simulated particles need to be represented accurately. Therefore, DDA calculations should be done on realistic particles that represent the physical properties of the simulated particles. As was shown in **Section 3.3**, the particles currently available do not provide enough flexibility in  $\phi$  as compared to the particles simulated with **McSnow**. Further, the  $m$  and  $D_{max}$  of the particles used for DDA calculations underestimate those of the particles simulated with **McSnow**. Therefore, the physical properties of the particles used to calculate the DDA need to be adjusted. Further, the physical properties of possible ice fragments are currently unknown. Holographic images of ice fragments obtained during the laboratory studies can be used to create virtual 3D particle models. These particle models can be used to calculate the scattering properties with DDA.

In the course of this work, an updraft was found to occur in the vicinity of  $-15^\circ\text{C}$ . It was hypothesised that this updraft might be caused by the latent heat release due to enhanced depositional growth of plate-like particles at  $-15^\circ\text{C}$ . This latent heat release might cause a buoyancy effect. This hypothesis could be investigated further with detailed models, such as **McSnow**, that explicitly predict the habit growth of ice particles and therefore the enhanced depositional growth at  $-15^\circ\text{C}$ . The latent heat released during growth might be estimated in such a model, and the concurrent buoyancy effect calculated.

**PROM-FRAGILE:**  
Second phase project of PROM (Fusion of Radar Polarimetry and Numerical Atmospheric Modelling Towards an Improved Understanding of Cloud and Precipitation processes): Exploring the role of **FRAG**mentation on ice particles by combining super-particle modelling, Laboratory studies and polarimetric radar observations

During this work it was found that aggregation between ice crystals in **McSnow** is more difficult than expected. In order to represent habit growth correctly, particles need to be initialised with  $D_{\max}$  close to  $10\text{ }\mu\text{m}$ . The initialised crystals therefore have very similar fall velocities and only small areas, which results in a small aggregation kernel (see [Equation 2.4](#)). When assumed that ice crystals are nucleated only within a narrow temperature regime (i.e. close to cloud top), the crystals develop a similar shape when growing through deposition. Therefore, even when the crystal sizes increase, the aggregation kernel is still small as all particles have similar  $D_{\max}$ , areas and fall velocities. In nature it can also be expected that particles nucleated at similar heights (and therefore similar thermodynamic environments) develop similar physical properties. However, in nature larger variability in ice particle  $D_{\max}$ ,  $m$  and fall velocity are observed. Also, as has been shown in [Chapter 4](#), aggregation is very efficient, especially at  $-15\text{ }^{\circ}\text{C}$ . The question arises, is aggregation not represented well in **McSnow**? Are there processes missing which enhance the aggregation of small ice crystals? Early investigations might suggest that turbulence plays an important role in the formation of initial aggregates, as it increases the fall velocity variance. However, further investigations and modelling studies are needed.

## RELATIVE HUMIDITY OBSERVATIONS

As has been explained in [Section 2.1.2.1](#), the super-saturation with respect to ice determines the secondary habit of ice crystals and the rate of growth of ice crystals. The branching and depositional growth rate in McSnow is also dependent on super-saturation. Therefore, accurate information on the relative humidity (RH) within clouds is needed to constrain the simulations and better understand the observations of crystal growth which were provided in [Chapter 4](#).

During the [TRIPEX-pol](#) campaign 16 radiosondes of type DFM-09 manufactured by GRAW Radiosondes GmbH & Co. KG were launched, observing atmospheric temperature, pressure and humidity. Unfortunately, for regions above 8 km, the RH were found to drop rapidly from close to 100% to 0%, indicating that the sensor was malfunctioning above 8 km (Dias Neto, 2021). Therefore, the RH information of these radiosondes is not used. During the later TRIPEX-scan campaign, 47 radiosondes of type RS-41 manufactured by Vaisala were launched. The TRIPEX-scan campaign took place at [JOYCE-CF](#) from December 2021 to February 2022. The humidity sensor has been tested against a frostpoint hygrometer during test soundings from the manufacturer. This revealed an uncertainty of  $< 4\%$  at  $RH_w$  between 0 and 100%. The humidity sensor of these radiosondes has been calibrated before each launch. Before the launch of the first radiosonde, the humidity sensor was further tested in an environment at water saturation, which the sensor was able to accurately measure. As the Vaisala radiosondes provide accurate RH information, the RH of the 47 launches was analysed further. The radiosondes were launched in predominantly cloudy conditions, where the clouds were expected to reach temperatures of  $-15^\circ\text{C}$  and colder. The median of the distribution of all  $RH_i$  and  $RH_w$  reveals that  $RH_i$  only slightly increases towards colder temperatures ([Figure A.1](#)). The median stays close to 105% at all temperatures.

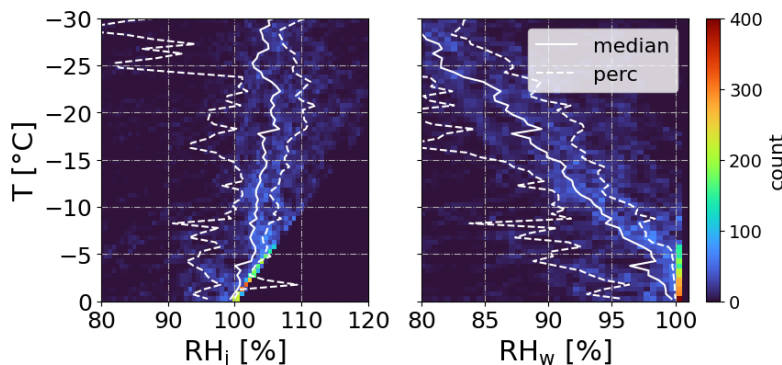


Figure A.1: Distribution of  $RH_i$  and  $RH_w$  of 47 radiosondes launched during the TRIPEX-scan campaign. The white solid line shows the median of the distribution, the dashed lines the 25<sup>th</sup> and 75<sup>th</sup> percentiles.



## MCSNOW SIMULATIONS OF AGGREGATION AND SECONDARY MODE

This chapter provides more detailed description of the setup of the secondary mode due to fragmentation and more detailed figures of the McSnow simulations investigating the link between aggregation and a secondary mode.

### B.1 PSD SETUP OF FRAGMENTATION MODE

As was described in [Section 3.2.6.2](#), the PSD of  $S_{n,frag}$  and  $S_{w,frag}$  was based on the PSD of graupel-graupel collisions found in Grzegorzcyk, 2022. In Grzegorzcyk, 2022, a total of 9 graupel-graupel collisions were performed. One graupel was hold in place by a wire and the second graupel was falling freely and colliding with the fixed graupel. In order to produce collisions with different collision kinetic energies (CKE), the second graupel was launched from different heights, allowing a falling distance between 80 cm (high CKE) and 5 cm (low CKE). Before the collisions, the fixed graupel was placed in an environment with an ambient temperature of  $-14^{\circ}\text{C}$  and a  $RH_i$  of 120% for 5 minutes, allowing dendritic structures to grow on the graupel. After the collision, the produced fragments were collected in a petri dish and the physical properties of the fragments were determined under a microscope. The resulting PSDs are shown in [Figure B.1](#).

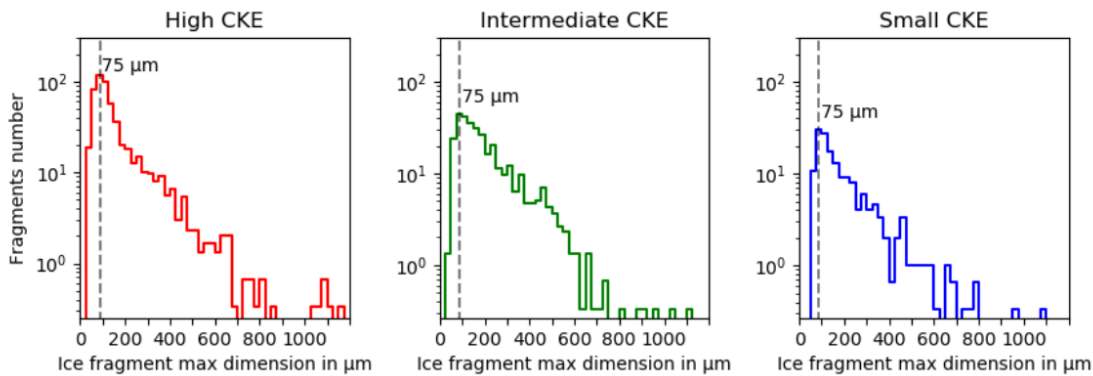


Figure B.1: Mean of distribution of fragment sizes obtained from three experiments with graupel-graupel collisions. The three panels indicate the different collision kinetic energies during the collisions. This plot was taken from Grzegorzcyk, 2022 and reproduced here with permissions from the author.

### B.2 PARTICLE PROPERTIES AND FORWARD SIMULATIONS

This section shows the particle properties and forward simulations of  $S_{n,2nd}$  and  $S_{w,2nd}$  ([Figure B.3](#)) and of  $S_{n,frag}$  and  $S_{w,frag}$  ([Figure B.5](#)). Further, the differences in number concentration,  $D_{max}$ , number of monomers,  $sZe$ ,  $DWR_{KaW}$ ,  $Ze$  and  $MDV$  between  $S_{wi}$  and  $S_{na}$  are shown in [Figure B.2](#). The differences between  $S_{wi}$  and  $S_{w,2nd}$  as well as

$S_{na}$  and  $S_{n,2nd}$  are provided in Figure B.4. Further, The differences between  $S_{wi}$  and  $S_{w,frag}$  as well as  $S_{na}$  and  $S_{n,frag}$  are provided in Figure B.6.

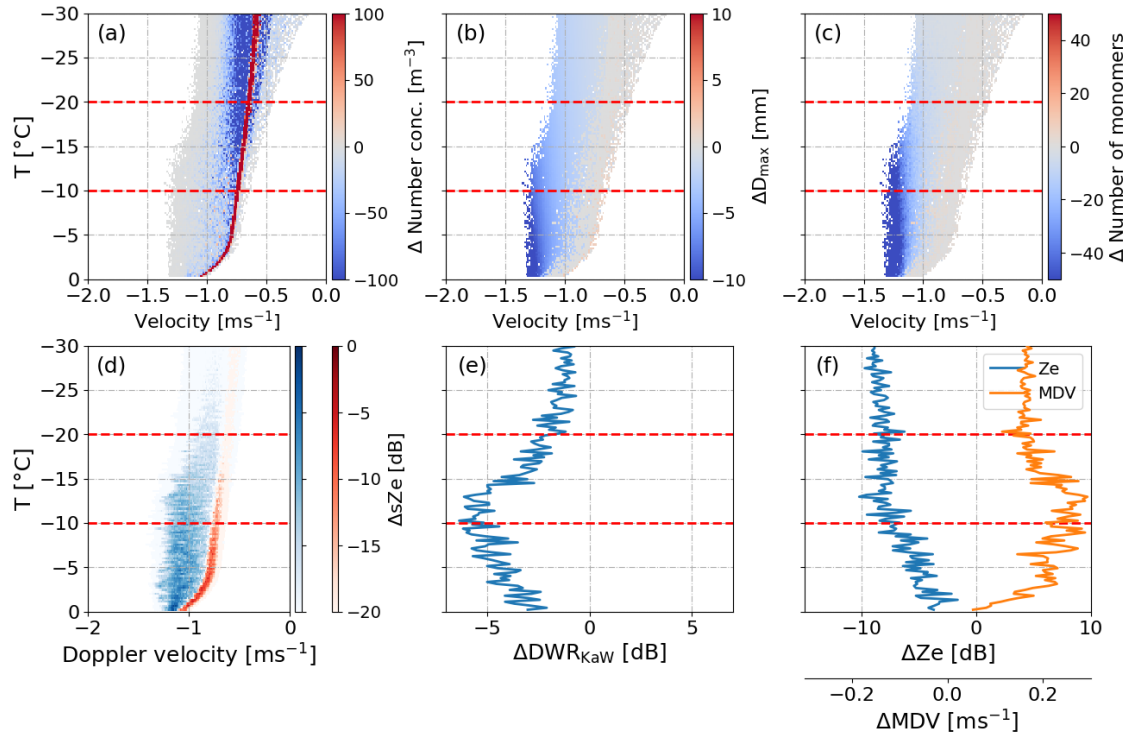


Figure B.2: Difference in particle properties and radar observables between  $S_{wi}$  and  $S_{na}$ . Shown is the difference in number concentration (a),  $D_{max}$  (b), number of monomers (c),  $sZe$  (d),  $DWR_{KaW}$  (e),  $Ze$  and  $MDV$  at Ka-Band (f). Negative values indicate that  $S_{na}$  has smaller values than  $S_{wi}$ .



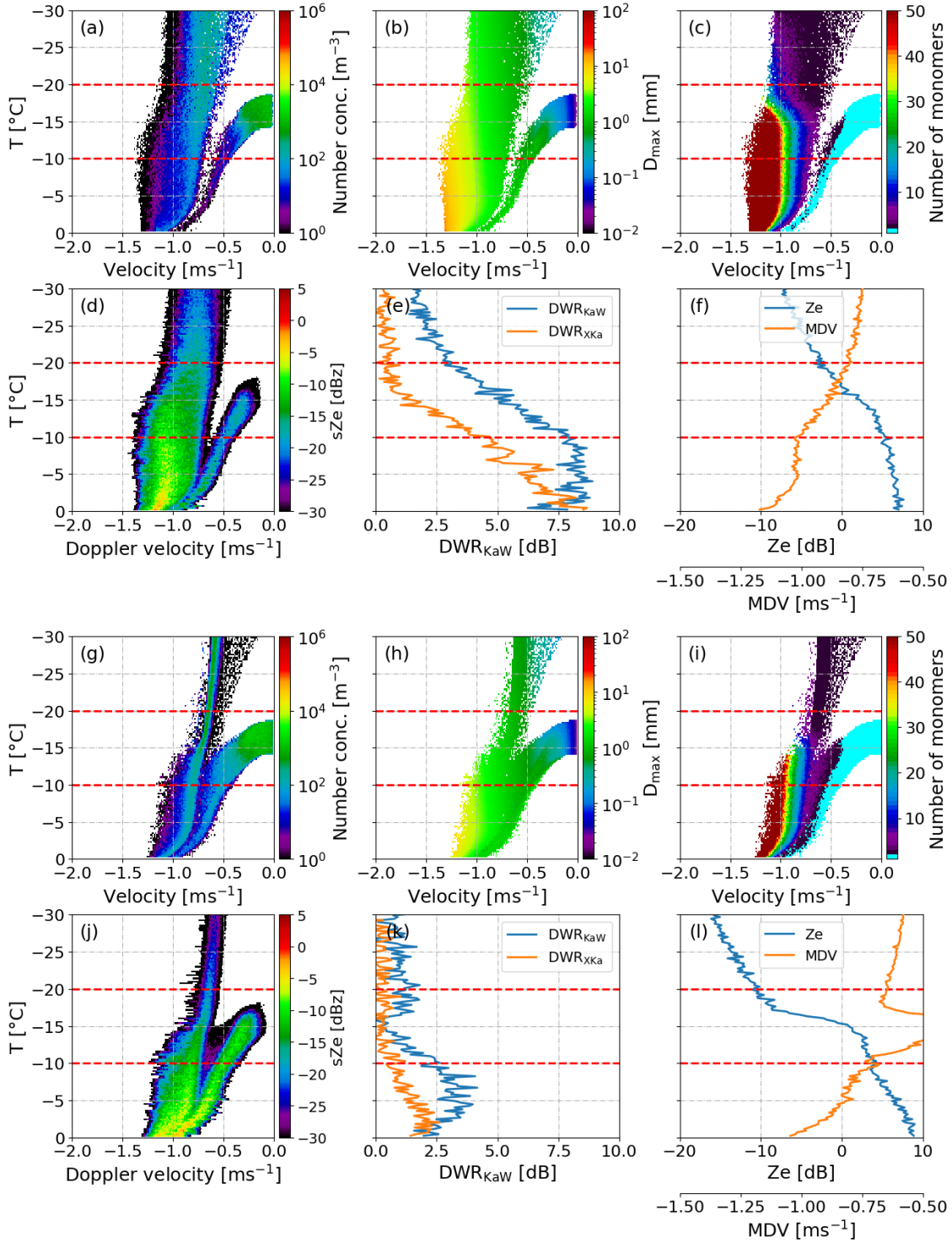


Figure B.3: Particle properties and forward simulation of  $S_{w,2nd}$  (top two rows) and  $S_{n,2nd}$  (bottom two rows). Shown are the number concentration (a, g), the  $D_{max}$  (b, h), number of monomers per particle (c, i), the forward simulated  $sZe$  (d, j), the  $DWR_{KaW}$  and  $DWR_{XKa}$  (e, k) and  $Ze$  and MDV at Ka-Band (f, l). The forward simulations were conducted with McRad, using SSRGA for all aggregates and the Rayleigh approximation for monomers

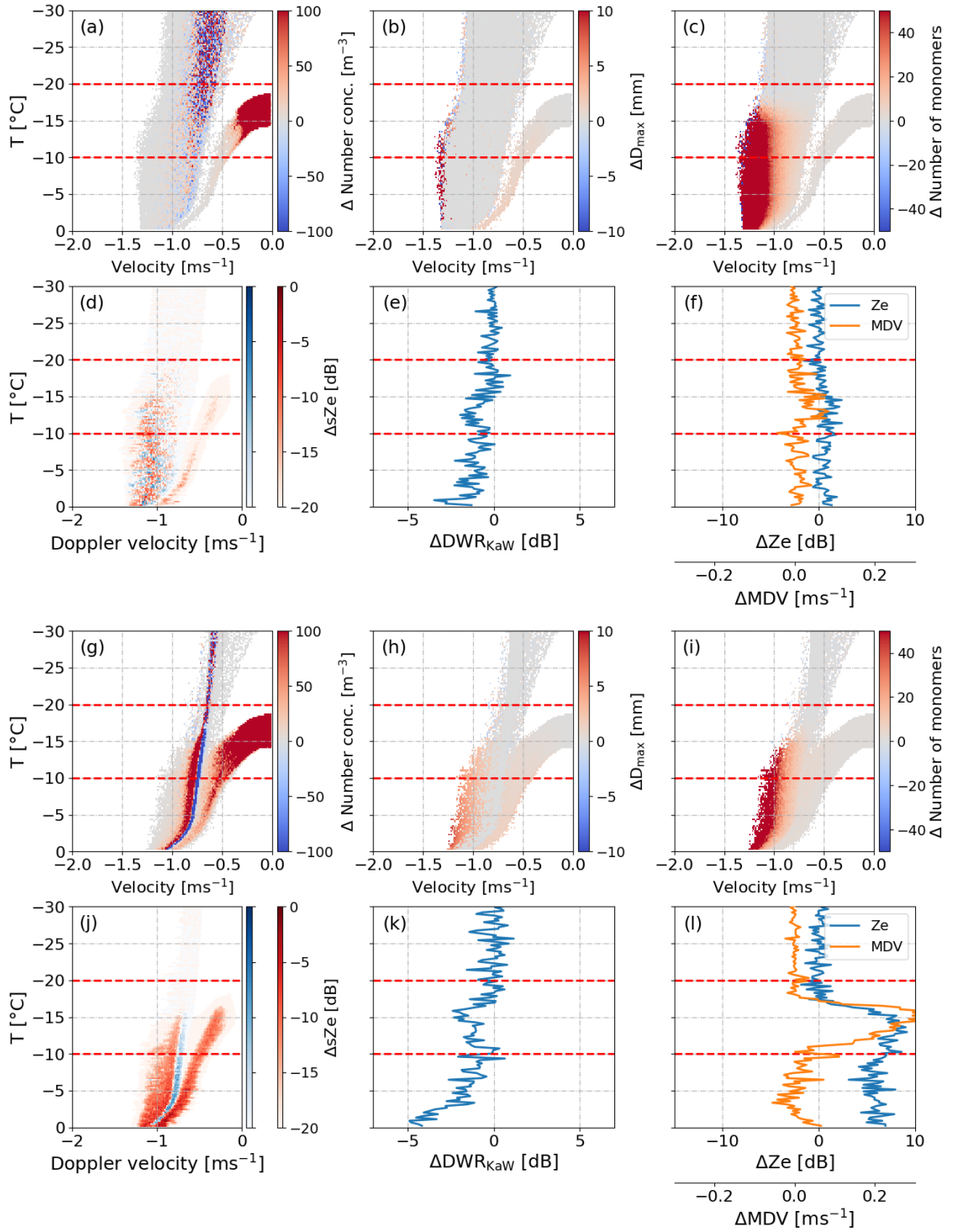
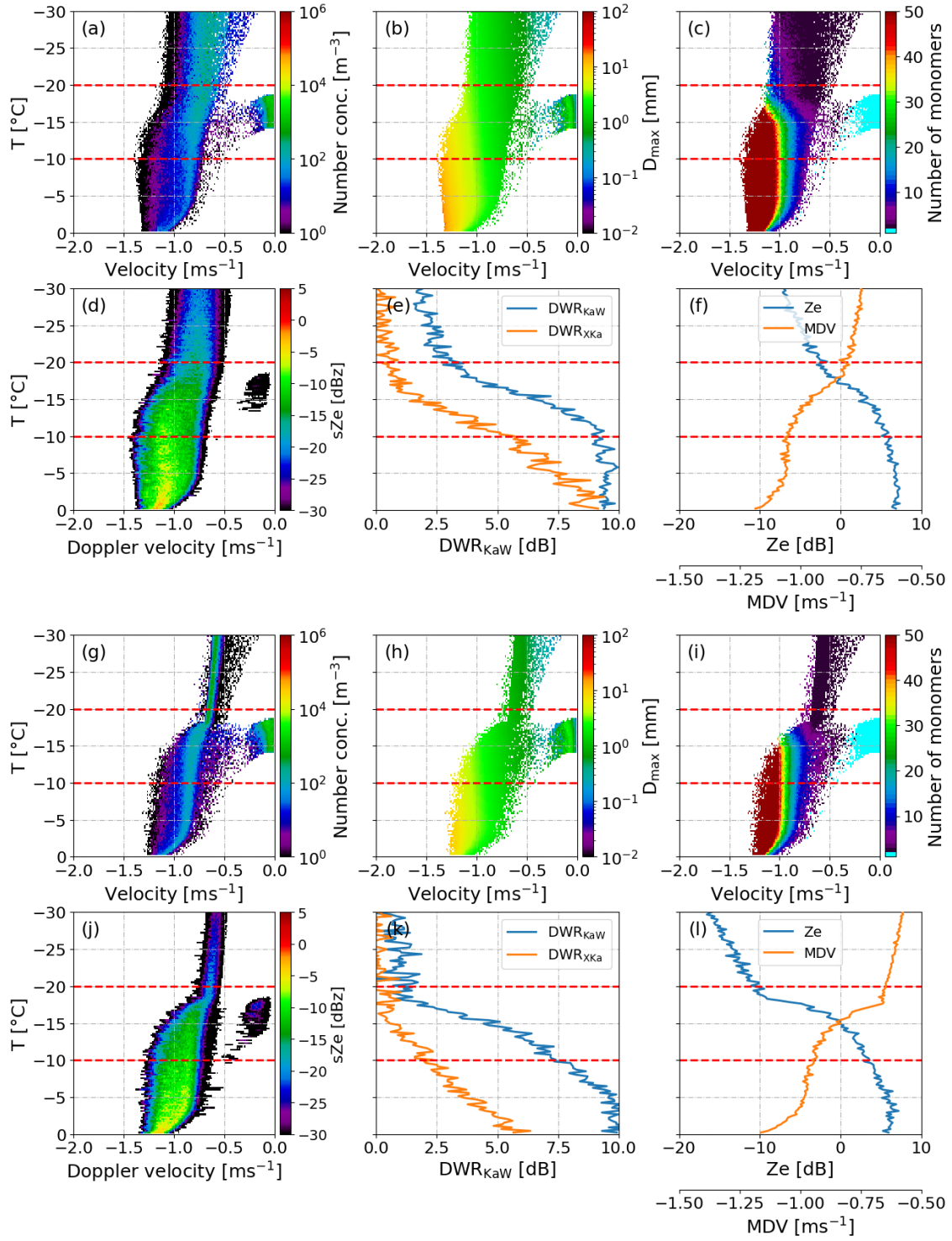


Figure B.4: Difference in particle properties and radar observables between  $S_{wi}$  and  $S_{w,2nd}$  (top two rows) and  $S_{na}$  and  $S_{n,2nd}$  (bottom two rows). Shown is the difference in number concentration (a,g),  $D_{max}$  (b,h), number of monomers (c,i),  $sZe$  (d,j),  $DWR_{KaW}$  (e,k),  $Ze$  and  $MDV$  at Ka-Band (f,j). Negative values indicate that  $S_{na}$  has smaller values than  $S_{wi}$ .

Figure B.5: As Figure B.3 but for  $S_{w,frag}$  and  $S_{n,frag}$ .

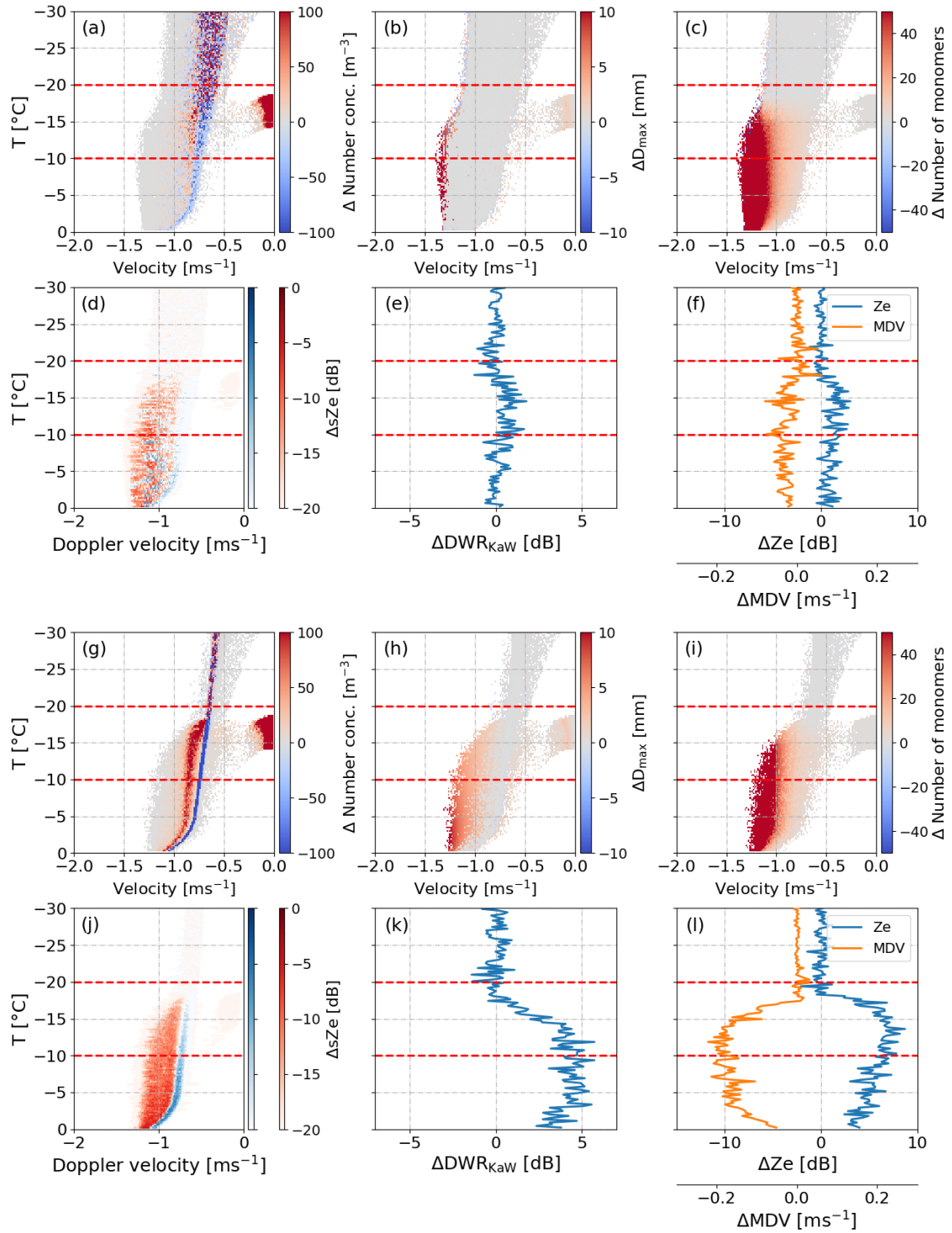


Figure B.6: As in Figure B.4 but for the difference between  $S_{wi}$  and  $S_{w,frag}$  (top two rows) and  $S_{na}$  and  $S_{n,frag}$  (bottom two rows).

## ACKNOWLEDGMENTS

---

I thank the German Research Foundation (DFG) for funding this work under grant PROM-IMPRINT (project number 408011764) as well as under grant KN 1112/2-2.

From the bottom of my heart, thanks to my supervisor Stefan Kneifel! Thanks for getting me interested in ice and snow during my Master! For giving me the opportunity to be a PhD candidate and work in his working group! For guiding me all these years academically, scientifically and personally. Thanks for being crazy enough to go to Jülich with me on Saturday nights just to launch radiosondes! And for being so passionate about my work, you were a great supervisor! Thanks also for the great discussions and comments that helped improve this thesis. I am looking forward to the coming three years of exciting research with you! I would also like to thank the OPTIMIce group. Even if we haven't spent as much time together in person as I had wished, you were a great help over the past years and I always enjoyed the lively discussions during our group meetings and on social activities such as ice skating or playing beach volleyball. Thanks especially to José who has played a huge part in the reprocessing of the dataset and with the statistical analysis. Also thanks to Davide for your wisdom about snowflake scattering and providing a lot of input on my work!

I would also like to thank Dmitri Moisseev for being part of my doctoral committee. Thanks for the great discussions and suggestions during our committee meetings and for guiding my research! And thanks to Professor Yaping Shao for accepting to be a reviewer of this thesis.

A huge thank you also to Axel Seifert, Jan-Niklas Welss and Christoph Siewert! Our monthly IMPRINT meetings have helped me a lot in understanding McSnow and my simulations!

Thanks especially to Yannick, Jan-Niklas, Imke and Melanie for proof-reading parts of this thesis! Thanks also to my writing group who have definitely helped me improve my writing style, which was not easy because writing is not something I particularly enjoy ;)

Thanks to Alexander Myagkov for answering all my radar questions and problems! Thanks for being part of the DGL statistics study, your knowledge and insights helped improve it a lot!

Mario, thanks for adopting me as your swimming partner, eating Indian food, drinking beer with me and helping out in times of need! Also thanks to my climbing crew, you gave me a new sport to love and the Monday/Tuesday afternoon climbing sessions always brightened up my week! Thanks to my Cologne friends for going partying, having game nights, working out together and so much more.

Und danke an die wichtigsten Menschen in meinem Leben. Mama und Papa, danke dass ihr immer für mich da seid! Danke dass ihr einfach so nach Köln fahrt wenn es mir schlecht geht! Und dass wir so viele tolle Tage zusammen auf meinem Balkon, in Italien, in Esslingen oder sonst wo auf der Welt zusammen verbracht haben! Danke dass ihr mir immer freie Wahl gelassen habt wie ich mein Leben gestalten und mich immer zu 100% unterstützt in allem was ich tue! Ohne euch wäre ich auf jeden Fall nicht da wo ich heute bin. Danke auch an Kim, für die vielen Telefonate, fürs zuhören, für Caipi Abende, Friends und tolle Urlaube! Danke Ingrid für deine Unterstützung, Plätzchen

backen, Wein trinken,... Es bedeutet mir sehr viel dass du mich schon mein ganzes Leben begleitet hast! Linda, ich bin sehr dankbar und glücklich jemanden zu haben auf den man sich immer verlassen kann und der mich so gut kennt wie du! Danke dass du für mich da bist in schwierigen Zeiten! Danke Philipp, dass wir uns schon immer kennen und trotzdem gut verstehen ;)



## BIBLIOGRAPHY

---

- Andrić, J., M. R. Kumjian, D. S. Zrnić, J. M. Straka, and V. M. Melnikov (2013). "Polarimetric Signatures above the Melting Layer in Winter Storms: An Observational and Modeling Study." In: *Journal of Applied Meteorology and Climatology* 52.3, pp. 682–700. ISSN: 1558-8424. DOI: [10.1175/JAMC-D-12-028.1](https://doi.org/10.1175/JAMC-D-12-028.1).
- Atlas, David (2002). "Radar calibration: Some simple approaches." In: *Bulletin of the American Meteorological Society* 83.9, pp. 1313–1316.
- Aufdermaur, A. N. and D. A. Johnson (1972). "Charge separation due to riming in an electric field." In: *Quarterly Journal of the Royal Meteorological Society* 98.416, pp. 369–382. DOI: [10.1002/qj.49709841609](https://doi.org/10.1002/qj.49709841609).
- Bader, M., J. Gloster, J.L. Brownscombe, and P. Goldsmith (1974). "The production of sub-micron ice fragments by water droplets freezing in free fall or on accretion upon an ice surface." In: *Quarterly Journal of the Royal Meteorological Society* 100.425, pp. 420–426.
- Bailey, M. P. and J. Hallett (2009). "A comprehensive habit diagram for atmospheric ice crystals: Confirmation from the laboratory, AIRS II, and other field studies." In: *Journal of the Atmospheric Sciences* 66.9, pp. 2888–2899. DOI: [10.1175/2009JAS2883.1](https://doi.org/10.1175/2009JAS2883.1).
- Bailey, Matthew and John Hallett (2004). "Growth rates and habits of ice crystals between -20 °C and -70 °C." In: *Journal of the Atmospheric Sciences* 61.5, pp. 514–544. ISSN: 00224928. DOI: [10.1175/1520-0469\(2004\)061<0514:GRAH0I>2.0.CO;2](https://doi.org/10.1175/1520-0469(2004)061<0514:GRAH0I>2.0.CO;2).
- Barrett, A. I., C. D. Westbrook, J. C. Nicol, and T. H. M. Stein (2019). "Rapid ice aggregation process revealed through triple-wavelength Doppler spectrum radar analysis." In: *Atmospheric Chemistry and Physics* 19.8, pp. 5753–5769. DOI: [10.5194/acp-19-5753-2019](https://doi.org/10.5194/acp-19-5753-2019).
- Bechini, R., L. Baldini, and V. Chandrasekar (2013). "Polarimetric radar observations in the ice region of precipitating clouds at C-Band and X-Band radar frequencies." In: *Journal of Applied Meteorology and Climatology* 52.5, pp. 1147–1169. DOI: [10.1175/JAMC-D-12-055.1](https://doi.org/10.1175/JAMC-D-12-055.1).
- Böhm, J. P. (1992a). "A general hydrodynamic theory for mixed-phase microphysics. Part I: Drag and fall speed of hydrometeors." In: *Atmospheric research* 27.4, pp. 253–274. DOI: [https://doi.org/10.1016/0169-8095\(92\)90035-9](https://doi.org/10.1016/0169-8095(92)90035-9).
- (1992b). "A general hydrodynamic theory for mixed-phase microphysics. Part II: Collision kernels for coalescence." In: *Atmospheric research* 27.4, pp. 275–290. DOI: [https://doi.org/10.1016/0169-8095\(92\)90036-A](https://doi.org/10.1016/0169-8095(92)90036-A).
- Bohren, Craig F and Donald R Huffman (1983). *Absorption and scattering of light by small particles*. John Wiley & Sons. ISBN: 0-471-05772-X.
- Boucher, O., D. Randall, P. Artaxo, C. Bretherton, G. Feingold, P. Forster, V. M. Kerminen, Y. Kondo, H. Liao, U. Lohmann, P. Rasch, S. K. Satheesh, S. Sherwood, B. Stevens, and X. Y. Zhang (2013). "Clouds and Aerosols. Chapter 7 Climate Change 2013: The Physical Science Basis. Contribution of Working Group I to the Fifth Assessment Report of the Intergovernmental Panel on Climate Change." In: pp. 571–657. DOI: [10.1017/CB09781107415324.016](https://doi.org/10.1017/CB09781107415324.016).
- Brdar, S. and A. Seifert (2018). "McSnow: A Monte-Carlo Particle Model for Riming and Aggregation of Ice Particles in a Multidimensional Microphysical Phase Space."

- In: *Journal of Advances in Modeling Earth Systems* 10.1, pp. 187–206. DOI: [10.1002/2017MS001167](https://doi.org/10.1002/2017MS001167).
- Brangi, V. N. and V. Chandrasekar (2001). *Polarimetric Doppler Weather Radar: Principles and Applications*. Cambridge University Press. DOI: [10.1017/CB09780511541094](https://doi.org/10.1017/CB09780511541094).
- Bundesministerium des Inneren und für Heimat, Bundesministerium der Finanzen (2022). *Bericht zur Hochwasserkatastrophe 2021: Katastrophenhilfe, Wiederaufbau und Evaluierungsprozesse*. Last accessed 14 September 2022. URL: [https://www.bmi.bund.de/SharedDocs/downloads/DE/veroeffentlichungen/2022/abschlussbericht-hochwasserkatastrophe.pdf?\\_\\_blob=publicationFile&v=1](https://www.bmi.bund.de/SharedDocs/downloads/DE/veroeffentlichungen/2022/abschlussbericht-hochwasserkatastrophe.pdf?__blob=publicationFile&v=1).
- Cantrell, W. and A. Heymsfield (2005). “Production of Ice in Tropospheric Clouds: A Review.” In: *Bulletin of the American Meteorological Society* 86.6, pp. 795–808. ISSN: 0003-0007. DOI: [10.1175/BAMS-86-6-795](https://doi.org/10.1175/BAMS-86-6-795).
- Chandrasekar, V., L. Baldini, N. Bharadwaj, and P. L. Smith (2015). “Calibration procedures for global precipitation-measurement ground-validation radars.” In: *URSI Radio Science Bulletin* 2015.355, pp. 45–73. DOI: [doi:10.23919/URSIRSB.2015.7909473](https://doi.org/10.23919/URSIRSB.2015.7909473).
- Chen, J.-P. and D. Lamb (1994). “The theoretical basis for the parameterization of ice crystal habits: Growth by vapor deposition.” In: *Journal of Atmospheric Sciences* 51.9, pp. 1206–1222. DOI: [https://doi.org/10.1175/1520-0469\(1994\)051<1206:TTBFTP>2.0.CO;2](https://doi.org/10.1175/1520-0469(1994)051<1206:TTBFTP>2.0.CO;2).
- Connolly, P. J., C. Emersic, and P. R. Field (2012). “A laboratory investigation into the aggregation efficiency of small ice crystals.” In: *Atmospheric Chemistry and Physics* 12.4, pp. 2055–2076. DOI: [10.5194/acp-12-2055-2012](https://doi.org/10.5194/acp-12-2055-2012).
- Connolly, P. J., C. P. R. Saunders, M. W. Gallagher, K. N. Bower, M. J. Flynn, T. W. Choulaton, J. Whiteway, and R. P. Lawson (2005). “Aircraft observations of the influence of electric fields on the aggregation of ice crystals.” In: *Quarterly Journal of the Royal Meteorological Society* 131.608, pp. 1695–1712. DOI: <https://doi.org/10.1256/qj.03.217>.
- Cotton, W. R., G. J. Tripoli, R. M. Rauber, and E. A. Mulvihill (1986). “Numerical simulation of the effects of varying ice crystal nucleation rates and aggregation processes on orographic snowfall.” In: *Journal of Climate and Applied Meteorology*. last accessed 2022/05/09, pp. 1658–1680. URL: <http://www.jstor.org/stable/26183490>.
- D., Shupe M. and Intrieri J. M. (2004). “Cloud Radiative Forcing of the Arctic Surface: The Influence of Cloud Properties, Surface Albedo, and Solar Zenith Angle.” In: *Journal of Climate* 17.3, pp. 616–628. DOI: [10.1175/1520-0442\(2004\)017<0616:CRF0TA>2.0.CO;2](https://doi.org/10.1175/1520-0442(2004)017<0616:CRF0TA>2.0.CO;2).
- DeMott, P. J., A. J. Prenni, X. Liu, S. M. Kreidenweis, M. D. Petters, C. H. Twohy, M. S. Richardson, T. Eidhammer, and D. C. Rogers (2010). “Predicting global atmospheric ice nuclei distributions and their impacts on climate.” In: *Proceedings of the National Academy of Sciences of the United States of America* 107.25, pp. 11217–22. DOI: [10.1073/pnas.0910818107](https://doi.org/10.1073/pnas.0910818107).
- Dias Neto, J (2021). “Investigating aggregation in ice and snow clouds using novel combination of triple-frequency cloud radars and radar Doppler spectra.” PhD thesis. Cologne: Universität zu Köln. URL: <https://kups.ub.uni-koeln.de/53405/>.
- Dias Neto, J., S. Kneifel, D. Ori, S. Trömel, J. Handwerker, B. Bohn, N. Hermes, K. Mühlbauer, M. Lenefer, and C. Simmer (2019). “The TRIPLE-frequency and Polarimetric radar Experiment for improving process observations of winter precipitation.” In: *Earth System Science Data* 11.2, pp. 845–863. DOI: [10.5194/essd-11-845-2019](https://doi.org/10.5194/essd-11-845-2019).

- Draine, B. T. and P. J. Flatau (2013). "User guide for the discrete dipole approximation code DDSCAT 7.3." In: *arXiv preprint arXiv:1305.6497*. DOI: <https://doi.org/10.48550/arXiv.1305.6497>.
- Eliasson, S., S. A. Buehler, M. Milz, P. Eriksson, and V. O. John (2011). "Assessing observed and modelled spatial distributions of ice water path using satellite data." In: *Atmospheric Chemistry and Physics* 11.1, pp. 375–391. DOI: [10.5194/acp-11-375-2011](https://doi.org/10.5194/acp-11-375-2011).
- Fabry, F. (2015). *Radar Meteorology - Principles and Practice*. Cambridge: Cambridge University Press. ISBN: 978-1-107-07046-2.
- Fabry, F. and I. Zawadzki (1995). "Long-Term Radar Observations of the Melting Layer of Precipitation and Their Interpretation." In: *Journal of the Atmospheric Sciences* 52.7, pp. 838–851. DOI: [10.1175/1520-0469\(1995\)052<0838:LTR00T>2.0.CO;2](https://doi.org/10.1175/1520-0469(1995)052<0838:LTR00T>2.0.CO;2).
- Field, P. R. (2000). "Bimodal ice spectra in frontal clouds." In: *Quarterly Journal of the Royal Meteorological Society* 126.563, pp. 379–392. DOI: <https://doi.org/10.1002/qj.49712656302>.
- Field, P. R. and A. J. Heymsfield (Feb. 2003). "Aggregation and Scaling of Ice Crystal Size Distributions." In: *Journal of the Atmospheric Sciences* 60.3, pp. 544–560. DOI: [10.1175/1520-0469\(2003\)060<0544:AAS0IC>2.0.CO;2](https://doi.org/10.1175/1520-0469(2003)060<0544:AAS0IC>2.0.CO;2).
- (2015). "Importance of snow to global precipitation." In: *Geophysical Research Letters* 42.21, pp. 9512–9520. DOI: <https://doi.org/10.1002/2015GL065497>.
- Findeisen, W. (1940). "über die Entstehung der Gewitterelektrizität." In: *Meteor. Z* 57.6, p. 201.
- Görsdorf, U., V. Lehmann, M. Bauer-Pfundstein, G. Peters, D. Vavriv, V. Vinogradov, and V. Volkov (2015). "A 35-GHz polarimetric Doppler radar for long-term observations of cloud parameters—Description of system and data processing." In: *Journal of Atmospheric and Oceanic Technology* 32.4, pp. 675–690. DOI: <https://doi.org/10.1175/JTECH-D-14-00066.1>.
- Grabowski, Wojciech W., Hugh Morrison, Shin-Ichiro Shima, Gustavo C. Abade, Piotr Dziekan, and Hanna Pawlowska (May 2019). "Modeling of Cloud Microphysics: Can We Do Better?" In: *Bulletin of the American Meteorological Society* 100.4, pp. 655–672. DOI: [10.1175/BAMS-D-18-0005.1](https://doi.org/10.1175/BAMS-D-18-0005.1).
- Griffin, E. M., T. J. Schuur, and A. V. Ryzhkov (2018). "A polarimetric analysis of ice microphysical processes in snow, using quasi-vertical profiles." In: *Journal of Applied Meteorology and Climatology* 57.1, pp. 31–50. DOI: [10.1175/JAMC-D-17-0033.1](https://doi.org/10.1175/JAMC-D-17-0033.1).
- Griggs, DJ and TW Choularton (1986). "A laboratory study of secondary ice particle production by the fragmentation of rime and vapour-grown ice crystals." In: *Quarterly Journal of the Royal Meteorological Society* 112.471, pp. 149–163.
- Grzegorzczak, P. (2022). "Exploring the role of fragmentation of ice particles by laboratory studies." MA thesis. Université Clermont Auvergne, France.
- Hallett, J. and S. C. Mossop (1974). "Production of secondary ice particles during the riming process." In: *Nature* 249.5452, pp. 26–28. DOI: [10.1038/249026a0](https://doi.org/10.1038/249026a0).
- Heymsfield, A. J. (1982). "A Comparative Study of the Rates of Development of Potential Graupel and Hail Embryos in High Plains Storms." In: *Journal of Atmospheric Sciences* 39.12, pp. 2867–2897. DOI: [10.1175/1520-0469\(1982\)039<2867:ACS0TR>2.0.CO;2](https://doi.org/10.1175/1520-0469(1982)039<2867:ACS0TR>2.0.CO;2).
- Heymsfield, A. J., C. Schmitt, C. C. J. Chen, A. Bansemer, A. Gettelman, P. R. Field, and C. Liu (2020). "Contributions of the Liquid and Ice Phases to Global Surface Precipitation: Observations and Global Climate Modeling." In: *Journal of the Atmospheric Sciences* 77.8, pp. 2629–2648. DOI: [10.1175/JAS-D-19-0352.1](https://doi.org/10.1175/JAS-D-19-0352.1).

- Heymsfield, A. J. and C. D. Westbrook (2010). "Advances in the estimation of ice particle fall speeds using laboratory and field measurements." In: *Journal of the Atmospheric Sciences* 67.8, pp. 2469–2482. DOI: <https://doi.org/10.1175/2010JAS3379.1>.
- Heymsfield, Andrew, Aaron Bansemer, Norman B Wood, Guosheng Liu, Simone Tanelli, Ousmane O Sy, Michael Poellot, and Chuntao Liu (2018). "Toward improving ice water content and snow-rate retrievals from radars. Part II: Results from three wavelength radar–collocated in situ measurements and CloudSat–GPM–TRMM radar data." In: *Journal of Applied Meteorology and Climatology* 57.2, pp. 365–389. DOI: <https://doi.org/10.1175/JAMC-D-17-0164.1>.
- Hildebrand, P. H. and R. S. Sekhon (1974). "Objective Determination of the Noise Level in Doppler Spectra." In: *Journal of Applied Meteorology* 13.7, pp. 808–811. DOI: [10.1175/1520-0450\(1974\)013<0808:ODOTNL>2.0.CO;2](https://doi.org/10.1175/1520-0450(1974)013<0808:ODOTNL>2.0.CO;2).
- Hobbs, P. V. and DA Burrows (1966). "The electrification of an ice sphere moving through natural clouds." In: *Journal of Atmospheric Sciences* 23.6, pp. 757–763. DOI: [10.1175/1520-0469\(1966\)023<0757:TEOATS>2.0.CO;2](https://doi.org/10.1175/1520-0469(1966)023<0757:TEOATS>2.0.CO;2).
- Hobbs, P. V. and A. L. Rangno (1985). "Ice particle concentrations in clouds." In: *Journal of the atmospheric sciences* 42.23, pp. 2523–2549. DOI: [https://doi.org/10.1175/1520-0469\(1985\)042<2523:IPCIC>2.0.CO;2](https://doi.org/10.1175/1520-0469(1985)042<2523:IPCIC>2.0.CO;2).
- (1990). "Rapid development of high ice particle concentrations in small polar maritime cumuliform clouds." In: *Journal of Atmospheric Sciences* 47.22, pp. 2710–2722. DOI: [https://doi.org/10.1175/1520-0469\(1990\)047<2710:RDOHIP>2.0.CO;2](https://doi.org/10.1175/1520-0469(1990)047<2710:RDOHIP>2.0.CO;2).
- (1998). "Microstructures of low and middle-level clouds over the Beaufort Sea." In: *Quarterly Journal of the Royal Meteorological Society* 124.550, pp. 2035–2071. DOI: <https://doi.org/10.1002/qj.49712455012>.
- Hogan, R. J., R. Honeyager, J. Tyynelä, and S. Kneifel (2017). "Calculating the millimetre-wave scattering phase function of snowflakes using the self-similar Rayleigh–Gans Approximation." In: *Quarterly Journal of the Royal Meteorological Society* 143.703, pp. 834–844. DOI: <https://doi.org/10.1002/qj.2968>.
- Hogan, R. J., A. J. Illingworth, and H. Sauvageot (2000). "Measuring crystal size in cirrus using 35- and 94-GHz radars." In: *Journal of Atmospheric and Oceanic Technology* 17.1, pp. 27–37. DOI: [10.1175/1520-0426\(2000\)017<0027:MCSICU>2.0.CO;2](https://doi.org/10.1175/1520-0426(2000)017<0027:MCSICU>2.0.CO;2).
- Hogan, R. J. and C. D. Westbrook (2014). "Equation for the microwave backscatter cross section of aggregate snowflakes using the self-similar Rayleigh–Gans approximation." In: *Journal of the Atmospheric Sciences* 71.9, pp. 3292–3301. DOI: <https://doi.org/10.1175/JAS-D-13-0347.1>.
- Hosler, C. L. and R. E. Hallgren (1960). "The aggregation of small ice crystals." In: *Discussions of the Faraday Society* 30, pp. 200–207. DOI: [10.1039/DF9603000200](https://doi.org/10.1039/DF9603000200).
- Illingworth, A. J., R. J. Hogan, E. J. O'Connor, D. Bouniol, M. E. Brooks, J. Delanoë, D. P. Donovan, J. D. Eastment, N. Gaussiat, J. W F Goddard, M. Haeffelin, H. Klein Baltinik, O. A. Krasnov, J. Pelon, J. M. Piriou, A. Protat, H. W J Russchenberg, A. Seifert, A. M. Tompkins, G. J. van Zadelhoff, F. Vinit, U. Willen, D. R. Wilson, and C. L. Wrench (2007). "Cloudnet: Continuous evaluation of cloud profiles in seven operational models using ground-based observations." In: *Bulletin of the American Meteorological Society* 88.6, pp. 883–898. DOI: [10.1175/BAMS-88-6-883](https://doi.org/10.1175/BAMS-88-6-883).
- Isaac, G., A. Korolev, J. W. Srapp, S. Cober, F. Boudala, D. Marcotte, and V. Reich (2006). "Assessing the collection efficiency of natural cloud particles impacting the Nevzorov



- total water content probe." In: *44th AIAA Aerospace Sciences Meeting and Exhibit*, p. 1221. DOI: <https://doi.org/10.2514/6.2006-1221>.
- Jensen, A. and J. Harrington (2015). "Modeling ice crystal aspect ratio evolution during riming: A single-particle growth model." In: *Journal of the Atmospheric Sciences* 72.7, pp. 2569–2590. DOI: <https://doi.org/10.1175/JAS-D-14-0297.1>.
- Kajikawa, M., K. Kikuchi, Y. Asuma, Y. Inoue, and N. Sato (2000). "Aggregation of needle snow crystals." In: *Atmospheric research* 55.2, pp. 131–138. DOI: [https://doi.org/10.1016/S0169-8095\(00\)00061-2](https://doi.org/10.1016/S0169-8095(00)00061-2).
- Kanji, Z., L. Ladino, H. Wex, Y. Boose, M. Burkert-Kohn, D. Cziczo, and M. Krämer (2017). "Overview of ice nucleating particles." In: *Meteorological Monographs* 58, pp. 1–1. DOI: <https://doi.org/10.1175/AMSMONOGRAPH5-D-16-0006.1>.
- Karrer, M. K., S. Kneifel, D. Ori, C. Siewert, A. Seifert, and A. von Lerber (2020). "Ice Particle Properties Inferred from Aggregation Modelling." In: *Earth and Space Science Open Archive*, p. 52. DOI: [10.1002/essoar.10502128.1](https://doi.org/10.1002/essoar.10502128.1).
- Karrer, M., A. Seifert, D. Ori, and S. Kneifel (2021). "Improving the representation of aggregation in a two-moment microphysical scheme with statistics of multi-frequency Doppler radar observations." In: *Atmospheric Chemistry and Physics* 21.22, pp. 17133–17166. DOI: <https://doi.org/10.5194/acp-21-17133-2021>, 2021.
- Keith, WD and CPR Saunders (1989). "The collection efficiency of a cylindrical target for ice crystals." In: *Atmospheric research* 23.1, pp. 83–95. DOI: [https://doi.org/10.1016/0169-8095\(89\)90059-8](https://doi.org/10.1016/0169-8095(89)90059-8).
- Kennedy, P. C. and S. A. Rutledge (2011). "S-band dual-polarization radar observations of winter storms." In: *Journal of Applied Meteorology and Climatology* 50.4, pp. 844–858. DOI: [10.1175/2010JAMC2558.1](https://doi.org/10.1175/2010JAMC2558.1).
- Khain, A. P. and M. Pinsky (2018). *Physical Processes in Clouds and Cloud Modeling*. Cambridge University Press. DOI: [10.1017/9781139049481](https://doi.org/10.1017/9781139049481).
- Khvorostyanov, V. and J. Curry (2005). "Fall velocities of hydrometeors in the atmosphere: Refinements to a continuous analytical power law." In: *Journal of the Atmospheric Sciences* 62.12, pp. 4343–4357. DOI: <https://doi.org/10.1175/JAS3622.1>.
- Kim, M.-J. (2006). "Single scattering parameters of randomly oriented snow particles at microwave frequencies." In: *Journal of Geophysical Research: Atmospheres* 111.D14. DOI: <https://doi.org/10.1029/2005JD006892>.
- Kneifel, S., M. S. Kulie, and R. Bennartz (2011). "A triple-frequency approach to retrieve microphysical snowfall parameters." In: *Journal of Geophysical Research Atmospheres* 116.11, pp. 1–15. DOI: [10.1029/2010JD015430](https://doi.org/10.1029/2010JD015430).
- Kneifel, S., J. Leinonen, J. Tyynelä, D. Ori, and A. Battaglia (2020). "Scattering of hydrometeors." In: *Satellite precipitation measurement*. Springer, pp. 249–276. DOI: [https://doi.org/10.1007/978-3-030-24568-9\\_15](https://doi.org/10.1007/978-3-030-24568-9_15).
- Kneifel, S., A. von Lerber, J. Tiira, D. Moisseev, P. Kollias, and J. Leinonen (2015). "Observed relations between snowfall microphysics and triple-frequency radar measurements." In: *Journal of Geophysical Research: Atmospheres* 120.12, pp. 6034–6055. DOI: <https://doi.org/10.1002/2015JD023156>.
- Koenig, L. R. (Jan. 1963). "The Glaciating Behavior of Small Cumulonimbus Clouds." In: *Journal of the Atmospheric Sciences* 20.1, pp. 29–47. DOI: [10.1175/1520-0469\(1963\)020<0029:TGBOSC>2.0.CO;2](https://doi.org/10.1175/1520-0469(1963)020<0029:TGBOSC>2.0.CO;2).
- Kollias, P., Puigdomènech T. B., and A. Protat (2019). "Calibration of the 2007–2017 record of Atmospheric Radiation Measurements cloud radar observations using CloudSat."

- In: *Atmospheric Measurement Techniques* 12.9, pp. 4949–4964. DOI: <https://doi.org/10.5194/amt-12-4949-2019>.
- Korolev, A. (2007). “Limitations of the Wegener–Bergeron–Findeisen Mechanism in the Evolution of Mixed-Phase Clouds.” In: *Journal of the Atmospheric Sciences* 64.9, pp. 3372–3375. DOI: [10.1175/JAS4035.1](https://doi.org/10.1175/JAS4035.1).
- Korolev, A., M. P. Bailey, J. Hallett, and G. A. Isaac (Apr. 2004). “Laboratory and In Situ Observation of Deposition Growth of Frozen Drops.” In: *Journal of Applied Meteorology* 43.4, pp. 612–622. DOI: [10.1175/1520-0450\(2004\)043<0612:LAIS00>2.0.CO;2](https://doi.org/10.1175/1520-0450(2004)043<0612:LAIS00>2.0.CO;2).
- Korolev, A., I. Heckman, M. Wolde, A. S. Ackerman, A. M. Fridlind, L. A. Ladino, R. P. Lawson, J. Milbrandt, and E. Williams (2020). “A new look at the environmental conditions favorable to secondary ice production.” In: *Atmospheric Chemistry and Physics* 20.3, pp. 1391–1429. DOI: [10.5194/acp-20-1391-2020](https://doi.org/10.5194/acp-20-1391-2020).
- Korolev, A. and G. Isaac (2005). “Shattering during sampling by OAPs and HVPS. Part I: Snow particles.” In: *Journal of Atmospheric and Oceanic Technology* 22.5, pp. 528–542. DOI: <https://doi.org/10.1175/JTECH1720.1>.
- Korolev, A. and T. Leisner (2020). “Review of experimental studies of secondary ice production.” In: *Atmospheric Chemistry and Physics* 20.20, pp. 11767–11797. DOI: [10.5194/acp-20-11767-2020](https://doi.org/10.5194/acp-20-11767-2020).
- Küchler, N., S. Kneifel, U. Löhnert, P. Kollias, H. Czekala, and T. Rose (2017). “A W-band radar-radiometer system for accurate and continuous monitoring of clouds and precipitation.” In: *Journal of Atmospheric and Oceanic Technology* 34.11, pp. 2375–2392. DOI: [10.1175/JTECH-D-17-0019.1](https://doi.org/10.1175/JTECH-D-17-0019.1).
- Kumjian, M. R. (2013). “Principles and Applications of Dual-Polarization Weather Radar. Part I: Description of the Polarimetric Radar Variables.” In: *Journal of Operational Meteorology* 1.19, pp. 226–242. DOI: [10.15191/nwajom.2013.0119](https://doi.org/10.15191/nwajom.2013.0119).
- Kumjian, M. R., O. P. Prat, K. J. Reimel, M. van Lier-Walqui, and H. C. Morrison (2022). “Dual-Polarization Radar Fingerprints of Precipitation Physics: A Review.” In: *Remote Sensing* 14.15, p. 3706. DOI: [10.3390/rs14153706](https://doi.org/10.3390/rs14153706).
- Kumjian, M. R. and A. Ryzhkov (2010). “The impact of evaporation on polarimetric characteristics of rain: Theoretical model and practical implications.” In: *Journal of Applied Meteorology and Climatology* 49.6, pp. 1247–1267. DOI: <https://doi.org/10.1175/2010JAMC2243.1>.
- Kumjian, Matthew R. (2018). “Weather Radars.” In: *Remote Sensing of Clouds and Precipitation*. Ed. by Constantin Andronache. Cham: Springer International Publishing, pp. 15–63. ISBN: 978-3-319-72583-3. DOI: [10.1007/978-3-319-72583-3\\_2](https://doi.org/10.1007/978-3-319-72583-3_2).
- Lamb, D and WD Scott (1972). “Linear growth rates of ice crystals grown from the vapor phase.” In: *Journal of Crystal Growth* 12.1, pp. 21–31. DOI: [https://doi.org/10.1016/0022-0248\(72\)90333-8](https://doi.org/10.1016/0022-0248(72)90333-8).
- Lamb, Dennis and Johannes Verlinde (2011). *Physics and chemistry of clouds*. Cambridge University Press.
- Latham, J. and B. J. Mason (1961). “Generation of electric charge associated with the formation of soft hail in thunderclouds.” In: *Proceedings of the Royal Society of London. Series A. Mathematical and Physical Sciences* 260.1303, pp. 537–549. DOI: <https://doi.org/10.1098/rspa.1961.0052>.
- Lawson, R. P., C. Gurganus, S. Woods, and R. Brientjes (2017). “Aircraft Observations of Cumulus Microphysics Ranging from the Tropics to Midlatitudes: Implications for a



- "New" Secondary Ice Process." In: *Journal of the Atmospheric Sciences* 74.9, pp. 2899–2920. DOI: [10.1175/JAS-D-17-0033.1](https://doi.org/10.1175/JAS-D-17-0033.1).
- Lawson, R. P., R. E. Stewart, and L. J. Angus (Nov. 1998). "Observations and Numerical Simulations of the Origin and Development of Very Large Snowflakes." In: *Journal of the Atmospheric Sciences* 55.21, pp. 3209–3229. DOI: [10.1175/1520-0469\(1998\)055<3209:OANSOT>2.0.CO;2](https://doi.org/10.1175/1520-0469(1998)055<3209:OANSOT>2.0.CO;2).
- Lawson, R. P., R. E. Stewart, J. W. Strapp, and G. A. Isaac (1993). "Aircraft observations of the origin and growth of very large snowflakes." In: *Geophysical Research Letters* 20.1, pp. 53–56. DOI: <https://doi.org/10.1029/92GL02917>.
- Leinonen, J (2013). *Python code for T-matrix scattering calculations*.
- Leinonen, J., S. Kneifel, and R. J. Hogan (2018). "Evaluation of the Rayleigh–Gans approximation for microwave scattering by rimed snowflakes." In: *Quarterly Journal of the Royal Meteorological Society* 144, pp. 77–88. DOI: <https://doi.org/10.1002/qj.3093>.
- Leinonen, J. and D. Moisseev (2015). "What do triple-frequency radar signatures reveal about aggregate snowflakes?" In: *Journal of Geophysical Research: Atmospheres* 120.1, pp. 229–239. DOI: <https://doi.org/10.1002/2014JD022072>.
- Leinonen, Jussi et al. (2013). "Impact of the microstructure of precipitation and hydrometeors on multi-frequency radar observations." PhD thesis.
- Li, Y. and G. A. Somorjai (2007). "Surface Premelting of Ice." In: *The Journal of Physical Chemistry C* 111.27, pp. 9631–9637. DOI: [10.1021/jp071102f](https://doi.org/10.1021/jp071102f).
- Liao, L., R. Meneghini, T. Iguchi, and A. Detwiler (2005). "Use of dual-wavelength radar for snow parameter estimates." In: *Journal of Atmospheric and Oceanic Technology* 22.10, pp. 1494–1506. DOI: <https://doi.org/10.1175/JTECH1808.1>.
- Liao, L., R. Meneghini, L. Tian, and G. M. Heymsfield (2008). "Retrieval of Snow and Rain From Combined X- and W-Band Airborne Radar Measurements." In: *IEEE Transactions on Geoscience and Remote Sensing* 46.5, pp. 1514–1524. DOI: [10.1109/TGRS.2008.916079](https://doi.org/10.1109/TGRS.2008.916079).
- Libbrecht, K. G. (2017). "Physical dynamics of ice crystal growth." In: *Annu. Rev. Mater. Res* 47.1, pp. 271–295. DOI: <https://doi.org/10.1146/annurev-matsci-070616-124135>.
- Liu, G. (2008). "A database of microwave single-scattering properties for nonspherical ice particles." In: *Bulletin of the American Meteorological Society* 89.10, pp. 1563–1570. DOI: <https://doi.org/10.1175/2008BAMS2486.1>.
- Locatelli, J. D. and P. V. Hobbs (1974). "Fall speeds and masses of solid precipitation particles." In: *Journal of Geophysical Research* (1896-1977) 79.15, pp. 2185–2197. DOI: [10.1029/JC079i015p02185](https://doi.org/10.1029/JC079i015p02185).
- Löffler-Mang, Martin and Jürg Joss (2000). "An optical disdrometer for measuring size and velocity of hydrometeors." In: *Journal of Atmospheric and Oceanic Technology* 17.2, pp. 130–139. ISSN: 07390572. DOI: [10.1175/1520-0426\(2000\)017<0130:AODFMS>2.0.CO;2](https://doi.org/10.1175/1520-0426(2000)017<0130:AODFMS>2.0.CO;2).
- Lohmann, U. (2016). *An introduction to clouds : from the microscale to climate*. Cambridge: Cambridge University Press. ISBN: 9781107018228.
- Löhnert, U., J. H. Schween, C. Acquistapace, K. Ebell, M. Maahn, M. Barrera-Verdejo, A. Hirsikko, B. Bohn, A. Knaps, E. O'Connor, C. Simmer, A. Wahner, and S. Crewell (2015). "JOYCE: Jülich Observatory for Cloud Evolution." In: *Bulletin of the American Meteorological Society* 96.7, pp. 1157–1174. DOI: [10.1175/BAMS-D-14-00105.1](https://doi.org/10.1175/BAMS-D-14-00105.1).
- Lubin, D., D. Zhang, I. Silber, R. C. Scott, P. Kalogeras, A. Battaglia, D. H. Bromwich, M. Cadetdu, E. Eloranta, A. Fridlind, A. Frossard, K. M. Hines, S. Kneifel, W. R. Leitch,

- W. Lin, J. Nicolas, H. Powers, P. K. Quinn, P. Rowe, L. M. Russell, S. Sharma, J. Verlinde, and A. M. Vogelmann (2020). "AWARE: The Atmospheric Radiation Measurement (ARM) West Antarctic Radiation Experiment." In: *Bulletin of the American Meteorological Society* 101.7, E1069–E1091. DOI: [10.1175/BAMS-D-18-0278.1](https://doi.org/10.1175/BAMS-D-18-0278.1).
- Maahn, M. (2015). "Exploiting vertically pointing Doppler radar for advancing snow and ice cloud observations." PhD thesis. Universität zu Köln.
- Macklin, W. C. (1960). "The production of ice splinters during riming." In: *Nubila* 3, pp. 30–33.
- Mason, B. J. (1953). "The growth of ice crystals in a supercooled water cloud." In: *Quarterly Journal of the Royal Meteorological Society* 79.339, pp. 104–111. DOI: <https://doi.org/10.1002/qj.49707933909>.
- Mason, B. J. and J. Maybank (1960). "The fragmentation and electrification of freezing water drops." In: *Quarterly Journal of the Royal Meteorological Society* 86.368, pp. 176–185. DOI: [10.1002/qj.49708636806](https://doi.org/10.1002/qj.49708636806).
- Mason, S. L., R. J. Hogan, C. D. Westbrook, S. Kneifel, and D. Moisseev (2019). "The importance of particle size distribution shape for triple-frequency radar retrievals of the morphology of snow." In: *Atmospheric Measurement Techniques Discussions*, pp. 1–30. DOI: [10.5194/amt-2019-100](https://doi.org/10.5194/amt-2019-100).
- Matrosov, S. Y. (1992). "Radar Reflectivity in Snowfall." In: *IEEE Transactions on Geoscience and Remote Sensing* 30.3, pp. 454–461. DOI: [10.1109/36.142923](https://doi.org/10.1109/36.142923).
- Mech, M., M. Maahn, S. Kneifel, D. Ori, E. Orlandi, P. Kollias, V. Schemann, and S. Crewell (2020). "PAMTRA 1.0: A Passive and Active Microwave radiative TRANSfer tool for simulating radiometer and radar measurements of the cloudy atmosphere." In: *Geoscientific Model Development Discussions* 2020, pp. 1–34. DOI: [10.5194/gmd-2019-356](https://doi.org/10.5194/gmd-2019-356).
- Mignani, C., J. M. Creamean, L. Zimmermann, C. Alewell, and F. Conen (2019). "New type of evidence for secondary ice formation at around -15 °C in mixed-phase clouds." In: *Atmospheric Chemistry and Physics* 19.2, pp. 877–886. DOI: [10.5194/acp-19-877-2019](https://doi.org/10.5194/acp-19-877-2019).
- Mishchenko, M. I. and L. D. Travis (1998). "Capabilities and limitations of a current FORTRAN implementation of the T-matrix method for randomly oriented, rotationally symmetric scatterers." In: *Journal of Quantitative Spectroscopy and Radiative Transfer* 60.3, pp. 309–324. DOI: [https://doi.org/10.1016/S0022-4073\(98\)00008-9](https://doi.org/10.1016/S0022-4073(98)00008-9).
- Mishchenko, M. I., L. D. Travis, and A. A. Lacis (2002). *Scattering, absorption, and emission of light by small particles*. Cambridge university press.
- Mishchenko, M. I., L. D. Travis, and D. W. Mackowski (1996). "T-matrix computations of light scattering by nonspherical particles: A review." In: *Journal of Quantitative Spectroscopy and Radiative Transfer* 55.5, pp. 535–575. DOI: [https://doi.org/10.1016/0022-4073\(96\)00002-7](https://doi.org/10.1016/0022-4073(96)00002-7).
- Mishchenko, M. I., G. Videen, V. A. Babenko, N. G. Khlebtsov, and T. Wriedt (2004). "T-matrix theory of electromagnetic scattering by particles and its applications: a comprehensive reference database." In: *J. Quant. Spectrosc. Radiat. Transfer* 88.1-3, pp. 357–406. DOI: [doi:10.1016/j.jqsrt.2004.05.002](https://doi.org/10.1016/j.jqsrt.2004.05.002).
- Mitchell, D. L. (1988). "Evolution of Snow-Size Spectra in Cyclonic Storms. Part I: Snow Growth by Vapor Deposition and Aggregation." In: *J. Atmos. Sci* 45, pp. 3431–3451. DOI: [https://doi.org/10.1175/1520-0469\(1988\)045<3431:E0SSSI>2.0.CO;2](https://doi.org/10.1175/1520-0469(1988)045<3431:E0SSSI>2.0.CO;2).
- Mitchell, D. L., S. K. Chai, Y. Liu, A. J. Heymsfield, and Y. Dong (1996). "Modeling cirrus clouds. Part I: Treatment of bimodal size spectra and case study analysis." In: *Journal*

- of the atmospheric sciences 53.20, pp. 2952–2966. DOI: [https://doi.org/10.1175/1520-0469\(1996\)053<2952:MCCPIT>2.0.CO;2](https://doi.org/10.1175/1520-0469(1996)053<2952:MCCPIT>2.0.CO;2).
- Moisseev, D. N. and V. Chandrasekar (2007). “Nonparametric estimation of raindrop size distributions from dual-polarization radar spectral observations.” In: *Journal of Atmospheric and Oceanic Technology* 24.6, pp. 1008–1018. DOI: <https://doi.org/10.1175/JTECH2024.1>.
- Moisseev, D. N., S. Lautaportti, J. Tyynela, and S. Lim (2015). “Dual-polarization radar signatures in snowstorms: Role of snowflake aggregation.” In: *Journal of Geophysical Research* 120.24, pp. 12,644–12,665. DOI: [10.1002/2015JD023884](https://doi.org/10.1002/2015JD023884).
- Moisseev, D. N., E. Saltikoff, and M. Leskinen (2009). *Dual-polarization weather radar observations of snow growth processes*. 34th Conf. on Radar Meteorology, Williamsburg, VA, Amer. Meteor. Soc., 13B. 2.
- Morrison, H., M. van Lier-Walqui, A. M. Fridlind, W. W. Grabowski, J. Y. Harrington, C. Hoose, A. Korolev, M. R. Kumjian, J. A. Milbrandt, H. Pawlowska, D. J. Posselt, O. P. Prat, K. J. Reimel, S.-I. Shima, B. van Didenhoven, and L. Xue (2020). “Confronting the Challenge of Modeling Cloud and Precipitation Microphysics.” In: *Journal of Advances in Modeling Earth Systems* 12.8. DOI: <https://doi.org/10.1029/2019MS001689>.
- Morrison, Hugh and Jason A. Milbrandt (Jan. 2015). “Parameterization of Cloud Microphysics Based on the Prediction of Bulk Ice Particle Properties. Part I: Scheme Description and Idealized Tests.” In: *Journal of the Atmospheric Sciences* 72.1, pp. 287–311. ISSN: 0022-4928. DOI: [10.1175/JAS-D-14-0065.1](https://doi.org/10.1175/JAS-D-14-0065.1).
- Mossop, S. C. (1978). “Some factors governing ice particle multiplication in cumulus clouds.” In: *Journal of Atmospheric Sciences* 35.10, pp. 2033–2037. DOI: [https://doi.org/10.1175/1520-0469\(1978\)035<2033:SFGIPM>2.0.CO;2](https://doi.org/10.1175/1520-0469(1978)035<2033:SFGIPM>2.0.CO;2).
- (1985). “Secondary ice particle production during rime growth: The effect of drop size distribution and rimer velocity.” In: *Quarterly Journal of the Royal Meteorological Society* 111.470, pp. 1113–1124. DOI: [10.1002/qj.49711147012](https://doi.org/10.1002/qj.49711147012).
- Mossop, S. C. and J. Hallett (1974). “Ice Crystal Concentration in Cumulus Clouds: Influence of the Drop Spectrum.” In: *Science* 186.4164, pp. 632–634. DOI: [10.1126/science.186.4164.632](https://doi.org/10.1126/science.186.4164.632).
- Mróz, K., A. Battaglia, S. Kneifel, L. P. D’Adderio, and J. Dias Neto (2020). “Triple-Frequency Doppler Retrieval of Characteristic Raindrop Size.” In: *Earth and Space Science* 7.3. DOI: [10.1029/2019EA000789](https://doi.org/10.1029/2019EA000789).
- Mróz, K., A. Battaglia, S. Kneifel, L. von Terzi, M. Karrer, and D. Ori (2021). “Linking rain into ice microphysics across the melting layer in stratiform rain: a closure study.” In: *Atmospheric Measurement Techniques* 14.1, pp. 511–529. DOI: <https://doi.org/10.5194/amt-14-511-2021>.
- Mülmenstädt, J., O. Sourdeval, J. Delanoë, and J. Quaas (2015). “Frequency of occurrence of rain from liquid-, mixed-, and ice-phase clouds derived from A-Train satellite retrievals.” In: *Geophysical Research Letters* 42.15, pp. 6502–6509. DOI: [10.1002/2015GL064604](https://doi.org/10.1002/2015GL064604).
- Myagkov, A., S. Kneifel, and T. Rose (2020). “Evaluation of the reflectivity calibration of W-band radars based on observations in rain.” In: *Atmospheric Measurement Techniques* 13.11, pp. 5799–5825. DOI: <https://doi.org/10.5194/amt-13-5799-2020>.
- Myagkov, A., P. Seifert, U. Wandinger, J. Bühl, and R. Engelmann (2016). “Relationship between temperature and apparent shape of pristine ice crystals derived from polarimetric cloud radar observations during the ACCEPT campaign.” In: *Atmospheric*

- Measurement Techniques* 9.8, pp. 3739–3754. DOI: <https://doi.org/10.5194/amt-9-3739-2016>.
- Ori, D., V. Schemann, M. Karrer, J. Dias Neto, L. von Terzi, A. Seifert, and S. Kneifel (2020). “Evaluation of ice particle growth in ICON using statistics of multi-frequency Doppler cloud radar observations.” In: *Quarterly Journal of the Royal Meteorological Society*. DOI: [10.1002/qj.3875](https://doi.org/10.1002/qj.3875).
- Ori, D., L. von Terzi, M. Karrer, and K. Kneifel (Mar. 2021). “SnowScatt 1.0: Consistent model of microphysical and scattering properties of rimed and unrimed snowflakes based on the self-similar Rayleigh-Gans approximation.” In: *Geoscientific Model Development* 14 (3), pp. 1511–1531. ISSN: 19919603. DOI: [10.5194/gmd-14-1511-2021](https://doi.org/10.5194/gmd-14-1511-2021).
- Oue, M., P. Kollias, A. Ryzhkov, and E. P. Luke (2018). “Toward exploring the synergy between cloud radar polarimetry and Doppler spectral analysis in deep cold precipitating systems in the Arctic.” In: *Journal of Geophysical Research: Atmospheres* 123.5, pp. 2797–2815. DOI: <https://doi.org/10.1002/2017JD027717>.
- Petty, G. W. and W. Huang (2011). “The Modified Gamma Size Distribution Applied to Inhomogeneous and Nonspherical Particles: Key Relationships and Conversions.” In: *Journal of the Atmospheric Sciences* 68.7, pp. 1460–1473. DOI: [10.1175/2011JAS3645.1](https://doi.org/10.1175/2011JAS3645.1).
- Petty, Grant W and Wei Huang (2010). “Microwave backscatter and extinction by soft ice spheres and complex snow aggregates.” In: *Journal of the Atmospheric Sciences* 67.3, pp. 769–787. DOI: <https://doi.org/10.1175/2009JAS3146.1>.
- Phillips, V. T.J., M. Formenton, A. Bansemer, I. Kudzotsa, and B. Lienert (2015). “A parameterization of sticking efficiency for collisions of snow and graupel with ice crystals: Theory and comparison with observations.” In: *Journal of the Atmospheric Sciences* 72.12, pp. 4885–4902. DOI: [10.1175/JAS-D-14-0096.1](https://doi.org/10.1175/JAS-D-14-0096.1).
- Phillips, V. T.J., S. Patade, J. Gutierrez, and A. Bansemer (2018). “Secondary ice production by fragmentation of freezing drops: Formulation and theory.” In: *Journal of the Atmospheric Sciences* 75.9, pp. 3031–3070. DOI: <https://doi.org/10.1175/JAS-D-17-0190.1>.
- Phillips, V. T.J., J.-I. Yano, and A. Khain (2017). “Ice multiplication by breakup in ice–ice collisions. Part I: Theoretical formulation.” In: *Journal of the Atmospheric Sciences* 74.6, pp. 1705–1719. DOI: <https://doi.org/10.1175/JAS-D-16-0224.1>.
- Protat, A. and C. R. Williams (2011). “The accuracy of radar estimates of ice terminal fall speed from vertically pointing doppler radar measurements.” In: *Journal of Applied Meteorology and Climatology* 50 (10), pp. 2120–2138. ISSN: 15588424. DOI: [10.1175/JAMC-D-10-05031.1](https://doi.org/10.1175/JAMC-D-10-05031.1).
- Pruppacher, H. R. and J. D. Klett (1997). *Microphysics of Clouds and Precipitation*. Dordrecht: Kluwer Academic Publishers. ISBN: 0792342119.
- Raghavan, S. (2003). *Radar Meteorology*. Kluwer Academic Publishers. ISBN: 9781402016042.
- Rangno, A. L. and P. V. Hobbs (2001). “Ice particles in stratiform clouds in the Arctic and possible mechanisms for the production of high ice concentrations.” In: *Journal of Geophysical Research: Atmospheres* 106.D14, pp. 15065–15075. DOI: <https://doi.org/10.1029/2000JD900286>.
- Rinehart, Ronald E (2005). *Radar for meteorologists, fifth edition*. Rinehart Publications.
- Schrom, R. S. and M. R. Kumjian (2016). “Connecting microphysical processes in Colorado winter storms with vertical profiles of radar observations.” In: *Journal of Applied Meteorology and Climatology* 55.8, pp. 1771–1787. DOI: <https://doi.org/10.1175/JAMC-D-15-0338.1>.



- Schrom, R. S., M. R. Kumjian, and Y. Lu (2015). "Polarimetric radar signatures of dendritic growth zones within Colorado winter storms." In: *Journal of Applied Meteorology and Climatology* 54.12, pp. 2365–2388. DOI: [10.1175/JAMC-D-15-0004.1](https://doi.org/10.1175/JAMC-D-15-0004.1).
- Schwarzenboeck, A., V. Shcherbakov, R. Lefevre, J. F. Gayet, Y. Pointin, and C. Duroure (2009). "Indications for stellar-crystal fragmentation in Arctic clouds." In: *Atmospheric Research* 92.2, pp. 220–228. DOI: [10.1016/j.atmosres.2008.10.002](https://doi.org/10.1016/j.atmosres.2008.10.002).
- Seifert, A. (2008). "On the Parameterization of Evaporation of Raindrops as Simulated by a One-Dimensional Rainshaft Model." In: *Journal of the Atmospheric Sciences* 65.11, pp. 3608–3619. DOI: [10.1175/2008JAS2586.1](https://doi.org/10.1175/2008JAS2586.1).
- Seifert, A., J. Leinonen, C. Siewert, and S. Kneifel (2019). "The Geometry of Rimed Aggregate Snowflakes: A Modeling Study." In: *Journal of Advances in Modeling Earth Systems* 11.3, pp. 712–731. DOI: <https://doi.org/10.1029/2018MS001519>.
- Shima, S., K. Kusano, A. Kawano, T. Sugiyama, and S. Kawahara (2009). "The super-droplet method for the numerical simulation of clouds and precipitation: a particle-based and probabilistic microphysics model coupled with a non-hydrostatic model." In: *Quarterly Journal of the Royal Meteorological Society* 135.642, pp. 1307–1320. DOI: <https://doi.org/10.1002/qj.441>.
- Shima, S., Y. Sato, A. Hashimoto, and R. Misumi (2020). "Predicting the morphology of ice particles in deep convection using the super-droplet method: development and evaluation of SCALE-SDM 0.2.5-2.2.0, -2.2.1, and -2.2.2." In: *Geoscientific Model Development* 13.9, pp. 4107–4157. DOI: [10.5194/gmd-13-4107-2020](https://doi.org/10.5194/gmd-13-4107-2020).
- Slater, B. and A. Michaelides (2019). "Surface premelting of water ice." In: *Nature Reviews Chemistry* 3.3, pp. 172–188. DOI: [10.1038/s41570-019-0080-8](https://doi.org/10.1038/s41570-019-0080-8).
- Sorensen, C. M. (2001). "Light scattering by fractal aggregates: a review." In: *Aerosol Science & Technology* 35.2, pp. 648–687. DOI: [10.1080/02786820117868](https://doi.org/10.1080/02786820117868).
- Stein, T. H.M., C. D. Westbrook, and J. C. Nicol (2015). "Fractal geometry of aggregate snowflakes revealed by triple-wavelength radar measurements." In: *Geophysical Research Letters* 42.1, pp. 176–183. DOI: <https://doi.org/10.1002/2014GL062170>.
- Stephens, Graeme, David Winker, Jacques Pelon, Charles Trepte, Deborah Vane, Cheryl Yuhas, Tristan L'ecuyer, and Matthew Lebsock (2018). "CloudSat and CALIPSO within the A-Train: Ten years of actively observing the Earth system." In: *Bulletin of the American Meteorological Society* 99.3, pp. 569–581. DOI: <https://doi.org/10.1175/BAMS-D-16-0324.1>.
- Stubenrauch, C. J., W. B. Rossow, S. Kinne, S. Ackerman, G. Cesana, H. Chepfer, L. Di Girolamo, B. Getzewich, A. Guignard, A. Heidinger, B. C. Maddux, W. P. Menzel, P. Minnis, C. Pearl, S. Platnick, C. Poulsen, J. Riedi, S. Sun-Mack, A. Walther, D. Winker, S. Zeng, and G. Zhao (2013). "Assessment of global cloud datasets from satellites: Project and database initiated by the GEWEX radiation panel." In: *Bulletin of the American Meteorological Society* 94.7, pp. 1031–1049. DOI: [10.1175/BAMS-D-12-00117.1](https://doi.org/10.1175/BAMS-D-12-00117.1).
- Sullivan, S. C., C. Hoose, A. Kiselev, T. Leisner, and A. Nenes (2018). "Initiation of secondary ice production in clouds." In: *Atmospheric Chemistry and Physics* 18.3, pp. 1593–1610. DOI: <https://doi.org/10.5194/acp-18-1593-2018>.
- Takahashi, T. (1993). "High ice crystal production in winter cumuli over the Japan Sea." In: *Geophysical Research Letters* 20.6, pp. 451–454. DOI: [10.1029/93GL00613](https://doi.org/10.1029/93GL00613).
- (2014). "Influence of Liquid Water Content and Temperature on the Form and Growth of Branched Planar Snow Crystals in a Cloud." In: *Journal of the Atmospheric Sciences* 71.11, pp. 4127–4142. DOI: [10.1175/JAS-D-14-0043.1](https://doi.org/10.1175/JAS-D-14-0043.1).

- Takahashi, T., Y. Nagao, and Y. Kushiya (1995). "Possible High Ice Particle Production during Graupel–Graupel Collisions." In: *Journal of the Atmospheric Sciences* 52.24, pp. 4523–4527. DOI: [10.1175/1520-0469\(1995\)052<4523:PHIPPD>2.0.CO;2](https://doi.org/10.1175/1520-0469(1995)052<4523:PHIPPD>2.0.CO;2).
- Thurai, M., G. J. Huang, V. N. Bringi, W. L. Randeu, and M. Schönhuber (2007). "Drop shapes, model comparisons, and calculations of polarimetric radar parameters in rain." In: *Journal of Atmospheric and Oceanic Technology* 24.6, pp. 1019–1032. DOI: <https://doi.org/10.1175/JTECH2051.1>.
- Trapp, R. J., D. M. Schultz, A. V. Ryzhkov, and R. L. Holle (2001). "Multiscale structure and evolution of an Oklahoma winter precipitation event." In: *Monthly weather review* 129.3, pp. 486–501. DOI: [https://doi.org/10.1175/1520-0493\(2001\)129<0486:MSAE0A>2.0.CO;2](https://doi.org/10.1175/1520-0493(2001)129<0486:MSAE0A>2.0.CO;2).
- Tridon, F. and A. Battaglia (2015). "Dual-frequency radar Doppler spectral retrieval of rain drop size distributions and entangled dynamics variables." In: *Journal of Geophysical Research: Atmospheres* 120.11, pp. 5585–5601. DOI: <https://doi.org/10.1002/2014JD023023>.
- Tridon, F., A. Battaglia, and S. Kneifel (2020). "Estimating total attenuation using Rayleigh targets at cloud top: applications in multilayer and mixed-phase clouds observed by ground-based multifrequency radars." In: *Atmospheric Measurement Techniques* 13.9, pp. 5065–5085. DOI: [10.5194/amt-13-5065-2020](https://doi.org/10.5194/amt-13-5065-2020).
- Trömel, S., A. V. Ryzhkov, B. Hickman, K. A. I. Mühlbauer, and C. Simmer (2019). "Polarimetric radar variables in the layers of melting and dendritic growth at X band—Implications for a nowcasting strategy in stratiform rain." In: *Journal of Applied Meteorology and Climatology* 58.11, pp. 2497–2522. DOI: [10.1175/JAMC-D-19-0056.1](https://doi.org/10.1175/JAMC-D-19-0056.1).
- Vardiman, L. (1978). "The Generation of Secondary Ice Particles in Clouds by Crystal–Crystal Collision." In: *Journal of Atmospheric Sciences* 35, pp. 2168–2180. ISSN: 0022-4928. DOI: [10.1175/1520-0469\(1978\)035<2168:TGOSIP>2.0.CO;2](https://doi.org/10.1175/1520-0469(1978)035<2168:TGOSIP>2.0.CO;2).
- Von Terzi, L., J. Dias Neto, D. Ori, A. Myagkov, and S. Kneifel (2022). "Ice microphysical processes in the dendritic growth layer: a statistical analysis combining multi-frequency and polarimetric Doppler cloud radar observations." In: *Atmospheric Chemistry and Physics* 22, pp. 11795–11821. DOI: <https://doi.org/10.5194/acp-22-11795-2022>.
- Ward, P. J., V. Blauhut, N. Bloemendaal, E. J. Daniell, C. M. De Ruiter, J. M. Duncan, R. Emberson, F. S. Jenkins, D. Kirschbaum, M. Kunz, S. Mohr, S. Muis, A. G. Riddell, A. Schäfer, T. Stanley, I. E.T. Veldkamp, and W. C. Hessel (Apr. 2020). "Review article: Natural hazard risk assessments at the global scale." In: *Natural Hazards and Earth System Sciences* 20 (4), pp. 1069–1096. DOI: [10.5194/nhess-20-1069-2020](https://doi.org/10.5194/nhess-20-1069-2020).
- Westbrook, C. D. (2014). "Rayleigh scattering by hexagonal ice crystals and the interpretation of dual-polarisation radar measurements." In: *Quarterly Journal of the Royal Meteorological Society* 140.683, pp. 2090–2096. DOI: <https://doi.org/10.1002/qj.2262>.
- Wieder, J., N. Ihn, C. Mignani, M. Haarig, J. Bühl, P. Seifert, R. Engelmann, F. Ramelli, Z. A. Kanji, U. Lohmann, and J. Henneberger (2022). "Retrieving ice nucleating particle concentration and ice multiplication factors using active remote sensing validated by in situ observations." In: *Atmospheric Chemistry and Physics Discussions* 22, pp. 9767–9797. DOI: <https://doi.org/10.5194/acp-22-9767-2022>.
- Yano, J.-I. and V. T.J. Phillips (2011). "Ice–ice collisions: An ice multiplication process in atmospheric clouds." In: *Journal of the Atmospheric Sciences* 68.2, pp. 322–333. DOI: <https://doi.org/10.1175/2010JAS3607.1>.



- Yano, J.-I., V. T.J. Phillips, and V. Kanawade (2016). "Explosive ice multiplication by mechanical break-up in ice-ice collisions: a dynamical system-based study." In: *Quarterly Journal of the Royal Meteorological Society* 142.695, pp. 867–879. DOI: <https://doi.org/10.1002/qj.2687>.
- Yurkin, M. A. and A. G. Hoekstra (2007). "The discrete dipole approximation: an overview and recent developments." In: *Journal of Quantitative Spectroscopy and Radiative Transfer* 106.1-3, pp. 558–589. DOI: <https://doi.org/10.1016/j.jqsrt.2007.01.034>.
- Yurkin, Maxim A and Alfons G Hoekstra (2011). "The discrete-dipole-approximation code ADDA: capabilities and known limitations." In: *Journal of Quantitative Spectroscopy and Radiative Transfer* 112.13, pp. 2234–2247. DOI: <https://doi.org/10.1016/j.jqsrt.2011.01.031>.
- Zawadzki, I (2013). "Observations of snow growth by a vertically pointing radar." In: *36th Conf. on Radar Meteorology*.
- Zawadzki, I., F. Fabry, and W. Szyrmer (2001). "Observations of supercooled water and secondary ice generation by a vertically pointing X-band Doppler radar." In: *Atmospheric Research* 59-60, pp. 343–359. DOI: [10.1016/S0169-8095\(01\)00124-7](https://doi.org/10.1016/S0169-8095(01)00124-7).
- Zubko, E., D. Petrov, Y. Grynko, Y. Shkuratov, H. Okamoto, K. Muinonen, T. Nousiainen, H. Kimura, T. Yamamoto, and G. Videen (2010). "Validity criteria of the discrete dipole approximation." In: *Applied optics* 49.8, pp. 1267–1279. DOI: <https://doi.org/10.1364/AO.49.001267>.



## LIST OF ACRONYMS AND VARIABLES

---

$A$	projected area
$\alpha$	attenuation along the path through the atmosphere at the transmitted wavelength
$\alpha_a$	deposition coefficient of axis a
$\alpha_c$	deposition coefficient of axis c
$\beta$	prefactor
$C$	electrical capacitance of the ice particle
$c_a$	thermal conductivity of moist air
CEL	constant elevation
CTT	cloud top temperature
$D$	diameter
$D_0$	median mass diameter
$d_f$	fractal dimension
$D_{max}$	maximum dimension
$D_v$	water vapour diffusivity in air
DDA	Discrete Dipole Approximation
DGL	dendritic growth layer
DSD	drop size distribution
DWD	german weather service
DWR	dual-wavelength ratio
$DWR_{att}$	DWR due to differential attenuation
$DWR_{hard}$	DWR due to hardware offsets
$DWR_{KaW}$	DWR at Ka-, W-band
$DWR_{scat}$	DWR due to differential scattering
$DWR_{XKa}$	DWR at X-, Ka-band
$E_{agg}$	aggregation efficiency
$E_c$	collision efficiency
$e_i$	vapour pressure
$\mathbf{E}^i$	incident electromagnetic field
$e_{s,i}$	saturation vapour pressure over ice
ECMWF	European Centre for Medium-Range Weather Forecast
EM	electromagnetic
$\epsilon$	complex refractive index

$\epsilon_o$	eccentricity of oblates
$\epsilon_p$	eccentricity of prolates
$E_s$	sticking efficiency
$E^s$	scattered electromagnetic field
$f$	frequency
$\bar{f}$	particle-average ventilation coefficient
$f_{RGA}$	form factor
FMCW	frequency modulated continuous wave
G	radar gain
$\gamma$	slope
$\Gamma$	inherent growth function
h	pulse width
HM	Hallett-Mossop
ICON	Icosahedral Nonhydrostatic Model
IFS	Integrated Forecast System
INP	ice nucleating particles
IWC	ice water content
IMP	ice microphysical processes
JOYCE-CF	Jülich ObservatorY for Cloud Evolution Core Facility
$ K ^2$	dielectric factor
$K_{agg}$	aggregation kernel
$\kappa$	kurtosis
KDP	specific differential phase shift
$\lambda$	wavelength
LDR	linear depolarisation ratio
$L_s$	latent heat of sublimation
m	mass
McSNOW	Monte-Carlo Lagrangian particle model
MDV	mean Doppler velocity
$MDV_{Ka}$	mean Doppler velocity at Ka-band
ML	melting layer
n	refractive index of the atmosphere
$n_{rp0}$	number of real particles
PAMTRA	Passive and Active Microwave TRAnsfer model
PARSIVEL	Particle Size and Velocity Disdrometer
$\Phi$	azimuth beam width
$\phi$	aspect ratio

$\phi_i$	phase shift
$\phi_{dp}$	differential phase shift
PPI	plan position indicator
$P_r$	received power
PSD	particle size distribution
$P_t$	transmitted power
QLL	quasi-liquid layer
RGAs	Rayleigh-Gans approximation
$RH_i$	relative humidity over ice
$RH_w$	relative humidity over water
RHI	range height indicator
$\rho$	density
$\rho_{depo}$	deposition density
$\rho_i$	density of solid ice
$\rho_{hv}$	co-polar correlation coefficient
$R_v$	gas constant of water vapour
$S_i$	ambient saturation ratio with respect to ice
$S_{na}$	simulation with a narrow PSD
$S_{n,2nd}$	simulation with a narrow PSD and secondary mode due to primary nucleation
$S_{n,frag}$	simulation with a narrow PSD and secondary mode due to fragmentation
$S_{wi}$	simulation with a wide PSD
$S_{w,2nd}$	simulation with a wide PSD and secondary mode due to primary nucleation
$S_{w,frag}$	simulation with a wide PSD and secondary mode due to fragmentation
$\sigma_b$	backscattering cross section
$\sigma_b$	backscattering cross section
SIP	secondary ice production
SLW	super-cooled liquid water
SNR	signal-to-noise ratio
<b>S</b>	amplitude scattering matrix
SSRGA	self-similar Rayleigh-Gans approximation
STSR	simultaneous transmit simultaneous receive
$S_w$	super-saturation with respect to water
SW	spectral width
sZDR	spectrally resolved ZDR

$sZDR_{\max}$	maximum sZDR
$sZDR_{\max,obs}$	observed $sZDR_{\max}$
$sZDR_{\max,sim}$	simulated $sZDR_{\max}$
$sZe$	spectral reflectivity
$\theta$	elevation beam width
$\Theta$	scattering angle
TRIPEX	Triple-frequency and polarimetric radar experiment for improving process observation of winter precipitation
TRIPEX-POL	Triple-frequency and polarimetric radar experiment for improving process observation of winter precipitation
$V$	volume
$v_D$	Doppler velocity
$X$	size parameter
$Z$	radar reflectivity factor
ZDR	differential reflectivity
$Ze$	equivalent radar reflectivity factor
$Ze_{Ka}$	equivalent radar reflectivity factor at Ka-band
$\zeta_i$	scaling factor

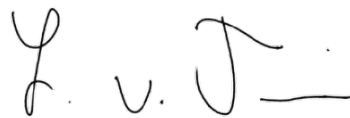


## ERKLÄRUNG

---

Hiermit versichere ich an Eides statt, dass ich die vorliegende Dissertation selbstständig und ohne die Benutzung anderer als der angegebenen Hilfsmittel und Literatur angefertigt habe. Alle Stellen, die wörtlich oder sinngemäß aus veröffentlichten und nicht veröffentlichten Werken dem Wortlaut oder dem Sinn nach entnommen wurden, sind als solche kenntlich gemacht. Ich versichere an Eides statt, dass diese Dissertation noch keiner anderen Fakultät oder Universität zur Prüfung vorgelegen hat; dass sie - abgesehen von unten angegebenen Teilpublikationen und eingebundenen Artikeln und Manuskripten - noch nicht veröffentlicht worden ist sowie, dass ich eine Veröffentlichung der Dissertation vor Abschluss der Promotion nicht ohne Genehmigung des Promotionsausschusses vornehmen werde. Die Bestimmungen dieser Ordnung sind mir bekannt. Darüber hinaus erkläre ich hiermit, dass ich die Ordnung zur Sicherung guter wissenschaftlicher Praxis und zum Umgang mit wissenschaftlichem Fehlverhalten der Universität zu Köln gelesen und sie bei der Durchführung der Dissertation zugrundeliegenden Arbeiten und der schriftlich verfassten Dissertation beachtet habe und verpflichte mich hiermit, die dort genannten Vorgaben bei allen wissenschaftlichen Tätigkeiten zu beachten und umzusetzen. Ich versichere, dass die eingereichte elektronische Fassung der eingereichten Druckfassung vollständig entspricht.

*Köln, 19. September 2022*



---

Leonie von Terzi

**First author publications**

**von Terzi, L., Dias Neto, J., Ori, D., Myagkov, A., and Kneifel, S. (2022): Ice micro-physical processes in the dendritic growth layer: a statistical analysis combining multi-frequency and polarimetric Doppler cloud radar observations, Atmos. Chem. Phys., 22, 11795–11821, <https://doi.org/10.5194/acp-22-11795-2022>**

**Co-author publications**

Mason, S. L., Hogan, R. J., Westbrook, C. D., Kneifel, S., Moisseev, D. and **von Terzi, L. (2019). The importance of particle size distribution and internal structure for triple-frequency radar retrievals of the morphology of snow. Atmospheric Measurement Techniques, 12.9, pp. 4993–5018, <https://doi.org/10.5194/amt-12-4993-2019>**

Ori, D., Schemann, V., Karrer, M., Dias Neto, J., **von Terzi, L.**, Seifert, A. and Kneifel, S. (2020). **Evaluation of ice particle growth in ICON using statistics of multi-frequency Doppler cloud radar observations. Quarterly Journal of the Royal Meteorological Society, 146.733, pp. 3830–3849. <https://doi.org/10.1002/qj.3875>**

Trömel, S., Simmer, C., Blahak, U., Blanke, A., Doktorowski, S., Ewald, F., Frech, M., Gergely, M., Hagen, M., Janjic, T. and Kalesse-Los, H., **von Terzi, L.** and others, (2021). **Overview: Fusion of radar polarimetry and numerical atmospheric modelling towards an improved understanding of cloud and precipitation processes. Atmospheric Chemistry and Physics, 21.23, pp. 17291–17314, <https://doi.org/10.5194/acp-21-17291-2021>**

Mróz, K., Battaglia, A., Kneifel, S., **von Terzi, L.**, Karrer, M. and Ori, D. (2021). **Linking rain into ice microphysics across the melting layer in stratiform rain: a closure study. Atmospheric Measurement Techniques, 14.1, pp. 511–529, <https://doi.org/10.5194/amt-14-511-2021>**

Ori, D., **von Terzi, L.**, Karrer, M. and Kneifel, S. (2021). **snowScatt 1.0: consistent model of microphysical and scattering properties of rimed and unrimed snowflakes based on the self-similar Rayleigh–Gans approximation. Geoscientific Model Development, 14.3., pp. 1511–1531, <https://doi.org/10.5194/gmd-14-1511-2021>**

Kneifel, S., Pospichal, B., **von Terzi, L.**, Zinner, T., Puh, M., Hagen, M., Mayer, B., Löhnert, U. and Crewell, S. (2021). **Multi-year cloud and precipitation statistics observed with remote sensors at the high-altitude Environmental Research Station Schneefernerhaus in the German Alps. Meteorologische Zeitschrift, 31.1, pp. 69–86, <https://doi.org/10.1127/metz/2021/1099>**

Karrer, M., Dias Neto, J., **von Terzi, L.** and Kneifel, S. (2022). **Melting Behavior of Rimed and Unrimed Snowflakes Investigated With Statistics of Triple-Frequency Doppler Radar Observations. Journal of Geophysical Research: Atmospheres, 127.9, p.e2021JD035907, <https://doi.org/10.1029/2021JD035907>**

## COLOPHON

This document was typeset using the typographical look-and-feel `classicthesis` developed by André Miede and Ivo Pletikosić. The style was inspired by Robert Bringhurst's seminal book on typography "*The Elements of Typographic Style*". `classicthesis` is available for both  $\text{\LaTeX}$  and  $\text{\LyX}$ :

<https://bitbucket.org/amiede/classicthesis/>

Happy users of `classicthesis` usually send a real postcard to the author, a collection of postcards received so far is featured here:

<http://postcards.miede.de/>

*Final Version* as of 19. November 2023 (`classicthesis` v4.6).